UiT
NORGES
ARKTISKE
UNIVERSITET

Faculty of Science and Technology

Methane bubbles in the Arctic Ocean

Quantification, variability analysis and modelling of free and dissolved methane from the seafloor to the atmosphere

—

Pär Jansson

A dissertation for the degree of Philosophiae Doctor – May 2018

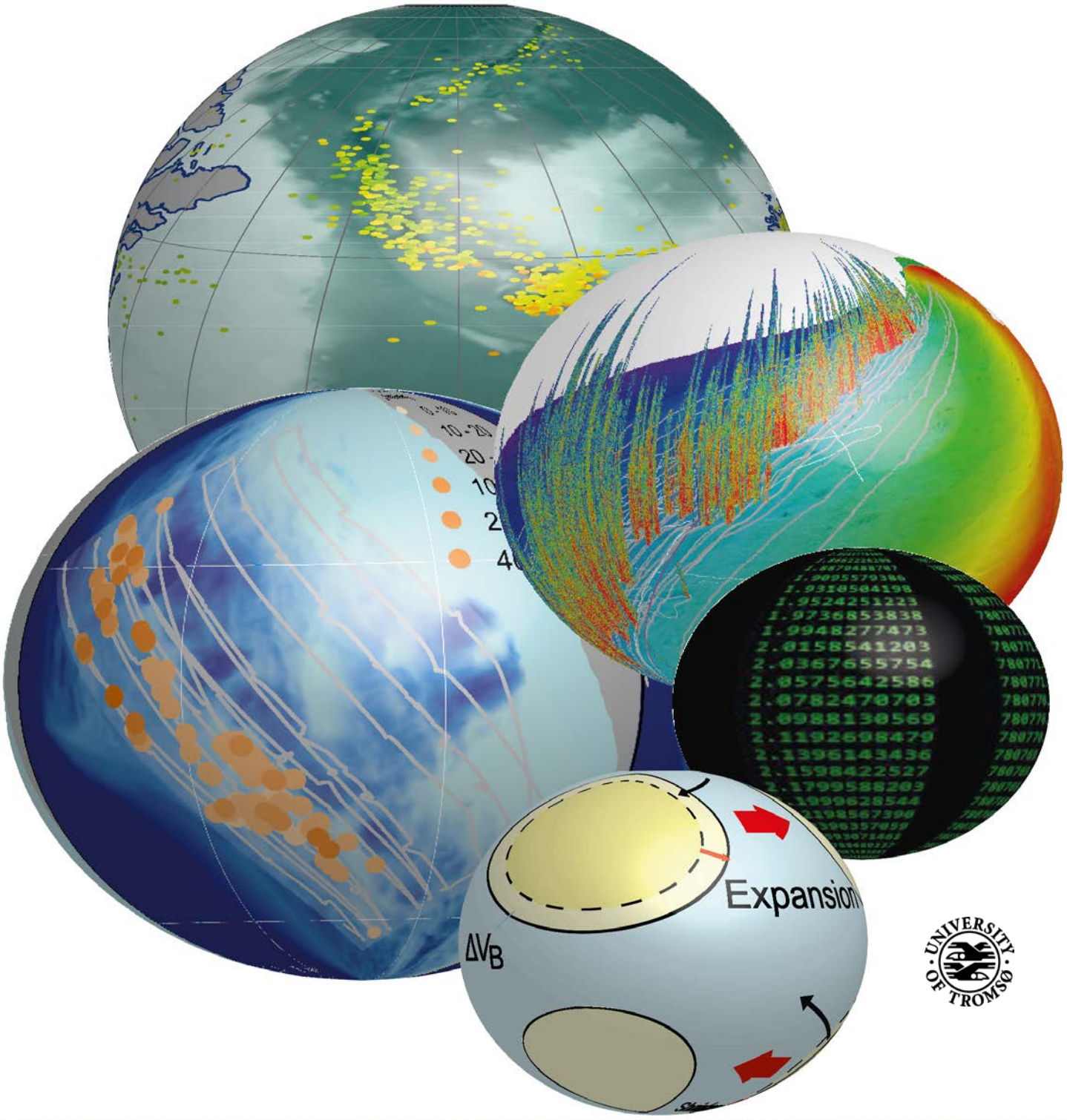

UNIVERSITY OF TROMSØ

Table of Contents

List of Tables

List of Figures

1 Acknowledgements

First, I would like to thank my supervisor Bénédicte Ferré for the support, both personally and scientifically, during the PhD appointment. You always answered my questions quickly and gave relevant and insightful feedback on my work. You made me feel welcome and important in the water column group of CAGE. Anna Silyakova deserves a big thank you for friendly and constructive criticism and helping me to stay focused on the most important tasks. I would like to thank Jens Greinert for inspiring me in the starting phase of the project. Knut Ola Dølven, always enthusiastic and supportive was a big motivator too. The technical staff and administration at the Department of Geosciences (IG) deserves a big thank you for all the support I needed to work with my research questions and take necessary courses and maintaining a very nice work environment. The staff at the IT department of faculty of Science and Technology and at IG. Without the support from the crew on board RV Helmer Hanssen, none of this research would have been possible, so thanks a lot to you all. Finally, I want to thank my family for the support and understanding during lengthy cruises, late night- and weekend work and the few and short vacations.

The research project and PhD appointment was funded by UiT, through its Centre of Excellence funding scheme for CAGE, project number 22359.

2 Preface

This thesis is submitted in partial fulfilment of the requirements for Philosophiae Doctor Degree, PhD, at UiT, the Arctic University of Norway in Tromsø. The PhD appointment started in May 2014 and was funded by UiT, through its Centre of Excellence funding scheme for CAGE, project number 22359 over a period of four years including one year of duty work for the Department of Geology.

The duty work, comprising in total 1655 hours, included participation in the Outreach program Forskningsdagene in 2014; assisting in teaching courses GEO-3182, Marine Geohazards in 2015, 2016, and 2017; GEO-2003, Quaternary Geology in 2015. It also included participation in scientific seagoing expeditions, mainly to areas offshore Svalbard and the Barents Sea. Cruises attended for duty work included CAGE cruises 14-5, 15-3, 15-5, 15-6, 16-2, 16-4, 16-5, 16-7, and 17-1 with RV Helmer Hanssen and PS93.2 with RV Polarstern. Also included was a teaching cruise within the framework of GEO-2010, Marine geology in 2017. The duty work carried out during the cruises included acquisition of data from CTD, ADCP, single beam echosounders and water sampling for CH_4 concentration, nutrients and CDOM. Moreover, the work included plankton net sampling, preparing, retrieving, and sectioning of gravity core sections with subsequent pore water sampling for chemical analysis and preparation of sediment samples for analysis of hydrocarbon gas (C_1-C_5). Assembly, deployment, recovery, disassembly and shipping of CAGE seafloor observatories (K-landers) was also included in the duty work as well as planning, deployment (at 79°4´N 4°7´E, ~2500 m water depth) and recovery of a methane sensor (METS, Franatech) attached to the deep sea lander in the Central Hausgarten (e.g. van Oevelen et al., 2011) in collaboration with Alfred Wegener Institute of Marine Research (AWI).

The thesis at hand comprises a synthesis of a selection of the work conducted during the PhD appointment: an introduction to methane in the water column and working areas with references to

manuscripts considered for the dissertation; a summary of each manuscript; a conclusion and outlook section and the four chosen manuscripts at their current states.

The included manuscripts and the state of their publication processes at the time of the submission of this thesis are detailed in section 3. A co-author declaration, specifying the contribution of all co-authors, is given in section 4. The four manuscripts included in this thesis are:

1. **Variability of acoustically evidenced methane bubble emissions offshore western Svalbard**

2. **Physical controls of dynamics of methane venting from a shallow seep area west of Svalbard.**

3. **A new numerical model for understanding free and dissolved gas progression towards the atmosphere in aquatic methane seepage.**

4. **Insights from underwater high resolution dissolved methane sensing over a known methane seepage site west of Svalbard.**

Apart from the four manuscripts included in this thesis, I also contributed to the following articles during the PhD period:

Lars Arneborg, Pär Jansson, André Staalstrøm, & Göran Broström. 2017. **Tidal Energy Loss, Internal Tide Radiation, and Local Dissipation for Two-Layer Tidal Flow over a Sill.** *Journal of Physical Oceanography, 47(7), pp. 1521-1538.* I contributed to this article with model simulations, analysis of model output and manuscript editing.

Cathrine Lund Myhre, Bénédicte Ferré, Stephen Matthew Platt, Anna Silyakova, Ove Hermansen, Allen Grant, Ignacio Pisso, Norbert Schmidbauer, Andreas Stohl, Jospeh Pitt, Pär Jansson, Jens Greinert, and others. 2016. **Extensive release of methane from Arctic seabed west of Svalbard during summer 2014 does not influence the atmosphere.** *Geophysical Research Letters, 43(9), pp. 4624-4631.* I contributed with 3D image preparation, collection/analysis of discrete dissolved CH_4 samples and with manuscript editing.

Giuliana Panieri, Stefan Bünz, Daniel J. Fornari, Javier Escartin, Pavel Serov, Pär Jansson, Marta E. Torres, Joel E. Johnson, Wei Li Hong, Simone Sauer, Rafael Garcia, Nuno Gracias. 2017. **An integrated view of the methane system in the pockmarks at Vestnesa Ridge, 79° N.** *Marine Geology, 390, pp. 282-300.* I contributed with free gas flow rate calculations based on single beam echosounder data, collection/analysis of water samples and manuscript writing and editing.

Roberto Grilli, Jack Triest, Jérôme Chappellaz, Michel Calzas, Thibault Desbois, Bénédicte Ferré, Christophe Guillerm, Pär Jansson, Loïc Lechevallier, Victor Ledoux, Daniele Romanini. **SUB-OCEAN: subsea dissolved methane measurements using an embedded laser spectrometer technology.** Submitted to *Environmental Science & Technology.* I performed analysis of methane concentrations using gas chromatography and contributed to the manuscript.

Bénédicte Ferré, Pär. Jansson, Manuel Moser, Pavel Serov, Friederike Gründger, Alexey Portnov, Carolyn A. Graves, Christian Berndt, Moritz Lehmann, Helge Niemann. **Cold Seep Hibernation: Seasonal variation of methane emission offshore Svalbard.** In preparation for submission to *Nature Communication.* I contributed with spatial analysis of echosounder data and manuscript preparation.

3 List of papers and co-author contributions

The four manuscripts, included in this thesis and their corresponding publication status at the time of the submission of the thesis are:

1. Mario E. Veloso-Alarcón, Pär Jansson, Marc De Batist, Timothy A. Minshull, Graham K. Westbrook, Heiko Pälike, Stefan Bünz, Ian Wright, Jens Greinert. ***Variability of acoustically evidenced methane bubble emissions offshore western Svalbard.*** Resubmitted to *Geophysical Research Letters*

2. Anna Silyakova, Pär Jansson, Pavel Serov, Bénédicte Ferré, Alexey Pavlov, Tore Hattermann, Carolyn A. Graves, Stephen Matthew Platt, Cathrine Lund Myhre, Friederike Gründger and Helge Niemann. ***Physical controls of dynamics of methane venting from a shallow seep area west of Svalbard.*** Submitted to *Journal of Geophysical Research - Oceans*.

3. Pär Jansson, Bénédicte Ferré, Anna Silyakova, Knut Ola Dølven, Anders Omstedt. ***A new numerical model for understanding free and dissolved gas progression towards the atmosphere in aquatic methane seepage systems.*** Submitted to *Oceanography and Limnology: Methods*.

4. Jack Triest, Pär Jansson, Roberto Grilli, Anna Silyakova, Bénédicte Ferré, Jérôme Chappellaz, Jürgen Mienert. ***Insights from underwater high resolution dissolved methane sensing over a known methane seepage site west of Svalbard.*** In preparation for submission to *Journal of Geophysical Research – Oceans*

3.1 Contributions

Table 1. Author contributions to the manuscripts included in the thesis.

	Paper 1	**Paper 2**	**Paper 3**	**Paper 4**
Concept and idea	MV, JG, MB	AS, BF	PJ, BF	JC, JM, JT, PJ
Study design and methods	MV, PJ	AS, PJ	PJ, BF, AS, AO	JT, PJ
Data gathering and interpretation	MV, PJ*	AS, PJ	PJ, BF	JT, PJ*, RG
Manuscript preparation	MV, PJ*, MB, TM, GW, HP, SB, IW, JG	AS, PJ, PS, BF, AP, TH, CG, SP, CL, FG, HN	PJ, BF, AS, KD, AO	JT, PJ*, RG, AS, BF, JC

** co-corresponding author*

***Authors in Alphabetical order: MB** = Marc De Batist; **SB** = Stefan Bünz; **JC** = Jérôme Chappellaz; **KD** = Knut Ola Dølven; **BF** = Bénédicte Ferré; **CG** = Carolyn Graves; **JG** = Jens Greinert; **RG** = Roberto Grilli; **FG** = Friederike Gründger; **TH** = Tore Hattermann; **PJ** = Pär Jansson; **CLM** = Cathrine Lund Myhre; **JM** = Jürgen Mienert; **TM** = Timothy A. Minshull; **HN** = Helge Niemann; **AO** = Anders Omstedt; **AP** = Alexey Pavlov; **SP** = Stephen Platt; **HP** = Heiko Pälike; **PS** = Pavel Serov; **AS** = Anna Silyakova; **JT** = Jack Triest; **MV** = Mario E. Veloso-Alarcón;*

***GW** = Graham Westbrook; **IW** = Ian Wright*

4 Introduction

One of the major challenges for humankind in the near future is to manage Earth's resources in a responsible way and to maintain an environment suitable for living in. The climate affects us all in daily life and we now experience rapid changes, possibly caused by human activity. It has become increasingly recognized that knowledge of the climate system, its driving forces and feedback mechanisms must be improved in order to help stakeholders, politicians and the general public to take appropriate actions. Climate change is however an extremely complicated subject and multiple processes contribute in ways we can only estimate by developing models. The greenhouse effect, originally suggested by Svante Arrhenius in 1895 (Fleming, 2005), has been a research focus for many decades and the consensus is that gases with warming potential cause heat to be trapped in the atmosphere (Pachauri et al., 2014) and that this is one of the most important topics to study. Methane (CH_4) is a powerful greenhouse gas, estimated to be 32 times more potent than carbon dioxide (CO_2) (Pachauri et al., 2014), contributing to approximately one-sixth of the total warming generated by greenhouse gases in the atmosphere (Kirschke et al., 2013). The oceans play an important role in the global gas budget since the hydrosphere (all oceans, rivers and lakes) stores enormous amounts of dissolved gases. Because gas is constantly exchanged between the atmosphere and the hydrosphere, the oceans can serve as a sink of greenhouse gas but may also contribute with a source to the atmosphere by diffusive equilibration between the dissolved gas in the upper layer of the oceans and the lower atmosphere (Broecker and Peng, 1974; Wanninkhof, 2014).

Moreover, large amounts of CH_4 in aqueous and gaseous form exist in the ocean sediments together with CH_4 in the form of hydrates (e.g. Kvenvolden, 1988; Ruppel and Kessler, 2016), ice-like crystal structures of solid water cages encapsulating non-polar guest molecules. The hydrate structure is stable only in cold environments with high pressure (Sloan, 1998), the so called hydrate stability zone (HSZ). CH_4 hydrates are found on continental margins worldwide and are abundant in the Arctic Ocean (Kvenvolden and Lorenson, 2001). As hydrates dissociate when any of the criteria for their stability is not met (i.e. temperature increases or pressure decreases), it is expected that hydrates located where conditions are close to the hydrate stability limit may dissociate with warming ocean bottom water (Westbrook et al., 2009; Berndt et al., 2014). The effect of dissociating natural gas hydrates would represent a climate feedback mechanism if the resulting CH_4 reached the atmosphere. The Arctic Ocean is currently warming rapidly (Ferré et al., 2012) and concerns have been raised that some CH_4 hydrates will dissociate and that free or dissolved CH_4 gas will seep into the water column and subsequently reach the atmosphere (Shakhova et al., 2010). Numerical modelling by Wallmann et al. (2018) shows that the dominating control mechanism for gas release offshore Svalbard is pressure release after the retreat of the ice-sheet following the last glaciation, rather than ocean anthropogenic effects such as increasing bottom water temperature.

The solubility of CH_4 is reduced at lower pressure and higher temperature. This could, if the concentration of dissolved CH_4 in pore water is high, cause gas to come out of solution (exsolve) and spontaneously form bubbles. Römer et al. (2016) showed that gas bubble release increased during decreasing tidal pressure at a site west of Vancouver. Flares were observed to recur at tidal frequency east of New Zealand (Linke et al., 2010). Thus, it is expected that pressure changes on short and long time scales is a controlling factor for the intensity of benthic gas release.

By geochemical modelling, Fischer et al. (2013) found a relation between a major earthquake in 1945 and increased upwards flux of CH_4, lasting for several decades in the area offshore Pakistan. As our study site (see section “Study Area”) is located in a seismically active zone (Plaza – Faverola et al., 2015) with frequent earthquakes in the vicinity (International Seismological Centre 2014), it may be expected that the seepage intensity is influenced by seismic activity.

It is imperative to understand these, and possibly other, controlling mechanisms on methane seepage activity. In Paper 1, we presented a conceptual model, bearing in mind the proposed controlling mechanisms, and we compared their variations with free gas flow rates inferred from echosounder data collected during 11 cruises and a time span of 8 years.

The fate of CH_4, bubbling from the seafloor, depends on physical oceanographic conditions, ocean-atmosphere interaction, and biochemical processes in the water column. Ocean currents carry dissolved methane away from the local bubble sources and therefore play a major role in the horizontal distribution of dissolved CH_4, together with mixing induced by horizontal eddies and diffusion. In Paper 2, we investigate the relation between seepage activity, subsequent release to the atmosphere, oceanographic conditions, and the observed resulting distribution of dissolved CH_4.

The vertical distribution of the bubble-mediated CH_4 is governed by the interaction of the bubbles with the ambient conditions. While bubbles rise through the water column, gas of all present species may dissolve or exsolve depending on whether the ambient concentration is lower or higher than the equilibrium concentration of the corresponding gas inside the bubble. The rate of gas transfer across the bubble rims depends on the magnitude of the concentration gradient, the gas diffusivity, the bubble rising speed, the local turbulence, the temperature and the salinity (e.g. Leifer and Patro, 2002; McGinnis et al., 2006). Therefore, the bubbles affect and are affected by the ambient conditions and must be understood simultaneously with the local water column conditions. In Paper 3, a new numerical model was presented, that resolves the dynamics between bubble- and dissolved gas. The model also included aerobic oxidation, which occurs when methanotrophic bacteria are present in the water column (Reeburgh, 2007).

At a site where the HSZ pinches out at the seafloor, it has been speculated that observed CH_4 bubbles derive from dissociating hydrates (Westbrook et al., 2009; Berndt et al., 2014). In Paper 4, we investigate this site, using the gas flow rate estimation method from Paper 1 together with the prediction of vertical CH_4 distribution from the process-based model in Paper 3.

5 Study area

During the period of this PhD project, several CAGE research cruises have visited at least five prominent seepage areas west and northwest of Prins Karls Forland (PKF) and the Barents Sea, as indicated by yellow stars in Figure 1.

In the Barents Sea, CAGE investigates at least three areas of seepage activity. Intense bubbling occurs from pingo-like features at 370 – 390 mbsl, south of Spitsbergen (Serov et al., 2017). At the so called Crater Area (330 – 360 mbsl), located in the Bjørnøy through, seepage exist from crater-like features, postulated to derive from blowout of free gas and hydrates as hydrates dissociated due to the pressure release after the last glacial period (Andreassen et al., 2017). Pingo like features with gas leakage have also been observed in the Maud Basin.

Persistent CH_4 seepage exist at Vestnesa Ridge (e.g. Panieri et al., 2017), near the spreading ridge system (Molloy Transform Fault; Spitsbergen Transform Fault; Molloy Ridge; Knipovich Ridge). The ridge area (~1200 mbsl) has been monitored by the Institute of Geoscience (IG) of The Arctic University of Norway, Tromsø, and CAGE since the discovery of CH_4 seepage from pockmarks in 2008 (Hustoft et al., 2009; Bünz et al., 2012). Seismic studies show that the Vestnesa Ridge sediments host hydrates and trapped gaseous CH_4, susceptible to release where and when fractures occur in the sediments due to tectonic stress (Plaza – Faverola et al., 2015).).

The main study area for this thesis was the location offshore PKF, where many gas flares have been observed. The seepage here can be divided into three areas, comprising the shallow shelf (~50 – 150 m water depth), the shelf break (~250 m), and the continental slope (~400 m). In Paper 1, we used data from 11 cruises which covered all three areas (Figure 1 and Table SI1 in Paper 1). In Paper 2, we focus on the shallow shelf, using three datasets from consecutive years, covering the same area. The seepage at the slope was examined with high resolution methane sensing, described in Paper 4 and was included as a case study for the model described in Paper 3.

Despite substantial research efforts, the origins and controls of gas seepage in this area are still not completely elucidated. The shallow shelf (~50 – 150 mbsl) is too shallow for gas hydrates to exist near the seafloor and it is believed that the seepage here presently occurs as a consequence of decreased pressure after the ice sheet retreated, following the last ice age (Portnov et al., 2016). This was also the control mechanism suggested for the crater Area in the Barents Sea.

At the slope (~ 400 mbsl), seepage has been associated with gas hydrates, since the conditions (high pressure, low temperature) for their stability are met. More precisely, the seafloor conditions here are at the limit of the stability for CH_4 hydrates and so short- and long-term temperature variations pushes the stability zone downslope during warm periods and upslope during cold. This, at least in theory, triggers dissociation of hydrates and varying CH_4 emissions. However, no hydrates have been recovered to date (Riedel et al., 2018), and the existence of hydrates has not been proven by seismic studies (Rajan et al., 2012). On the other hand, Rajan et al. (2012) did not rule out the possibility that hydrates are present and Wallmann et al. (2018) found evidence of hydrate dissociation in the pore water composition. The authors consequently suggested that temporal hydrate formation and dissociation controls CH_4 migration pathways. Such dynamic blockings would explain seasonality of benthic free gas seepage intensity (Ferré et al., submitted to *Nature Communications*).

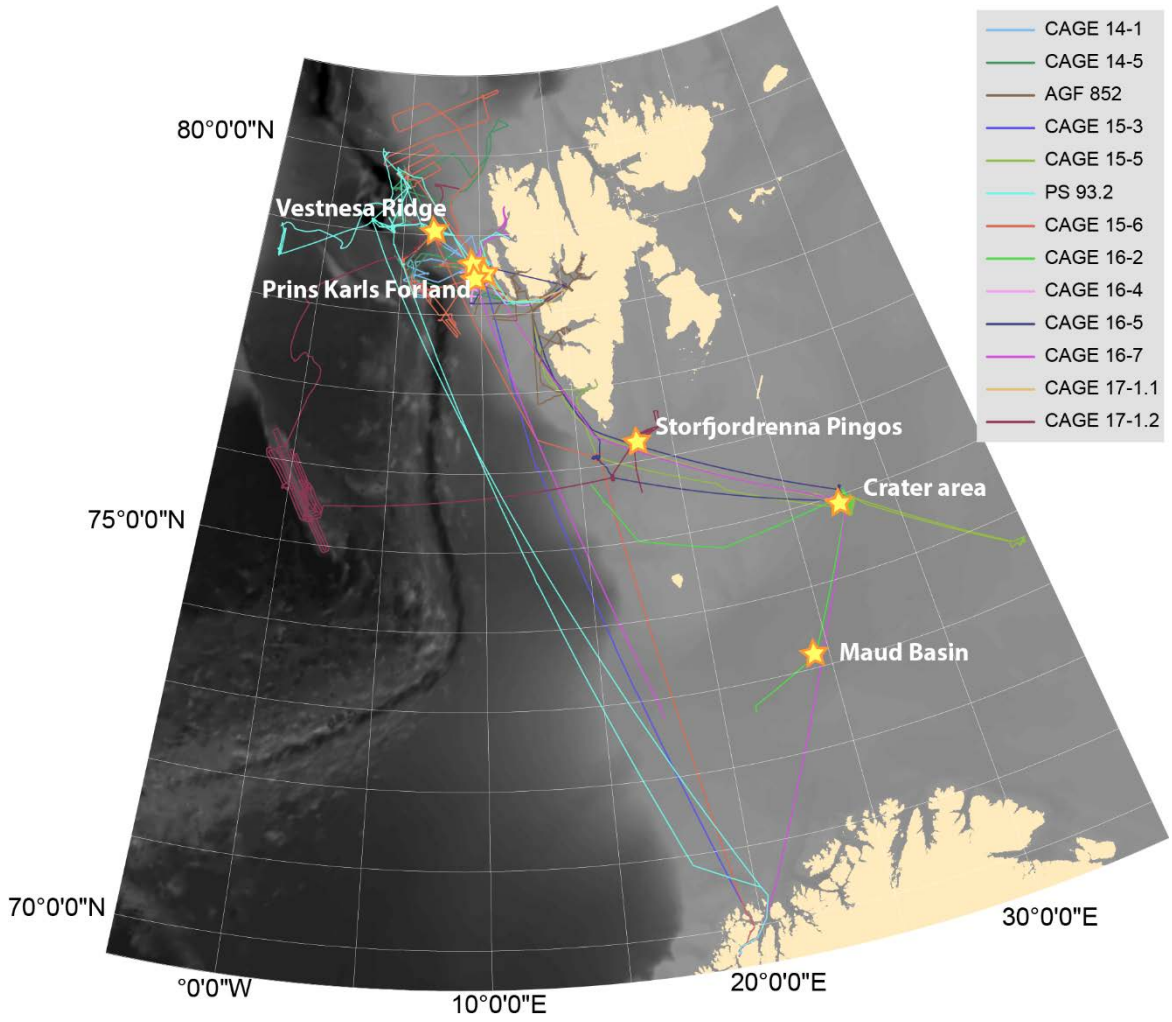

Figure 1. Overview of cruises and investigated methane seepage areas. Stars indicate observed methane seepage areas and lines indicate vessel cruise tracks of attended cruises. Place names and water currents are detailed in paper 1, Figure 1.

It would also explain the findings in Paper 1, namely that gas release intensity varies inversely between the slope (~400 mbsl) and the shelf break (~250 mbsl). We suggested that the two areas are connected through sub seafloor gas migration pathways and that seasonal blocking and opening of the pathways control the seepage intensity at the two locations. Seismic evidence of permeable and impermeable strata, providing such gas migration pathways, was presented by Rajan et al. (2012).

The fate of the bubble-mediated CH_4 emissions largely depends on water column properties and movement by currents (Figure 1, paper 1). The study area hydrography is mainly controlled by the West Spitsbergen Current (WSC), which carries relatively warm and saline Atlantic Water (T>3.0°C in the warm season; S>34.65 PSU; σ <27.92 kg m^{-3} (Cottier et al., 2005)). In addition, the Coastal Current (CC), the extension of the East Spitsbergen Current (ESC), carries colder and less saline water along the western Spitsbergen coast. The front between WSC and CC meanders longitudinally across the slope (Steinle et al., 2015) and is subject to instabilities, and so eddies are ubiquitous on the slope and shelf (Appen et al., 2016). The interplay between the two currents, each carrying different water

masses, results in variable water properties on the shelf, which are additionally affected by local processes such as river run-off and cooling/ heating from the atmosphere.

6 Methods

6.1 Detection and quantification of benthic gas emissions

Owing to the contrasting acoustic properties of free gas and water, bubbles in the water column can be detected by acoustic methods (e.g. Medwin and Clay, 1997; Nikolovska et al., 2008; Weber et al., 2014). The EK60 split-beam echosounder was developed for the fishing industry for quantification and identification of fish stocks (e.g. MacLennan, 1990) but has frequently been used to detect free gas bubbles in the water column (e.g. Haeckel et al., 2004; Maksimov and Sosedko, 2005; Greinert et al., 2006). So-called flares (acoustic signatures of bubble streams in the water column, seen in echograms) can be extracted from echosounder data and easily visualized with the Fledermaus Midwater module (www.qps.nl/display/fledermaus/). This makes mapping of gas seepage relatively simple as shown in Figure 2, which shows flares from surveys conducted in 2010, 2013 and 2015 over the slope seepage area west of PKF.

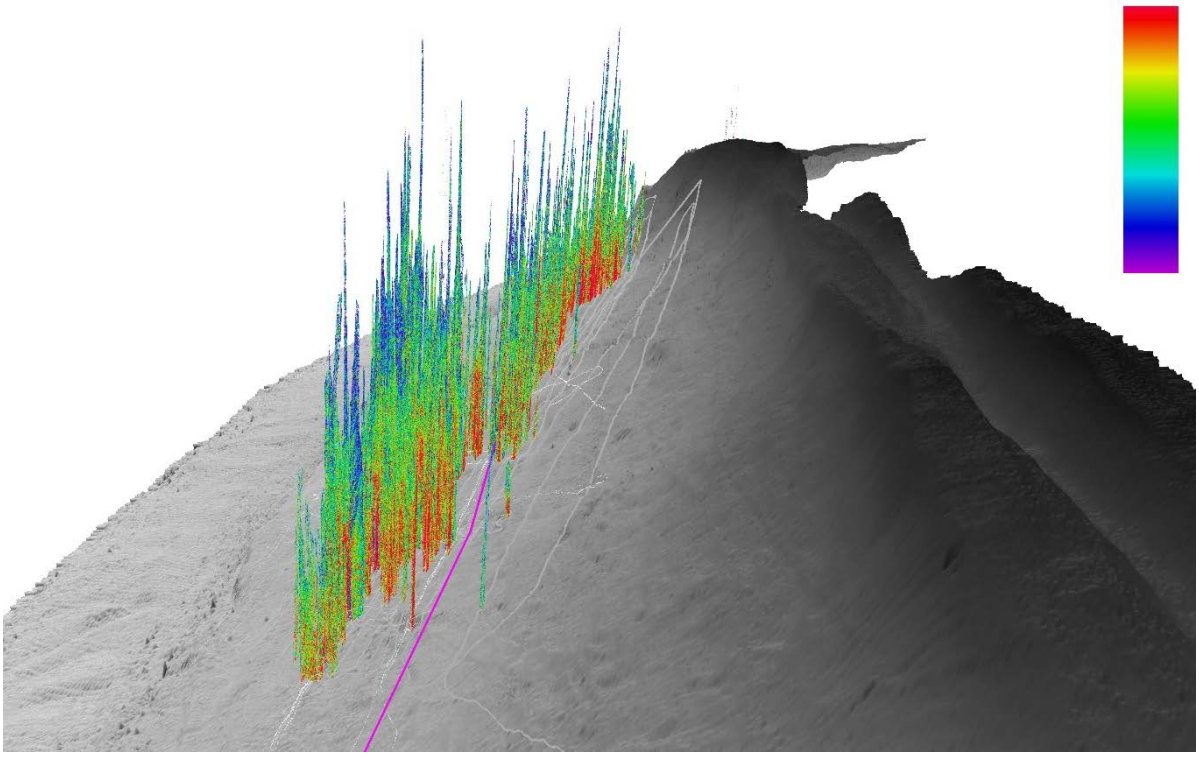

Figure 2. 3D visualization of free gas in the water column detected by echosounder View of free gas in the water column, produced with the Fledermaus QPS software. The echosounder data displayed here stem from cruises in 2010, 2013, and 2015 on the ~400m seepage site west of PKF. Coloured scale indicates the target strength (TS, dB) of the acoustic backscatter. Ship tracks are seen as grey lines and a modelled outcrop of the gas hydrate stability is shown as a purple line.

The mapping allows for comparison with seafloor features such as pockmarks, faults and chimneys and possibly cold-water coral reefs (Hovland and Thomsen, 1997).

The amount of free gas in the water column can also be acoustically quantified with calibrated single-beam echosounders. Provided knowledge of pressure, gas composition, temperature, size and rising speed of the detected bubbles, flow rates can be estimated (Veloso et al., 2015) and repeated echosounder surveys may elucidate on the spatial and temporal variability of free gas emissions.

For our analysis described in Paper 1, echosounder data was collected during eleven cruises using split-beam echosounders mounted on research vessels RV Helmer Hanssen (UiT, The Arctic University of Norway) and RV James Clark Ross (British Antarctic Survey). The split beam echosounder SIMRAD EK60 was operated at 38 kHz, which has been the preferred frequency for detecting bubbles in the water column (e.g. Artemov et al., 2007; Sauter et al., 2006; Veloso et al., 2015).

Estimation of free gas flow rates requires knowledge of water properties, such as temperature, salinity, and pressure. Hence, we gathered oceanographic data for the calculations, described in the section *Oceanographic influence* and seen in Figure 7.

Echosounder data was analysed with the Fledermaus Midwater software and acoustic flares were identified and separated from other scattering objects such as fish, seafloor, strong density gradients, and interference from other acoustic instruments (Figure 3). Subsequently, free gas flowrates were calculated with the FlareHunter software and the FlareFlow Module embedded in the same software bundle (Veloso et al., 2015).

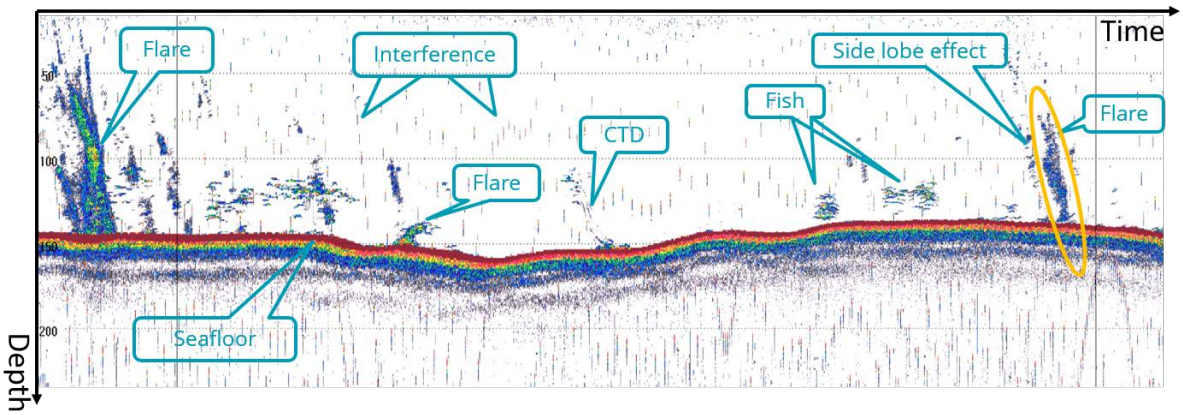

Figure 3. Typical echogram showing flares (An example is highlighted by the yellow oval) and other scattering objects in the water column as indicated by the callouts.

We distinguish bubble streams (flares) from other scattering objects by visual inspection of the echograms (Figure 3). Flares typically extend almost vertically from the seafloor and have a larger vertical than horizontal extent, whereas fish schools are often seen in midwater and do not extend vertically. The seafloor is easily detected as it fills the echosounder beam completely and therefore returns a large fraction of the acoustic signal. Interference from other instruments, typically acoustic Doppler current profilers (ADCPs), multibeam echosounders (MBEs) and frequency-modulated sounders (CHIRPs), is easily distinguished as it occurs in single pings and regular patterns (Figure 3).

In paper 2, we reported on free gas flow rates from echosounder data collected during three research cruises and three consecutive years (2014 – 2016), which covered the same area west of PKF. The surveyed area was approximately 400 km^2 with water depths varying between 50 and 150 m and the ship tracks were 300 – 430 km, resulting in beam coverage between 3.8 and 5.5 km^2.

We calculated echosounder/Flarehunter derived flow rates from a cruise to the slope area west of PKF in October 2015. In paper 3, a new numerical marine 2-phase gas model in one dimension (M2PG1) was presented, for which we used the acquired flow rate data to force case study simulations.

In Paper 4 we used the mapped and calculated flow rates in conjunction with results from M2PG1 to force a 2-dimensional model, and as flux approximation to an analytical steady state calculation.

6.2 Dissolved CH_4

Dissolved CH_4 can be measured by direct sampling of small water quantities and subsequent headspace gas chromatography (GC). This is common praxis in the research field of marine methane. Alternatively, concentrations can be measured using in-situ deployed sensors.

6.2.1 Discrete sampling

Measurements of dissolved CH_4 can be used to map the distribution of CH_4 in the water column in three dimensions. The method is however, time consuming and gives sparse data. Typically, the water is sampled at discrete sampling depths at each sampling station and the possible vertical resolution depends on the number of Niskin bottles available on the rosette. In oceanographic surveys, it is typical to sample seawater in a resolution of kilometres to hundreds of kilometres. However, for the purpose of mapping CH_4 emanating from the seafloor it is beneficial to sample denser grids. Sampling with Niskin Bottles attached to a rosette is standard procedure and subsequent subsampling into serum bottles allow for various chemical analysis. Dissolved CH_4 can be analysed after introduction of headspace gas with zero or known CH_4 content. The headspace is allowed to equilibrate with the water sample and is further analysed by gas chromatography (GC) with a flame ionization detector. The method is detailed in Paper 2 and is similar to the method presented in Magen et al. (2014). In Paper 2, we present dissolved CH_4 data acquired from 64 stations from which we sampled during three surveys in three consecutive years 2014 – 2016. In Paper 3, discrete sampling of CH_4 was used to assess the agreement between measurements and model results. The vertical profiles obtained by discrete sampling and model results were also used as input to a 2-dimensional model in Paper 4.

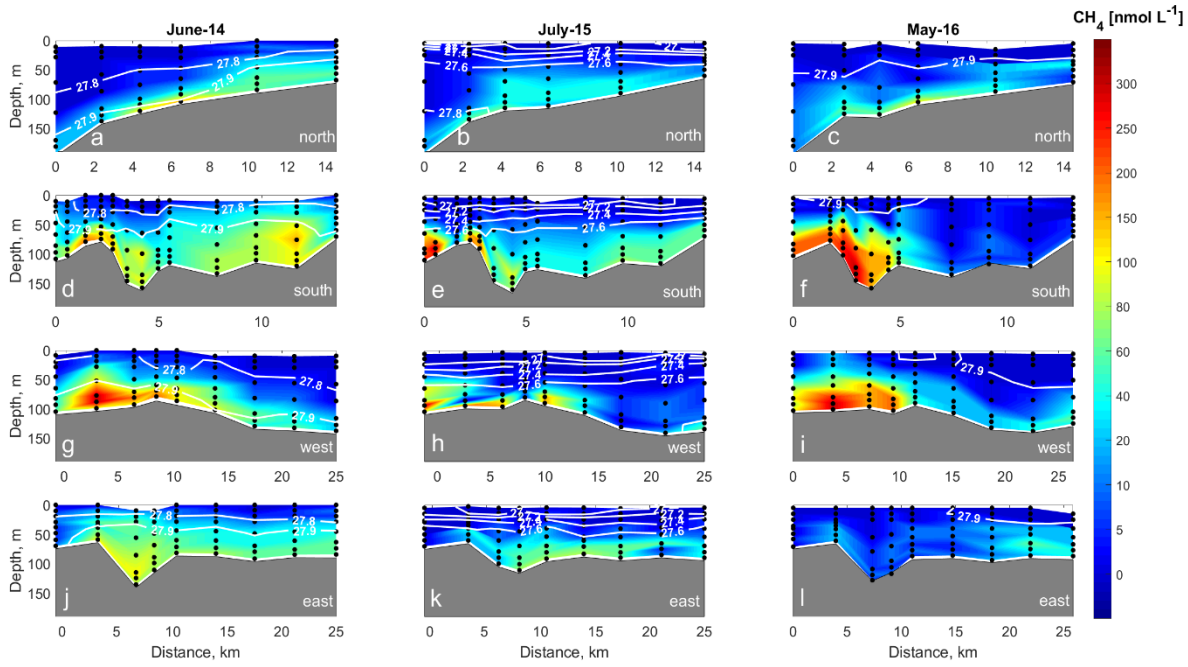

Figure 4. Example of CH_4 concentrations acquired from discrete water sampling. Coloured contours indicate data interpolated between discrete sample depths (black dots). The white lines indicate isolines of density anomaly (kg m^{-3}).

6.2.2 High-resolution measurements

During a three-day survey (October 21 – 23) offshore Svalbard in October 2015, we performed high-resolution CH_4 measurements with a newly developed Membrane Inlet Laser Spectrometer (MILS) (Grilli et al., submitted to *Environmental Science & Technology*) towed behind the research vessel. Sampling with the MILS at a frequency of 1 Hz allowed for unprecedented spatial resolution during both vertical casts and horizontal towing at depths down to 400 mbsl. In Paper 4, the data from the instrument was compared with echograms and showed high values and strong gradients close to gas seepage locations (Figure 6). It resolved the CH_4 concentrations much better than a commonly used reference sensor.

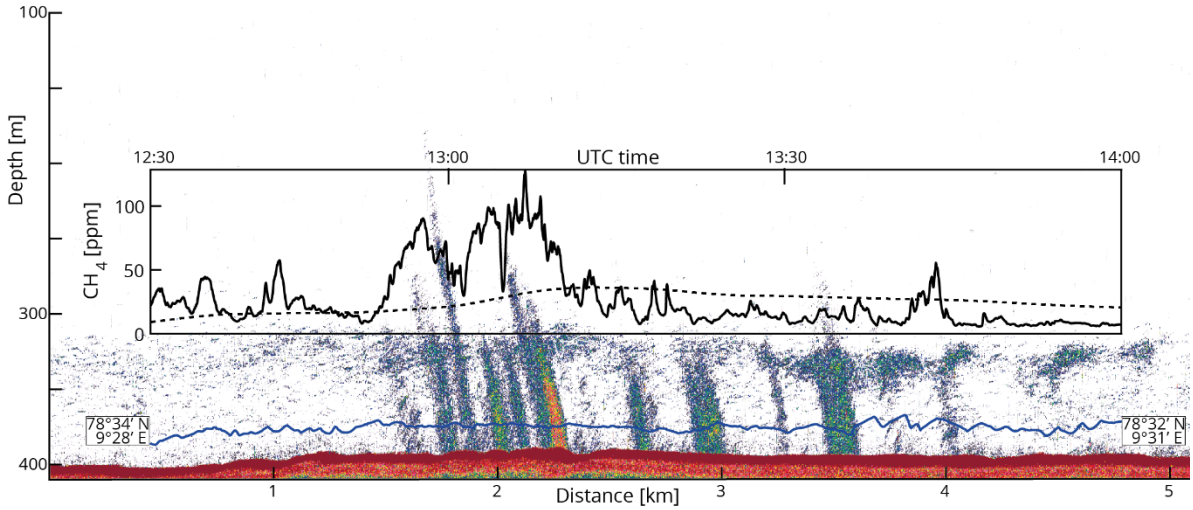

Figure 5. Example data from the towed instrument campaign during the CAGE 15-6 cruise. The top inset panel shows temperature- (red) and salinity- (black) anomaly. The lower inset panel shows MILS data (solid line) and reference sensor data (dashed line). The blue line indicates instrument depth and the background shows backscatter intensity (TS values (dB).

We assessed the agreement between discrete and continuous CH_4 data in Paper 4.

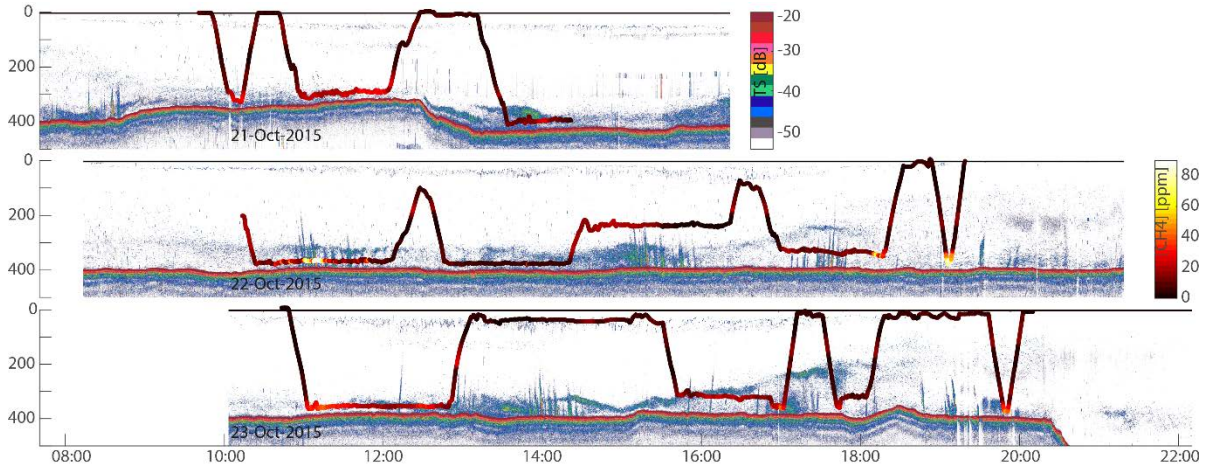

Figure 6. High-resolution measurements with MILS superimposed on echosounder data. The position of the dark red to light yellow track starting around 10 AM each day represents the depth of the MILS sensor and the colour indicates CH_4 mixing ratios measured by the MILS. The background represents the acoustic target Strength (TS), acquired with the echosounder, with a minimum cut-off at -55 dB. High values (red) indicate large abundance of CH_4 bubbles in the water column. The time axis represents local time (2 hours ahead of UTC, for comparison with Figure 5)

6.3 Oceanographic influence

In the framework of working with free and dissolved gas in seawater, it is imperative to know the water properties. In our studies, the water properties influence; a) the free gas quantification method (Flarehunter) because they affect the bubbles' acoustic properties and their rising speeds; b) the process based modelling because they influence the gas dynamics though gas solubility, bubble rising speed and gas transfer efficiency across the bubble rims; c) the control volume model and 2D model are affected through the current velocity and eddy diffusivity.

For the quantification of benthic CH_4 emissions with Flarehunter, conveyed in Paper 1 – 4, knowledge of pressure, salinity, and temperature is necessary. For that purpose, we used CTD (Conductivity, Temperature, and Depth) profiles from hydrocasts performed during the corresponding cruises, and where no such data was available, we downloaded relevant salinity, temperature, and pressure data from the World Ocean Database, managed by the National Oceanographic Data Center: https://www.nodc.noaa.gov/cgi-in/OC5/NPclimatology/arctic.pl

Profiles of seawater density and sound velocity were calculated from the pressure, temperature, salinity profiles, using the GSW Oceanographic Toolbox (McDougall and Barker, 2011), as seen in Figure 7.

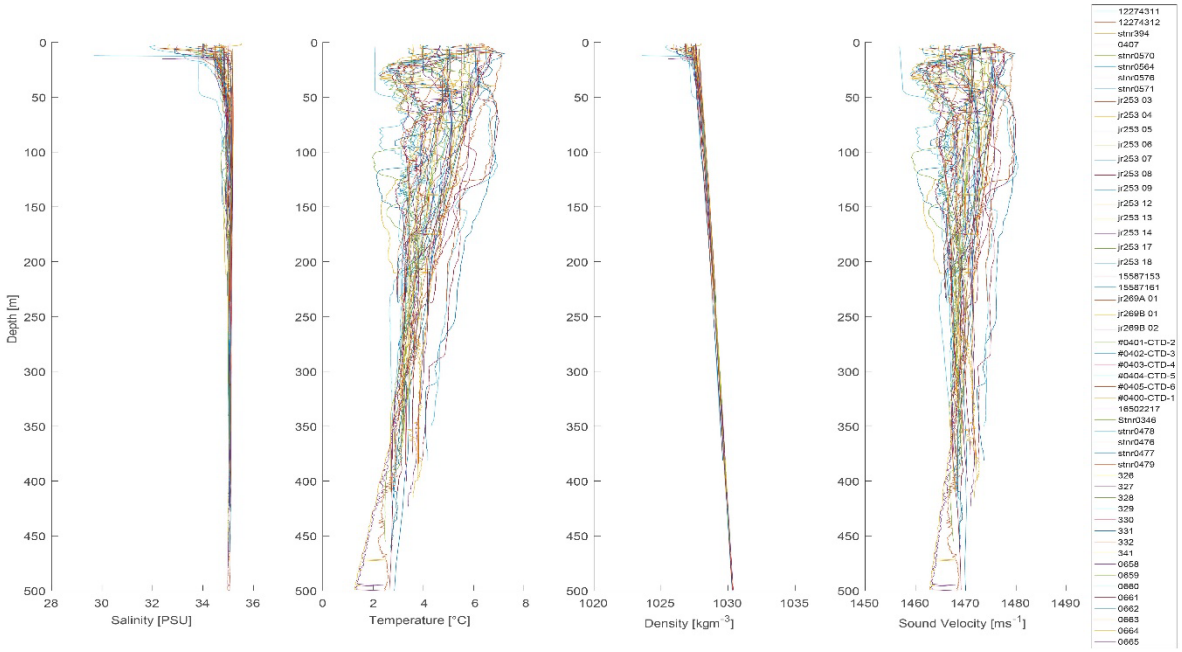

Figure 7. Water properties used for flow rate calculations. Most of the data was acquired during cruises and when not available (profiles 12274311, 12274312 and 165502217), downloaded from the World Ocean Database.

We further used the acquired bottom water temperatures for comparison with temporal seepage activity changes as described in Paper 1.

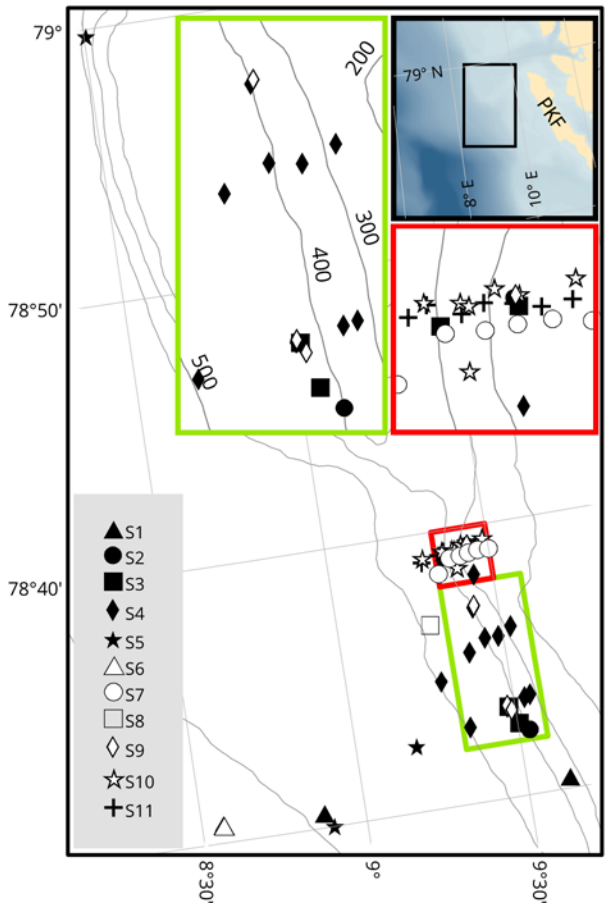

Figure 8. Map of CTD-stations used for flow rate calculations in Paper 1. The shelf break area is boxed with red lines and the slope area is boxed with green lines. Legend indicates which survey the CTD cast refers to. The inset coloured frames show zooms of the two areas and the black framed map shows the location of the sites offshore PKF. Data from the individual CTD casts are shown in Figure 7.

In Paper 2, we show some of the variability in water properties on the shelf based on three surveys repeating a CTD cast grid consisting of 64 stations. To understand the fate of CH_4 coming from seepage on the shelf, we used an existing ocean circulation model (Svalbard 800) (Hattermann et al., 2016) and performed synthetic neutrally buoyant drifter experiments, where the drifters represented inert CH_4.

We estimated the WSC velocity based on the inclination of flares in Paper 4, and subsequently incorporated it in the 2-dimensional model, the control volume model, and the analytical solution to the steady-state CH_4-budget model, all described in section 6.4 (this thesis) and in Paper 4.

6.4 Modelling free and dissolved gas

Three types of models were constructed for Paper 3 and Paper 4.

Paper 3 presents a newly developed numerical model resolving the exchange of gas over bubble rims while bubbles rise through the water column. Bubble shape- and size-changing, aerobic oxidation of dissolved methane and eventual release of gas to the atmosphere is predicted by the model called M2PG1 (Marine 2-Phase Gas model in 1 dimension). M2PG1 is fully Eulerian with multi-sized bubbles containing gas of several species and it accounts for non-ideal gas behaviour and includes the latest parameterizations of solubility, diffusivity, and molar volumes available in the literature. M2PG1 was developed in order to predict the vertical distribution of dissolved CH_4 resulting from the release of bubbles from the seafloor and along vertical bubble trajectories. Although it was originally intended to resolve methane dynamics, it simultaneously models other included gas species (N_2, O_2, CO_2 and Ar) allowing for numerical experiments with gas bubbles containing any or all of these gas species. Paper 3 describes the numerical construction of the model, provides a sensitivity analysis and compares the model output with observations made at the slope offshore PKF, which is known for intensive CH_4 seepage offshore Svalbard (e.g. Berndt et al., 2014; Westbrook et al., 2008).

A 4.5 km long and 400 m high 2-dimensional model was constructed along the slope offshore Svalbard, at ~38.5°N, 9.3°E, which corresponded to line 3, described in Paper 4. The model resolved horizontal diffusion of CH_4 across the domain and advection with water currents. It was run to steady state and thereafter compared with high-resolution (MILS) CH_4 data. We calculated flow rates from the echosounder data with Flarehunter and its bundled Flare Flow Module and constructed a map with quantified sources of bubble-mediated CH4. The mapped flare positions and flow rates were used as input to the new 2-d model. The vertical distribution of the bubble-mediated CH_4, predicted by the M2PG1 Case study, described in Paper 3, was used to distribute the CH_4 source vertically in the 2-d domain. Different diffusion coefficients were tried and the best model agreement with MILS data was achieved with a 2 m^2s^{-1} diffusion coefficient. Paper 4 describes the construction of the 2D model and compares its output with the high-resolution CH_4 measurements.

An analytical solution to a steady-state model was derived in order to comprehend elevated mean CH_4 concentrations in a defined water volume. We assumed that the CH_4 concentration within the volume (V) was affected by inflow (in the x-direction) of seawater carrying background concentration of CH_4 and outflow of water carrying momentary CH_4 concentration. Further alteration of the CH_4 concentration in the volume was provided from bubble sources and diffusion (in the y-direction). The equation for the temporal concentration change in the volume was thus:

$$\frac{dC}{dt} = \frac{Q_{IN} \times C_B}{V} - \frac{Q_{OUT} \times C}{V} + \frac{F_{CH4}}{V} + k\frac{\partial^2 C}{\partial y^2},$$

Where C and C_B are the temporal and background concentrations respectively and k is the horizontal mixing coefficient. This equation is a first order differential, and realizing that the second gradient can be discretized $\left(\frac{\partial^2 C}{\partial y^2} = \frac{2(C_B - C)}{(\Delta y)^2}\right)$, one can calculate the steady state concentration:

$$C_{t=\infty} = \frac{\left(\frac{Q_{IN} \times C_B}{V} + \frac{F_{CH_4}}{V} + \frac{2k \times C_B}{(\Delta y)^2}\right)}{\frac{Q_{OUT}}{V} + \frac{2k}{(\Delta y)^2}}$$

The results from the analytical steady state model are presented in Paper 4.

7 Summary of manuscripts

7.1 Paper 1

Mario E. Veloso-Alarcón, Pär Jansson, Marc De Batist, Timothy A. Minshull, Graham K. Westbrook, Heiko Pälike, Stefan Bünz, Ian Wright, Jens Greinert, ***Variability of acoustically evidenced methane bubble emissions offshore western Svalbard.*** Resubmitted to Geophysical research letters

In this study, we examined the variability of free gas emission from the seafloor to the water column in an area west of Svalbard (Figure 1). We processed echosounder data from eleven surveys conducted between 2008 and 2014. For the first time, free gas emission inferred from an acoustic method over a large area has been collected over a longer period. Flares, the acoustic signature of gas bubbles in the water column, were identified mostly in three distinct areas offshore Svalbard on the continental shelf (water depth ~70-150 m), shelf break (depth ~250 m) and on the slope (depth ~400 m).

We estimated that the three prominent seepage areas (Figure 9) emit in total 2900–4500 t CH_4 y^{-1}. Because the beam width of the single beam echosounder is narrow, and ship-tracks are never identical between surveys, it is clear that data from different surveys never have identical coverage. It was thus necessary to develop a comparison method only taking into account the small areas that were covered by the echosounder beam several times. This so-called common area comparison (CAC) showed that flow rates from two adjacent seepage areas, the Shelf break and Slope, varied inversely with time, suggesting that the two areas are interconnected by sub-seafloor features (permeable layers) where the gas can migrate horizontally. No trend toward increased seepage could be inferred from the analysis, as would have been expected from long-term bottom water warming (Ferré et al., 2012). We attempted to establish a correlation between free gas flow rates and pressure changes induced by tides (Boles et al., 2001) and compared modelled sea surface heights (Egbert and Erofeeva, 2002) with calculated flowrates but we found only a small correlation. A similar analysis comparing earthquake data with the backscatter intensity showed no correlation. We found no evidence for migration of seep locations over time, as would have been expected from bottom water warming and subsequent offshore migration of the Methane hydrate stability limit.

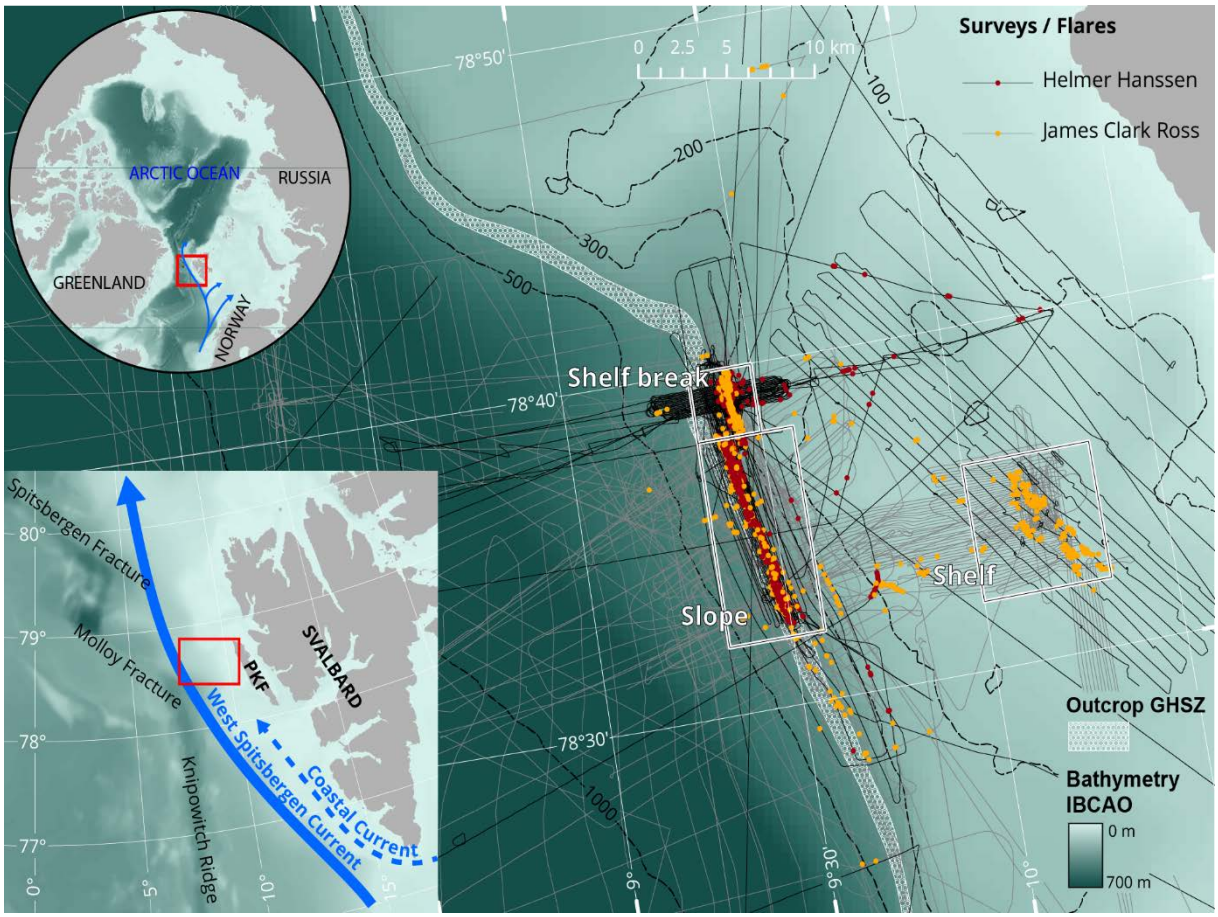

Figure 9. The study site and defined seepage areas. Black lines and red dots indicate ship tracks and flare observations by RV Helmer Hanssen. Grey lines and orange dots represent RV James Clark Ross tracks and flares observations. The outcrop of the gas hydrate stability zone (GHSZ), showed as a hex pattern was inferred from the migration between 360 and 410 m. water depth, suggested by Berndt et al. (2014).

The paper was well received by the editor but two reviewers requested restructuring and a revised manuscript was submitted. After the re-submission, both reviewers were satisfied but a third reviewer suggested further changes. We are currently working on a third version of the manuscript, which should be submitted in October 2018.

7.2 Paper 2

Anna Silyakova, Pär Jansson, Pavel Serov, Bénédicte Ferré, Alexey Pavlov, Tore Hattermann, Carolyn A. Graves, Stephen Matthew Platt, Cathrine Lund Myhre, Friederike Gründger and Helge Niemann. ***Physical controls of dynamics of methane venting from a shallow seep area west of Svalbard.*** Submitted to JGR Oceans.

The area offshore Svalbard has been well studied since methane bubble streams were discovered on the shallow shelf, the shelf break, and the continental slope. We present data from three seagoing research expeditions, repeatedly covering the same area of approximately 400 km^2 with water depths ranging between 50 and 150 m. We performed 64 hydrocasts during each expedition, collecting water samples and CTD data (salinity, temperature, depth). The collected water samples were later analysed for methane concentration using headspace gas chromatography.

We also acquired echosounder data, using the shipborne EK60 echosounder, which we analysed for acoustic gas flares (signatures of bubble streams emanating from the seafloor) with the FlareHunter software (Veloso et al., 2015). In order to obtain unbiased CH_4 flow rate estimates for each cruise, the acquired flow rates were upscaled using ArcGIS in a manner so that the different lengths of the ship tracks and echosounder beam coverage did not influence the resulting area-flow rates. The upscaling method was described in the SI of Paper 2. Figure 9 shows the flare positions and the upscaled CH_4 flow rates.

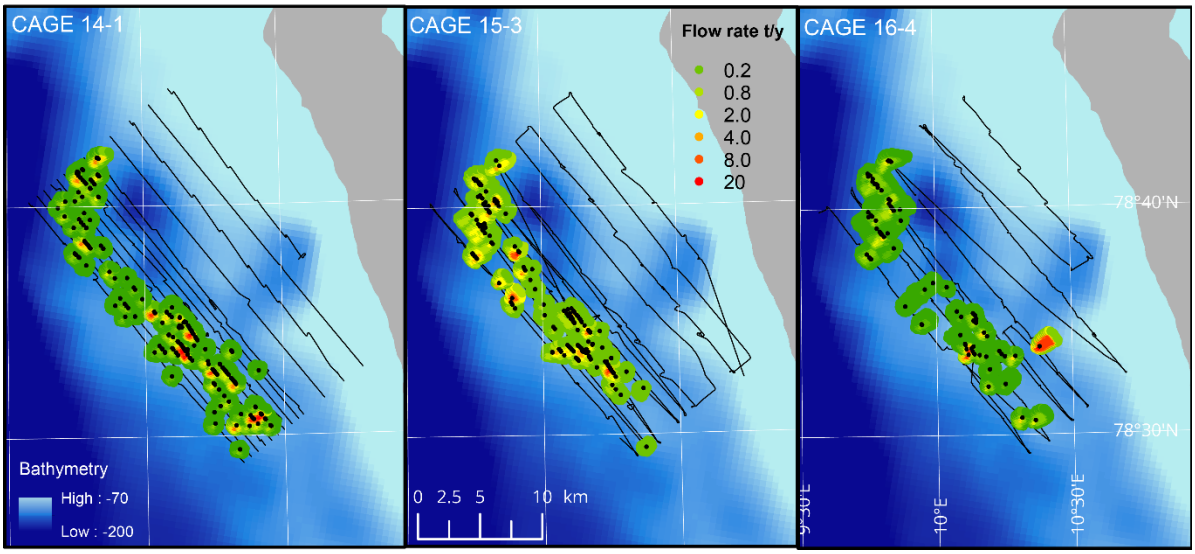

Figure 10. Upscaled flow rates from cruises in June-14, July-15 and May-16. Observed flares (point sources) are shown as black dots. Colour scale from green to red indicates the upscaled flow rates on a 100 x 100 m grid.

We found that the upscaled flow rates were largest in June 2014, with 3774 t y^{-1} and that this coincided with high methane content in a defined water volume. In July 2015, the flow rates were slightly lower (3004 t y^{-1}) and correspondingly, the weighted average methane content in the same volume were lower. In May 2016, both the flow rates and methane content were at the lowest level at 2356 t y^{-1}.

The bubble-mediated dissolved CH_4 measured with discrete sampling and headspace GC, did not reach high into the water column during any of the surveys. The occurrence of water density

stratification in July-15 and the lack thereof in June 2014 and May 2016 did not affect the vertical extent of the aqueous CH_4, which we attributed to fast dissolution of bubbles near the seafloor and inefficient diapycnal mixing also when stratification was weak.

We analysed numerical ocean-circulation model data, and performed synthetic neutral buoyancy particle drifter experiments, comparing with the observed CH_4 distributions. The numerical model showed seasonal efficiency of particle dispersion. A large area was particle covered in January to May, whereas a smaller area of high particle concentrations was modelled for the summer months. These modelling results suggested that dissolved CH_4 is less dispersed during summer. Key to how this correlates with our findings is understanding the temporal dispersion pattern: In May 2016, we observed high concentrations in a limited area around the flares wand otherwise low concentrations. This is predicted by the model which predicts intense dispersion in spring. Efficient dispersion was taking place while CH_4 was emitted at a few places only, explaining the observed CH_4 distribution.

Equilibration of CH_4 with the atmosphere was calculated, using the surface-water CH_4 concentration, atmospheric mixing ratio, and wind speeds. During our surveys, the diffusive CH_4-flux to the atmosphere was small with the exception of an area in the south corner of the defined area in May 2016, where some enhanced CH_4 was observed near the surface.

In summary, the content of CH_4 in the water column was related to the magnitude of the bubble seepage and the distribution depended on the efficiency of horizontal mixing processes. The vertical density gradient did not have an influence on the flux to the atmosphere in our study.

7.3 Paper 3

Pär Jansson, Bénédicte Ferré, Anna Silyakova, Knut Ola Dølven, Anders Omstedt. ***A new numerical model for understanding free and dissolved gas progression towards the atmosphere in aquatic methane seepage systems***. Submitted to Oceanography and Limnology: Methods

We developed a numerical model which resolves both free and dissolved gas in the water column. It was, to our knowledge, the first model that used multi-size bubbles containing several gas species and which resolved the evolution of dissolved gas while bubbles ascend towards the sea surface. The developed model was used to study the progression of methane gas contained in bubbles escaping from the seafloor. The study included a detailed explanation of the numerical construction and inherent parameterizations, an analysis of the sensitivity to different parameterizations and to environmental conditions. We also compared model output with observations at the slope offshore PKF. In spite of the more complex construction, the numerical precision of M2PG1 compared well with an existing single bubble model (Vielstädte et al., 2015). Like in all Eulerian models, numerical diffusion occurred and the model results can therefore not be directly compared with existing single bubble models. However, the modelled rise height of bubbles compared well with the flare heights seen in the echograms acquired during the CAGE 15-6 cruise. The modelled profiles of dissolved CH_4 compared well (R better than 0.9) with an exponential fit to discrete measurements of CH_4 concentrations collected during the same cruise. The best model fit with observations was achieved with a Gaussian bubble size distribution peaking at 1 mm.

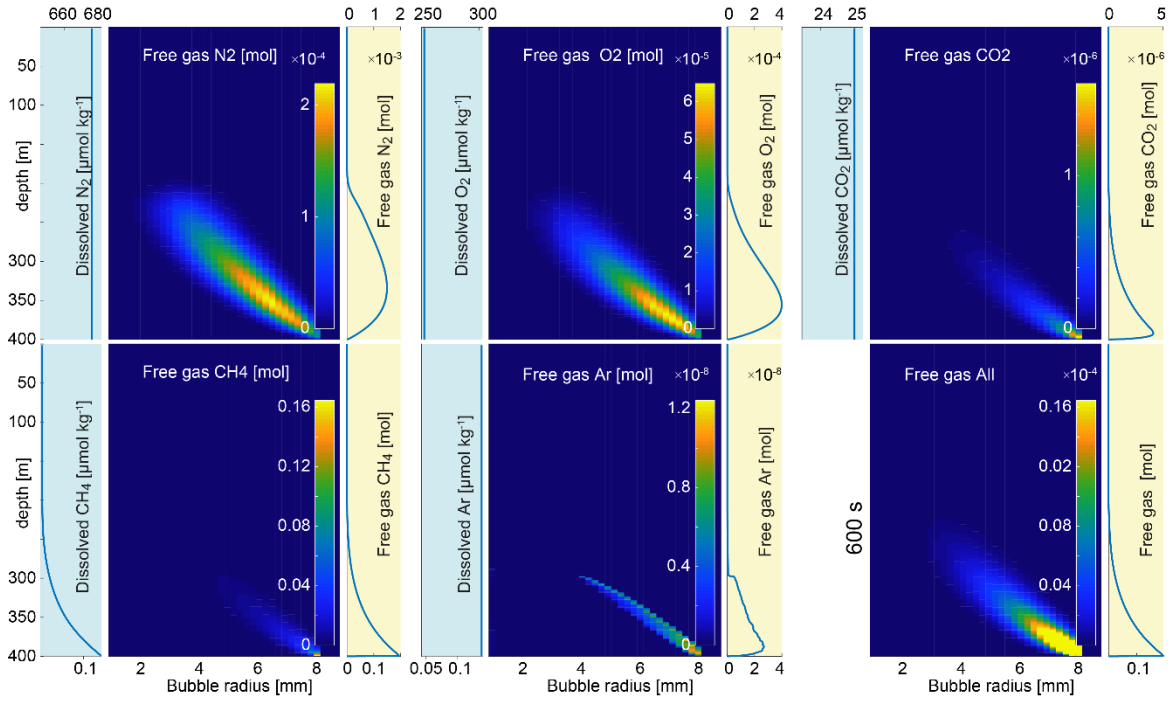

Figure 11. Example of a M2PG1 simulation. Five gas species are represented in their depth- size distribution. Blue to yellow colour scale represents the molar content of free gas in the respective cells. Profiles on yellow background represents the summation of free gas across the bubble sizes at each specific depth. Profiles on blue background shows the dissolved gas concentration. Because the modelled horizontal domain was relatively large, the dissolved gas profiles were largely unaffected by seepage and only the dissolved CH_4 showed an anomaly near the seafloor. The bubble size distribution of the emitted bubbles in this case was single-size of 8 mm equivalent radius.

7.4 Paper 4

Jack Triest, Pär Jansson, Roberto Grilli, Anna Silyakova, Bénédicte Ferré, Jérôme Chappellaz, Jürgen Mienert. **Insights from underwater high resolution dissolved methane sensing over a known methane seepage site west of Svalbard**. In preparation for submission to JGR Ocean

The seepage at the slope offshore PKF was investigated during a three-day campaign in October 2015, using the MILS in addition to our standard oceanographic equipment. The MILS was developed for CH_4 sensing during ice-core drilling in Antarctica. It was designed and built by Jack Triest and Roberto Grilli at the National Centre of Scientific Research in France (https://www.cnrs.fr/), and a modified version was made for seawater deployment, which was tested in July 2014, in the Mediterranean Sea (Grilli et al., submitted). The sensor was, during our survey, for the first time deployed in an environment with substantially CH_4–enriched seawater. The MILS data was in good agreement with sparse discrete sampling and subsequent GC analysis, but MILS revealed unprecedented details of the aqueous CH_4 distribution, both during vertical casts and horizontal towing. Along one of the five horizontal tow-lines (line 3, Figure 12), the CH_4 concentrations were high and the distribution heterogeneous. Simultaneously with towing of the MILS, we monitored echosounder data in real time, which revealed immense CH_4 bubble expulsion along the same line.

Offline flare mapping, using data from the EK60 ship-mounted split-beam echosounder and the Fledermaus software revealed intense flare activity along the slope at about 390 mbsl, which coincided with line 3.

In order to understand the observed heterogeneity, we developed a 2-dimensional model, reconstructing the CH_4 distribution along the tow-line. The 2D model is described in the section *Modelling free and dissolved gas* in the *methods* section of this synthesis. In Paper 4, we report on the 2D modelling procedure and compare the modelled CH_4 distribution with the discrete samples CH_4 and the CH_4 measured with the MILS. The model agreed well with observations but displayed downstream tailing, which we did not see in the MILS data. This is explained by the construction of the model, which only considers turbulent mixing across the domain, whereas, in reality, mixing occurs in all directions.

The analytical solution to the steady state model was calculated by assuming a volume 75 m high, 50 m wide and 4500 m long, which corresponded to the 2D model domain and line 3. In our case the mixing coefficient, *k*, determined by the 2-d modelling, was 1.5 m^2s^{-1}. The observed flow rates were used as input to the volume and the model reached a steady state CH_4 concentration of 23.5 nmol kg^{-1}, twice the background concentration in the area, which was also estimated from the MILS measurements.

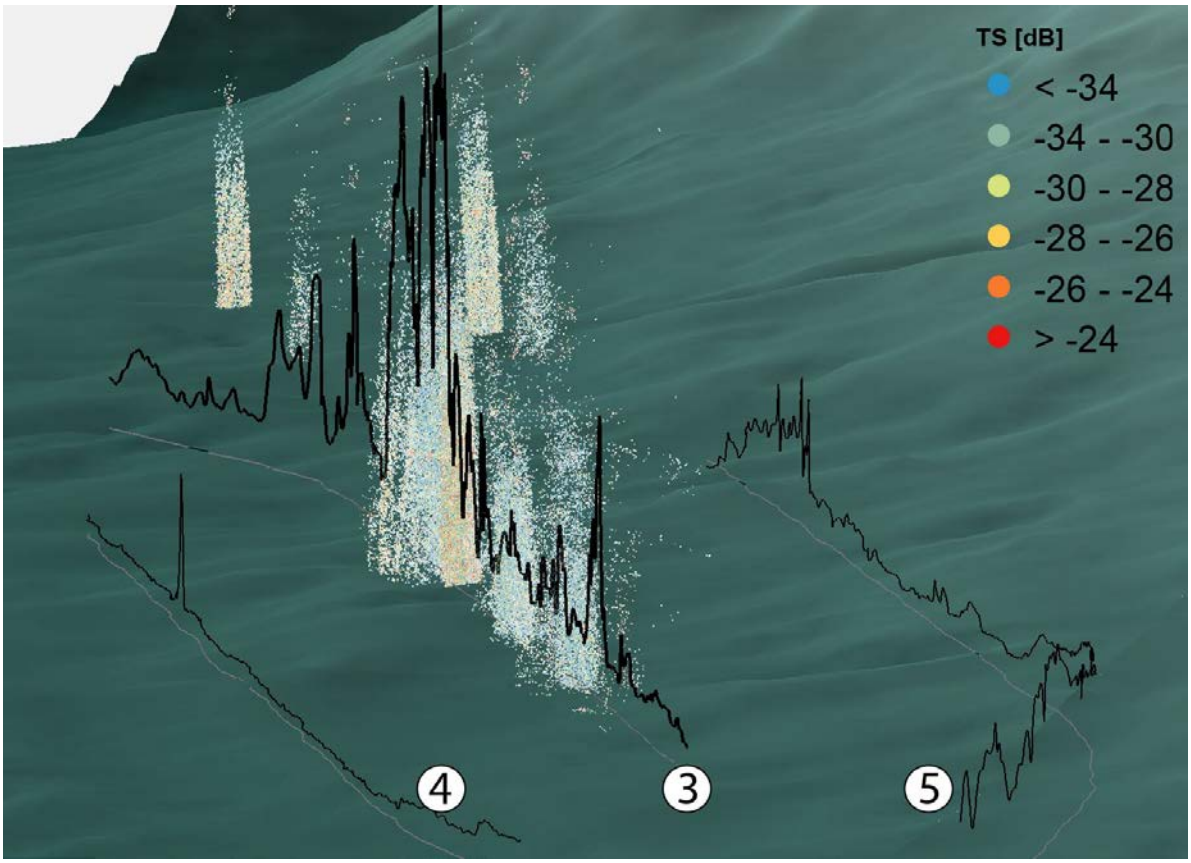

Figure 12. Visualization of gas flares and dissolved CH_4. Target strength (dB) of extracted acoustic data, depicting bubbles in the water column, is shown as coloured dots. Ship track lines 3, 4 and 5, projected on the seafloor, are shown as grey lines and the CH_4 concentration along the lines are shown as black lines.

8 Concluding remarks and outlook

The research conducted during the Ph.D. commitment has substantially improved the understanding of the fate of CH_4 emitted from the seafloor in general and specifically on the western Svalbard continental shelf. We quantified CH_4 emissions from the seafloor and subsequent release to the atmosphere. We compared the variability of CH_4 release with the postulated triggering processes (Paper 1). And developed one- (Paper 3) and two- (Paper 4) dimensional models predicting dissolved CH_4 resulting from free gas emissions from the seafloor. A new fast-response CH_4 sensor was tested (Paper 4) and the data was compared with modelling results with good agreement. Combining the newly developed methods while investigating the same area increased our confidence in the different methods. For example, mapped and quantified CH_4 emissions from the seafloor was incorporated in the new process based 2-phase model and 2D model, which reproduced the observations from high-resolution MILS sensing.

Echosounder data is routinely and extensively collected and used for assessment of fish stocks. Old and new echosounder data could give insights to new CH_4 seepage locations and may help elucidating the development of seepage sites.

Removal rates of CH_4 due to oxidation (MOx) depend on the local CH_4 concentration and the activity of the microbes. MOx can be quantified using ex-situ incubation methods and its efficiency has been noted to increase downstream of CH_4 sources (Mau et al., 2017) as the methanotrophic community grows. Rather than assuming a constant MOx efficiency, the dynamic growth and decay of the methanotrophic community could be included in simulations of future improved versions of M2PG1.

Methane contained in bubbles that are being ejected from the seafloor dissolves in a layer close to the seafloor and a fraction of the dissolved CH_4 is converted to CO_2 due to aerobic oxidation. The additional CO_2 may alter the carbonate system, acidify the seawater, and potentially affect benthic and pelagic ecosystems. Coupling the carbonate system with M2PG1would give increased insight to the acidification effect of CH_4 emissions from the seafloor. CO_2 bubbling from the seafloor can already be modelled with M2PG1 and would possibly be of interest for projects monitoring carbon storage and sequestration.

Future versions of M2PG1 could be used for modelling the fate of substances emitted from the seafloor at hydrothermal vents.

9 References

Andreassen, K., Hubbard, A., Winsborrow, M., Patton, H., Vadakkepuliyambatta, S., Plaza-Faverola, A., Gudlaugsson, E., Serov, P., Deryabin, A., Mattingsdal, R., Mienert, J. & Bünz, S. 2017. Massive blow-out craters formed by hydrate-controlled methane expulsion from the Arctic seafloor. *Science*, 356(6341), pp. 948-953. doi: 10.1126/science.aal4500.

Appen, W.-J. v., Schauer, U., Hattermann, T. & Beszczynska-Möller, A. 2016. Seasonal Cycle of Mesoscale Instability of the West Spitsbergen Current. *Journal of Physical Oceanography*, 46(4), pp. 1231-1254. doi: 10.1175/JPO-D-15-0184.1.

Artemov, Y. G., Egorov, V., Polikarpov, G. & Gulin, S. 2007. Methane emission to the hydro-and atmosphere by gas bubble streams in the Dnieper paleo-delta, the Black Sea.

Berndt, C., Feseker, T., Treude, T., Krastel, S., Liebetrau, V., Niemann, H., Bertics, V. J., Dumke, I., Dünnbier, K., Ferré, B., Graves, C., Gross, F., Hissmann, K., Hühnerbach, V., Krause, S., Lieser, K., Schauer, J. & Steinle, L. 2014. Temporal Constraints on Hydrate-Controlled Methane Seepage off Svalbard. *Science*, 343(6168), p. 284. doi: 10.1126/science.1246298.

Boles, J., Clark, J., Leifer, I. & Washburn, L. 2001. Temporal variation in natural methane seep rate due to tides, Coal Oil Point area, California. *Journal of Geophysical Research: Oceans*, 106(C11), pp. 27077-27086. doi: 10.1029/2000JC000774.

Broecker, W. S. & Peng, T. H. 1974. Gas exchange rates between air and sea1. *Tellus*, 26(1-2), pp. 21-35. doi: 10.3402/tellusa.v26i1-2.9733.

Bünz, S., Polyanov, S., Vadakkepuliyambatta, S., Consolaro, C. & Mienert, J. 2012. Active gas venting through hydrate-bearing sediments on the Vestnesa Ridge, offshore W-Svalbard. *Marine Geology*, 332-334, pp. 189-197. doi: 10.1016/j.margeo.2012.09.012.

Cottier, F., Tverberg, V., Inall, M., Svendsen, H., Nilsen, F. & Griffiths, C. 2005. Water mass modification in an Arctic fjord through cross-shelf exchange: The seasonal hydrography of Kongsfjorden, Svalbard. *Journal of Geophysical Research: Oceans*, 110(C12). doi: 10.1029/2004JC002757.

Egbert, G. D. & Erofeeva, S. Y. 2002. Efficient inverse modeling of barotropic ocean tides. *Journal of Atmospheric and Oceanic Technology*, 19(2), pp. 183-204. doi: 10.1175/1520-0426(2002)019<0183:EIMOBO>2.0.CO;2.

Ferré, B., Mienert, J. & Feseker, T. 2012. Ocean temperature variability for the past 60 years on the Norwegian-Svalbard margin influences gas hydrate stability on human time scales. *Journal of Geophysical Research: Oceans (1978–2012)*, 117(C10). doi: 10.1029/2012JC008300.

Fischer, D., Mogollón, J. M., Strasser, M., Pape, T., Bohrmann, G., Fekete, N., Spiess, V. & Kasten, S. 2013. Subduction zone earthquake as potential trigger of submarine hydrocarbon seepage. *Nature Geoscience*, 6, p. 647. doi: 10.1038/ngeo1886.

Fleming, J. R. 2005. *Historical perspectives on climate change*. Oxford University Press.

Greinert, J., Artemov, Y., Egorov, V., De Batist, M. & McGinnis, D. 2006. 1300-m-high rising bubbles from mud volcanoes at 2080m in the Black Sea: Hydroacoustic characteristics and temporal variability. *Earth and Planetary Science Letters*, 244(1), pp. 1-15. doi: 10.1016/j.epsl.2006.02.011.

Haeckel, M., Suess, E., Wallmann, K. & Rickert, D. 2004. Rising methane gas bubbles form massive hydrate layers at the seafloor. *Geochimica et Cosmochimica Acta*, 68(21), pp. 4335-4345. doi: 10.1016/j.gca.2004.01.018.

Hattermann, T., Isachsen, P. E., Appen, W. J., Albretsen, J. & Sundfjord, A. 2016. Eddy-driven recirculation of Atlantic Water in Fram Strait. *Geophysical Research Letters*, 43(7), pp. 3406-3414. doi: 10.1002/2016GL068323.

Hovland, M. & Thomsen, E. 1997. Cold-water corals—are they hydrocarbon seep related? *Marine Geology*, 137(1-2), pp. 159-164. doi: 10.1016/S0025-3227(96)00086-2.

Hustoft, S., Bünz, S., Mienert, J. & Chand, S. 2009. Gas hydrate reservoir and active methane-venting province in sediments on< 20 Ma young oceanic crust in the Fram Strait, offshore NW-Svalbard. *Earth and Planetary Science Letters*, 284(1), pp. 12-24. doi: 10.1016/j.epsl.2009.03.038.

Kirschke, S., Bousquet, P., Ciais, P., Saunois, M., Canadell, J. G., Dlugokencky, E. J., Bergamaschi, P., Bergmann, D., Blake, D. R., Bruhwiler, L., Cameron-Smith, P., Castaldi, S., Chevallier, F., Feng, L., Fraser, A., Heimann, M., Hodson, E. L., Houweling, S., Josse, B., Fraser, P. J., Krummel, P. B., Lamarque, J.-F., Langenfelds, R. L., Le Quere, C., Naik, V., O'Doherty, S., Palmer, P. I., Pison, I., Plummer, D., Poulter, B., Prinn, R. G., Rigby, M., Ringeval, B., Santini, M., Schmidt, M., Shindell, D. T., Simpson, I. J., Spahni, R., Steele, L. P., Strode, S. A., Sudo, K., Szopa, S., van der Werf, G. R., Voulgarakis, A., van Weele, M., Weiss, R. F., Williams, J. E. & Zeng, G. 2013. Three decades of global methane sources and sinks. *Nature Geoscience*, 6(10), pp. 813-823. doi: 10.1038/ngeo1955.

Kvenvolden, K. A. 1988. Methane hydrate—a major reservoir of carbon in the shallow geosphere? *Chemical Geology*, 71(1), pp. 41-51. doi: 10.1016/0009-2541(88)90104-0.

Kvenvolden, K. A. & Lorenson, T. D. 2001. *The global occurrence of natural gas hydrate*. Wiley Online Library.

Leifer, I. & Patro, R. K. 2002. The bubble mechanism for methane transport from the shallow sea bed to the surface: A review and sensitivity study. *Continental Shelf Research*, 22(16), pp. 2409-2428. doi: 10.1016/S0278-4343(02)00065-1.

Linke, P., Sommer, S., Rovelli, L. & McGinnis, D. F. 2010. Physical limitations of dissolved methane fluxes: The role of bottom-boundary layer processes. *Marine Geology*, 272(1-4), pp. 209-222. doi: 10.1016/j.margeo.2009.03.020.

MacLennan, D. N. 1990. Acoustical measurement of fish abundance. *The Journal of the Acoustical Society of America*, 87(1), pp. 1-15. doi: 10.1121/1.399285.

Magen, C., Lapham, L. L., Pohlman, J. W., Marshall, K., Bosman, S., Casso, M. & Chanton, J. P. 2014. A simple headspace equilibration method for measuring dissolved methane. *Limnol. Oceanogr. Methods*, 12, pp. 637-650. doi: 10.4319/lom.2014.12.637.

Maksimov, A. & Sosedko, E. 2005. Dynamics of sea bubbles covered by a hydrate skin. *XVI Session of the Russian Acoustical Society M*, pp. 459-462.

Mau, S., Römer, M., Torres, M. E., Bussmann, I., Pape, T., Damm, E., Geprägs, P., Wintersteller, P., Hsu, C.-W. & Loher, M. 2017. Widespread methane seepage along the continental margin off Svalbard-from Bjørnøya to Kongsfjorden. *Scientific reports*, 7, p. 42997. doi: 10.1038/srep42997.

McDougall, T. J. & Barker, P. M. 2011. Getting started with TEOS-10 and the Gibbs Seawater (GSW) oceanographic toolbox. *SCOR/IAPSO WG*, 127, pp. 1-28.

McGinnis, D., Greinert, J., Artemov, Y., Beaubien, S. & Wüest, A. 2006. Fate of rising methane bubbles in stratified waters: How much methane reaches the atmosphere? *Journal of Geophysical Research: Oceans (1978–2012)*, 111(C9). doi: 10.1029/2005JC003183.

Medwin, H. & Clay, C. S. 1997. *Fundamentals of acoustical oceanography*. Academic Press.

Nikolovska, A., Sahling, H. & Bohrmann, G. 2008. Hydroacoustic methodology for detection, localization, and quantification of gas bubbles rising from the seafloor at gas seeps from the eastern Black Sea. *Geochemistry, Geophysics, Geosystems*, 9(10). doi: 10.1029/2008GC002118

Pachauri, R. K., Allen, M. R., Barros, V. R., Broome, J., Cramer, W., Christ, R., Church, J. A., Clarke, L., Dahe, Q. & Dasgupta, P. 2014. *Climate change 2014: synthesis report. Contribution of Working Groups I, II and III to the fifth assessment report of the Intergovernmental Panel on Climate Change*. IPCC.

Panieri, G., Bünz, S., Fornari, D. J., Escartin, J., Serov, P., Jansson, P., Torres, M. E., Johnson, J. E., Hong, W. & Sauer, S. 2017. An integrated view of the methane system in the pockmarks at Vestnesa Ridge, 79° N. *Marine Geology*, 390, pp. 282-300. doi: 10.1016/j.margeo.2017.06.006.

Plaza-Faverola, A., Bünz, S., Johnson, J. E., Chand, S., Knies, J., Mienert, J. & Franek, P. 2015. Role of tectonic stress in seepage evolution along the gas hydrate-charged Vestnesa Ridge, Fram Strait. *Geophysical Research Letters*, 42(3), pp. 733-742. doi: 10.1002/2014GL062474.

Portnov, A., Vadakkepuliyambatta, S., Mienert, J. & Hubbard, A. 2016. Ice-sheet-driven methane storage and release in the Arctic. *Nature communications*, 7, p. 10314. doi: 10.1038/ncomms10314.

Rajan, A., Mienert, J. & Bünz, S. 2012. Acoustic evidence for a gas migration and release system in Arctic glaciated continental margins offshore NW-Svalbard. *Marine and Petroleum Geology*, 32(1), pp. 36-49. doi: 10.1016/j.marpetgeo.2011.12.008.

Reeburgh, W. S. 2007. Oceanic Methane Biogeochemistry. *Chemical Reviews*, 107(2), pp. 486-513. doi: 10.1021/cr050362v.

Riedel, M., Wallmann, K., Berndt, C., Pape, T., Freudenthal, T., Bergenthal, M., Bünz, S. & Bohrmann, G. 2018. In Situ Temperature Measurements at the Svalbard Continental Margin: Implications for Gas Hydrate Dynamics. *Geochemistry, Geophysics, Geosystems*, 19(4), pp. 1165-1177. doi: 10.1002/2017GC007288.

Ruppel, C. D. & Kessler, J. D. 2016. The Interaction of Climate Change and Methane Hydrates. *Reviews of Geophysics*. doi: 10.1002/2016RG000534.

Römer, M., Riedel, M., Scherwath, M., Heesemann, M. & Spence, G. D. 2016. Tidally controlled gas bubble emissions: A comprehensive study using long-term monitoring data from the NEPTUNE cabled observatory offshore Vancouver Island. *Geochemistry, Geophysics, Geosystems*, 17(9), pp. 3797-3814. doi: 10.1002/2016GC006528.

Sauter, E. J., Muyakshin, S. I., Charlou, J.-L., Schlüter, M., Boetius, A., Jerosch, K., Damm, E., Foucher, J.-P. & Klages, M. 2006. Methane discharge from a deep-sea submarine mud volcano into the upper water column by gas hydrate-coated methane bubbles. *Earth and Planetary Science Letters*, 243(3-4), pp. 354-365. doi: 10.1016/j.epsl.2006.01.041.

Serov, P., Vadakkepuliyambatta, S., Mienert, J., Patton, H., Portnov, A., Silyakova, A., Panieri, G., Carroll, M. L., Carroll, J., Andreassen, K. & Hubbard, A. 2017. Postglacial response of Arctic Ocean gas hydrates to climatic amelioration. *Proceedings of the National Academy of Sciences*, 114(24), pp. 6215-6220. doi: 10.1073/pnas.1619288114.

Shakhova, N., Semiletov, I., Salyuk, A., Yusupov, V., Kosmach, D. & Gustafsson, Ö. 2010. Extensive Methane Venting to the Atmosphere from Sediments of the East Siberian Arctic Shelf. *Science*, 327(5970), pp. 1246-1250. doi: 10.1126/science.1182221.

Sloan, E. 1998. Physical/chemical properties of gas hydrates and application to world margin stability and climatic change. *Geological Society, London, Special Publications*, 137(1), pp. 31-50.

Steinle, L., Graves, C. A., Treude, T., Ferre, B., Biastoch, A., Bussmann, I., Berndt, C., Krastel, S., James, R. H., Behrens, E., Boning, C. W., Greinert, J., Sapart, C.-J., Scheinert, M., Sommer, S., Lehmann, M. F. & Niemann, H. 2015. Water column methanotrophy controlled by a rapid oceanographic switch. *Nature Geosci*, 8(5), pp. 378-382. doi: 10.1038/ngeo2420.

van Oevelen, D., Bergmann, M., Soetaert, K., Bauerfeind, E., Hasemann, C., Klages, M., Schewe, I., Soltwedel, T. & Budaeva, N. E. 2011. Carbon flows in the benthic food web at the deep-sea

observatory HAUSGARTEN (Fram Strait). *Deep Sea Research Part I: Oceanographic Research Papers*, 58(11), pp. 1069-1083. doi: 10.1016/j.dsr.2011.08.002.

Veloso, M., Greinert, J., Mienert, J. & De Batist, M. 2015. A new methodology for quantifying bubble flow rates in deep water using splitbeam echosounders: Examples from the Arctic offshore NW-Svalbard. *Limnology and Oceanography: Methods*. doi: 10.1002/lom3.10024.

Vielstädte, L., Karstens, J., Haeckel, M., Schmidt, M., Linke, P., Reimann, S., Liebetrau, V., McGinnis, D. F. & Wallmann, K. 2015. Quantification of methane emissions at abandoned gas wells in the Central North Sea. *Marine and Petroleum Geology*. doi: 10.1016/j.marpetgeo.2015.07.030.

Wallmann, K., Riedel, M., Hong, W., Patton, H., Hubbard, A., Pape, T., Hsu, C., Schmidt, C., Johnson, J. & Torres, M. 2018. Gas hydrate dissociation off Svalbard induced by isostatic rebound rather than global warming. *Nature communications*, 9(1), p. 83. doi: 10.1038/s41467-017-02550-9.

Wanninkhof, R. 2014. Relationship between wind speed and gas exchange over the ocean revisited. *Limnology and Oceanography: Methods*, 12(6), pp. 351-362. doi: 10.4319/lom.2014.12.351.

Weber, T. C., Mayer, L., Jerram, K., Beaudoin, J., Rzhanov, Y. & Lovalvo, D. 2014. Acoustic estimates of methane gas flux from the seabed in a 6000 km2 region in the Northern Gulf of Mexico. *Geochemistry, Geophysics, Geosystems*. doi: 10.1002/2014GC005271.

Westbrook, G., Chand, S., Rossi, G., Long, C., Bünz, S., Camerlenghi, A., Carcione, J., Dean, S., Foucher, J.-P. & Flueh, E. 2008. Estimation of gas hydrate concentration from multi-component seismic data at sites on the continental margins of NW Svalbard and the Storegga region of Norway. *Marine and Petroleum Geology*, 25(8), pp. 744-758. doi: 10.1016/j.marpetgeo.2008.02.003.

Westbrook, G. K., Thatcher, K. E., Rohling, E. J., Piotrowski, A. M., Pälike, H., Osborne, A. H., Nisbet, E. G., Minshull, T. A., Lanoisellé, M. & James, R. H. 2009. Escape of methane gas from the seabed along the West Spitsbergen continental margin. *Geophysical Research Letters*, 36(15). doi: 10.1029/2009GL039191.

Paper 1

Variability of acoustically evidenced methane bubble emissions offshore western Svalbard

Mario E. Veloso-Alarcón[1,2], Pär Jansson[3], Marc De Batist[2], Timothy A. Minshull[4], Graham K. Westbrook[5], Heiko Pälike[4], Stefan Bünz[3], Ian Wright[6], Jens Greinert[1,2,3]

[1]GEOMAR Helmholtz Centre for Ocean Research Kiel, Wischhofstr. 1-3 24148 Kiel, Germany.
[2]Renard Centre of Marine Geology, Ghent University, Krijgslaan 281 s.8 B-9000 Ghent, Belgium.
[3]CAGE-Centre for Arctic Gas Hydrate, Environment and Climate, Department of Geosciences, UiT-The Arctic University of Norway, Postboks 6050 Langnes, N-9037 Tromsø, Norway.
[4]National Oceanography Centre Southampton, University of Southampton, European Way, Southampton SO14 3ZH, United Kingdom.
[5]School of Geography, Earth and Environmental Sciences, University of Birmingham, Edgbaston, United Kingdom.
[6]Vice-Chancellor's Office, University of Canterbury, Private Bag 4800, Christchurch, New Zealand.

Corresponding author: Mario E. Veloso-Alarcón (mveloso@geomar.de)

Key Points

- Hydroacoustically derived flow-rates from three areas offshore Svalbard range from 2900 to 4500 t CH_4 y^{-1}
- No clear trend of CH_4-bubble fluxes over time can be identified
- Alternating CH_4-bubble seepage between two areas suggests geological interconnectivity between them.
- No spatial migration of bubble-seepage over time at the landward limit of the hydrate stability zone was observed.

Abstract

Large reservoirs of methane present in Arctic marine sediments are susceptible to rapid warming, promoting increasing methane emissions. Gas bubbles in the water-column can be detected and flow-rates can be quantified using hydroacoustic survey methods, making it possible to monitor spatiotemporal variability. We present methane (CH_4) bubble flow-rates derived from hydroacoustic datasets acquired during 11 research expeditions to the western Svalbard continental margin (2008-2014). Three seepage areas emit in total 2900–4500 t CH_4 y^{-1} and bubble fluxes are up to 8 kg $m^{-2}yr^{-1}$. Bubble fluxes vary between different surveys but no clear trend can be identified. Flux variability analyses suggest that two areas are geologically interconnected, displaying alternating flow changes. No spatial migration of bubble-seepage over time at the landward limit of the hydrate stability zone was observed, suggesting that shallow hydrate dissociation is not significant enough to be observed by changes in bubble emissions.

1 Introduction

Underwater CH_4-bubble emissions were thought to contribute significantly to global climate change (Hornafius et al., 1999; Kvenvolden, 1993; Shakhova et al., 2010, 2014), but recent evidence has challenged this suggestion. Numerical bubble modeling has shown that, except in water depths shallower than ca. 100 m, CH_4 bubbles mostly dissolve (e.g., McGinnis et al., 2006; Vielstädte et al., 2015) and methane is oxidized before it reaches the atmosphere/ocean interface(Steinle et al., 2016). Additionally, CH_4 seepage has been postulated to contribute to ocean acidification (Biastoch et al., 2011; Pohlman et al., 2011) and deoxygenation (Boetius & Wenzhöfer, 2013; Yamamoto et al., 2014) . Arctic marine sediments sequester large quantities of CH_4 in natural gas deposits, submarine permafrost and gas hydrates (O'Connor et al., 2010; Shakhova et al., 2014). Mechanisms for CH_4 release from these reservoirs are poorly constrained but likely comprise hydrate dissociation (Westbrook et al., 2009), submarine permafrost thawing with increased anaerobic organic matter degradation due to ongoing bottom-water warming (James et al., 2016), or pressure decrease from deglaciation and sea-level change (Andreassen et al., 2017).

Sediments on the western Svalbard continental margin are influenced by the northward inflow of rapidly warming Atlantic water (AW). Therefore, gas hydrates, if present therein, are more susceptible to dissociation than elsewhere. West of Prins Karls Forland (PKF), a significant number of methane seeps were identified in 2008 (Westbrook et al., 2009) and this area received additional attention because the seepage was attributed to ocean-warming-induced hydrate destabilization (Berndt et al., 2014; Sahling et al., 2014). The area was investigated to reveal the gas origin (e.g., Gentz et al., 2014; Sahling et al., 2014), describe sub-seabed migration mechanisms (e.g., Mau et al., 2017; Rajan et al., 2012; Sarkar et al., 2012), determine the fate of gas released into the water-column (e.g., Graves et al., 2015; Steinle et al., 2015), evaluate the warming potential due to CH_4 transfer to the atmosphere (e.g., Fisher et al., 2011; Pisso et al., 2016; Pohlman et al., 2017), and in general elucidate a possible relationship between bubble-release and ocean warming (e.g., Berndt et al., 2014; Mau et al., 2017).

Acoustic flares, the hydroacoustic expression of underwater bubble release, were first detected in the area in 2008 (Westbrook et al., 2009) and hydroacoustic evidence of bubble-seepage has been reported repeatedly since then (Berndt et al., 2014; Lund Myhre et al., 2016; Sarkar et al., 2012; Veloso et al., 2015). Our study comprises single-beam echosounder (SBES) data collected during 11 surveys carried

out between 2008 and 2014 by R/V Helmer Hanssen (RVHH) and RRS James Clark Ross (RRSJCR). The data allow the first spatiotemporal variability analysis of submarine bubble seepage offshore PKF and its first quantitative comparison over several years using the hydroacoustic information.

The study area is located west of Svalbard at the shelf offshore PKF (Fig.1), where the distribution of flares shows three active sub-areas (Fig.1) that we name SBreak-Area (shelf-break, ~200 mbsl), Slope-Area (upper slope, 300-400 mbsl) and Shelf-Area (shelf, ~90 mbsl). Isotope analysis of gas collected at the seabed in SBreak-Area and Slope-Area ($\delta^{13}C_{CH4}$ = - 55.7 ‰; Mau et al., 2017; Sahling et al., 2014) and CH_4 in sea surface waters in Shelf-Area ($\delta^{13}C_{CH4}$ =−54.6‰, Pohlman et al., 2017) suggest a microbial methane origin. High-resolution seismic data in SBreak-Area and Slope-Area suggest that fluids migrate through vertical pathways from deeper hydrocarbon reservoirs and flow upslope along near-horizontal permeable layers (Rajan et al., 2012; Sarkar et al., 2012). It has been proposed that the main seepage locations are determined by sediment permeability at Slope-Area (Sarkar et al., 2012) and by the intersection with the seabed of the latest prograding glacigenic sequence at SBreak-Area (Rajan et al., 2012). Seepage at Slope-Area has been hypothesized to be a consequence of hydrate dissociation triggered by bottom-water warming because flares seem to be aligned with the landward limit of the gas hydrate stability zone (LGHZ) (Westbrook et al., 2009). So far, no hydrates have been recovered near SBreak-Area and no clear and widespread bottom-simulating reflector has been observed close to the bubbling area. However, negative-polarity seismic bright spots have been found at the base of the theoretical gas hydrate stability zone (GHSZ) in that area, so the presence of hydrates cannot be disregarded (Sarkar et al., 2012). Seepage at Shelf-Area has been attributed to hydrate dissociation triggered by ice-sheet unloading, with the present-day seepage locations marking previous GHSZ pinch-out locations (Portnov et al., 2016). This hypothesis is supported by similar evidence from the formerly glaciated continental margin of the Barents Sea (Andreassen et al., 2017). Earthquakes related to extension of the nearby spreading ridge system (Fig.1) may influence bubble-seepage indirectly (Plaza-Faverola et al., 2015).

Two ocean currents control the water properties in the area; the West Spitsbergen Current introduces warm and saline AW from the south; and the Coastal Current contributes fresher and colder Transformed Atlantic Water to the northward flow (Graves et al., 2015; Nilsen et al., 2016). Bottom-water temperature changes on seasonal to decadal timescales have been proposed to cause shallow hydrate formation and dissociation in Slope-Area, yielding a positive correlation between ocean temperature and bubble release (Berndt et al., 2014; Westbrook et al., 2009). However, the hydrate occurrence zone is expected to be thinner than the GHSZ because hydrate formation is limited by supply of water and CH_4 in excess of its solubility, and by anaerobic oxidation in the sulfate reduction zone (SRZ) (Ruppel & Kessler, 2017). Therefore, hydrates are unlikely to be present within a few meters of the seabed, where a seasonal heat-pulse could be transmitted, and bubble-seepage modulation associated with seasonal hydrate formation/dissociation is likely to be weak.

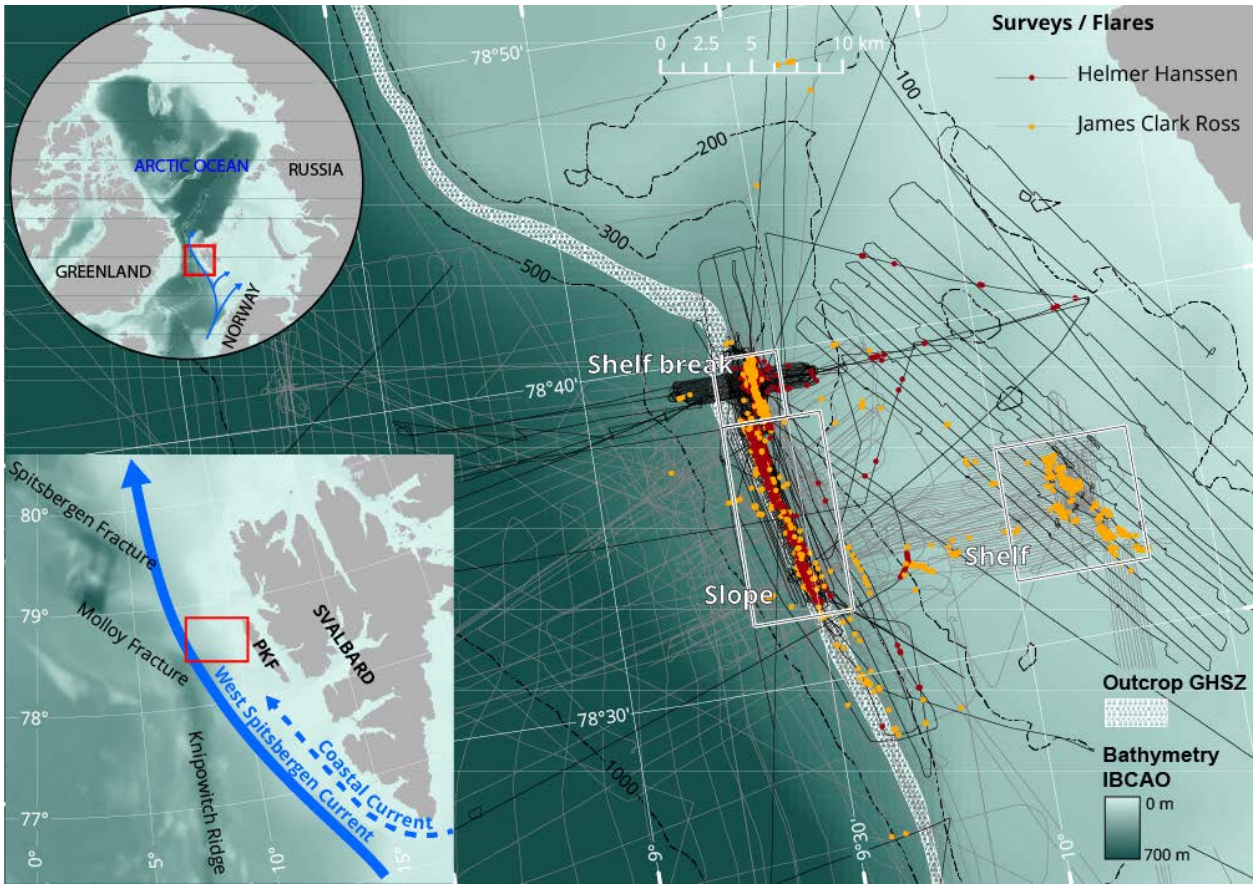

Figure 1. Bathymetric map of the study area. Black tracks with red flare locations mark RVHH surveys and grey tracks with yellow flare locations mark RRSJCR surveys. White hex pattern marks migration of the LGHZ (360-410 m isobaths; Westbrook et al., 2009). Rectangles indicate the survey areas.

2 Materials, Methods, and Results

2.1 Hydroacoustic detection of gas venting

We analyzed hydroacoustic water-column data from 11 surveys conducted during 2008–2014: S1 (08/2008); S2 (07/2009) S3 (10/2010); S4 (07/2011); S5 (08/2011); S6 (07/2012); S7 (07/2012); S8 (07/2013); S9 (10/2013); S10 (06/2014); S11 (10/2014); see supplementary information (SI); Table SI1. Data were acquired with an EK60 SBES (Kongsberg) and calibrated routinely, using moving spheres (Foote, 1987), allowing for unbiased comparison of absolute target-strength values (TS; logarithm of ratio between scattered and incident acoustic intensities; dB re 1 m^2). We used the 38 kHz frequency for this study because it is common between the two vessels and it presented the best backscattering response of bubbles, with the lowest signal-to-noise ratio at depths relevant to the study area (SI, Fig. SI1). We identified 3145 acoustic flares (SI, Fig. SI2) and selected those flares that could be traced clearly from the seabed and were well above the background noise (10 dB-TS above average background-noise of ~70 dB-TS). A representative TS of each flare in a layer 5-10 m above the seafloor was extracted with the FlareHunter graphical user interface (FH-GUI; http://www.geomar.de/en/research/fb2/fb2-mg/deepsea-monitoring/software/flarehunter-and-fluxmodule/) . The representative TS was calculated by averaging discrete TS values of the central pings within a flare and within the 5m thick layer above the seafloor. The georeferenced center of this virtual footprint was obtained by averaging the motion-compensated beam centers of the selected pings projected at the layer average depth. A virtual footprint-area was derived for this location and depth (SI, Text SI1).

Subsequently, CH_4 flow rates (amount per time unit) for individual flares were calculated, using the inverse hydroacoustic method embedded in the FH-GUI (Veloso et al., 2015). A bubble size distribution (BSD) derived from video observations conducted during cruises S2 and S3 (Veloso et al., 2015; SI, Fig. SI4), and various bubble rising speed models (BRSM's) for 'clean´ and ´dirty´ bubbles (Leifer et al., 2000, 2015; Leifer & Patro, 2002; Mendelson, 1967; Woolf, 1993; Woolf & Thorpe, 1991; SI, Fig. SI5; all included in FH-GUI) were used. Ambient water properties, gas, and environmental constants used for CH_4 flow rate quantification are specified in the SI (Table SI2).

2.2 Areal flow-rates

Areal flow-rates were calculated for the three areas by integrating the calculated flare flow-rates from all the surveys. Flares were clustered if their footprints overlapped, to avoid flow rate overestimations resulting from repeatedly insonified bubbling-sectors. Equivalent cluster fluxes were calculated by averaging the individual fluxes (flare flow-rates normalized by their respective virtual footprint-area) of flares within a cluster. A cluster flow-rate was derived by multiplying the equivalent cluster-flux by the cluster-area (Veloso et al., 2015; SI, Text SI4). Finally, areal flow rates were derived by summation of cluster flow-rates and isolated flare flow-rates (no overlap with other flares) for the three sub-areas (Table 1)

2.3 Flux through time

Each dataset results in a unique insonified area; even if tracks between surveys were identical, the insonified areas at the seafloor were not, due to vessel motion. Therefore, flow rates derived from different surveys cannot be compared directly as temporal analysis will have spatial bias. However, bubble fluxes (flow rates normalized by insonified areas) can be used for variability analysis. We developed a common area flux method (CAF; SI, Text SI5) based on the comparison of fluxes from bubbling areas that were repeatedly insonified during surveys (including clustered and isolated flares, and their respective flux values). The method follows the same technique described in section 2.2 but instead only flares from the same survey are clustered. The georeferenced flare and cluster areas were gridded creating a regular survey matrix with respective flux values for each cell. A common bubbling area between surveys was extracted from the survey matrices (SI, Fig. SI9) and a representative flux (Q_{RF}) was calculated, using the arithmetic mean of fluxes in the common area (Fig. 2). No grid cell was covered by all 11 surveys but small areas were covered by up to 8 surveys. Our analysis included multiple combinations of survey matrices with a minimum of two overlapping surveys for area SBreak-Area and Slope-Area (Fig. 1). Several Q_{RF} were obtained for each survey from the multiple combinations. The average of these values per survey ($\overline{Q}_{RF}$) is shown in Fig. 2. Shelf-Area was not considered in this analysis since it was only surveyed once. Since flux magnitudes and their changes are very similar when using different ‘clean’ and ‘dirty’ BRSMs, we only show the results for clean bubbles using the ‘Leifer’ rising speed model (Leifer et al., 2015).

Table 1. Volumetric and mass flow rates of CH4 calculated using merged hydroacoustic information of SBreak-Area, Slope-Area, and Shelf-Area using different BRSM's (SI, Figure SI5; M1C: "Leifer" clean; M2C: "Mendelson" clean; M3C: "Leifer & Patro" clean; M1D:"Leifer" clean; M2D: "Leifer & Patro" dirty; M3D: "Woolf93"; M4D: "Thorpe 91" dirty).

	Clean bubble models			Dirty bubble models			
A-SBreak	**M1C**	**M2C**	**M3C**	**M1D**	**M2D**	**M3D**	**M4D**
Flow-rate vol (L/min)	122.96	158.28	156.43	101.32	126.91	158.40	136.33
Flow-rate mass (T/yr)	1032.03	1328.57	1313.00	850.41	1065.19	1329.51	1144.31
Area with acoustic data [m^2]				646234			
Mean annual flow-rate [T/yr]		1224.53			1097.35		
Standard deviation flow-rate BRSM [T/yr]		166.89			198.42		
***Mean relative error flow-rate BRSM [%]**		± ~ 10			± ~ 12		
A-Slope	**M1C**	**M2C**	**M3C**	**M1D**	**M2D**	**M3D**	**M4D**
Flow-rate vol (L/min)	150.49	195.18	192.92	124.01	156.46	195.28	168.08
Flow-rate mass (T/yr)	1949.25	2528.28	2499.05	1606.23	2026.77	2529.69	2177.31
Area with acoustic data [m^2]				1466867			
Mean annual flow-rate [T/yr]		2325.53			2085.00		
Standard deviation flow-rate BRSM [T/yr]		326.19			382.48		
***Mean relative error flow-rate BRSM [%]**		± ~ 10			± ~ 12		
A-Shelf	**M1C**	**M2C**	**M3C**	**M1D**	**M2D**	**M3D**	**M4D**
Flow-rate vol (L/min)	60.80	78.53	77.62	50.10	62.96	78.58	67.64
Flow-rate mass (T/yr)	555.96	718.50	710.14	458.12	576.02	718.95	618.82
Area with acoustic data [m^2]				507447			
Mean annual flow-rate [T/yr]		661.53			592.98		
Standard deviation flow-rate BRSM [T/yr]		126.21			108.03		
***Mean relative error flow-rate BRSM [%]**		± ~ 10			± ~ 12		

*mean relative error (%) = $\frac{100}{N}\sum_{i=1}^{N}\frac{|x_i-\overline{x}|}{\overline{x}}$

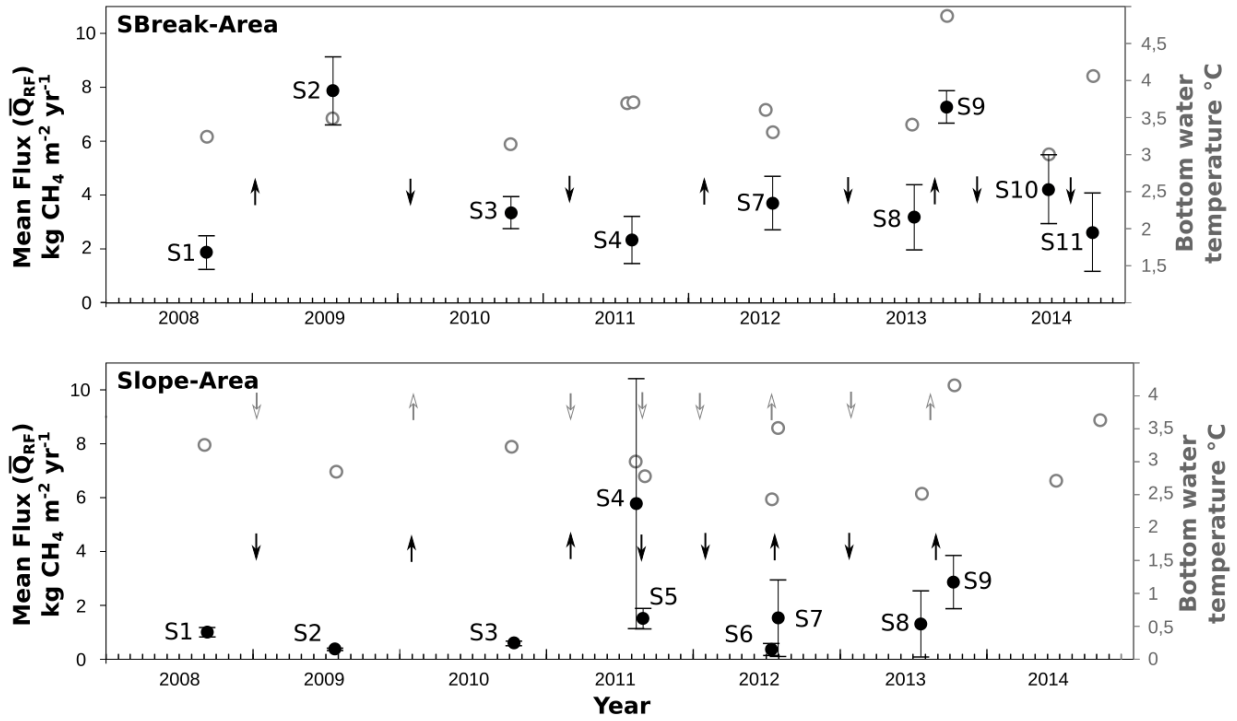

Figure 2. Temporal variability of CH_4-fluxes in SBreak-Area and Slope-Area derived with the CAF method using BRSM M1C. Black dots represent mean Q_{RF} fluxes; error bars show the standard deviation of fluxes from common areas used to calculate the mean Q_{RF} flux. Grey open dots represent the mean bottom-water temperatures (SI, Excel and Matlab files). Grey (open) and black arrows indicate changes in temperature and fluxes between surveys, respectively.

3 Discussion

3.1. Quantifying bubble-emissions

Assuming continuous release of pure CH4 bubbles, we estimate yearly emissions of ~850-1300, 1600-2500, and 450-700 tons for SBreak-Area, Slope-Area, and Shelf-Area, respectively. These results are comparable with other estimates for sub-areas of SBreak-Area and Slope-Area (Sahling et al., 2014), and are similar to comparable seepage areas elsewhere (Römer et al., 2014, 2012a, 2012b; Sauter et al., 2006; Schneider von Deimling et al., 2011; Torres et al., 2002; SI, Table SI5). Previously obtained flow rates from a sub-section of SBreak-Area using the same hydroacoustic method (Veloso et al., 2015) are half of the values presented here. This difference can be attributed to the difference in the area covered and its location. The risk of missing bubbling areas is reduced by increasing the SBES coverage, so the flow-rates derived from our larger dataset (merging of 9 surveys) represent better the bubble release for SBreak-Area (~ 850-1300 t CH4 yr^{-1} from ~13.4 km^2) than those determined by Veloso et al. (2015) using two surveys. Variations can also be introduced by inaccurate flare locations, which result in a flow rate overestimation if the same flare is considered multiple times. Transient bubble release creates another uncertainty since short-term variability is neglected when data from different surveys are combined.

A survey at PKF combining multibeam echosounder (MBES) and a ROV-based visual inspection (Sahling et al., 2014) suggested that 433 and 417 t CH_4 yr^{-1} are emitted from areas comparable to SBreak-Area and Slope-Area, respectively. This is 2.5 to 5 times lower than our results (1075 and 2050 t CH_4 yr^{-1}), but our estimate in sub-area SBreak-Area is within the uncertainty of that study. The difference can be attributed to uncertainties in both methods. While flow rates calculated from optical methods are more precise than those from SBES-data inversion, uncertainties arise when extrapolating flow rates from a few visual-observations to a larger number of MBES-detected flares. SBES-data inversion may decrease these uncertainties by using the backscatter heterogeneity of all detected flares to derive flow rates, but incorporates other uncertainties (e.g., from the backscattering model, BRSM's, and BSD observations; see Veloso et al., 2015). Future surveys should consider the combination of both methods to improve the flow rate assessment of large seepage areas.

3.2 Seepage variability

Our results show that CAF values in SBreak-Area vary between 2 and 8 kg CH_4 m^{-2} yr^{-1} with a standard deviation of 0.6-1.4 kg CH_4 $m^{-2}yr^{-1}$ (Fig. 2). This result indicates that common areas used to calculate a $\overline{Q}_{RF}$ during each survey have similar gas emissions. Fluxes fluctuate around a mean of 3 kg CH_4 $m^{-2}yr^{-1}$, except during S2 and S9, which exhibit higher fluxes (~7.8 and ~7.2 kg CH_4 yr^{-1} m^{-2}, respectively). In Slope-Area, fluxes range from 0.35 to 5.7 kg CH_4 yr^{-1} m^{-2} with a mean of 1.7 kg CH_4 yr^{-1} m^{-2}. A peak flux is observed for survey S4, with a standard deviation of ~4.68 kg CH_4 yr^{-1} m^{-2}, which is perhaps high due to spatial separation of the common areas involved in the mean Q_{RF} calculation. All other $\overline{Q}_{RF}$ values exhibit lower standard deviations (< 1.5 kg CH_4 yr^{-1} m^{-2}).

No clear increase of bubble seepage over the investigation time is evident (Fig. 2). Nor is there a trend of increasing seabed temperature. However, increased bottom water temperatures are associated with increased fluxes and vice versa at the Slope-Area, except for the period between S3 and S4. This correlation could be attributed to shallow hydrate formation/dissociation due to bottom water temperature fluctuations. However, our temperature data do not reveal the duration of heat pulses prior to acoustic measurement and thus, any interpretation about bottom water temperature influencing gas hydrate occurrence remains speculative. Large and rapid temperature changes have been reported for this area (Berndt et al., 2014); such changes are unlikely to penetrate the sediment sufficiently to drive hydrate formation/dissociation. In addition, hydrate is unlikely to be present very close to the seabed, so gas hydrate decomposition is unlikely to be an important factor in the observed temporal variation of bubble fluxes.

Instead, we hypothesize that the observed changes are controlled by two environmental driving forces: *a) Hydrostatic pressure changes.* Hydrostatic pressure influences the sediment effective stress, controlling bubble seepage through the activation of previously non-active pore throats (Boles et al., 2001) and/or the dilation of conduits and/or fractures (Scandella et al., 2011). Bubble seepage modulation by hydrostatic pressure changes has been shown to be driven in shallow waters by high-amplitude and long-period ocean waves related to tidal cycles (Römer et al., 2016), storms (Shakhova et al., 2014), and tsunamis (Lapham et al., 2013). Additionally, atmospheric pressure fluctuations have been shown to control bubble-seepage (Mattson & Likens, 1990). *b) Tectonic activity.* Pressure waves produced by earthquakes have the potential to increase the sediment pore pressure and therefore create, close, or reactivate gas/fluid migration pathways (Judd & Hovland, 2009; Plaza-Faverola et al., 2015). Resulting overpressure could initiate capillary gas migration or seepage of trapped gas due to mechanical failure (Fischer et al., 2013). Hence, earthquakes may cause a redistribution of the resistance/capacitance system associated with the gas/fluid pathway network fed by a common reservoir. This redistribution may directly affect the seepage spatial distribution and the intensity of the seepage (Leifer & Boles, 2005). Increased bubbling and dissolved CH_4 concentrations in the bottom water have been previously linked to tectonic events (Fischer et al., 2013; Obzhirov et al., 2004) and as the study area is close to the tectonically active Molloy-Knipovich ridge system (4-8 earthquakes per year; SI, Table SI6), we hypothesize that earthquakes influence the gas emissions. These two mechanisms are summarized in the conceptual model of Fig. 3 for the PKF area west of Svalbard. So far, this hypothesis remains speculative since our hydroacoustic dataset lacks continuous records (see correlation attempt in SI; Texts SI6 and SI7) and is thus unable to associate bubble seepage to the postulated trigger mechanisms. Long-term continuous records would be needed to validate this hypothesis.

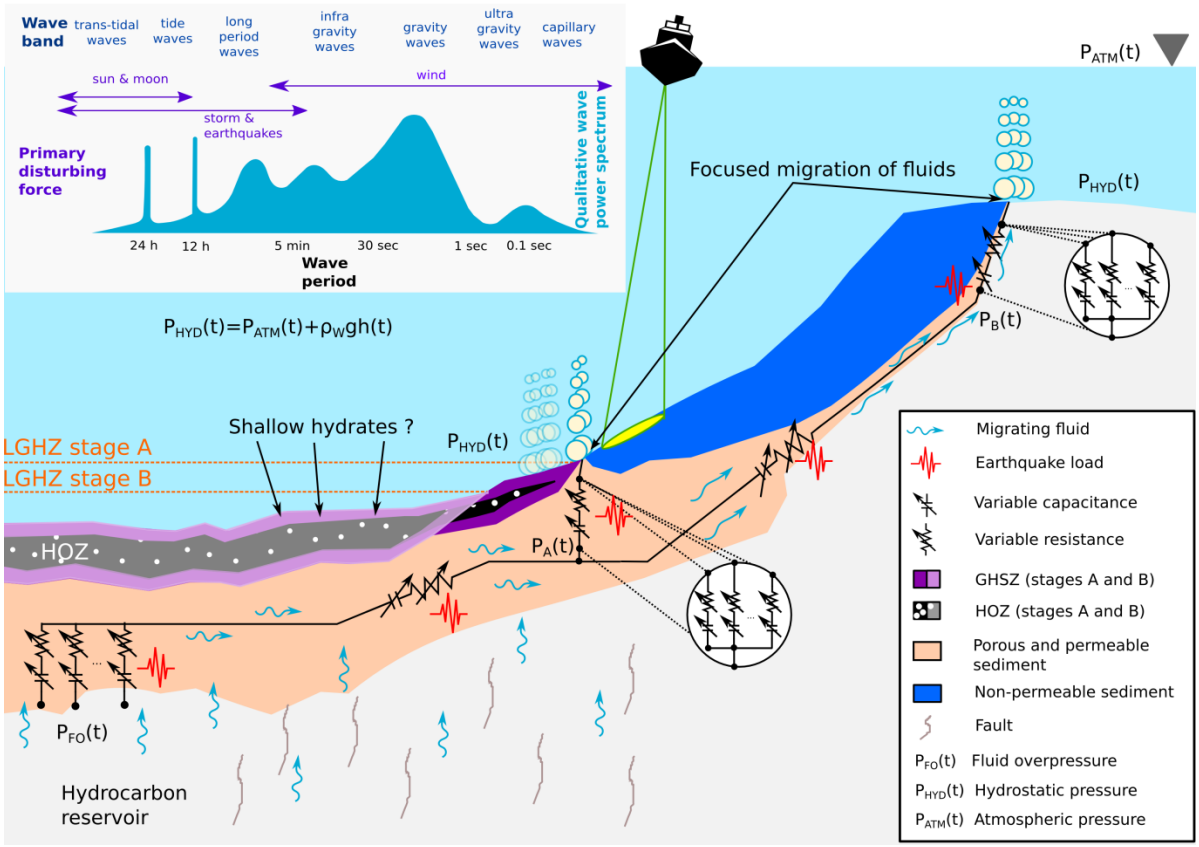

Figure 3. Conceptual model of natural driving mechanisms controlling bubble seepage offshore PKF. The schematic illustrates the hypothesized control mechanisms: a) hydrostatic pressure changes over bubble-vents; b) modification of gas migration pathway network triggered by earthquakes. The model is inspired by the high-resolution seismic studies of Rajan et al. (2012) and Sarkar et al. (2012) and an electrical model of a conduit network (Leifer & Boles, 2005). Additionally, a hypothetical spatial shift of bubble seepage triggered by an eventual long-term ocean warming scenario is shown. The figure illustrates the downward migration of the GHSZ and the hydrate occurrence zone (HOZ) from cooler (A) to warmer (B) bottom water temperature. The top left inset graph shows the ocean wave period spectra and the associated qualitative power spectrum to highlight wave periods with large effect on hydrostatic pressure.

3.3 Sub-seafloor fluid network

Increased fluxes in SBreak-Area correlate with decreased fluxes in Slope-Area, except for surveys S8 and S9 (Fig. 2). Thus, we suggest that the two areas are connected in the sub-seafloor and form parts of the same fluid migration system. Given the tectonic activity in the region, the observed alternating fluxes could be a result of changing resistance/capacitance of a joint fluid migration network (Fig. 3). Alternatively, hydrate formation/dissociation could cause blocking/opening of conduits feeding seepage areas further upslope. When pathways downslope are open, less gas will be supplied to the upslope seep area, resulting in alternating seepage intensity between SBreak-Area and Slope-Area.

3.4. Seepage migration at the LGHZ

A seasonal lateral shift of ca. 2 km of the LGHZ at Slope-Area (from 360 to 410 mbsl) was predicted between summer 2011 and winter 2012 as a response to bottom-water temperature fluctuations (Berndt et al., 2014). Seepage migration associated with this lateral shift, and in general to seasonal

modulation of the LGHZ, can be expected only if: a) shallow hydrates are present; b) a seasonal heat pulse reaches and destabilizes hydrates; c) new unimpeded gas pathways downslope exist or can form rapidly. Our surveys occurred during summer and autumn, and although bottom-water temperatures differed between the surveys, the seep site/flare spatial distribution near the LGHZ remained unaltered. This observation supports that seasonal hydrate formation/dissociation, if exist, did not influence the bubble-seepage spatial distribution. Unfortunately, the same observation does not prove or disprove seasonal shallow hydrate formation/dissociation, since even if this process is taking place, gas migrating towards the seabed could remain trapped in the sediment. An alternative hypothesis is that CH_4-seepage is mainly fed by sources in deeper sediment strata and its upward migration is mainly controlled by geological features. Based on the low probability of shallow hydrate presence, the time required for a heat pulse to migrate into the sediment, and our results showing unaltered distribution of bubble seepage, we suggest that seepage at this location is explained by the second hypothesis. We do not exclude that bubble-seepage offshore PKF could be partly influenced by hydrate dissociation triggered by ocean warming and therefore it may spatially migrate. However, hydrates are more likely to respond to longer time scale bottom water temperature changes (centennial to millennial) but also sea level changes could compensate their dissociation effects.

4 Conclusions

The analyses of 11 hydroacoustic seep surveys offshore PKF between 2008 and 2014 showed no significant trend in flux or spatial migration of seep locations. Mean yearly CH_4 free gas fluxes at the Shelf break (~240 mbsl.) are 3 kg CH_4 m^{-2} yr^{-1}, while 1.5 kg CH_4 m^{-2} yr^{-1} was obtained for the area close to the LGHZ in (~380 mbsl.). Mean fluxes and flow rates provide validated average values that consider short (days, weeks; duration of cruises) and long term (month and years) natural fluctuations; these may be considered for future modeling of methane input to the Arctic Ocean. The observed interconnectivity between seepage areas supports that seepage is controlled by focused migration pathways (Rajan et al., 2012; Sarkar et al., 2012). Our data analysis shows that ship-based hydroacoustic methods can be an efficient tool for repeated monitoring of bubble release. Applied in a standardized way it will help to establish the response of gas rich sediments to internal and external forcing mechanisms in the Arctic and elsewhere. Increasing water temperatures are likely to have a long-term impact on gas release intensity and the seep distribution offshore PKF; for a conclusive study this would require long-time observations most likely in an international effort with standardized methods.

Acknowledgments and Data

We are thankful for the support given by the crew -embers of RV Helmer Hanssen (UiT the Arctic University of Norway, N-9037 Tromsø) and RRS James Clark Ross (British Antarctic Survey). M. Veloso and J. Greinert both received support via COST Action ES0902 (PERGAMON) to join research cruises and acquire data. M. Veloso thanks the ERASMUS Mundus program of the EU (grant VECCEU) and the BECAS CHILE: CONICYT PAI/INDUSTRIA 79090016” program of the Chilean government. P. Jansson was supported by the Centre of Excellence: Arctic Gas Hydrate, Environment and Climate (CAGE) funded by the Norwegian Research Council (grant no. 223259). Data acquisition on RRS James Clark Ross was supported by Natural Environment Research Council grants NE/D005728, NE/H002732/1 and NE/H022260/1. We thank Joana Beja De Almeida E Silva for giving us technical support with data supplied by the National Oceanography Centre. EK60 data are available at (here PANGEA link). This is publication XXX of the Deep Sea Monitoring Group at GEOMAR.

References

Andreassen, K., Hubbard, A., Winsborrow, M., Patton, H., Vadakkepuliyambatta, S., Plaza-Faverola, A.,… Bünz, S. (2017). Massive blow-out craters formed by hydrate-controlled methane expulsion from the Arctic seafloor. *Science*, *356*(6341), 948–953. https://doi.org/10.1126/science.aal4500

Berndt, C., Feseker, T., Treude, T., Krastel, S., Liebetrau, V., Niemann, H., … Steinle, L. (2014). Temporal Constraints on Hydrate-Controlled Methane Seepage off Svalbard. *Science*, *343*(6168), 284–287. https://doi.org/10.1126/science.1246298

Biastoch, A., Treude, T., Rüpke, L. H., Riebesell, U., Roth, C., Burwicz, E. B., … Wallmann, K. (2011). Rising Arctic Ocean temperatures cause gas hydrate destabilization and ocean acidification. *Geophysical Research Letters*, *38*(8), L08602. https://doi.org/10.1029/2011GL047222

Boetius, A., & Wenzhöfer, F. (2013). Seafloor oxygen consumption fuelled by methane from cold seeps. *Nature Geoscience*, *6*(9), 725–734. https://doi.org/10.1038/ngeo1926

Boles, J. R., Clark, J. F., Leifer, I., & Washburn, L. (2001). Temporal variation in natural methane seep rate due to tides, Coal Oil Point area, California. *Journal of Geophysical Research: Oceans*, *106*(C11), 27077–27086. https://doi.org/10.1029/2000JC000774

Fischer, D., Mogollón, J. M., Strasser, M., Pape, T., Bohrmann, G., Fekete, N., … Kasten, S. (2013). Subduction zone earthquake as potential trigger of submarine hydrocarbon seepage. *Nature Geoscience*, *6*(8), 647–651. https://doi.org/10.1038/ngeo1886

Fisher, R. E., Sriskantharajah, S., Lowry, D., Lanoisellé, M., Fowler, C. M. R., James, R. H., … Nisbet, E. G. (2011). Arctic methane sources: Isotopic evidence for atmospheric inputs. *Geophysical Research Letters*, *38*(21), L21803. https://doi.org/10.1029/2011GL049319

Foote, K. G. (1987). Calibration of acoustic instruments for density estimation: a practical guide. *Int. Counc. Explor. Sea. Coop. Res. Rep.*, *144*, 57p.

Gentz, T., Damm, E., Schneider von Deimling, J., Mau, S., McGinnis, D. F., & Schlüter, M. (2014). A water column study of methane around gas flares located at the West Spitsbergen continental margin. *Continental Shelf Research*, *72*, 107–118. https://doi.org/10.1016/j.csr.2013.07.013

Graves, C. A., Steinle, L., Rehder, G., Niemann, H., Connelly, D. P., Lowry, D., … James, R. H. (2015). Fluxes and fate of dissolved methane released at the seafloor at the landward limit of the gas hydrate stability zone offshore western Svalbard. *Journal of Geophysical Research: Oceans*, *120*(9), 6185–6201. https://doi.org/10.1002/2015JC011084

Hornafius, J. S., Quigley, D., & Luyendyk, B. P. (1999). The world's most spectacular marine hydrocarbon seeps (Coal Oil Point, Santa Barbara Channel, California): Quantification of emissions. *Journal of Geophysical Research: Oceans*, *104*(C9), 20703–20711. https://doi.org/10.1029/1999JC900148

James, R. H., Bousquet, P., Bussmann, I., Haeckel, M., Kipfer, R., Leifer, I., … Greinert, J. (2016). Effects of climate change on methane emissions from seafloor sediments in the Arctic Ocean: A review. *Limnology and Oceanography*, n/a-n/a. https://doi.org/10.1002/lno.10307

Judd, A. G., & Hovland, M. (2009). *Seabed fluid flow: the impact of geology, biology and the marine environment* (Digitally print. version). New York, NY: Cambridge Univ. Press.

Kvenvolden, K. A. (1993). Gas hydrates—geological perspective and global change. *Reviews of Geophysics*, *31*(2), 173–187.

Lapham, L., Wilson, R., Riedel, M., Paull, C. K., & Holmes, M. E. (2013). Temporal variability of in situ methane concentrations in gas hydrate-bearing sediments near Bullseye Vent, Northern Cascadia Margin. *Geochemistry, Geophysics, Geosystems*, *14*(7), 2445–2459. https://doi.org/10.1002/ggge.20167

Leifer, I., & Boles, J. (2005). Measurement of marine hydrocarbon seep flow through fractured rock and unconsolidated sediment. *Marine and Petroleum Geology*, *22*(4), 551–568. https://doi.org/10.1016/j.marpetgeo.2004.10.026

Leifer, I., Patro, R. K., & Bowyer, P. (2000). A Study on the Temperature Variation of Rise Velocity for Large Clean Bubbles. *Journal of Atmospheric and Oceanic Technology*, *17*(10), 1392–1402. https://doi.org/10.1175/1520-0426(2000)017<1392:ASOTTV>2.0.CO;2

Leifer, I., Solomon, E., Schneider von Deimling, J., Rehder, G., Coffin, R., & Linke, P. (2015). The fate of bubbles in a large, intense bubble megaplume for stratified and unstratified water: Numerical simulations of 22/4b expedition field data. *Marine and Petroleum Geology*, *68*, 806–823. https://doi.org/10.1016/j.marpetgeo.2015.07.025

Leifer, I., & Patro, R. K. (2002). The bubble mechanism for methane transport from the shallow sea bed to the surface: A review and sensitivity study. *Continental Shelf Research*, *22*(16), 2409–2428. https://doi.org/10.1016/S0278-4343(02)00065-1

Lund Myhre, C., Ferré, B., Platt, S. M., Silyakova, A., Hermansen, O., Allen, G., … Mienert, J. (2016). Extensive release of methane from Arctic seabed west of Svalbard during summer 2014 does not influence the atmosphere. *Geophysical Research Letters*, 2016GL068999. https://doi.org/10.1002/2016GL068999

Mattson, M. D., & Likens, G. E. (1990). Air pressure and methane fluxes. *Nature*, *347*(6295), 718–719. https://doi.org/10.1038/347718b0

Mau, S., Römer, M., Torres, M. E., Bussmann, I., Pape, T., Damm, E., … Bohrmann, G. (2017). Widespread methane seepage along the continental margin off Svalbard - from Bjørnøya to Kongsfjorden. *Scientific Reports*, *7*, 42997. https://doi.org/10.1038/srep42997

Mendelson, H. D. (1967). The prediction of bubble terminal velocities from wave theory. *AIChE Journal*, *13*(2), 250–253. https://doi.org/10.1002/aic.690130213

Nilsen, F., Skogseth, R., Vaardal-Lunde, J., & Inall, M. (2016). A Simple Shelf Circulation Model: Intrusion of Atlantic Water on the West Spitsbergen Shelf. *Journal of Physical Oceanography*, *46*(4), 1209–1230. https://doi.org/10.1175/JPO-D-15-0058.1

Obzhirov, A., Shakirov, R., Salyuk, A., Suess, E., Biebow, N., & Salomatin, A. (2004). Relations between methane venting, geological structure and seismo-tectonics in the Okhotsk Sea. *Geo-Marine Letters*, *24*(3), 135–139. https://doi.org/10.1007/s00367-004-0175-0

O'Connor, F. M., Boucher, O., Gedney, N., Jones, C. D., Folberth, G. A., Coppell, R., … Johnson, C. E. (2010). Possible role of wetlands, permafrost, and methane hydrates in the methane cycle under future climate change: A review. *Reviews of Geophysics*, *48*(4), RG4005. https://doi.org/10.1029/2010RG000326

Pisso, I., Myhre, C. L., Platt, S. M., Eckhardt, S., Hermansen, O., Schmidbauer, N., … Stohl, A. (2016). Constraints on oceanic methane emissions west of Svalbard from atmospheric in situ measurements and Lagrangian transport modeling. *Journal of Geophysical Research. Atmospheres*, *121*(23), 14188–14200. https://doi.org/10.1002/2016JD025590

Plaza-Faverola, A., Bünz, S., Johnson, J. E., Chand, S., Knies, J., Mienert, J., & Franek, P. (2015). Role of tectonic stress in seepage evolution along the gas hydrate-charged Vestnesa Ridge, Fram Strait. *Geophysical Research Letters*, *42*(3), 2014GL062474. https://doi.org/10.1002/2014GL062474

Pohlman, J. W., Greinert, J., Ruppel, C., Silyakova, A., Vielstädte, L., Casso, M., … Bünz, S. (2017). Enhanced CO2 uptake at a shallow Arctic Ocean seep field overwhelms the positive warming potential of emitted methane. *Proceedings of the National Academy of Sciences*, *114*(21), 5355–5360. https://doi.org/10.1073/pnas.1618926114

Pohlman, J. W., Bauer, J. E., Waite, W. F., Osburn, C. L., & Chapman, N. R. (2011). Methane hydrate-bearing seeps as a source of aged dissolved organic carbon to the oceans. *Nature Geoscience*, *4*(1), 37–41. https://doi.org/10.1038/ngeo1016

Portnov, A., Vadakkepuliyambatta, S., Mienert, J., & Hubbard, A. (2016). Ice-sheet-driven methane storage and release in the Arctic. *Nature Communications*, *7*, 10314. https://doi.org/10.1038/ncomms10314

Rajan, A., Mienert, J., & Bünz, S. (2012). Acoustic evidence for a gas migration and release system in Arctic glaciated continental margins offshore NW-Svalbard. *Marine and Petroleum Geology*, *32*(1), 36–49. https://doi.org/10.1016/j.marpetgeo.2011.12.008

Römer, M., Sahling, H., Pape, T., Bahr, A., Feseker, T., Wintersteller, P., & Bohrmann, G. (2012). Geological control and magnitude of methane ebullition from a high-flux seep area in the Black Sea—the Kerch seep area. *Marine Geology*, *319–322*, 57–74. https://doi.org/10.1016/j.margeo.2012.07.005

Römer, M., Sahling, H., Pape, T., dos Santos Ferreira, C., Wenzhöfer, F., Boetius, A., & Bohrmann, G. (2014). Methane fluxes and carbonate deposits at a cold seep area of the Central Nile Deep Sea Fan, Eastern Mediterranean Sea. *Marine Geology*, *347*, 27–42. https://doi.org/10.1016/j.margeo.2013.10.011

Römer, M., Riedel, M., Scherwath, M., Heesemann, M., & Spence, G. D. (2016). Tidally controlled gas bubble emissions: A comprehensive study using long-term monitoring data from the NEPTUNE cabled observatory offshore Vancouver Island. *Geochemistry, Geophysics, Geosystems*, *17*(9), 3797–3814. https://doi.org/10.1002/2016GC006528

Römer, M., Sahling, H., Pape, T., Bohrmann, G., & Spieß, V. (2012). Quantification of gas bubble emissions from submarine hydrocarbon seeps at the Makran continental margin (offshore Pakistan). *Journal of Geophysical Research: Oceans*, *117*(C10), C10015. https://doi.org/10.1029/2011JC007424

Ruppel, C. D., & Kessler, J. D. (2017). The interaction of climate change and methane hydrates. *Reviews of Geophysics*, *55*(1), 2016RG000534. https://doi.org/10.1002/2016RG000534

Sahling, H., Römer, M., Pape, T., Bergès, B., dos Santos Fereirra, C., Boelmann, J., … Bohrmann, G. (2014). Gas emissions at the continental margin west of Svalbard: mapping, sampling, and quantification. *Biogeosciences*, *11*(21), 6029–6046. https://doi.org/10.5194/bg-11-6029-2014

Sarkar, S., Berndt, C., Minshull, T. A., Westbrook, G. K., Klaeschen, D., Masson, D. G., … Thatcher, K. E. (2012). Seismic evidence for shallow gas-escape features associated with a retreating gas hydrate zone offshore west Svalbard. *Journal of Geophysical Research: Solid Earth*, *117*(B9), B09102. https://doi.org/10.1029/2011JB009126

Sauter, E. J., Muyakshin, S. I., Charlou, J.-L., Schlüter, M., Boetius, A., Jerosch, K., … Klages, M. (2006). Methane discharge from a deep-sea submarine mud volcano into the upper water column by gas hydrate-coated methane bubbles. *Earth and Planetary Science Letters*, *243*(3–4), 354–365. https://doi.org/10.1016/j.epsl.2006.01.041

Scandella, B. P., Varadharajan, C., Hemond, H. F., Ruppel, C., & Juanes, R. (2011). A conduit dilation model of methane venting from lake sediments. *Geophysical Research Letters*, *38*(6), L06408. https://doi.org/10.1029/2011GL046768

Schneider von Deimling, J., Rehder, G., Greinert, J., McGinnnis, D. F., Boetius, A., & Linke, P. (2011). Quantification of seep-related methane gas emissions at Tommeliten, North Sea. *Continental Shelf Research*, *31*(7–8), 867–878. https://doi.org/10.1016/j.csr.2011.02.012

Shakhova, N., Semiletov, I., Salyuk, A., Yusupov, V., Kosmach, D., & Gustafsson, Ö. (2010). Extensive Methane Venting to the Atmosphere from Sediments of the East Siberian Arctic Shelf. *Science*, *327*(5970), 1246–1250. https://doi.org/10.1126/science.1182221

Shakhova, N., Semiletov, I., Leifer, I., Sergienko, V., Salyuk, A., Kosmach, D., … Gustafsson, Ö. (2014). Ebullition and storm-induced methane release from the East Siberian Arctic Shelf. *Nature Geoscience*, *7*(1), 64–70. https://doi.org/10.1038/ngeo2007

Steinle, L., Graves, C. A., Treude, T., Ferré, B., Biastoch, A., Bussmann, I., … Niemann, H. (2015). Water column methanotrophy controlled by a rapid oceanographic switch. *Nature Geoscience*, *8*(5), 378–382. https://doi.org/10.1038/ngeo2420

Steinle, L., Schmidt, M., Bryant, L., Haeckel, M., Linke, P., Sommer, S., … Niemannn, H. (2016). Linked sediment and water-column methanotrophy at a man-made gas blowout in the North Sea:

Implications for methane budgeting in seasonally stratified shallow seas. *Limnology and Oceanography*, *61*(S1), S367–S386. https://doi.org/10.1002/lno.10388

Torres, M. E., McManus, J., Hammond, D. E., de Angelis, M. A., Heeschen, K. U., Colbert, S. L., … Suess, E. (2002). Fluid and chemical fluxes in and out of sediments hosting methane hydrate deposits on Hydrate Ridge, OR, I: Hydrological provinces. *Earth and Planetary Science Letters*, *201*(3–4), 525–540. https://doi.org/10.1016/S0012-821X(02)00733-1

Veloso, M., Greinert, J., Mienert, J., & De Batist, M. (2015). A new methodology for quantifying bubble flow rates in deep water using splitbeam echosounders: Examples from the Arctic offshore NW-Svalbard: Quantifying bubble flow rates in deep water. *Limnology and Oceanography: Methods*, *13*(6), 267–287. https://doi.org/10.1002/lom3.10024

Westbrook, G. K., Thatcher, K. E., Rohling, E. J., Piotrowski, A. M., Pälike, H., Osborne, A. H., … Aquilina, A. (2009). Escape of methane gas from the seabed along the West Spitsbergen continental margin. *Geophysical Research Letters*, *36*(15), L15608. https://doi.org/10.1029/2009GL039191

Woolf, D. K. (1993). Bubbles and the air-sea transfer velocity of gases. *Atmosphere-Ocean*, *31*(4), 517–540. https://doi.org/10.1080/07055900.1993.9649484

Woolf, D. K., & Thorpe, S. A. (1991). Bubbles and the air-sea exchange of gases in near-saturation conditions. *Journal of Marine Research*, *49*(3), 435–466. https://doi.org/10.1357/002224091784995765

Yamamoto, A., Yamanaka, Y., Oka, A., & Abe-Ouchi, A. (2014). Ocean oxygen depletion due to decomposition of submarine methane hydrate. *Geophysical Research Letters*, *41*(14), 2014GL060483. https://doi.org/10.1002/2014GL060483

Geophysical Research Letters

Supporting Information for

Variability of seafloor methane emissions evidenced by repeated hydroacoustic surveys offshore Svalbard

M. E. Veloso-Alarcón[1,2]*, P. Jansson[3], M. De Batist[2], T. A. Minshull[4], G. Westbrook[5], H. Pälike[4], S. Bünz[3], I. Wright[6], J. Greinert[1,2,3]

[1]GEOMAR Helmholtz Centre for Ocean Research Kiel, Wischhofstr. 1-3 24148 Kiel, Germany.

[2]Renard Centre of Marine Geology, Ghent University, Krijgslaan 281 s.8 B-9000 Ghent, Belgium.
[3]CAGE-Centre for Arctic Gas Hydrate, Environment and Climate, Department of Geosciences, UiT- The Arctic University of Norway, Postboks 6050 Langnes, N-9037 Tromsø, Norway.
[4]National Oceanography Centre Southampton, University of Southampton, European Way, Southampton SO14 3ZH, United Kingdom.
[5]School of Geography, Earth and Environmental Sciences, University of Birmingham, Edgbaston, United Kingdom.
[6]Vice-Chancellor's Office, University of Canterbury, Private Bag 4800, Christchurch, New Zealand

Contents of this file

Additional Supporting Information (Files uploaded separately)

Excel file with CTD dataset

Matlab files and script to generate CTD profiles

Introduction

This supplementary material contains information about the echosounder data acquisition (Table SI1), its online availability and information about data processing methodology. The first data processing steps, leading to flow rate estimations are described in full detail in Veloso et al. (2015).

Text SI1.

Footprint of acoustic flares

Acoustic flares in SBES echograms appear when the echosounder beam insonifies single or multiple bubble streams. The acoustic backscattering increases as the echosounder beam approaches the bubbles, and reaches a maximum amplitude when the beam insonifies the maximum number of bubbles. Subsequently, the backscattering starts to decrease as the SBES beam moves away from the bubbles. The central pings of a flare (strongest backscattering; Fig. SI3) thus contain information about the maximum number of bubbles captured by the echosounder beam.

In order to calculate the flow rate of individual flares, we manually select backscatter values of the central pings within a layer 5-10 meters above the seafloor (selected matrix Fig. SI3). The representative target strength $\overline{TS}$ of the flare is calculated by the geometrical average of the acoustical cross-sections (which is the arithmetic mean of the target strength $TS_{i,j}$ of the samples included in the selection).

The $\overline{TS}$ represents the backscattering of a sample volume with dimensions of a truncated conical section vertically bounded by the sample thickness (derived from the sampling interval and the sound speed in the water). Thus, we interpret that the calculated flare flow rate derived from$\overline{TS}$corresponds to bubbles within a virtual sample volume (Fig. SI3) for which the dimensions and central position are derived from the average information of the samples within the selection. The geo-referenced central position of the virtual sample given by$\overline{X}$, $\overline{Y}$ and $\overline{Z}$ is obtained from the arithmetic mean of the sample in UTM coordinates and the water depth. Similarly, a radius$R_F$and a geo-referenced area $A_F$of the virtual flare footprint (which is assumed to be circular) were calculated using the average depth $\overline{Z}$ of the selected layer and the equivalent echosounder beam angle α_B (equations SI1.a and SI1.b).

$$R_F = \overline{Z} tan\left(\frac{\alpha_B}{2}\right) \quad \text{(SI1.a)}$$

$$A_F = \pi {R_F}^2 \quad \text{(SI1.b)}$$

The $\overline{TS}$ values used in our flare-flow rate calculations are restricted to an area not larger than$A_F$where the highest population of bubbles forming a flare can be found. Since clusters of bubble streams that originate flares may cover a surface larger than the echosounder footprint, the use of averaged target strengths is recognized to be a potential source of flow rate underestimations. Additionally, underestimation of flow rates can also occurs when the backscattering coming from a bubble stream cluster (or single bubble vent), with an areal coverage smaller than the footprint, is captured by a sector from the directivity pattern less sensitive than its axis.

Text SI2.

Bubble size distribution

Visual observation of bubbles at the study area were conducted during surveys S2 and S3 using a submersible video-camera system developed at NIOZ. Images were analyzed and used for bubble size measurements (McGovern 2012). As a result, a bubble size distribution (a required input in our inverse hydroacoustic method) was obtained from a total of 641 individual bubble observations (Fig. SI4).

Text SI3.

Bubble rising speed models

Bubble rising speed (Fig. SI5) were calculated using the bubble size spectra obtained from the visual information and a MATLAB script provided by Ira Leifer (Bubbleology Research International) which includes several bubble rise models (Mendelson 1967; Woolf and Thorpe 1991; Woolf 1993; Leifer et al. 2000; Leifer and Patro 2002, Leifer et al.,2015). Models consider both 'clean' and 'dirty' bubbles.

Text SI4.

Clustering of spatially overlapping flares

In order to assign an average flow rate to a cluster of flares forming a seep site, flares were clustered if their geo-referenced virtual footprints spatially overlapped at the average depth of the selected layer (Fig. SI6; Veloso et al., 2015). Once a cluster was found, the flux of each flare Q_{Fi} (flow rate normalized by the virtual footprint area; see Text SI1) was used to find an average cluster flux Q_C (equation SI2),

$$Q_C = \frac{1}{n_F}\sum_i^{n_F} Q_{Fi}, \quad \text{(SI2)}$$

where$n_F$represents the number of flares that form the cluster.

Finally, a flow rate of the cluster $F_C$can be calculated by multiplying the average cluster flux with the area covered by the cluster A_C (equation SI3)

$$F_C = Q_C A_C \quad \text{(SI3)}$$

Text SI5.

Common Area Flux Method (CAF Method)

The temporal analysis of seep activity is based on the comparison of areas containing hydroacoustic data related to bubble release that have been repeatedly insonified during surveys (Figs. SI7 and SI8).

For this comparison, acoustic flares that belong to a survey with geographically overlapping beam-footprints were clustered and an average flux was assigned to each cluster (Text SI4). An average flux was obtained by normalizing the mean flow rate of all flares within the cluster with the cluster area. The georeferenced areas of all clusters were gridded in MATLAB using a cell size of 1x1 m and a mean flux of the cluster was assigned to each individual cluster cell. The common area including the flux per cell was extracted from the combination of the survey matrices (Fig. SI9) using commands of the Generic Mapping Tools (GMT; Wessel et al., 2013). A representative flux (Q_{RF}) was calculated using the arithmetic mean of the fluxes associated with the common area grids (equation 1).

$$Q_{RF} = \frac{\sum_j^m \sum_i^n q_{i,j}}{Ne} \quad [1]$$

Where,

$q_{i,j}$: Flux at the i, j grid

Ne : Number of cells with flux values

No grid cell was covered by all 11 surveys but small areas were covered by up to 8 surveys. For our analyses we included a total of 29 and 35 different combinations (min. two overlapping survey) for areas A1 and A2, respectively (Tables SI3 and SI4). The final mean flux (Q_{RF}) per survey was calculated by averaging the obtained representative flux values Q_{RF} within a survey.

Text SI6.

Correlation between results and changes of static pressure (tides, storms, tsunamis)

We hypothesize that hydrostatic pressure is a driving force affecting the gas seepage in the study area and therefore might be in part responsible for the gas emission fluctuations observed. To test this hypothesis we correlated TS values from area A1 (most densely surveyed area) with modeled sea surface tide-related heights (*SSH*) using the software TPXO (Egbert and Erofeeva 2002). Only flares observed several times were included in the tide correlation analysis. This filtering targets the temporal variability by excluding flares that are only observed once.

We normalize the target strength (*TS*) values with the footprint area and bin depth in order to find a non-biased backscatter value for the analysis. The resulting volume backscatter strength S_V is:

$$S_V = 10log_{10}\left(\frac{10^{\left(\frac{TS}{10}\right)}}{A_F ct/2}\right), \quad \text{(SI4)}$$

where A_F is the footprint area (m^2), c is the sound velocity (m/s) and t is the pulse length (s) of the echosounder transducer.

The standard deviation of S_V is high, yielding a low S_V/*SSH* correlation (r=0.0095, Fig. SI10). We also correlated the time-derivative of the modeled sea-surface-height (*dSSH/dt*, Fig.SI10) with S_V, in order to attribute pressure drop to observed free gas in the water column. Considering that it takes time for bubbles originating at some sediment depth to reach the water column where they are detected, we applied time lags to the S_V observations. These time-shifted S_V values and *dSSH/dt* correlate weakly, and for the best-fitted time lag of 75 minutes, the correlation is r=-0.1181 (Fig. SI10), giving little support to the hypothesis. We conclude that the presented data neither supports nor falsifies the hypothesis that gas emissions increase when hydrostatic pressure drops.

Text SI7.

Correlation between results and tectonic activity

Due to the proximity to the tectonically active Molloy-Knipovich ridge system (4-8 earthquakes per year; Table SI6), it is hypothesized that earthquakes may influence the CH4-bubble seepage at our study area. As fluid migration is thought to occur along near-horizontal permeable pathways connected to deeper reservoirs (Rajan et al., 2012; Sarkar et al., 2012), earthquake loading may influence the conduit network at deeper sedimentary sections closer to the spreading-ridge system. To test our hypothesis and arrive at a first order correlation between free gas flow and earthquake events, we used earthquake data (International Seismological Centre 2014) from the area 65°N – 90°N and 30°W - 30°E between Jan 1st 2008 and Dec 31st 2014. 8,589 corresponding earthquakes were found in the database and 7,443 had magnitudes given.

The local influence of remote or nearby earthquakes events with magnitude M and distance R from our study site is not well constrained because the earth structure is too complicated for such a quantity to be well defined. However, seismologists have done substantial work in order to derive ground motion prediction equations. In order to acquire a first order estimate of the local impact, we chose the simple equation of L. Esteva and E. Rosenblueth (1964) which is given in Douglas (2011) in order to have a first order estimate of the local acceleration.

$$a = ce^{\alpha M} R^{-\beta} \qquad \text{(SI5)}$$

Where a is the local acceleration (cm s^{-2}), c=2000, α=0.8 and β=2. M is the magnitude of the earthquake and R is the distance (km) from the epicenter or hypocenter. The magnitude M is taken from the downloaded dataset (isc.ac.uk), and the distance is calculated as the distance from the center of our study site to the earthquake position. The earthquake magnitudes are max=6.4, mean=2.0 with a standard deviation of 0.85. Fig. SI11 shows the calculated acceleration a (max=35.9, mean=0.3, std=1.1 cm s^{-2}) and observed TS (max=-23.7, min=-55 dB) from all nine included surveys. We did not observe any features in this data suggesting either positive or negative influence on the free gas observations. Dividing the dataset into nine “cruise subsets”, yields close-up analysis of the TS values vs. calculated local acceleration. No correlation between higher seismic activity and increased gas release or vice versa could be inferred from this analysis.

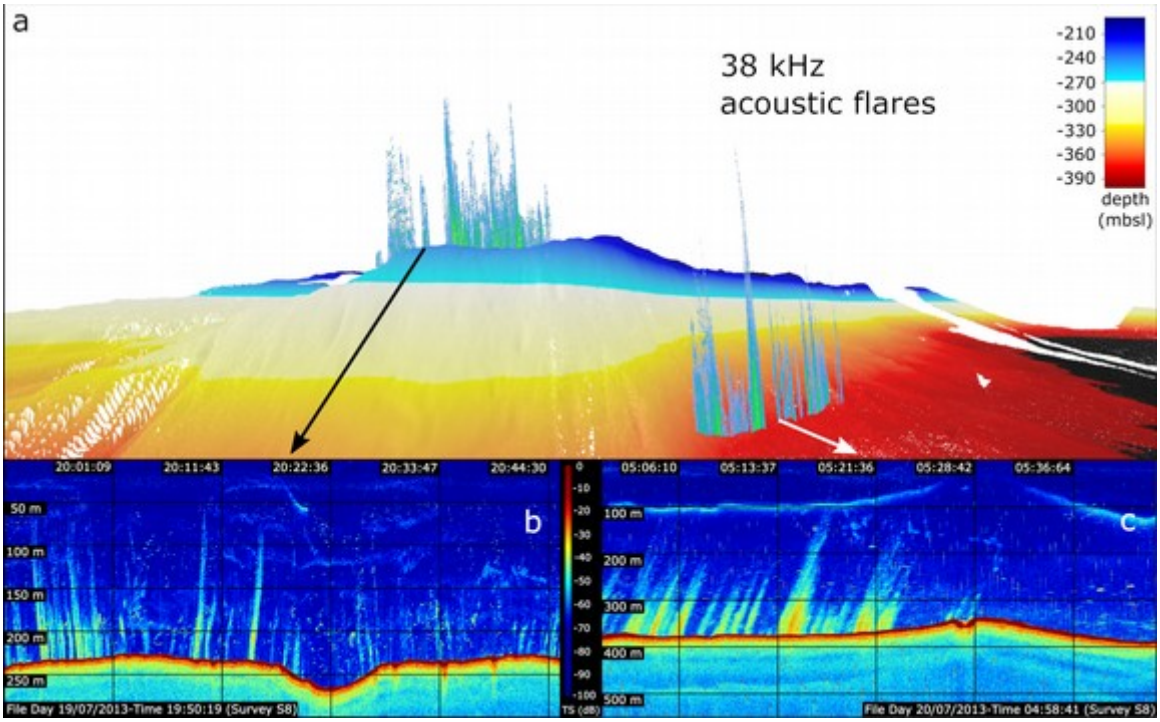

Figure SI1. Acoustic flares at PKF displayed in Fledermaus and Flarehunter GUI. a) 3-dimensional image produced with Fledermaus, showing flares and bathymetry. b, c) Echograms shown in Flarehunter GUI. Color scale indicates the Target strength (TS) of the backscatter signal. Flares are located at ~230 mbsl (SBreak-Area) and ~380 mbsl (Slope-Area).

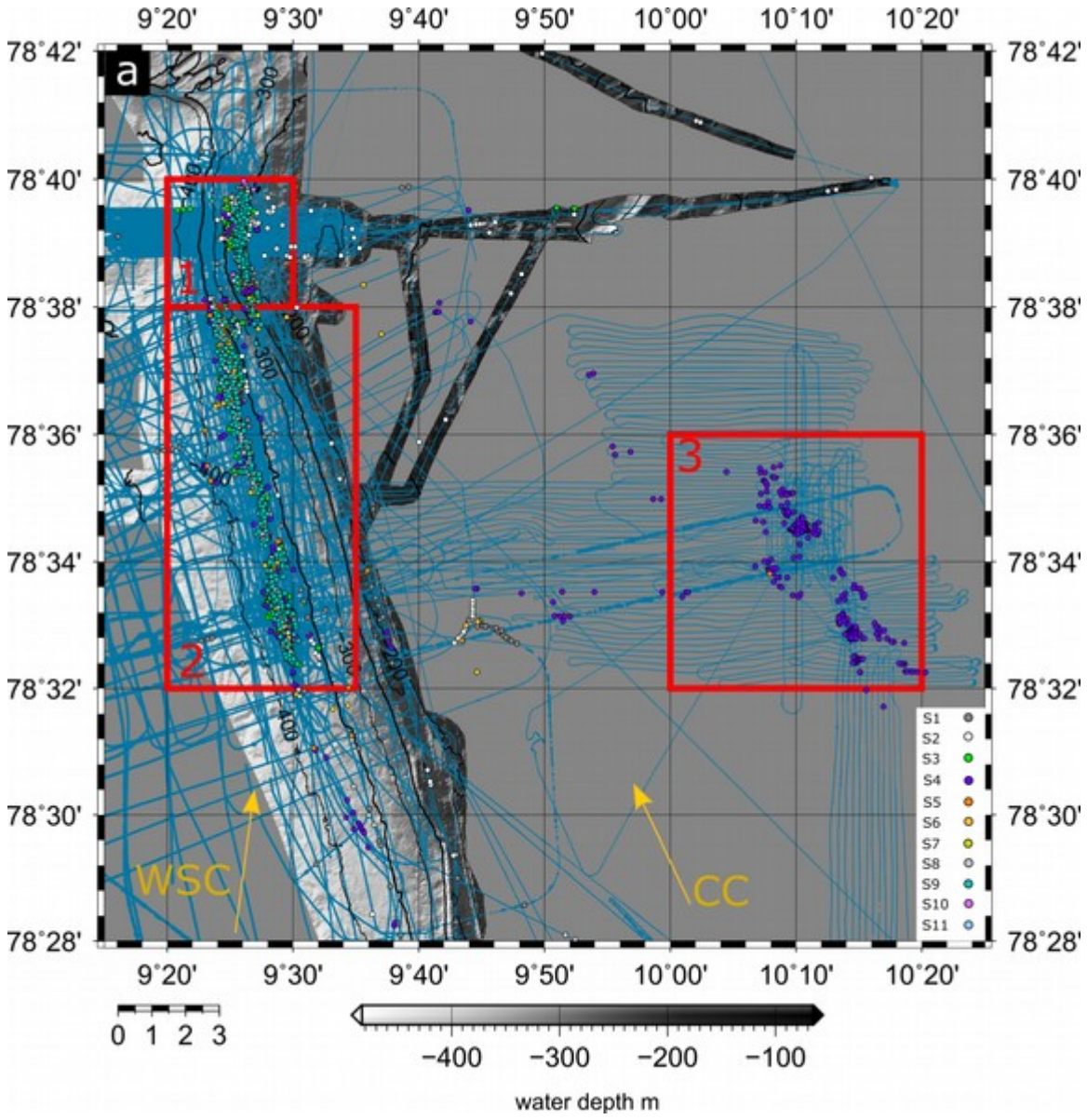

Figure SI2. Map of the study area. Gray scale shows the bathymetry and blue indicates the echosounder coverage at the seafloor. Colored dots indicate detected acoustic flares from different surveys. The red rectangles indicate the three defined sub-areas: (1) SBreak-Area, (2) Slope-Area, and (3) Shelf-Area). Yellow arrows indicate the influence of the West Spitsbergen Current (WSC) and the Coastal Current (CC).

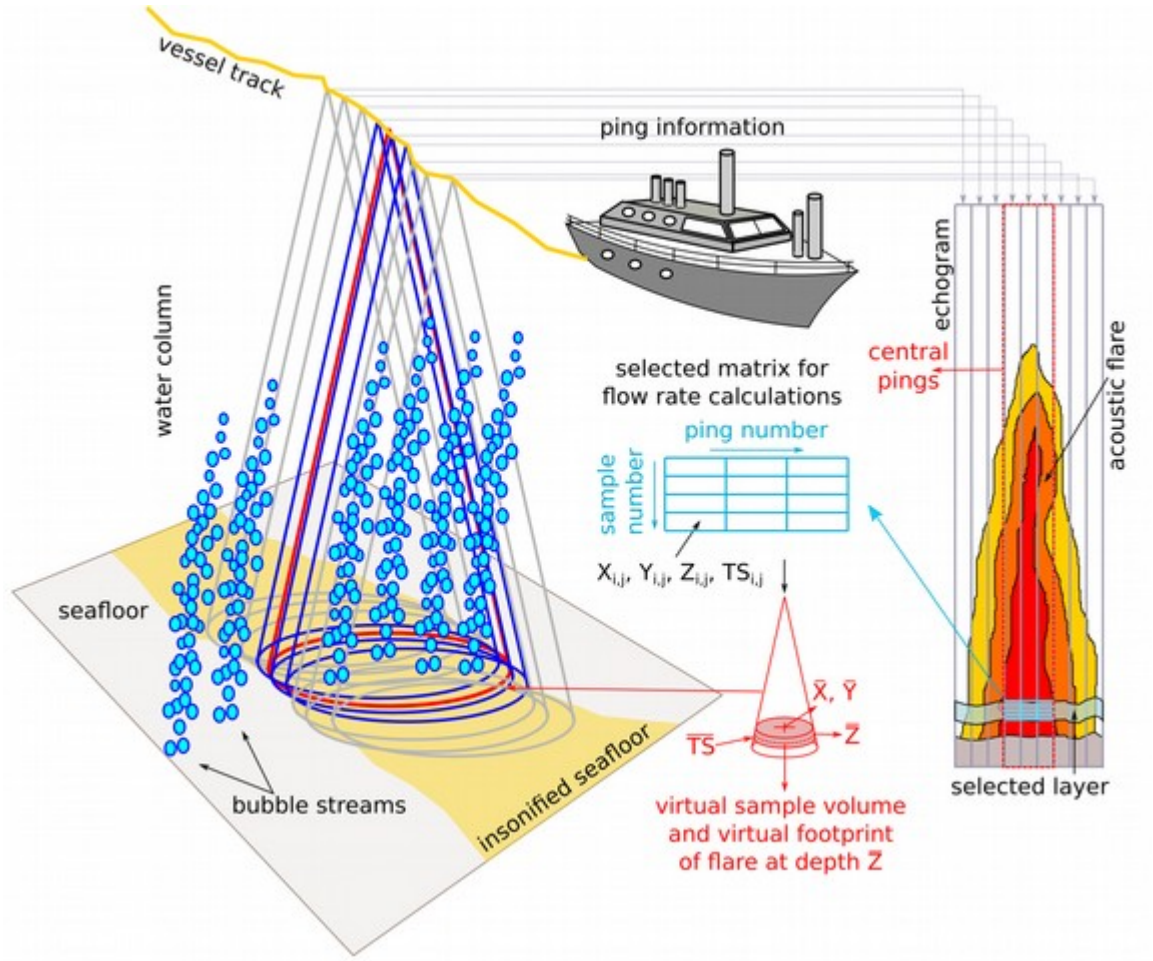

Figure SI3. Schematic illustrating the echosounder data collection, physical representation of a flare, data selection and the virtual footprint used in the flow rate calculations.

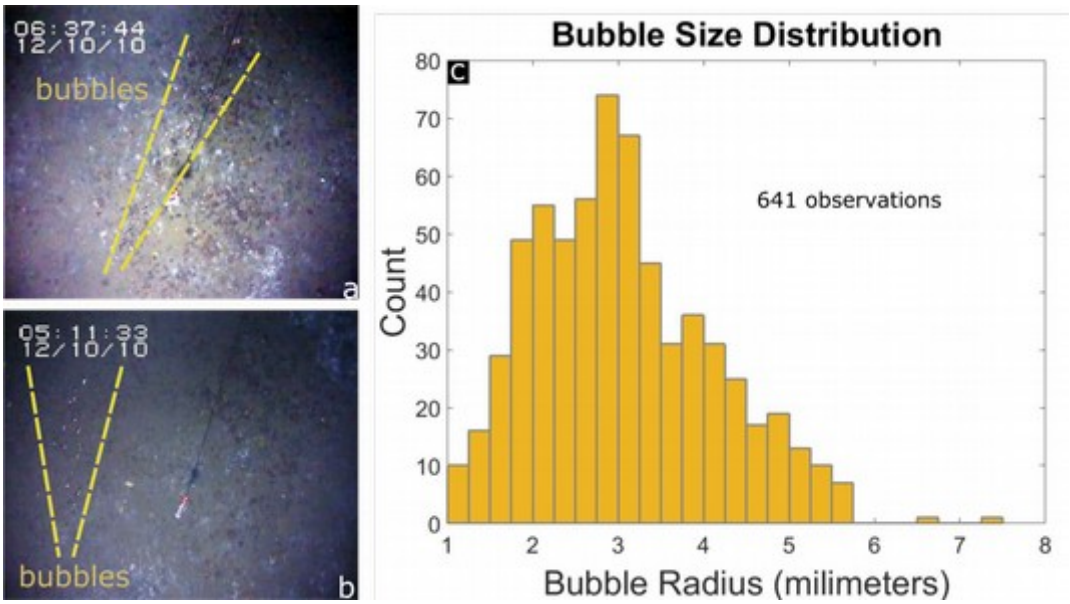

Figure SI4. a-b) examples of bubbles captured by the submersible video-camera system during survey S2. c) Bubble size distribution obtained from 641 bubble observations (Mc Govern, 2012)

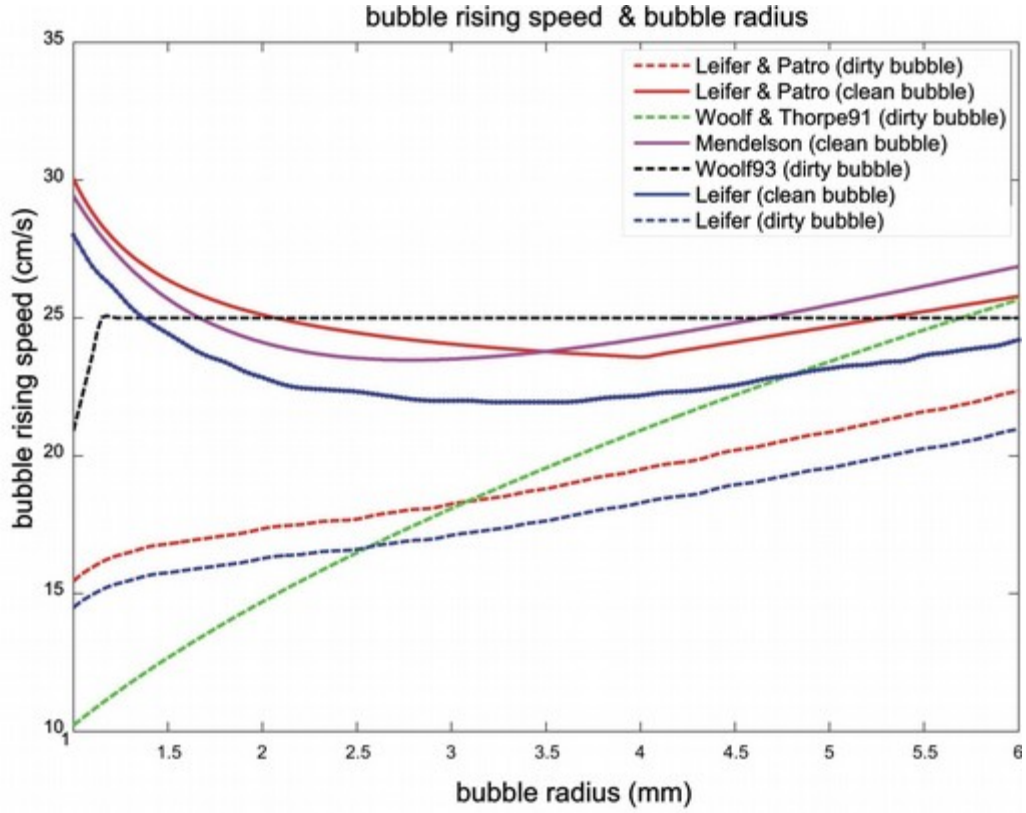

Figure SI5. Bubble rising speeds as functions of bubble radius (1 to 6 mm) using different models (Mendelson 1967; Woolf and Thorpe 1991; Woolf 1993; Leifer et al. 2000; Leifer and Patro 2002; Leifer et al., 2015). Figure from (Veloso et al. 2015).

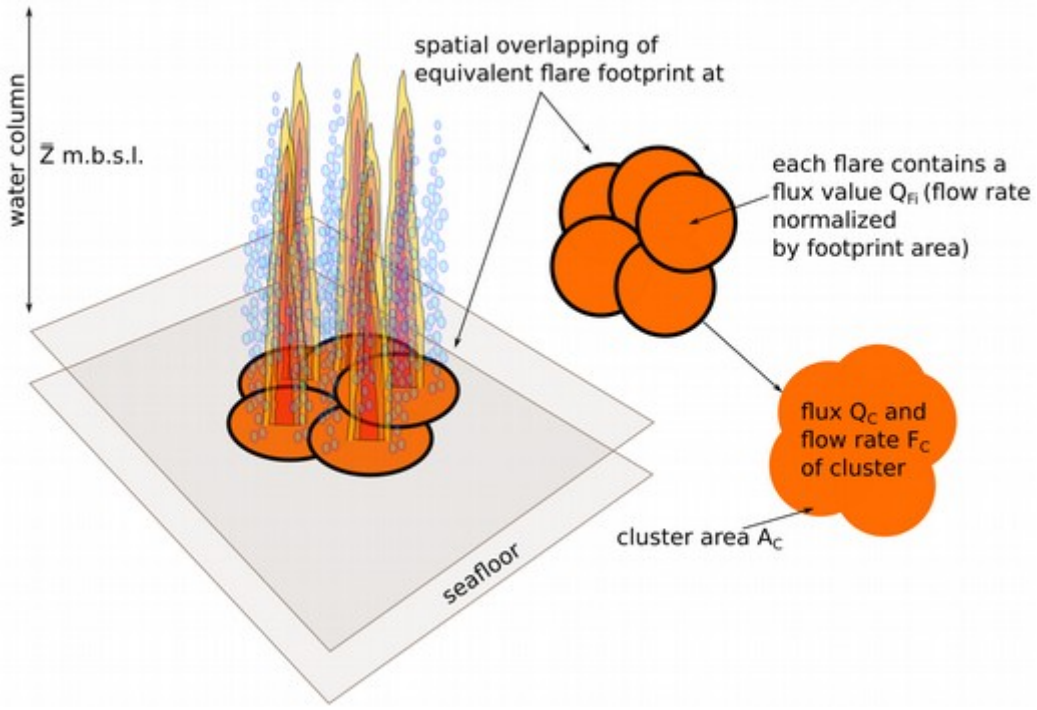

Figure SI6. Schematic illustrating the clustering process of acoustic flares that spatially overlap.

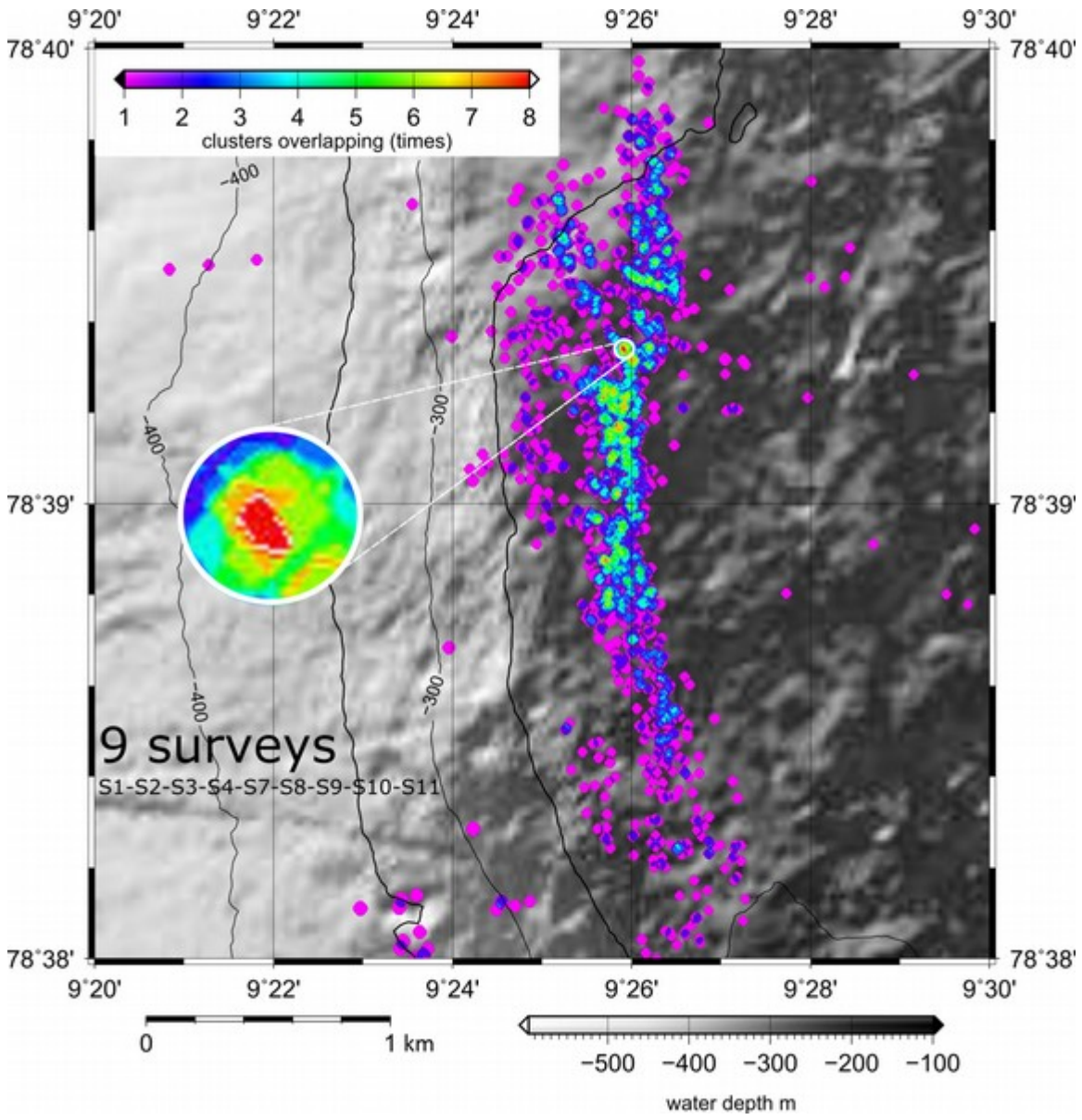

Figure SI7. Map of flare clusters in area A1. Colors indicate how many surveys that have identified the flare clusters. From 9 surveys (S1, S2, S3, S4, S7, S8, S9, S10, S11) the maximum overlap was 8 times.

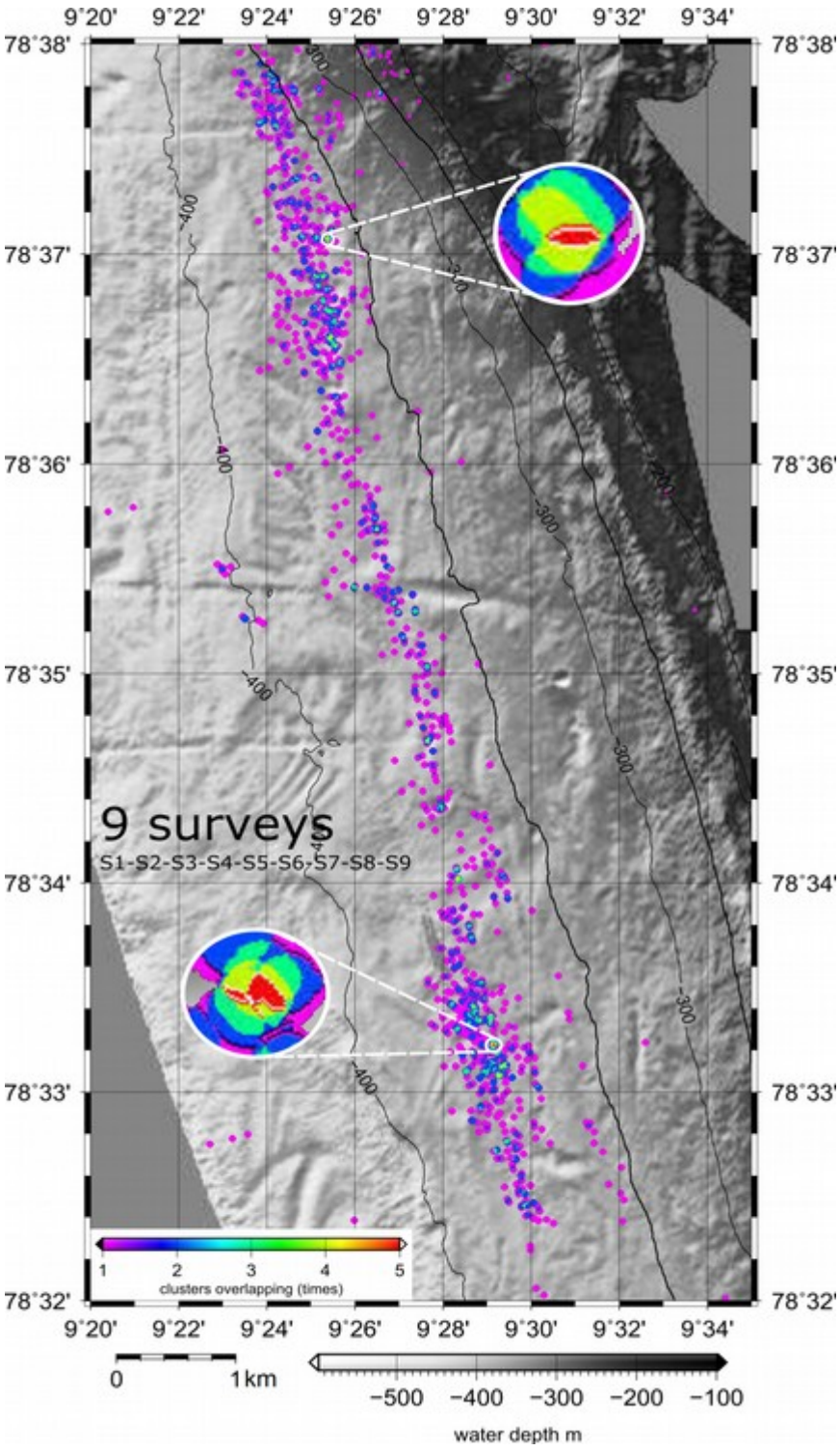

Figure SI8. Map of flare clusters in area A2. Colors indicate how many times flare clusters were covered during different surveys. From 9 surveys (S1, S2, S3, S4, S5, S6, S7, S8, S9) the maximum overlap obtained was 5 times.

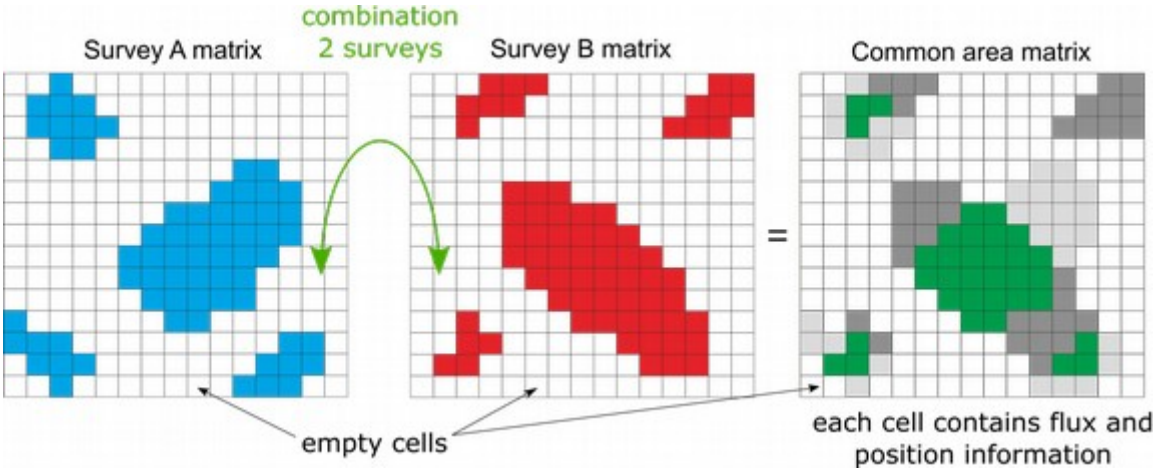

Figure SI9. Example of the combination of hydroacoustic information associated to bubble- seeping areas between two surveys.

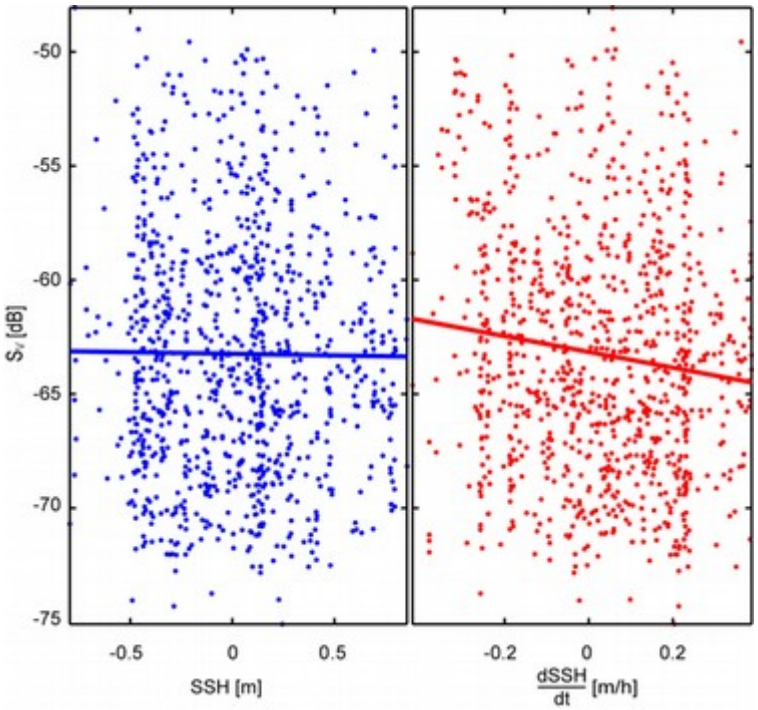

Figure SI10. Correlation between SSH and S_V. Left panel shows S_V values plotted against sea surface height (m) in blue dots and a linear regression as a blue line. Right panel shows S_V against the time derivative of SSH and a linear regression line (red dots and line).

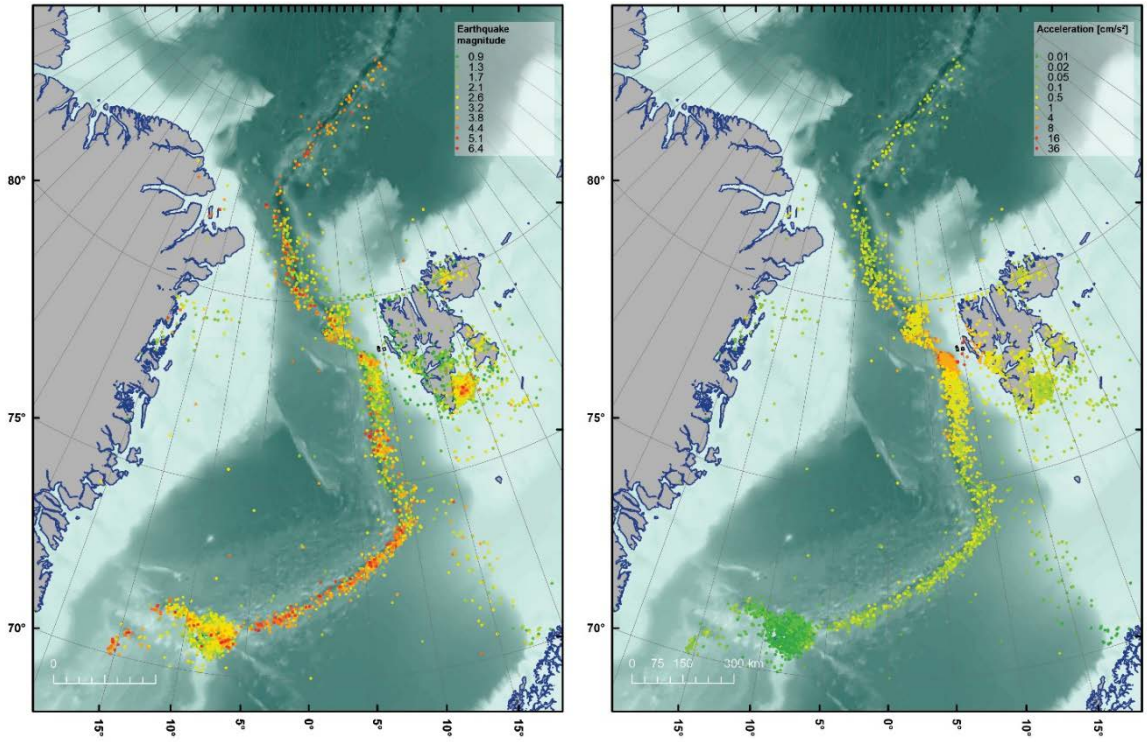

Figure SI11. Map of earthquake events. Left panel shows the earthquake Richter scale magnitude (mb, MC, MD or ML) and the right panel shows the local acceleration as calculated from equation 1 relative to the center of the study area.

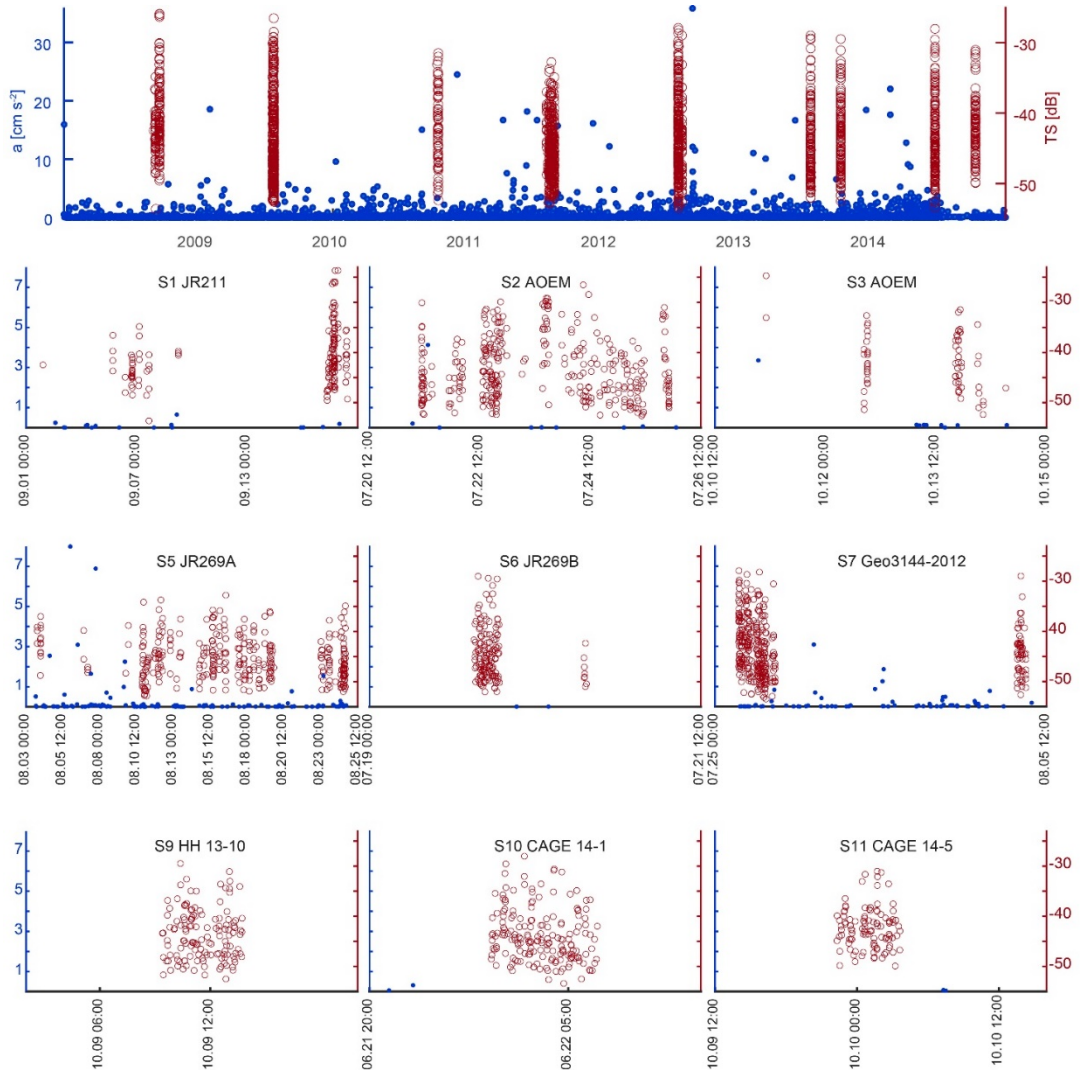

Figure SI12. Earthquake correlation with echosounder data. Blue dots are calculated accelerations (cm s^{-2}) (equation SI5) and the red circles denote TS values (dB) from the nine surveys in area A1.

Table SI1. List of hydroacoustic surveys considered in this study.

Survey number	Survey name	Month-year	Vessel
S1	JR211	August-2008	RV James Clark Ross
S2*	AOEM	July-2009	RV Helmer Hanssen
S3*	AOEM	October-2010	RV Helmer Hanssen
S4	JR253	July-2011	RV James Clark Ross
S5	JR269A	August-2011	RV James Clark Ross
S6	JR269B	July-2012	RV James Clark Ross
S7	Geo3144_2012	July-2012	RV Helmer Hanssen
S8	HH_13-7	July-2013	RV Helmer Hanssen
S9	HH_13-10	October-2013	RV Helmer Hanssen
S10	CAGE_14-1	June-2014	RV Helmer Hanssen
S11	CAGE 14_5	October-2014	RV Helmer Hanssen

*Surveys that include visual observations for BSD measurements (McGovern, 2012)

Table SI2. Water, gas and ambient constants used to evaluate flow rates of acoustic flares using the inverse hydroacoustic method

Constant Average	**Unit**	**Value**
Temperature water	C°	From CTD profiles (Excel File SI)
Static pressure at surface	Pa	101325
Water salinity	PSU	From CTD profiles (Excel File SI)
Water density	kg/m^3	From CTD profiles (Excel File SI)
Average sound speed in the water	m/s	From CTD profiles (Excel File SI . Del Grosso eq.)
Water shear viscosity	Pa·s	0.0014
Water surface tension	N/m	0.074
Gas density at the surface (CH_4)	kg/m^3	0.66
Acceleration of gravity	m/s^2	9.8
Specific heat capacity, CH_4	$J/(kg \cdot m^3)$	2191
Ratio of specific heat of gas	dimensionless	1.4

Table SI3. Common area fluxes for SBreak-Area. Fluxes are detailed for different surveys involved in the common area combination. All 29 combinations are shown. Average fluxes, standard deviation and relative errors are also detailed.

	S1	S2	S3	S4	S7	S8	S9	S10	S11	Common area (m^2)
Flux Kg/(yr·m^2)		7.16	1.67		2.96		7.61	2.89		5284
		9.39	3.80					6.19	2.41	9156
	1.15	8.02	3.33	4.06				6.80	4.05	8
		7.11			3.23					140924
		7.30			3.47	2.84	7.20			19512
					5.31	6.04	8.45	4.99	2.91	4916
		7.50				2.54	7.05			28708
		7.88						3.76		82248
		4.06						3.59	1.64	59612
		7.42		1.97	2.85					6708
					3.21	2.22	6.82			31588
						1.92	6.59			48960
								3.59	1.64	59612
	1.83	8.78	3.11				6.84	3.15		2868
	1.65	8.26	3.20		3.08	3.81				68
	1.34	10.09	3.57		5.48	3.59		6.34		1740
	2.34	8.97	3.81		4.62	3.41	6.10		6.10	1684
	1.40	8.45	3.35		3.97		7.36	3.37		2640
	1.22		3.72		5.35		7.74		1.83	1328
	2.88	7.98	3.67		3.62			4.52		5412
	2.85	8.25	3.91					4.94	1.93	2956
	1.76	7.16			2.96		7.61	2.89		5284
	2.32	7.47						3.48	1.91	9096
	1.28		3.12		3.78		7.25	3.49		3152
	2.19							3.24	1.66	15260
				1.49	2.61					15816
				2.35	2.76	3.22				3564
				2.07		2.16				7056
				2.05			7.68			5912
Mean	1.86	7.84	3.35	2.33	3.70	3.17	7.25	4.20	2.60	
Stdev	0.60	1.25	0.60	0.88	0.97	1.19	0.59	1.28	1.44	
Relative error (%)	26.99	10.75	11.67	24.90	21.22	24.92	6.30	25.48	40.21	

Table SI4. Common area fluxes for Slope-Area. Fluxes are detailed for different surveys involved in the common area combination. All 35 combinations are shown. Average fluxes, standard deviation and relative errors per each survey are also detailed.

	S1	S2	S3	S4	S5	S6	S7	S8	S9	Common area (m2)
Flux Kg/(yr·m^2)			0.57	1.45	1.27	0.23		0.46	3.32	20
		0.39	0.53							6724
		0.39							2.70	15052
			0.63				1.86			16828
			0.86				0.83	5.23	1.51	148
			0.58					1.01	3.02	10568
			0.53						1.54	138064
			0.57	4.03						86816
			0.63	5.94				1.36		7744
			0.57	1.54				0.76	2.74	1608
			0.52	2.98					2.08	21992
			0.59	5.14	2.37					8628
			0.62	1.26	1.44			1.56		772
			0.57	1.45	1.27	0.23		0.46		216
			0.57	1.45	1.27	0.23			3.32	684
			0.57	1.45		0.23		0.46		216
			0.59		1.59					34656
			0.57		1.27	0.23		0.46		228
								1.54	3.23	54400
	1.16		0.58							6396
	0.84		0.59						3.74	1684
	1.18		0.58	10.70						1776
	0.85		0.59	17.63					3.74	1032
				6.34				1.91	3.63	11580
				13.09	1.39	0.64		0.51		1760
				1.44	1.35	0.35			3.42	992
		0.31					0.44			16
							0.89	0.51	0.59	21148
				9.70			5.17			18248
				10.68			2.13	1.79		6824
				5.01			0.53	1.59	3.89	1488
				6.79			0.75		3.85	4484
				3.16	2.02		0.29			412
					1.20		1.33			4444
						0.77	2.55			4264
Mean	1.00	0.35	0.59	5.77	1.50	0.36	1.52	1.30	2.86	
Stdev	0.18	0.04	0.06	4.63	0.37	0.21	1.41	1.21	0.97	
Relative error (%);	15.92	27.95	6.20	136.56	18.51	47.44	66.87	59.28	27.39	

Table SI5. Flow rates of methane for seep sites located at PKF and around the world.

Annual Flow rate (T CH_4 y^{-1})	**Water depth (m)**	**Study area**	**Reference**
1075 (850 -1300)	193-352	PKF Area 1	This study
2050 (1600 -2500)	194-410	PKF Area 2	This study
575 (450 - 700)	67-117	PKF Area 3	This study
440 -675	~240	PKF 78°38'30''-78°40'N; 9°23'- 9°28' E	Veloso et al., 2015
433 (80-1090)	240-245	PKF Area 2 (comparable to Area 1 in this article)	Sahling et al., 2014
417 (64-802)	380-390	PKF Area 3 (comparable to Area 2 in this article)	Sahling et al., 2014
304	1250–1270	Håkon Mosby Mud Volcano– all three emission sites	Sauter et al., 2006
32-1395	890	Kerch Flare, Black Sea	Römer et al, 2012a
21.9	600–700	Northern summit of Hydrate Ridge, offshore Oregon	Torres et al., 2002
24	65–75	Tommeliten field, North Sea	Schneider von Deimling et al., 2011
641.6 (±513.28)	575–2870	Makran continental margin (50 km broad segment)	Römer et al, 2012b
3.6892 to 36.892	1690	Carbonate slab, Nile Deep Sea Fan	Römer et al, 2014

Table SI6. Earthquakes event occurrences with significant magnitudes during each year (2008-2014). Magnitudes are given in the Richter scale. All earthquakes with magnitude 4 or larger are in mb units but for some of the less powerful earthquakes the magnitude is given in ML.

Year	2008	2009	2010	2011	2012	2013	2014
Count 3<M<4	11	31	20	18	8	20	12
Count M>=4	5	8	5	4	6	5	4

Paper 2

Physical controls of dynamics of methane venting from a shallow seep area west of Svalbard

A. Silyakova[1], P. Jansson[1], P. Serov[1], B. Ferré[1], A. K. Pavlov[2], T. Hattermann[3,4], C. A. Graves[5,6], S. M. Platt[7], C. Lund Myhre[7], F. Gründger[1] and H. Niemann[8,1,9]

[1]CAGE-Centre for Arctic Gas Hydrate, Environment and Climate, UiT the Arctic University of Norway in Tromsø, Department of Geosciences, Tromsø, Norway
[2]Norwegian Polar Institute, Fram Centre, Tromsø, Norway
[3]Akvaplan-niva AS, Fram Centre, Tromsø, Norway
[4]Alfred Wegener Institute, Helmholtz Centre for Polar and Marine Research, Bremerhaven, Germany
[5]Leibniz Institute for Baltic Sea Research Warnemünde, Rostock, Germany
[6]Centre for Environment, Fisheries and Aquaculture Science, Lowestoft, UK
[7]NILU - Norwegian Institute for Air Research, Kjeller, Norway
[8]University of Basel, Basel, Switzerland
[9]NIOZ Royal Netherlands Institute for Sea Research, Department of Marine Microbiology & Biogeochemistry, the Netherlands

Corresponding author: Anna Silyakova (**anna.silyakova@uit.no**)

Key Points:

- Gas seepage intensity and lateral water mass movements are key controls of water column methane content
- Vertical methane transport is limited irrespective of stratification
- Eddies play a key role in horizontal advection and dispersion of dissolved methane

Abstract

We investigate methane seepage on the shallow shelf west of Svalbard during three consecutive years, using discrete sampling of the water column, echosounder-based gas flux estimates, water mass properties, and numerical dispersion modelling. The results reveal three distinct hydrographic conditions in spring and summer, showing that the methane content in the water column is controlled by a combination of free gas seepage intensity and lateral water mass movements, which disperse and displace dissolved methane horizontally away from the seeps. Horizontal dispersion and displacement of dissolved methane are promoted by eddies originating from the West Spitsbergen Current and passing over the shallow shelf, a process that is more intense in winter and spring than in the summer season. Most of the methane injected from seafloor seeps resides in the bottom layer even when the water column is well mixed, implying that the controlling effect of water column stratification on vertical methane transport is small. Only small concentrations of methane are found in surface waters, and thus the escape of methane into the atmosphere above the site of seepage is also small. The magnitude of the sea to air methane flux is controlled by wind speed, rather than by the concentration of dissolved methane in the surface ocean.

1 Introduction

The Arctic Ocean holds vast reservoirs of the powerful greenhouse gas methane in the form of free and dissolved gas (Lammers et al., 1995; Damm et al., 2005), gas entrapped in subsea permafrost (Shakhova et al., 2010), and gas hydrates in sediments (Hester and Brewer, 2009; Westbrook et al., 2009; Berndt et al., 2014). In particular, gas that is bound in hydrates may be released as a result of temperature induced gas hydrate destabilization (Kretschmer et al., 2015; James et al., 2016), which makes the warming Arctic Ocean a potential hot spot of future methane emission (Shakhova et al., 2010; Kort et al., 2012; Parmentier et al., 2015). Methane release from the seafloor has been documented from numerous areas along the Arctic Ocean continental margin: the West Spitsbergen continental margin and shelf (Knies et al., 2004; Damm et al., 2005; Westbrook et al, 2009; Sahling et al., 2014; Smith et al., 2014; Graves et al., 2015; Mau et al., 2017), the Barents Sea (Lammers et al., 1995; Serov et al., 2017; Andreassen et al., 2017), the Kara Sea shelf (Portnov et al., 2013; Serov et al., 2015), the East Siberian Shelf (Shakhova et al., 2010, 2013), and the Beaufort Sea (Kvenvolden et al., 1993; Paull et al., 2007). Methane release from the West Spitsbergen margin has been ongoing for several millennia and is, at least partly, temperature controlled (Berndt et al., 2014).

Indeed, Arctic air temperatures are increasing twice as fast as the global average because of Arctic amplification (Graversen et al., 2008; Serreze and Francis, 2006; IPCC 2014). The annual average Arctic air temperature is now 3.5°C warmer compared to the beginning of 20th century (Soreide et al., 2016). As a result, expanding areas of ice-free Arctic Ocean waters are being exposed to solar radiation and elevated air temperatures. Combined with an increase of heat input from adjacent ocean basins, e.g. warmer than usual Atlantic Water (AW) propagating deeper into the Arctic Ocean (Polyakov et al., 2004; 2007; 2010), this results in a present day Arctic Ocean sea surface temperature which is 5°C warmer than the 1982-2010 average for the Barents and Chukchi seas and around Greenland (Soreide et al., 2016). The effect of increasing temperature in the future Arctic may therefore become more important for Arctic seafloor methane liberation (Westbrook et al., 2009; Ferré et al., 2012; Marín Moreno et al., 2015).

Several processes determine the fate of methane released into the water column from sediments and, most importantly, its release to the atmosphere. Methane contained in bubbles emanating from the seafloor dissolves in seawater and can be rapidly transported from the area by the advection of water masses (Graves et al., 2015). The upward transport of dissolved methane has been found to be limited by water column stratification (e.g. Schmale et al., 2005; Leifer et al., 2009). Studies by Myhre et al., (2016) and Gentz et al., (2014) conducted on the shallow shelf and upper continental slope off Svalbard, west of Prins Karls Forland (PKF) revealed waters enriched with dissolved methane below the pycnocline. However, the methane concentrations above the pycnocline were generally in equilibrium with the atmospheric mixing ratio. This suggested that the pycnocline may act as a physical barrier, preventing dissolved methane from entering the well-mixed upper layer of the water column and thus also the atmosphere, instead trapping methane in the lower sphere of the water column. The open Arctic Ocean is stratified throughout the year (Rudels et al., 1994). In shallower areas, however, the stratification of the entire water column is subject to an annual cycle and a seasonal erosion of the pycnocline e.g. through winter time convection or wind induced mixing (Cottier et al., 2010). If controlled by stratification, the escape of methane to the atmosphere would also follow this seasonality. In other words, the potential for methane to be liberated to the atmosphere

from these areas is higher when there is no stratification during stormy seasons (von Deimling et al., 2011).

Another important process determining the fate of methane in the water column is its removal by aerobic methane oxidation (MOx), mediated by aerobic methanotrophic bacteria (Hanson & Hanson, 1996; Reeburg, 2007; Steinle et al., 2015). Methane removal from deep-water sources through MOx is more efficient than that from shallow sources, because the distance between methane liberation from the seafloor and potential methane evasion to the atmosphere is greater and methanotrophs in the water column have more time for methane consumption (Steinle et al., 2015; Graves et al., 2015; James et al., 2016). For example, in the deep Gulf of Mexico (~1500 meters water depth), most of the methane discharged following the Deepwater Horizon oil spill was consumed by water column methanotrophs (Kessler et al., 2011), while most of methane seeping from the shallow seafloor on the East-Siberian Shelf (~50 m water depth) was liberated to the atmosphere, especially during storm-induced mixing events (Shakhova et al., 2013).

Marine environments in the Arctic Ocean characterized by ongoing methane release are ideal natural laboratories for studying the effects of potentially enhanced seafloor methane venting in warming waters, and the processes that regulate the transport of this methane. In this paper, we study the dynamics of methane venting from shallow gas-bearing sediments (water depth: 50-120 meters) west of PKF off the Svalbard archipelago; and the physical processes in the water column that control methane dispersion and displacement away from the seeps. We conducted oceanographic surveys to determine the flux of free gas (i.e. bubbled methane) from sediments, concentrations of dissolved methane in the water column, sea-air methane fluxes, and water mass properties. Measurements were repeated in a defined study area during three consecutive years to investigate the dynamics of venting methane under varying hydrographic conditions. Model simulations place these detailed observations into the broader seasonal context, and allow a better understanding of the oceanographic processes controlling methane dynamics in the area of study.

The paper is structured as follows: Section 2 provides an overview of the study region and summarizes the different datasets and methods used in the analysis. Section 3 presents the results and successively examines the controls of the methane fluxes from the sediment (sources), the controls of the sea-air methane fluxes (sink I), the controls of the methane content in the water column (sink II), the controls of the vertical distribution of the dissolved methane, and the controls of the horizontal distribution of the dissolved methane. Section 4 discusses the implications of main findings on the controls of the methane distribution and provides the conclusions of the paper

2 Methods

2.1 Study area

Our study area (423 km^2; 50 - 120 m water depth) is located west of PKF (Fig. 1). The seafloor in this area is complex and characterized by abundant depressions and a sequence of pronounced end moraine ridges: the Forlandet moraine complex (Landvik et al., 2005). Several hundred methane flares were found during the present study and previous expeditions (e.g. Sahling et al., 2014 and references therein). Similar to the adjacent shelf break, gas seepage is not related to pockmarks or other fluid leakage related structures and the origin of the methane remains unconfirmed (Westbrook et al., 2009; Berndt et al., 2014). Although hydrates have never been recovered in the area and seismic evidence of

gas hydrates is missing, sediment cores drilled outside PKF contained freshwater presumably originating from dissociated gas hydrates (Wallmann et al., 2018). Previous studies also suggest that free gas may originate from gas hydrate dissociation deeper on the continental slope (>300 m) where gas hydrates have been found (Sarkar et al., 2012) and migrate along the permeable zones towards the shelf (Westbrook et al., 2009). An alternate hypothesis is that glacial rebound at the beginning of the Holocene resulted in gas hydrate dissociation, which allowed for the formation of shallow gas pockets that continue to release methane into the water column (Portnov et al., 2016; Wallmann et al., 2018).

The water masses and circulation in the study area are controlled to a large extent by the interaction of coastal processes on the shelf with the West-Spitsbergen Current (WSC) that circulates northward along the shelf break as the northernmost extension of the North-Atlantic Current, transporting AW into the Arctic Ocean. The core of the WSC is at 250-800 meters water depth (Perkin and Lewis, 1984) and the stream follows the slope of the continental margin (Aagaard et al., 1987). By bringing large amounts of salt and heat, it affects the water column structure in the entire area. Other currents in the area are the East Spitsbergen Current (ESC) that advects Arctic waters into the region, and the coastal surface current, associated with the West Spitsbergen Polar Front (Nilsen et al., 2016). Local scale physical processes affecting water mass circulation include exchange of water masses between the WSC and shelf waters due to instability of the WSC core and resulting eddies (Teigen et al., 2010; Hattermann et al., 2016; Appen et al., 2016); as well as wind forcing and resulting upwelling events (Berge et al., 2005; Cottier et al., 2007).

2.2 Survey design

We conducted research expeditions with the R/V Helmer Hansen in the study area during three consecutive years: 25-27 June 2014 (hereafter, June-14), 01 – 03 July 2015 (July-15), 02 – 04 May 2016 (May-16). Each year we visited 64 hydrographic stations. Stations were positioned in a grid for comprehensive coverage of the water column above active methane seeps (Fig. 1). We collected hydrocast data from each station including continuous measurements of conductivity, temperature, depth (CTD), and sampled the water column at discrete depths for subsequent dissolved methane concentration measurements (see details in section 2.4). The entire grid was subsampled within 3 days during each survey. Underway hydro-acoustic scanning of the water column was performed to acquire information on gas flares (section 2.3). Ship-mounted meteorological instruments continuously recorded air temperature, atmospheric pressure, wind speed and direction. Furthermore, atmospheric methane mixing ratios were recorded continuously with a Cavity Ring-Down Spectrometer (CRDS, PICARRO G2401) with an air intake at 22.4 m above sea level.

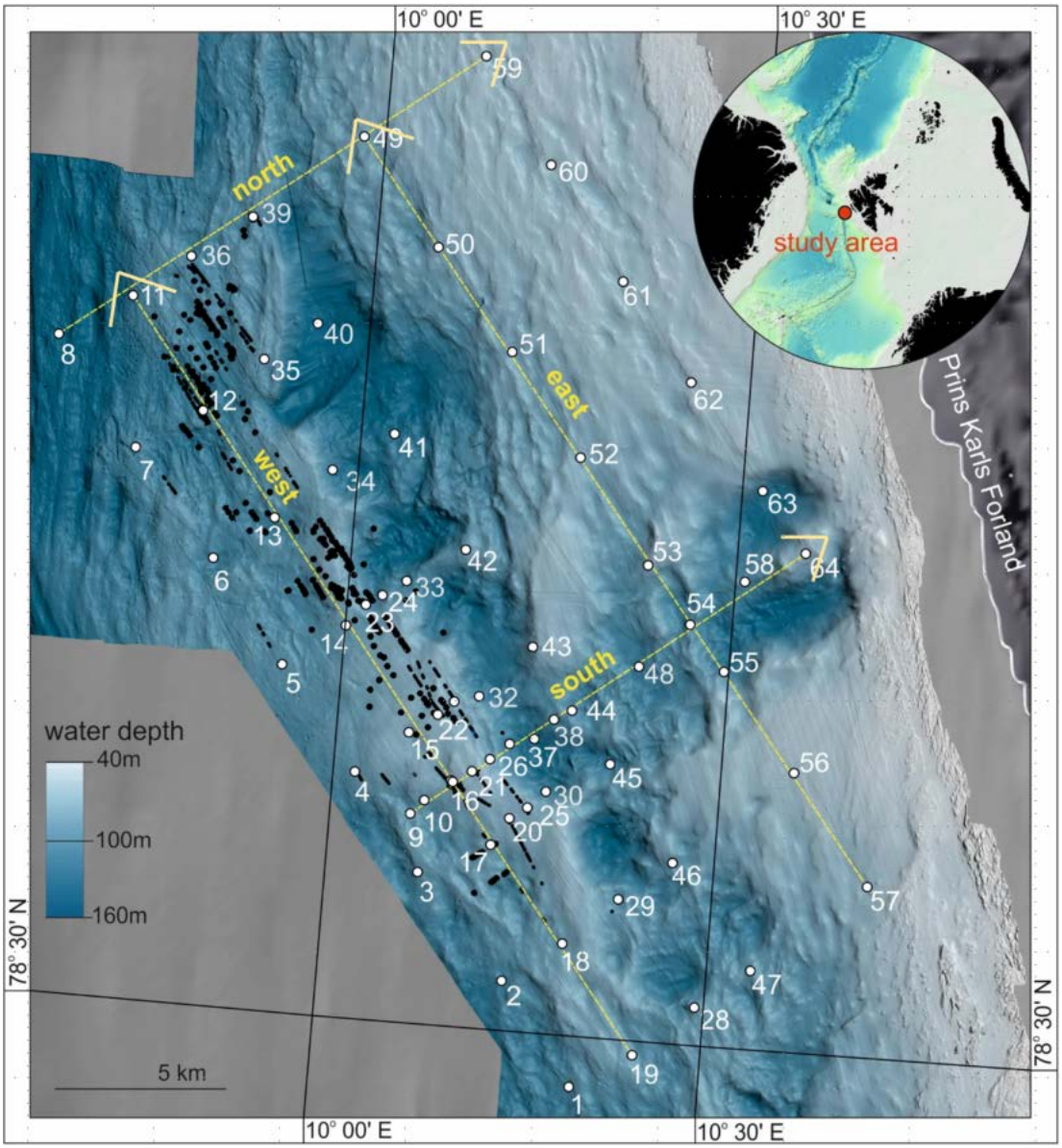

Figure 1. Bathymetric map of the study area with 64 hydrographic stations (white dots) for oceanographic measurements west of the Svalbard archipelago (overview map). Black dots indicate locations of methane seeps detected on echograms during all three surveys. Yellow dashed arrows indicate transects shown in Fig. 4. Bathymetry data were acquired on board with a Kongsberg Simrad EM 300 multibeam echo sounder (frequency of 30 kHz).

2.3 Hydroacoustic data acquisition and gas flux calculations

Gas bubbles in the water column were detected as acoustic signatures (flares) with a Kongsberg Simrad EK60 single beam echosounder system. This system is primarily designed for the fishery industry, but is also used to detect gas bubbles in the water column (Ostrovsky et al., 2008; Nikolovska et al., 2008). Data were acquired at 38 kHz as this is the most appropriate frequency to detect gas bubbles of sizes expected for cold seeps (Greinert et al., 2006). We used the FlareHunter program (Veloso et al., 2015) to distinguish flares from other echo signals such as fish, seafloor, and interference artifacts, and calculated flow rates from echosounder backscatter based on beam compensated Target Strength (TS, dB) in a 5-10 meter layer above the seafloor. We report free gas

flow rates as mean values calculated from seven different bubble rising peed models (BRSMs). The relative uncertainty between BRSM estimates is 16 % (Veloso et al., 2015). The total length of our survey line was 408 km in June-14, 427 km in July-15, and 300 km in May-16. Accounting for water depth and the resulting beam width radii of 5 – 20 m, the area of the seafloor investigated by the echosounder was 5.5 km^2 in June-14 and July-15, and 3.8 km^2 in May-16, which amounts to ~1 % of the total study area. Since the fraction of the study area covered by echosounder was small and slightly different between the three surveys, we applied Kriging interpolation to scale up estimates over the entire study area and thus facilitate comparison (details are provided in supporting information Text S1 and Fig. S1). Note that Fig. 2 shows observed flow rates of single sources. For comparison with other studies we present flow rates for the whole study area in Table 2 calculated as: (i) integrated over the entire area volumetric flow rate (L min^{-1}); (ii) converted into mass flow rate (t y^{-1}) using the ideal gas law and accounting for the average depth within each cell; and (iii) mean flux averaged over the whole area (mmol m^{-2} d^{-1}), converted from mass flow rate using the molecular weight of methane and divided by the survey area (423 km^2).

2.3 CTD profiling and water sample analyses

Vertical profiles of seawater temperature, salinity and pressure were recorded with a SBE 911 plus CTD probe at a rate of 24 Hz. The probe was mounted on a rosette including 12 5-litre Niskin bottles. The Niskin bottles were closed during the up-cast (at speed of 1 m s^{-1}). For analysis of hydrographic profiles, only down-casts were considered. Water samples were taken at 5, 15 and 25 meters above the seafloor and below the sea surface, and an additional two samples were collected at evenly spaced depth levels between 25 m above the seafloor an 25 m below the sea surface. In total, eight depths were sampled during all surveys.

Immediately upon recovery, sub-samples from the Niskin bottles were collected through silicon tubing into 60 ml plastic syringes (June-14) or 120 ml serum glass bottles (Jule-15, May-16) with rinsing by 2 – 3 overflow volumes. Syringes were closed with a 2-way valve and serum bottles were crimp-sealed with butyl rubber septa. 5 ml N_2 headspace was added to the syringes and serum bottles. Syringes/serum bottles with headspace were vigorously shaken for two minutes to allow the headspace N_2 to equilibrate with the dissolved methane in the water sample. Headspace methane mixing ratios were determined by gas chromatography (GC). During the June-14 survey a ThermoScientific FOCUS GC equipped with a flame ionization detector (FID), and a Resteck 2 m packed column HS-Q 80/100 with hydrogen (40 ml min) as a carrier gas was used. During the July-15 and May-16 surveys a ThermoScientific Trace 1310 GC equipped with an FID, and a Restek 30 m Alumina BOND/Na_2SO_4 column with hydrogen as a carrier gas (40 ml min^{-1}) was used. The column temperature was held constant at 40°C. The systems were calibrated with external standards (2 ppm and 30 ppm in June-14 (Air Liquide); 10 ppm, 50 ppm, and 100 ppm in July-15 and May-16 (Carbagas). Finally, water column methane concentrations were calculated from headspace methane mixing ratios according to Wiesenburg & Guinasso (1979) with consideration of salinity, sample temperature and ambient atmospheric pressure.

2.4 Calculations of water column methane content

To account for the uneven bathymetry (bottom depths of 50 to 120 m), when comparing bottom, intermediate and surface waters, we divide the water column in three layers (Fig. S2): (1) a bottom layer (0-15 meters above seafloor), (2) an intermediate layer (15 meters above seafloor to 20 m water depth; the upper boundary roughly follows the depth of the pycnocline during the July-15 survey,

which we determined as a function of the Brunt–Väisälä frequency, see Fig. 5) and (3) a surface layer (20 m water depth to sea surface). Detailed calculations of the methane content (in mol) within the study area can be found in supporting information Text S2.

2.5 Calculations of the sea-air methane flux

The sea-air methane flux F (mol m^{-2} s^{-1}) was calculated according to Wanninkhof et al. (2009):

$$F = k(Cw - Co), \text{ (Eq. 1)}$$

where k is the gas transfer velocity (m s^{-1}), Co is the methane concentration (mol m^{-3}) at the ocean surface in presumed equilibrium with the atmosphere and Cw is the measured concentration of methane (mol m^{-3}) in the well-mixed surface layer, typically measured at 5 m water depth. The flux is positive and the ocean emits methane into the atmosphere if the measured concentration in the surface layer is greater than the equilibrium concentration. Co (mol m^{-3}) is defined as:

$$Co = \beta\, pCH_4, \text{ (Eq. 2)}$$

where β is the Bunsen solubility (mol m^{-3} atm^{-1}) of methane in seawater (Wiesenburg and Guinasso, 1979):

$$\beta = \exp[-68.8862 + 101.4956\left(\frac{100}{T_w}\right) + 28.7314\left[\ln\left(\frac{T_w}{100}\right)\right] + S(-0.076146 + 0.04397\left(\frac{T_w}{100}\right) - 0.0068672\left(\frac{T_w}{100}\right)^2], \text{ (Eq. 3)}$$

where T_W is the water temperature (K) and S is the salinity.

pCH_4 is the partial pressure of methane in the air, derived from the mixing ratio of methane in the atmosphere xCH_4 (mol mol^{-1}) measured by the on board CRDS at a height of 22.4 m (1902 ppb in June-14, 1917 ppb in July-15 and 1955 ppb in May-16). The pCH_4 was calculated according to Pierrot et al., (2009):

$$pCH_4 = xCH_4 * [P_{atm} - P_{wvapor}], \text{ (Eq. 4)}$$

accounting for the atmospheric pressure P_{atm} (atm) measured by the meteorological station on board, and the water vapor pressure P_{wvapor} (atm) calculated according to Weiss and Price (1980):

$$P_{wvapor} = exp[24.4543 - 67.4509\left(\frac{100}{T_A}\right) - 4.8489\ln\left(\frac{T_A}{100}\right) - 0.000544S], \text{ (Eq. 5)}$$

where T_A is the air temperature (K) from the ships' meteorological station and S is the salinity of spray in overlaying atmosphere, here assumed equal to the salinity of surface water.

The gas transfer velocity k is wind dependent and calculated as described in Graves et al. (2015) and references therein:

$$k = 0.24 * u_{10}^2 (\frac{Sc}{660})^{-0.5}, \text{ (Eq. 6)}$$

where u_{10} (m s^{-1}) is the wind speed at 10 m above the sea surface, recalculated from the wind speed u_{meas} (m s^{-1}) measured by the ships' anemometer at height 22.4 m (z_{meas}) after Hsu et al., 1994:

$$u_{10} = u_{meas} * (\frac{Z_{meas}}{10})^{-0.11}, \text{ (Eq. 7)}$$

The Schmidt number *Sc* in Eq. 6 is the non-dimensional ratio of gas diffusivity and water kinematic viscosity, and was defined as 677 in accordance with Wanninkhof et al., (2009).

2.6 Modelling of water mass properties and particle release experiments

To study seasonal variations in water mass properties and circulation and to scale up our observations to a full year, we used a high-resolution regional ocean sea ice model. A more detailed description and validation of the Svalbard 800 m horizontal resolution model (the S800-model hereafter) can be found elsewhere (Albretsen et al., 2017; Hattermann et al., 2016; Crews et al., 2017). Briefly, the S800-model provides hindcast ocean sea ice simulations for the Svalbard and the Fram Strait region based on the Regional Ocean Modelling System (ROMS, Shchepetkin and McWilliams, 2005) and a coupled sea ice component (Budgell, 2005). Boundary conditions are provided by a 4 km pan-Arctic setup (A4-model). Bathymetry is based on the ETOPO1 topography (Amante, 2009). Vertically, the model is discretized into 35 levels with a layer thickness of less than 1 m near the surface over the continental shelf. The S800-model is initialized and forced with daily averages from the A4-model, for which boundary conditions and forcing fields are based on reanalyses (Storkey et al., 2010). Atmospheric forcing is provided by ERA-interim reanalysis (Dee et al., 2011) and climatological river input from major rives in the area, including freshwater runoff from the Svalbard archipelago (details in Hattermann et al., 2016). The S800-model was initialized from January 2005, and the data shown in this study are based on model runs from July 2005 to July 2010, averaged every month over that period.

Modelling results were extracted from a modelled field that included 41×56 grid points and corresponded to the geographic area of the survey between CTD stations 1, 8, 57, 59, 64 (Fig.1; also red polygons in Fig. 10).

To investigate seasonal features of methane dispersion and displacement in the study area, we conducted numerical experiments by simulative release of neutrally buoyant Lagrangian drifters (hereafter particles) that were advected by the model velocity field. We released particles from the polygon where the most intense seeps were observed during the surveys. The polygon enclosed CTD stations 3 (113 m water depth), 4 (103 m water depth), 15 (91 m water depth), and 17 (97 m water depth) (Fig. 1). Due to varying water depths at these stations, we chose to release particles from uniform depths between 80 and 100 m. Trajectories were computed using Lagrangian particle tracking algorithm TRACMASS (Döös et al. 2017) based on the daily S800-model output (see Hattermann et al. 2016 for details). Particles were released every day and were tracked for a maximum lifetime of ten days. From the end positions of all particles released within a respective month, histograms of particle distributions were computed by bin-counting particle positions on the S800-model lattice. The histograms were normalized to the total number of particles and used as a proxy for mapping the particle dispersion in the region. In addition, monthly averages were computed according to the distance of particles from their source (as a measure of the particle displacement) and to the distance from their mean position at t = 5 days (particle dispersion).

3 Results and discussion

3.1 Controls on flare abundance and methane flux from sediments

We observed the densest flare cluster in the western and northwestern part of the study area (Fig. 2). This cluster was venting free gas during all cruises. In contrast, there was a difference in flare density between surveys in the southern part of the study area, with the highest flare density during the June-14 survey, and much lower densities during the July-15 and May-16 surveys. In total, we counted 225

individual flares in June-14, 208 in July-15 and only 92 during the May-16 survey. The estimated gas flux from individual flares ranged between 20 and 600 ml min^{-1} (Fig. 2). As a consequence of the decreasing flare density from June-14 to May-16, the calculated total volumetric gas flow rate over the surveyed area was larger for June-14 (900 L min^{-1}) than for the July-15 (665 L min^{-1}) and May-16 surveys (540 L min^{-1}) (Table 1).

We carefully checked for factors that may have potentially biased our estimates. The May-16 survey was substantially shorter in distance (~70% compared to June-14 and July-15), decreasing the confidence in scaling up our observations to the entire area. Yet, the western part of the study area, where we always observed the highest flare density, was investigated during all three surveys. Considering only this area, we could still identify a substantial decrease in both flare density and volume flux. Consequently, artefacts from the scaling up the observations made during surveys of different distance cannot explain the observed differences in seepage activity.

Temporal variability in the activity of seafloor methane seeps has been reported previously (e.g. Greinert et al., 2006; Klaucke et al., 2010; Kannberg et al., 2013). Römer et al. (2016) investigated a cold seep offshore Canada at 1250 m water depth and suggested that the pressure change of 1.9 dbar between low and high tide affected seepage activity with increasing gas flux during falling tides. However, our survey time period lasted for ~3 days, i.e. ~6 tidal cycles, so that potential forcing by tides should be equalized and tides cannot be the reason for differences in seepage activity between the surveys.

Variability in gas flux in our study area (highest in June-14, lower in July-15 and lowest in May-16) follows observed between-survey differences in bottom water temperature (Fig. S3). This was highest in June-14 (3.63±0.2°C), lower in July-15 (3.49±0.2°C) and the lowest in May-16 (1.77±0.1 °C). Indeed, it has been proposed that seasonal fluctuations in bottom water temperature modulate seepage activity off Svalbard, but from gas hydrate bearing sediments at the termination of the gas hydrate stability zone (Berndt et al., 2014). However, gas hydrates have never been found in our study area, which is at ~200 m shallower water depth than that of gas hydrate stability limit (>300 m water depth), so that we can only speculate about the mechanisms of a potential temperature control on seepage activity. Nevertheless, potentially modulating effects of bottom water temperature would imply seasonal fluctuations in seepage activity in our study area.

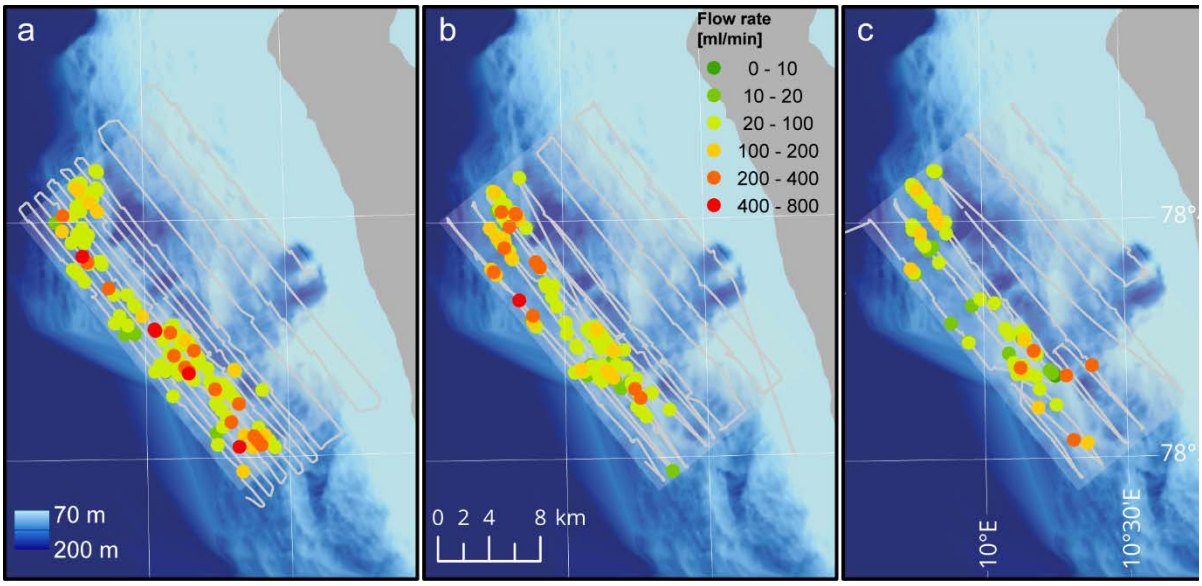

Figure 2. Flow rates from single sources (flares) during June-14 (**a**), July-15 (**b**) and May-16 (**c**) surveys. Coloured circles indicate gas flow rates in ml min^{-1} from individual flares on the seafloor. The grey line represents the ship track and echosounder beam coverage.

Table 1. Methane fluxes from sediments in different surveys

Survey	Total volumetric flow rate in the area (L min^{-1})	Total mass flow rate in the area (t y^{-1})	Average methane flux from sediments (mmol m^{-2} d^{-1})
June-14	899	3774	1.53
July-15	665	3004	1.21
May-16	542	2356	0.96

3.2 Controls of sea-air methane flux

The highest sea-air methane flux of 15 µmol m^2 d^{-1} was observed during the June-14 survey, a lower flux of 11 µmol m^2 d^{-1} was observed in July-15, and the lowest flux of only 2 µmol m^2 d^{-1} was observed during the May-16 survey (Fig. 3 d-f). The temporal pattern of atmospheric methane mixing ratios was the opposite of that of the flux, i.e. we found the lowest mixing ratios in June-14 (1902 ± 0.52 ppb), higher during the July-15 (1917 ± 3.30 ppb) and the highest during the May-16 survey (1955 ± 25.4 ppb) (data given as average ± standard deviation of all observations during each survey). Thus, the atmospheric mixing ratio of methane was one of the main controls on sea-air fluxes resulting in a suppressed flux in case of higher atmospheric methane values (e.g. lower fluxes in May-16 compared to the highest encountered atmospheric methane mixing ratios). A further key control on sea-air methane fluxes is the concentration of methane in the well-mixed surface waters, which was 9 nmol L^{-1} in June-14, and 3 nmol L^{-1} during the July-15 and May-16 surveys (Table 2). Despite the similar surface water concentrations in July-15 and May-16, sea-air methane fluxes were 5 times higher in July-15 than in May-16. This can be explained by the wind speed, which was comparably low and varied very little during the June-14 (4-8 m s^{-1}) and May-16 surveys (1-6 m s^{-1}), but increased from calm 4-6 m s^{-1} to strong 10-12 m s^{-1} towards the end of the 3-day July-15 survey (Fig. 3b). Generally, the differences between the atmospheric methane mixing ratio and surface water methane content as well as wind speed determine the variation in average sea-air flux. However, we argue that wind speed plays the most important role in our study area with respect to sea-air methane fluxes. High wind speeds can intensify efflux to the atmosphere even if the surface water methane concentration is relatively low as long as the surface waters are supersaturated with respect to the atmosphere.

To further test how the wind speed affects sea-air methane flux, we determined what the flux would have been if the wind speed had been a 5 m s^{-1} throughout all surveys. In other words, we used the observed values of surface water methane concentrations and atmospheric methane mixing ratios measured during each survey, but instead of the measured wind data, we calculated fluxes for a constant wind speed of 5 m s^{-1}, which is the climatological average wind speed for late spring to early summer in our study area (The Norwegian Meteorological Institute, www.yr.no). The meteorological mean was lower than the measured wind speed in June-14 and July-15, but higher than the measured wind speed in May-16. Therefore, our flux calculations with the mean values produced lower flux values for the June-14 (10 µmol m^2 d^{-1}) and July-15 (4 µmol m^2 d^{-1}) surveys, but higher values for the May-16 (3.5 µmol m^2 d^{-1}) survey (Fig. 3 g-i). This comparison between sea-air methane flux with

actual measured and constant wind speeds highlights the importance of wind speed in modifying methane emission to the atmosphere in our study area.

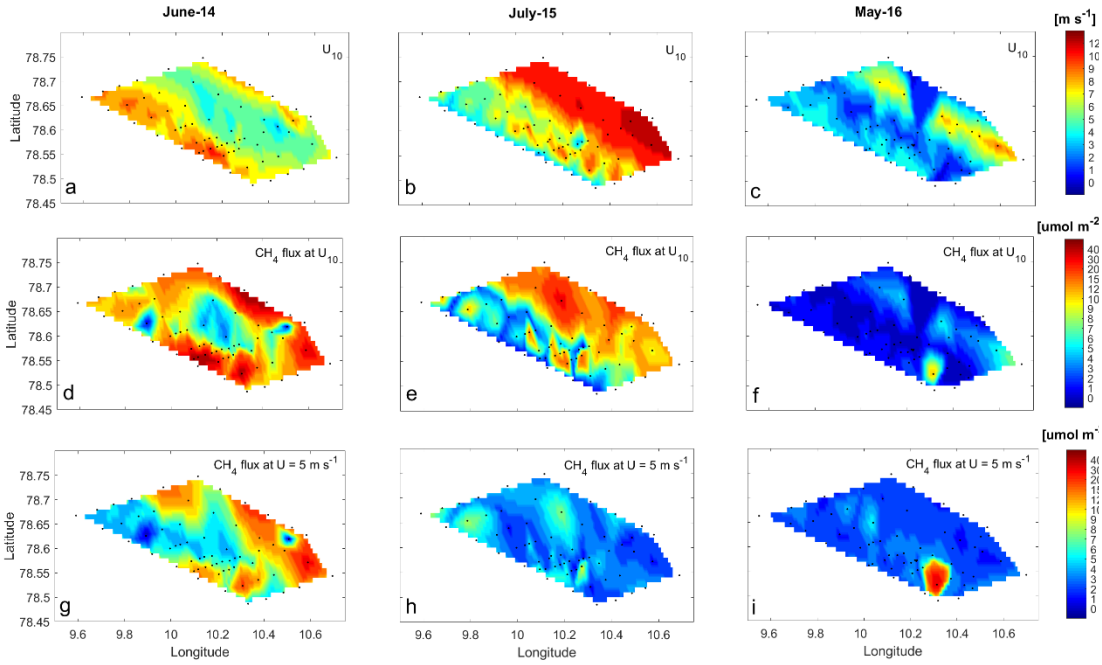

Figure 3. Wind speed measured at 22.4 m above sea level (upper panel: **a**, **b**, **c**), Methane flux at the air-sea interface at measured wind speed u_{10} (mid panel: **d**, **e**, **f**) and methane flux at the air-sea interface at constant wind speed U=5 m s^{-1} for May-July (lower panel: **g**, **h**, **i**), for the entire grid and the three surveys.

3.3 Controls of water column methane content

The water column above active methane flares in the study area was divided into three layers in order to estimate differences between methane content in the bottom 15 m, where presumably most of released methane dissolves; the surface 20 m which roughly corresponds to the thickness of the well mixed surface layer in summer and from which outgassing most of methane to the atmosphere occurs; and the intermediate layer between the bottom and surface layers, which is the thickest and presumably accumulates most of the released methane. When comparing different layers, the highest methane concentrations were found in bottom layer as expected. However, in all surveys the overall highest methane content was found in the intermediate layer because it contains the highest volume of water (extends through the largest depth interval). When comparing different surveys, we observed the highest total methane content in June-14 (23×10^5 mol), lower in July-15 (15×10^5 mol) and lowest during the May-16 (14×10^5 mol) survey (Table 2).

The change in dissolved methane content in the water column between the surveys is similar to the trend in the number of observed flares and the volume of released gas, and, to a smaller extent, the sea-air methane flux. Although the correlation between the amount of released methane and its content in the water is anticipated, there are number of processes that we did not measure, some of which could alter the methane content in the entire water column, and some, in surface waters alone.

One of these processes is aerobic methane oxidation (MOx), which leads to methane under saturation of deep waters in the entire ocean (Reeburgh, 2007). During MOx, methane is removed from the water column when it is consumed by bacteria who use methane as a source of carbon and energy. To test how important the role of MOx is in the removal of methane from the system, we used MOx rates reported for the regions near our study area. Gentz et al. (2014) reported MOx rate of 0.8 nmol L^{-1} d^{-1} in bottom waters and 0.2 in surface waters in the water column above methane flares with absolute depth of ~250 m, while Steinle et al. (2015) found higher rates of 2 nmol L^{-1} d^{-1} in bottom water alongside lower rates of only 0.1 nmol L^{-1} d^{-1} in surface waters above methane flares with an absolute water depth of 360 m. After vertical and horizontal integration of these estimates over our area, we found that less than 10% of the released methane in our study area per day is likely to be removed from the system through MOx, suggesting that this process does not play a major role in the removal of methane injected from sediments at this site.

Table 2. Average dissolved methane concentrations and content in different layers during each survey

Layer → Survey ↓	Surface (surface-20 m water depth)	Intermediate (variable depth depending on water depth)	Bottom (bottom-15 m above the bottom)	Total
	Average methane concentrations (nmol L^{-1})			
June-14	9.4	55.4	92.3	
July-15	3.1	31.9	70	
May-16	3.2	26.6	61.3	
	Average content ($\times 10^{-3}$ mol m^{-2})			
June-14	0.17	3.79	1.39	5.35
July-15	0.06	2.36	1.04	3.46
May-16	0.07	2.32	0.91	3.30
	Total content in the surveyed area ($\times 10^{5}$ mol)			
June-14	0.73	16	5.87	23
July-15	0.26	10	4.40	15
May-16	0.28	9.8	3.85	14
	Total mass of methane in the surveyed area (t)			
June-14	1.17	25.73	9.41	36.31
July-15	0.43	16.00	7.05	23.50
May-16	0.44	15.77	6.17	22.38

Another process mediating methane content in the water column is aerobic methane production by microbes under phosphorus limiting conditions (Karl et al., 2008). In the oceanic interior, this process leads to methane super saturation in the surface water column above the pycnocline (Reeburgh, 2007). Such methane super saturation in surface waters was found in the Fram Strait to the west from our study area, but only reached maximum concentrations of 9 nM at 10-20 m depth (Damm et al., 2015). We observed only one case of isolated high surface methane concentration (of 20 nmol L^{-1}) during the June-14 and May-16 surveys, but in most cases surface concentrations were close to atmospheric equilibrium, thus we assume that in our study area the methane contribution from this process is of low importance.

These two biological processes are important on the scale of entire ocean but are minor mediators of methane content in our study area, which experiences rapid methane injection into the system at the seabed and methane concentrations hundreds of times higher than the average oceanic concentrations. For example, considering a total injection of methane from sediments of 5.2×10^5 mol d^{-1} (averaged over the three surveys), a loss through sea-air gas exchange of 0.04×10^5 mol d^{-1}, and a MOx rate of 0.58×10^5 mol d^{-1} (based on estimates from Gentz et al. (2014) and Steinle et al. (2015) for nearby waters), the resulting amount of methane in the water column would be 4.6 mol $\times 10^5$ mol d^{-1}. Our total methane content averaged over the three surveys is 17×10^5 mol, which is 3.8 times higher than the resulting content, implying a residence time of methane in the study area of about 3.8 days. However, methane is likely transported beyond our survey area during this time through transport by lateral water movement (section 3.5). To see how efficient this transport is and what affects it in our study area, we look further into vertical and horizontal distribution of methane in different surveys.

3.4 Controls of the vertical distribution of dissolved methane

Highest dissolved methane concentrations were found in the bottom layer (> 300 nmol L^{-1}) in the southwestern part of the sampling area during all three surveys (Figs. 4d-i, 4d-i). Waters supersaturated with methane were found around flares from the seafloor up to 50 (July-15) and 20 meters water depth (June-14, May-16). Methane supersaturated waters have methane concentrations > 3.7 nmol L^{-1}, which would be in equilibrium with the atmosphere for a salinity of 35 at 0° C and atmospheric mole fraction of methane 1.9 ppb (average value for all three surveys) (Wiesenburg and Guinasso, 1979). In all three surveys, the intermediate layer methane concentration averaged over the entire area was only half of the bottom layer concentration, while the surface water concentrations were 25 times lower than the bottom layer concentrations.

Our results show methane enriched bottom and intermediate waters, and surface water which are only slightly supersaturated or close to atmospheric equilibrium. These results agree well with earlier measurements near our study area (e.g. Gentz et al., 2014; Westbrook et al., 2009; Mau et al., 2017), which showed high methane concentrations in bottom waters above methane flares, and rapid decreases in methane concentrations towards the surface. This pattern in vertical distribution can be explained by ongoing gas exchange between rising methane bubbles and the surrounding seawater (e.g. McGinnis et al., 2006). This leads to continuous replacement of methane in the bubbles with N_2 and O_2 from the seawater and methane enrichment of seawater along the bubble ascent. Modelling approaches suggest that the bulk of methane is already stripped out from rising bubbles close to the seafloor, so that bottom waters become more enriched with dissolved methane (McGinnis et al., 2006). Bubbles observed close to the surface are thus mostly comprised of N_2/O_2. Only bubbles of >20 mm in diameter may still contain 1% of their initial methane content at the surface, but such bubbles typically break apart during their ascent (McGinnis et al., 2006).

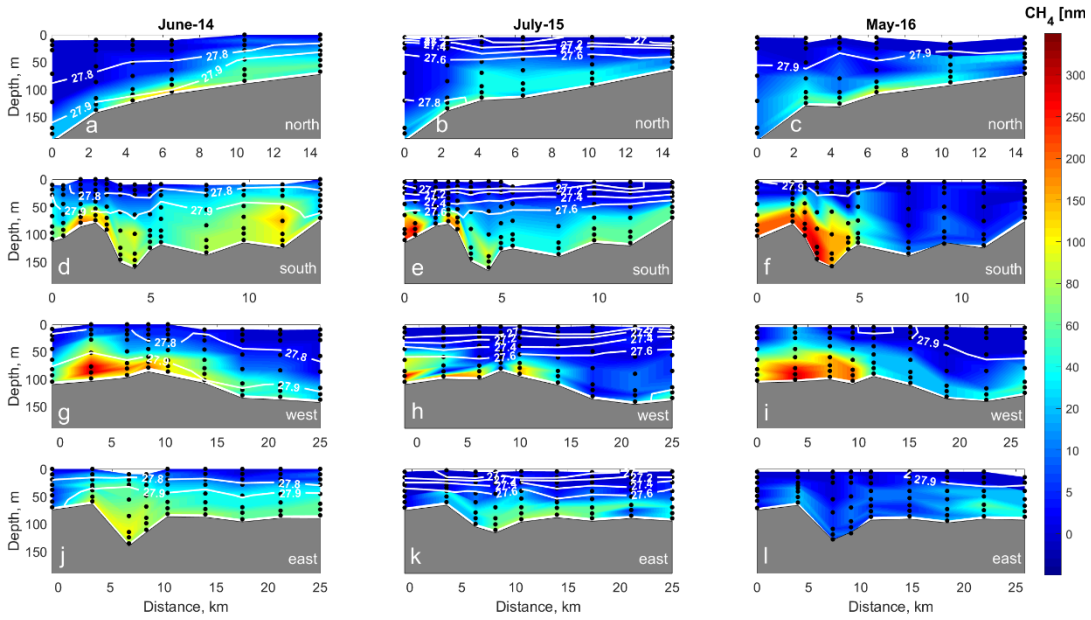

Figure 4. Distribution of dissolved methane along four transects (north (**a**, **c**, **d**), south (**d**, **e**, **f**), west (**g**, **h**, **i**) and east (**j**, **k**, **l**); c.f. Fig. 1 for location and direction of each transect). Seawater density (in kg m^{-3}) is indicated by white contour lines. Locations of discrete samples for methane concentration measurements are indicated by black dots.

Vertical transport of dissolved methane that has already escaped bubbles has been proposed to be limited by water column vertical stratification, when a pycnocline acts as a barrier for vertical mixing of methane rich waters in strongly stratified waters (Gentz et al., 2014; Myhre et al., 2016). As a proxy for water column vertical stratification, we calculated the Brunt–Väisälä frequency (N^2) in our study area (Millard et al., 1990), which generally peaked at ~20m water depth, and was the highest in July-15 (4×10^{-4} s^{-2}), ~8 times lower during the June-14 survey (0.5×10^{-4} s^{-2}) and near zero in the entire water column during the May-16 survey (0.1×10^{-4} s^{-2}) (Fig. 5c). In July-15 the observed strong stratification was formed by a temperature drop from 5.5 °C at the surface to 3.5°C at 50 m water depth forming pronounced thermocline (Fig. 5a); and by a salinity increase from 34.1 at the surface to 34.9 at 100 m depth along a continuous halocline (Fig. 5b). Conversely, in May-16 the water column was well-mixed, with almost uniform temperature and salinity with depth, and the near- absence of a pycnocline.

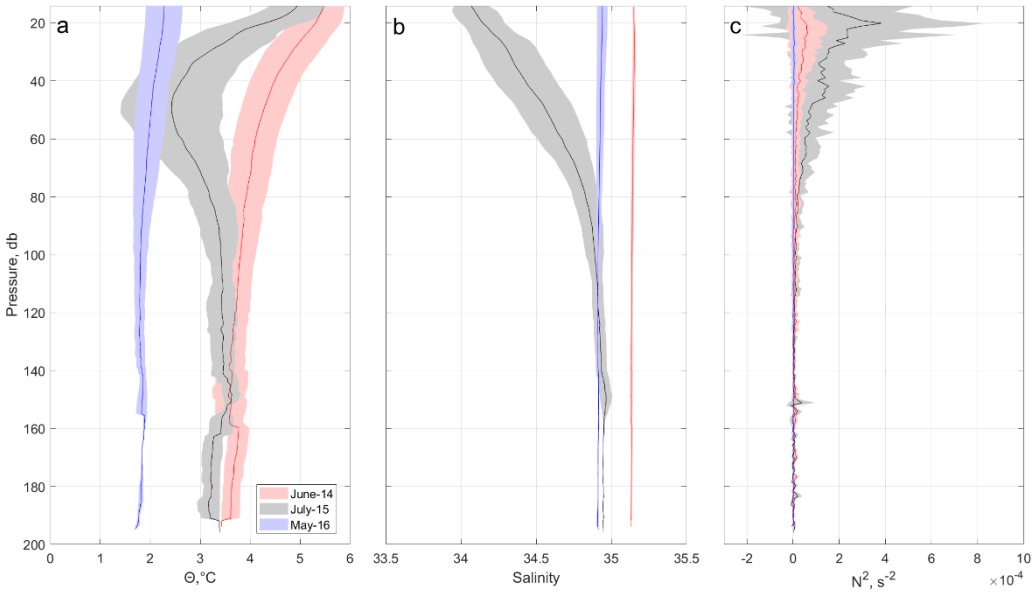

Figure 5. (**a**) Potential temperature (Θ, °C), (**b**) salinity and (**c**) Brunt–Väisälä frequency (N^2, s^{-2}) averaged over all CTD stations for each survey with standard deviation shown as shaded error bars. Colors indicate: June-14 (red), July-15 (black) and May-16 (blue).

Despite the difference in stratification between the three surveys (Fig. 5c), the vertical distribution of dissolved methane (high bottom water methane concentrations and low surface water concentrations) was similar across all three surveys (Fig. 4). This indicates that methane released from the sediments and dissolved in seawater did not rise above 20-50 m water depth towards the sea surface, even in the absence of a pycnocline. Our findings thus suggest that water density stratification may not always play the principle role in the vertical distribution of dissolved methane in cold seeps areas, in contrast to the conclusions of previous studies in this area (Myhre et al., 2016: Gentz et al., 2014). Furthermore, our results do not show an influence of stratification on water column methane content or the sea-air gas flux.

3.5 Controls of horizontal distribution of dissolved methane

The horizontal distribution and patchiness of methane differed between the three surveys. During the June-14 survey, we observed elevated dissolved methane concentrations in the bottom and mid-depth layers (Fig. 6d and g) spread over the entire survey area. In contrast, during May-16, methane concentrations were high (up to 400 nmol L^{-1}) only above flares clustered in the south-western part of the area, and decreased considerably to < 40 nmol L^{-1} within a few hundred meters away from the flares (Fig. 6i). Elevated methane concentrations also spread horizontally in July-15, but to a lesser extent than during the June-14 survey.

In the surface layer, methane concentrations were generally low and near the atmospheric equilibrium (Fig 6a-c). Some elevated surface methane concentrations (~20 nmol L^{-1}) were observed at one station in the southeast part of the study area in June-14 and in the southwestern part of the study area during the May-16 survey.

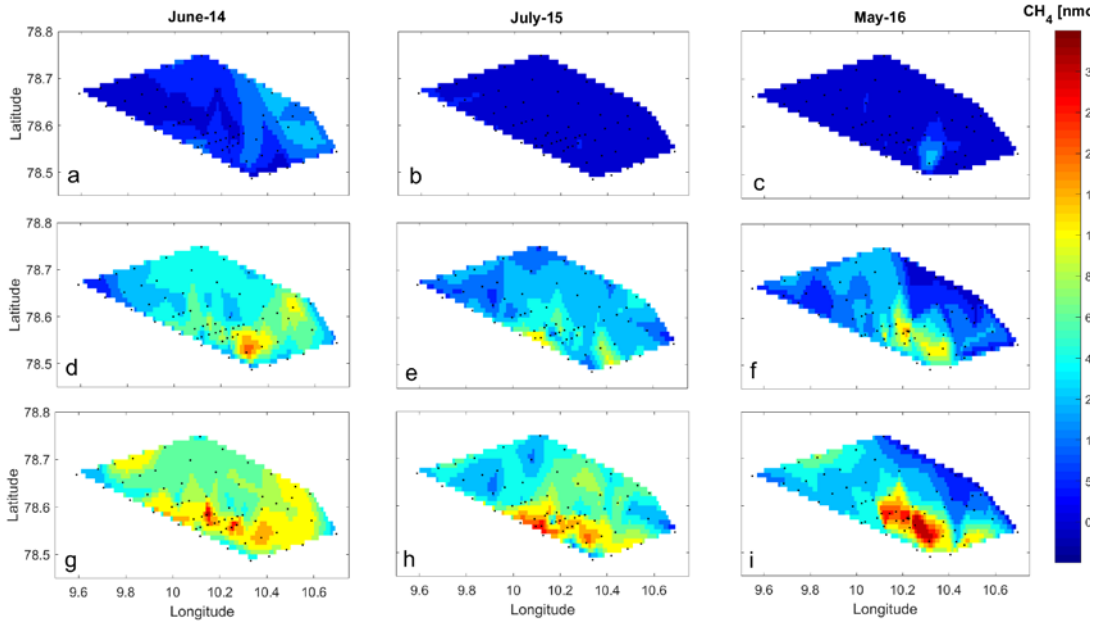

Figure 6. Average methane concentrations in the surface (0-20 m, **a**, **b**, **c**), intermediate (20 m –15 m from the seafloor, **d**, **e**, **f**) and bottom water (within 15 m of the seafloor, **g**, **h**, **i**), layers for the entire grid during the three surveys as indicated above the figures.

High variability in water mass properties indicates that circulation during all surveys was controlled by several factors. We used the classification of water masses suggested by Cottier et al. (2005) for Svalbard fjords and adjacent shelf regions to describe the oceanographic setting in our study area. During the June-14 survey we observed only warm and saline AW (temperature Θ >3°C, absolute salinity S_A >34.65) (Fig. 7a), brought to the study area with the WSC. In contrast, water in July-15 was substantially colder and less saline (Fig. 7b), mainly comprised of AW, with some Transformed Atlantic Water (TAW, 1 < Θ < 3°C, S_A >34.65), and to the largest extent, Intermediate Water (IW, Θ >1°C, 34 < S_A < 34.65). IW originates from fjords and forms as AW that cools over winter in fjords, and is freshened by glacial melt, sea ice melt and river runoff during summer. IW can also be a mix of AW and Arctic Water masses (ArW, -1.5° < Θ < 1°C, 34.3 < S_A < 34.8) transported from the Northern Barents Sea around southern tip of Svalbard with the ESC. During the May-16 survey (Fig. 7c), the

water column mainly comprised TAW with absolute salinity values similar to AW but with potential temperatures around 1.5 – 3°C, which is colder than the typical AW with temperature defined as above 3°C. There was a strong presence of AW on the shelf and adjacent fjords in 2016 (F. Nilsen, pers. comm.). The core of the AW in May is always above 2.5°C (Beszczynska-Möller et al., 2012). Our measured colder seawater temperatures in the area could indicate that AW was cooled by the atmosphere or surrounding waters, either locally or before it was advected from adjacent basins.

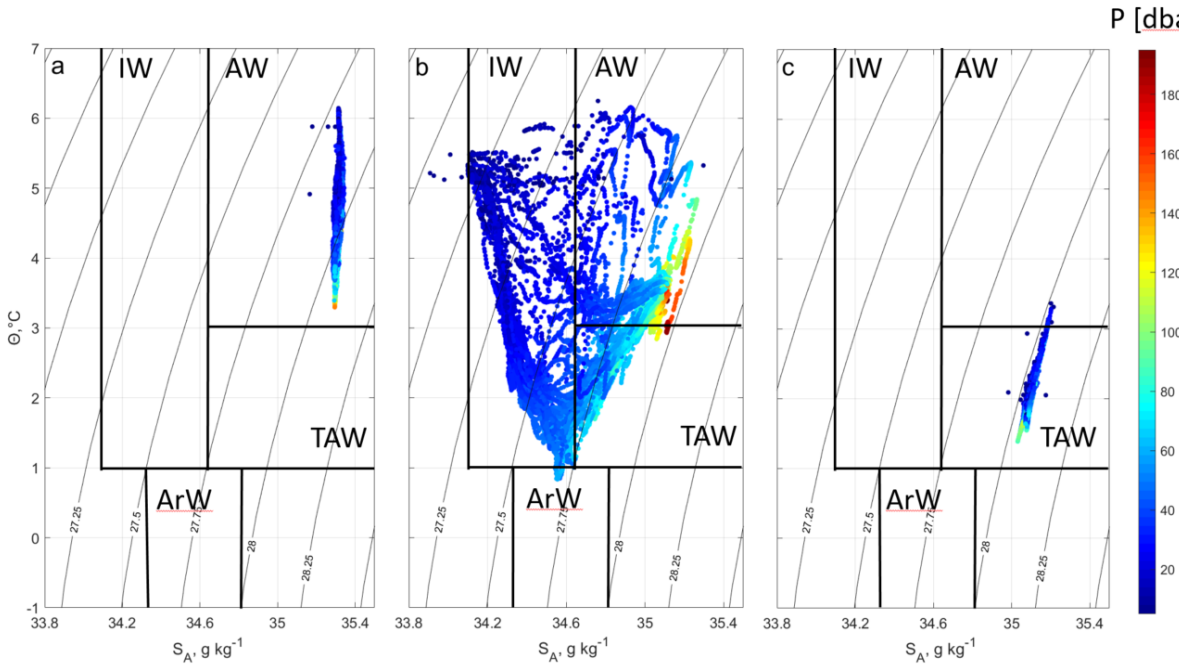

Figure 7. Potential temperature (Θ, °C) – absolute salinity (S_A, g kg^{-1}) diagrams for the June-14 (**a**), July-15 (**b**) and May-16 (**c**) surveys. Θ, °C calculated according to the International Thermodynamic Equation of Seawater (Fofonoff and Millard, 1983). Absolute salinity calculated based on measured practical salinity, and is expressed in terms of g of salt per kg of water. Grey contours indicate isopycnals (kg m^{-3}).

Seawater temperature and salinity modelled with the S800-model (Hattermann et al., 2016) for the study area indicate a shift from AW to IW properties towards summer and autumn months due to surface warming and freshening (Fig. 8), hence revealing the annual cycle of water mass formation. Salinity shows a seasonal cycle only at the surface, where it decreases from 35 in June to 34.4 in September (Fig. 9). Summer freshening of the surface results from freshwater runoff from land, glacial and sea ice melt, and a varying presence of ArW in the study area. Bottom water salinity of about 35 is constant throughout the year, such that the seasonal cycle of density near the seafloor is controlled by temperature. Surface and bottom water temperatures rise towards summer, following atmospheric temperatures, regardless of which water mass is present in the area (Fig. 9). Temperatures increase towards summer from 2.5 to 6°C at the surface, and from 1.5 to 4°C at the bottom. The maximum temperature in the surface water is observed in July-August and one month later near the bottom. Winter surface and bottom temperatures vary between 1.5 and 2.5°C indicating that the water column is cooled down by heat loss to the atmosphere or surrounding waters (Nilsen et al., 2016). Warming of the water column in the study area throughout the year occurs through intermittent heat exchange with

the WSC that floods the shallow shelf (Nilsen et al., 2016), likely in a form of baroclinic eddies, which are abundant in this region (Appen et al., 2016, Hattermann et al., 2016).

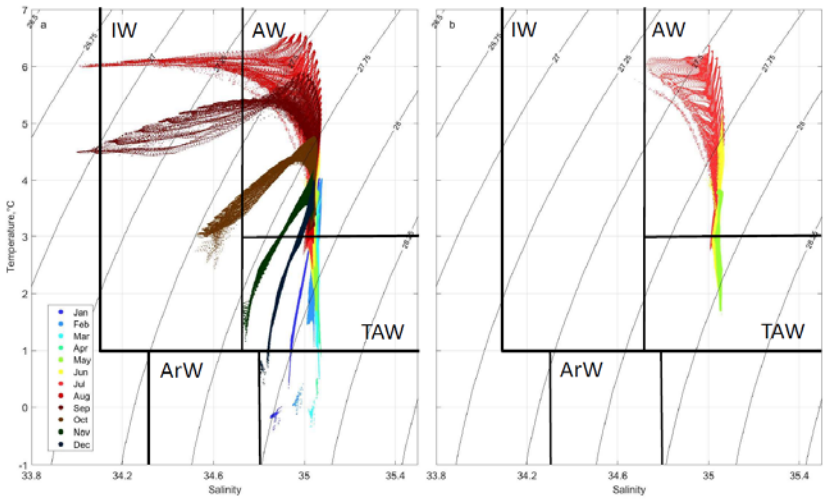

Figure 8. TS diagrams based on S800-model data for the study area, monthly average over the period July 2005 – July 2010 (**a**); monthly average in May, June and July as these months are when the surveys were conducted (**b**). Colors indicate month of the year as shown in the legend. Background contour lines show isopycnals (kg m^{-3}).

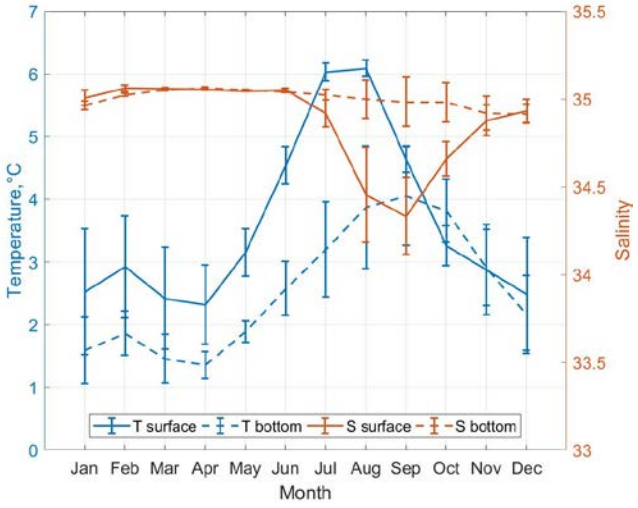

Figure 9. Annual cycle of bottom and surface seawater temperature and salinity in the study area, modelled with S800-model. Lines show mean values for the study area, bars indicate spatial variability.

3.6 Eddy driven seasonal dispersion on the shelf

Our observations indicated a large spatial variability of dissolved methane concentrations, alongside limited vertical penetration of dissolved methane from the sources at the seafloor towards the sea surface irrespective of vertical stratification. Based on this, we propose that lateral advection near the seafloor plays an important role in dispersing methane horizontally away from the seep locations. The

continuous replacement of methane-enriched water with water containing low methane concentrations allows efficient dissolution of methane released in bubbles from the sediments.

As shown on Fig. 6 (g-i), dissolved methane was spread horizontally in the bottom layer during June-14 and July-15 while it was more concentrated around the source in May-16. The water mass analysis suggests that this variability in horizontal dispersion is related to different circulation patterns on the shelf. As previously discussed, circulation of waters on the shallow shelf west of PKF is influenced by the combination of the WSC and superimposed local factors and their seasonality. The sole presence of the AW on the shelf in June-14 for example, which led to high dispersion of dissolved methane above the bottom, can be explained by an AW flooding event from the WSC over the shelf (Nilsen et al., 2008; Nilsen et al., 2016). Thereby, the lateral transport of waters above the PKF shelf during such flooding events disperses the dissolved methane and reduces the residence time of dissolved methane above gas flares.

While the WSC core generally flows further offshore than the shallow PKF shelf (Aagaard et al., 1987), instabilities of the WSC result in formation of numerous eddies that transport AW onto the shallow shelf (Appen et al., 2016, Hattermann et al. 2016, Wekerle et al., 2017). The transport occurs across the slope near the seafloor and plays an important role in the exchange of AW with shelf waters in our study region (Tverberg and Nøst, 2009). We propose that the observed large dispersion of dissolved methane above the bottom during the June-14 survey is a result of eddy activity on the shallow shelf, and that eddies play an important role in the cross-frontal transport of waters and its constituents.

Appen et al. (2016) found increased eddy kinetic energy (EKE) and enhanced baroclinic instability in the WSC in winter and spring and it is likely that this seasonality will affect the number of flooding events over the shallow shelf and the residence time of methane above gas flares. To investigate the relationship between the seasonality of eddy activity and the variability of dissolved methane dispersion on the shelf, we used the S800-model to run numerical experiments releasing and tracking particles simulating methane in our most intense flare area (see Methods 2.5). The particles are freely advected by the three dimensional model velocity field and provide a first order assessment of the role of the circulation in methane dispersion. The buoyancy driven motion of bubbles and the aerobic oxidation of dissolved methane will add further complexity to the dispersion process, but as discussed in section 3.3, are likely to be of secondary importance compared to the advective controls. In the numerical experiment, we observed a clear seasonality in particle dispersion with a much wider area being covered by the particles from January to May as opposed to a limited area of high particle concentrations during the summer months (Fig. 10).

During all months, the particles are mainly advected northward along the shelf and into the Kongsfjorden Trough that crosses the shelf at 79° N. However, in winter and spring, the pattern becomes more dispersive and particles are advected westward off the shelf, suggesting a greater influence of the WSC on water mass exchange with the shallow shelf area. The residence time within our study area follows the seasonal evolution of EKE (Fig 11a), with 50 % (80 %) of the released particles having left the study area after 3 days (6 days) between January to April, when EKE in the study area is largest. Furthermore, particles with the largest displacement (up to 80 – 100 km five days after the release, Fig. 11b) are associated with the highest seawater density of 27.9 – 28.1 kg m^{-3}, which is consistent with the hypothesis that methane is efficiently dispersed by eddies that lift dense AW onto the shelf (Tverberg and Nøst, 2009, Hattermann et al. 2016). Although our observations

during a 3-day period in each year do not resolve the seasonal cycle seen in the model, they support this principal mechanism, with the most dispersed methane concentrations being observed during the June-14 and July-15 surveys when AW was present in the bottom layer. Thus, our combination of observations and modelling suggests that eddies play an important role in dispersing outgassing methane over the continental shelf and in controlling the water column methane content, with potential direct implications for methane related biogeochemical processes.

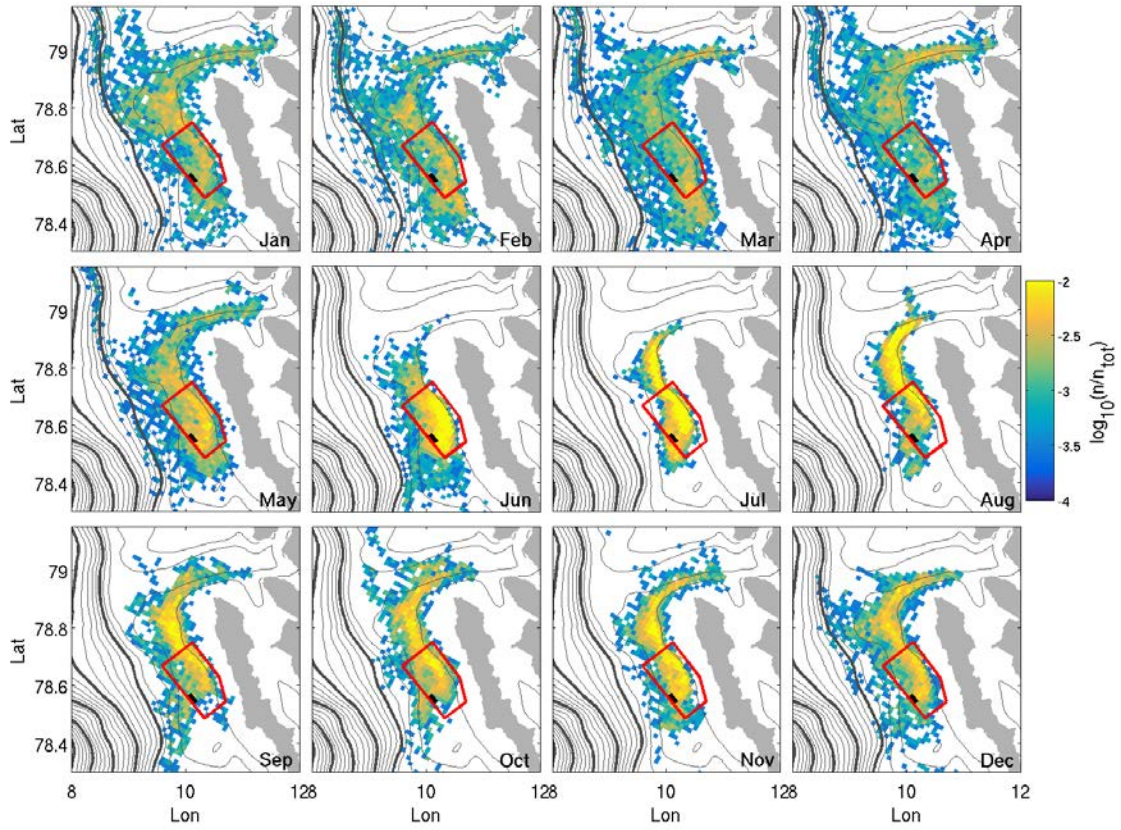

Figure 10. Monthly maps of particle dispersion 5 days after the particle release between 80 and 100 m water depth at the positions indicated by the black rectangle. Colors indicate the number of particles per grid cell normalized by the total number of particles in the respective month, using a logarithmic scale. The red polygon delineates the location of the sampling sites, contours show the isobaths with 100 m intervals thicker lines indicating 500 m intervals.

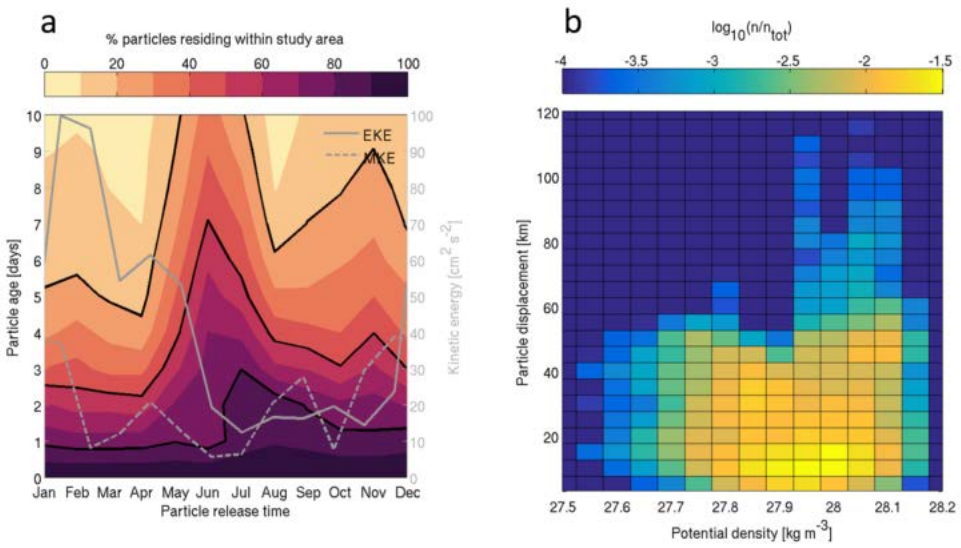

Figure 11. (**a**) Time series showing the residence time of particles within the study area indicated by the red polygon in Fig. 10 (color shade), together with monthly averaged mean- (MKE) and eddy (EKE) kinetic energy (right axis), averaged for the same region. Black curves indicate times when 20 %, 50 % and 80 % of particles have left the study area. (**b**) Two-dimensional histogram of particle displacement vs. potential density at the particle position after five days. Colors indicate the normalized frequency of occurrence on a logarithmic scale, showing that many particles remains within 20 km of the source and that the largest displacements are associated with the highest densities.

4 Conclusions

To our knowledge, this is the first study of the water column above cold methane seeps that combines a series of oceanographic surveys with stations positioned on a grid within a defined polygon. This study clearly benefits from the grid station design when compared to more frequently conducted single synoptic transects. Acquiring data in a four dimensional array in time and space allowed us to fully evaluate the methane content in the entire water body above methane flares and identify the major processes mediating water column methane content and transport.

Our results suggest the possibility of enhanced methane flux from the sediments triggered by elevated bottom water temperature in the absence of underlying gas hydrate. In light of warming waters of the Arctic Ocean, not only gas hydrate containing sediments, but all methane gas bearing sediments could potentially become sources of methane release into the water column. Further study of the processes involved and the links between gas bearing sediments and bottom water temperature is required to improve our understanding.

Comparison between the three different hydrographic regimes observed across the three surveys reveals that most of the released methane in our shallow shelf area remains in the bottom and intermediate waters irrespective of the strength of stratification. Therefore, hypotheses by e.g. von Deimling et al., (2011), who suggested that all methane could be liberated to the atmosphere from shallow shelf areas as a result of a well-mixed water column and absence of stratification appear not to be valid in this shallow shelf study area. Small amounts of methane could be liberated to the

atmosphere, but mainly as a result of strong winds increasing the rate of air-sea gas exchange, not weak stratification.

Instead of vertical transport processes, we find that horizontal advection is the main mechanism that controls the dispersion of dissolved methane on the Prins Karls Forland shelf. In particular, our results highlight the role of mesoscale eddies in controlling the methane content above, dispersion around, and displacement away from gas flares. This implies that eddies and horizontal dispersion may also have important effects on methane related biogeochemical process and the magnitude of different methane sinks. For example, one could anticipate that a potential for methane sink through MOx could be higher when eddy activity is high in winter and spring season, because by dispersing dissolved methane over a larger area, eddies promote delivery of dissolved methane to methane oxidizing bacteria that consequently capture and consume this methane. Further seasonal measurements and/or process oriented modelling will be required to scrutinize these ideas, but these results could considerably shift our understanding of the seasonality of sinks of dissolved methane and allow better estimates of the balance between amounts of methane released from sediments, methane liberated into the atmosphere, and methane removed from the system through microbial processes.

Acknowledgements

We would like to thank the crew of RV Helmer Hanssen during the June-14 (CAGE 14-1), July-15 (CAGE 15-3) and May-16 (CAGE 16-4) cruises. We acknowledge the project MOCA- Methane Emissions from the Arctic Ocean to the Atmosphere: Present and Future Climate Effects, which is funded by the Research Council of Norway, grant no. 225814 and the Fram Centre Arctic Ocean flagship project ModOIE, grant no. 66060/299. Authors thank S. Buenz for leading the CAGE 14-1 survey and J. Greinert for suggesting the survey grid and providing sampling tools and instrumentation for gas analyses during the CAGE 14-1 cruise. Authors thank F. Nilsen for valuable discussions on seasonal water mass presence in the study area. SP was supported by the Norwegian Research Council SIS project Signals from the Arctic Ocean in the Atmosphere-SOCA. This study is a part of CAGE (Centre for Arctic Gas Hydrate, Environment and Climate), Norwegian Research Council grant no. 223259. The data used in this study have been deposited in the UiT Open Research Data repository (https://dataverse.no/dataverse/uit, doi:10.18710/VGQYLQ).

References

Aagaard, K., Foldvik, A., & Hillman, S. (1987). The West Spitsbergen Current: disposition and water mass transformation. Journal of Geophysical Research: Oceans, 92(C4), 3778-3784.

Albretsen, J., Hattermann, T., & Sundfjord, A. (2017). Ocean and sea ice circulation model results from Svalbard area (ROMS) [Data set]. Norwegian Polar Institute.

Amante, C. (2009). ETOPO1 1 arc-minute global relief model: procedures, data sources and analysis. http://www. ngdc. noaa. gov/mgg/global/global. html.

Andreassen, K., Hubbard, A., Winsborrow, M., Patton, H., Vadakkepuliyambatta, S., Plaza-Faverola, A., . . . Mattingsdal, R. (2017). Massive blow-out craters formed by hydrate-controlled methane expulsion from the Arctic seafloor. Science, 356(6341), 948-953.

Appen, W.-J. v., Schauer, U., Hattermann, T., & Beszczynska-Möller, A. (2016). Seasonal cycle of mesoscale instability of the West Spitsbergen Current. Journal of Physical Oceanography, 46(4), 1231-1254.

Berge, J., Johnsen, G., Nilsen, F., Gulliksen, B., & Slagstad, D. (2005). Ocean temperature oscillations enable reappearance of blue mussels Mytilus edulis in Svalbard after a 1000 year absence. Marine Ecology Progress Series, 303, 167-175.

Berndt, C., Feseker, T., Treude, T., Krastel, S., Liebetrau, V., Niemann, H., . . . Ferré, B. (2014). Temporal constraints on hydrate-controlled methane seepage off Svalbard. Science, 343(6168), 284-287.

Beszczynska-Möller, A., Fahrbach, E., Schauer, U., & Hansen, E. (2012). Variability in Atlantic water temperature and transport at the entrance to the Arctic Ocean, 1997–2010. ICES Journal of Marine Science, 69(5), 852-863.

Budgell, W. (2005). Numerical simulation of ice-ocean variability in the Barents Sea region. Ocean Dynamics, 55(3-4), 370-387.

Cottier, F., Nilsen, F., Inall, M., Gerland, S., Tverberg, V., & Svendsen, H. (2007). Wintertime warming of an Arctic shelf in response to large-scale atmospheric circulation. Geophysical Research Letters, 34(10).

Cottier, F., Tverberg, V., Inall, M., Svendsen, H., Nilsen, F., & Griffiths, C. (2005). Water mass modification in an Arctic fjord through cross-shelf exchange: The seasonal hydrography of Kongsfjorden, Svalbard. Journal of Geophysical Research: Oceans, 110(C12).

Cottier, F. R., Nilsen, F., Skogseth, R., Tverberg, V., Skarðhamar, J., & Svendsen, H. (2010). Arctic fjords: a review of the oceanographic environment and dominant physical processes. Geological Society, London, Special Publications, 344(1), 35-50.

Crews, L., Sundfjord, A., Albretsen, J., & Hattermann, T. (2018). Mesoscale eddy activity and transport in the Atlantic Water inflow region north of Svalbard. Journal of Geophysical Research: Oceans, 123(1), 201-215.

Damm, E., Mackensen, A., Budéus, G., Faber, E., & Hanfland, C. (2005). Pathways of methane in seawater: Plume spreading in an Arctic shelf environment (SW-Spitsbergen). Continental Shelf Research, 25(12), 1453-1472.

Damm, E., Thoms, S., Beszczynska-Möller, A., Nöthig, E.-M., & Kattner, G. (2015). Methane excess production in oxygen-rich polar water and a model of cellular conditions for this paradox. Polar Science, 9(3), 327-334.

Dee, D. P., Uppala, S., Simmons, A., Berrisford, P., Poli, P., Kobayashi, S., . . . Bauer, P. (2011). The ERA-Interim reanalysis: Configuration and performance of the data assimilation system. Quarterly Journal of the royal meteorological society, 137(656), 553-597.

Döös, K., Jönsson, B., & Kjellsson, J. (2017). Evaluation of oceanic and atmospheric trajectory schemes in the TRACMASS trajectory model v6. 0. Geoscientific Model Development, 10(4), 1733.

Ferré, B., Mienert, J., & Feseker, T. (2012). Ocean temperature variability for the past 60 years on the Norwegian-Svalbard margin influences gas hydrate stability on human time scales. Journal of Geophysical Research: Oceans, 117(C10).

Fofonoff, N. P., & Millard Jr, R. (1983). Algorithms for the computation of fundamental properties of seawater.

Gentz, T., Damm, E., von Deimling, J. S., Mau, S., McGinnis, D. F., & Schlüter, M. (2014). A water column study of methane around gas flares located at the West Spitsbergen continental margin. Continental Shelf Research, 72, 107-118.
Graversen, R. G., Mauritsen, T., Tjernström, M., Källén, E., & Svensson, G. (2008). Vertical structure of recent Arctic warming. Nature, 451(7174), 53.
Graves, C. A., Steinle, L., Rehder, G., Niemann, H., Connelly, D. P., Lowry, D., . . . James, R. H. (2015). Fluxes and fate of dissolved methane released at the seafloor at the landward limit of the gas hydrate stability zone offshore western Svalbard. Journal of Geophysical Research: Oceans, 120(9), 6185-6201.
Greinert, J., Artemov, Y., Egorov, V., De Batist, M., & McGinnis, D. (2006). 1300-m-high rising bubbles from mud volcanoes at 2080 m in the Black Sea: Hydroacoustic characteristics and temporal variability. Earth and Planetary Science Letters, 244(1-2), 1-15.
Hanson, R. S., & Hanson, T. E. (1996). Methanotrophic bacteria. Microbiological reviews, 60(2), 439-471.
Hattermann, T., Isachsen, P. E., Appen, W. J., Albretsen, J., & Sundfjord, A. (2016). Eddy-driven recirculation of Atlantic Water in Fram Strait. Geophysical Research Letters, 43(7), 3406-3414.
Hester, K. C., & Brewer, P. G. (2009). Clathrate hydrates in nature. Annual review of marine science, 1, 303-327.
Hsu, S., Meindl, E. A., & Gilhousen, D. B. (1994). Determining the power-law wind-profile exponent under near-neutral stability conditions at sea. Journal of Applied Meteorology, 33(6), 757-765.
Jakobsson, M., Mayer, L., Coakley, B., Dowdeswell, J. A., Forbes, S., Fridman, B., . . . Rebesco, M. (2012). The international bathymetric chart of the Arctic Ocean (IBCAO) version 3.0. Geophysical Research Letters, 39(12).
James, R. H., Bousquet, P., Bussmann, I., Haeckel, M., Kipfer, R., Leifer, I., . . . Rehder, G. (2016). Effects of climate change on methane emissions from seafloor sediments in the Arctic Ocean: A review. Limnology and Oceanography, 61(S1).
Kannberg, P. K., Tréhu, A. M., Pierce, S. D., Paull, C. K., & Caress, D. W. (2013). Temporal variation of methane flares in the ocean above Hydrate Ridge, Oregon. Earth and Planetary Science Letters, 368, 33-42.
Karl, D. M., Beversdorf, L., Björkman, K. M., Church, M. J., Martinez, A., & Delong, E. F. (2008). Aerobic production of methane in the sea. Nature Geoscience, 1(7), 473.
Kessler, J. D., Valentine, D. L., Redmond, M. C., Du, M., Chan, E. W., Mendes, S. D., . . . Werra, L. M. (2011). A persistent oxygen anomaly reveals the fate of spilled methane in the deep Gulf of Mexico. Science, 331(6015), 312-315.
Knies, J., Damm, E., Gutt, J., Mann, U., & Pinturier, L. (2004). Near-surface hydrocarbon anomalies in shelf sediments off Spitsbergen: Evidences for past seepages. Geochemistry, Geophysics, Geosystems, 5(6).
Kort, E., Wofsy, S., Daube, B., Diao, M., Elkins, J., Gao, R., . . . Moore, F. (2012). Atmospheric observations of Arctic Ocean methane emissions up to 82 north. Nature Geoscience, 5(5), 318.
Kretschmer, K., Biastoch, A., Rüpke, L., & Burwicz, E. (2015). Modeling the fate of methane hydrates under global warming. Global Biogeochemical Cycles, 29(5), 610-625.
Kvenvolden, K. A., Lilley, M. D., Lorenson, T. D., Barnes, P. W., & McLaughlin, E. (1993). The Beaufort Sea continental shelf as a seasonal source of atmospheric methane. Geophysical Research Letters, 20(22), 2459-2462.
Lammers, S., Suess, E., & Hovland, M. (1995). A large methane plume east of Bear Island (Barents Sea): implications for the marine methane cycle. Geologische Rundschau, 84(1), 59-66.
LANDVIK, J. Y., Ingolfsson, O., MIENERT, J., LEHMAN, S. J., Solheim, A., ELVERHØI, A., & Ottesen, D. (2005). Rethinking Late Weichselian ice-sheet dynamics in coastal NW Svalbard. Boreas, 34(1), 7-24.
Leifer, I., Jeuthe, H., Gjøsund, S. H., & Johansen, V. (2009). Engineered and natural marine seep, bubble-driven buoyancy flows. Journal of Physical Oceanography, 39(12), 3071-3090.
Marín-Moreno, H., Minshull, T. A., Westbrook, G. K., & Sinha, B. (2015). Estimates of future warming-induced methane emissions from hydrate offshore west Svalbard for a range of climate models. Geochemistry, Geophysics, Geosystems, 16(5), 1307-1323.

Mau, S., Römer, M., Torres, M. E., Bussmann, I., Pape, T., Damm, E., . . . Loher, M. (2017). Widespread methane seepage along the continental margin off Svalbard-from Bjørnøya to Kongsfjorden. Scientific reports, 7, 42997.
McGinnis, D. F., Greinert, J., Artemov, Y., Beaubien, S., & Wüest, A. (2006). Fate of rising methane bubbles in stratified waters: How much methane reaches the atmosphere? Journal of Geophysical Research: Oceans, 111(C9).
Millard, R., Owens, W., & Fofonoff, N. (1990). On the calculation of the Brunt-Väisäla frequency. Deep Sea Research Part A. Oceanographic Research Papers, 37(1), 167-181.
Myhre, C. L., Ferré, B., Platt, S. M., Silyakova, A., Hermansen, O., Allen, G., . . . Pitt, J. (2016). Extensive release of methane from Arctic seabed west of Svalbard during summer 2014 does not influence the atmosphere. Geophysical Research Letters, 43(9), 4624-4631.
Nikolovska, A., Sahling, H., & Bohrmann, G. (2008). Hydroacoustic methodology for detection, localization, and quantification of gas bubbles rising from the seafloor at gas seeps from the eastern Black Sea. Geochemistry, Geophysics, Geosystems, 9(10).
Nilsen, F., Cottier, F., Skogseth, R., & Mattsson, S. (2008). Fjord–shelf exchanges controlled by ice and brine production: the interannual variation of Atlantic Water in Isfjorden, Svalbard. Continental Shelf Research, 28(14), 1838-1853.
Nilsen, F., Skogseth, R., Vaardal-Lunde, J., & Inall, M. (2016). A simple shelf circulation model: Intrusion of Atlantic water on the West Spitsbergen shelf. Journal of Physical Oceanography, 46(4), 1209-1230.
Ostrovsky, I., McGinnis, D. F., Lapidus, L., & Eckert, W. (2008). Quantifying gas ebullition with echosounder: the role of methane transport by bubbles in a medium-sized lake. Limnology and Oceanography: Methods, 6(2), 105-118.
Parmentier, F.-J. W., Silyakova, A., Biastoch, A., Kretschmer, K., & Panieri, G. (2015). Natural marine methane sources in the Arctic. In: Arctic Monitoring and Assessment Programme (AMAP).
Paull, C. K., Ussler, W., Dallimore, S. R., Blasco, S. M., Lorenson, T. D., Melling, H., . . . McLaughlin, F. A. (2007). Origin of pingo-like features on the Beaufort Sea shelf and their possible relationship to decomposing methane gas hydrates. Geophysical Research Letters, 34(1).
Perkin, R., & Lewis, E. (1984). Mixing in the West Spitsbergen current. Journal of Physical Oceanography, 14(8), 1315-1325.
Pierrot, D., Neill, C., Sullivan, K., Castle, R., Wanninkhof, R., Lüger, H., . . . Cosca, C. E. (2009). Recommendations for autonomous underway pCO2 measuring systems and data-reduction routines. Deep Sea Research Part II: Topical Studies in Oceanography, 56(8-10), 512-522.
Polyakov, I., Alekseev, G., Timokhov, L., Bhatt, U., Colony, R., Simmons, H., . . . Zakharov, V. (2004). Variability of the intermediate Atlantic water of the Arctic Ocean over the last 100 years. Journal of Climate, 17(23), 4485-4497.
Polyakov, I., Timokhov, L., Dmitrenko, I., Ivanov, V., Simmons, H., Beszczynska-Möller, A., . . . Gascard, J. C. (2007). Observational program tracks Arctic Ocean transition to a warmer state. Eos, Transactions American Geophysical Union, 88(40), 398-399.
Polyakov, I. V., Timokhov, L. A., Alexeev, V. A., Bacon, S., Dmitrenko, I. A., Fortier, L., . . . Ivanov, V. V. (2010). Arctic Ocean warming contributes to reduced polar ice cap. Journal of Physical Oceanography, 40(12), 2743-2756.
Portnov, A., Smith, A. J., Mienert, J., Cherkashov, G., Rekant, P., Semenov, P., . . . Vanshtein, B. (2013). Offshore permafrost decay and massive seabed methane escape in water depths> 20 m at the South Kara Sea shelf. Geophysical Research Letters, 40(15), 3962-3967.
Portnov, A., Vadakkepuliyambatta, S., Mienert, J., & Hubbard, A. (2016). Ice-sheet-driven methane storage and release in the Arctic. Nature communications, 7, 10314.
Reeburgh, W. S. (2007). Oceanic methane biogeochemistry. Chemical reviews, 107(2), 486-513.
Römer, M., Riedel, M., Scherwath, M., Heesemann, M., & Spence, G. D. (2016). Tidally controlled gas bubble emissions: A comprehensive study using long-term monitoring data from the NEPTUNE cabled observatory offshore Vancouver Island. Geochemistry, Geophysics, Geosystems, 17(9), 3797-3814.

Rudels, B., Jones, E., Anderson, L., & Kattner, G. (1994). On the intermediate depth waters of the Arctic Ocean. The polar oceans and their role in shaping the global environment, 33-46.
Sahling, H., Römer, M., Pape, T., Bergès, B., dos Santos Fereirra, C., Boelmann, J., . . . Dimmler, W. (2014). Gas emissions at the continental margin west of Svalbard: mapping, sampling, and quantification. Biogeosciences, 11(21), 6029.
Sarkar, S., Berndt, C., Minshull, T. A., Westbrook, G. K., Klaeschen, D., Masson, D. G., . . . Thatcher, K. E. (2012). Seismic evidence for shallow gas-escape features associated with a retreating gas hydrate zone offshore west Svalbard. Journal of Geophysical Research: Solid Earth, 117(B9).
Schmale, O., Greinert, J., & Rehder, G. (2005). Methane emission from high-intensity marine gas seeps in the Black Sea into the atmosphere. Geophysical Research Letters, 32(7).
Serov, P., Portnov, A., Mienert, J., Semenov, P., & Ilatovskaya, P. (2015). Methane release from pingo-like features across the South Kara Sea shelf, an area of thawing offshore permafrost. Journal of Geophysical Research: Earth Surface, 120(8), 1515-1529.
Serov, P., Vadakkepuliyambatta, S., Mienert, J., Patton, H., Portnov, A., Silyakova, A., . . . Andreassen, K. (2017). Postglacial response of Arctic Ocean gas hydrates to climatic amelioration. Proceedings of the National Academy of Sciences, 201619288.
Serreze, M. C., & Francis, J. A. (2006). The Arctic amplification debate. Climatic change, 76(3-4), 241-264.
Shakhova, N., Semiletov, I., Leifer, I., Sergienko, V., Salyuk, A., Kosmach, D., . . . Tumskoy, V. (2013). Ebullition and storm-induced methane release from the East Siberian Arctic Shelf. Nature Geoscience, 7(1), ngeo2007.
Shakhova, N., Semiletov, I., Salyuk, A., Yusupov, V., Kosmach, D., & Gustafsson, Ö. (2010). Extensive methane venting to the atmosphere from sediments of the East Siberian Arctic Shelf. Science, 327(5970), 1246-1250.
Shchepetkin, A. F., & McWilliams, J. C. (2005). The regional oceanic modeling system (ROMS): a split-explicit, free-surface, topography-following-coordinate oceanic model. Ocean modelling, 9(4), 347-404.
Smith, A. J., Mienert, J., Bünz, S., & Greinert, J. (2014). Thermogenic methane injection via bubble transport into the upper Arctic Ocean from the hydrate-charged Vestnesa Ridge, Svalbard. Geochemistry, Geophysics, Geosystems, 15(5), 1945-1959.
Soreide, N. N., Jeffries, M., Richter-Menge, J., & Overland, J. (2016). The Arctic Report Card. Bulletin of the American Meteorological Society, 97(8), 1339-1341.
Steinle, L., Graves, C. A., Treude, T., Ferré, B., Biastoch, A., Bussmann, I., . . . Behrens, E. (2015). Water column methanotrophy controlled by a rapid oceanographic switch. Nature Geoscience, 8(5), 378.
Storkey, D., Blockley, E., Furner, R., Guiavarc'h, C., Lea, D., Martin, M., . . . Siddorn, J. (2010). Forecasting the ocean state using NEMO: The new FOAM system. Journal of operational oceanography, 3(1), 3-15.
Teigen, S. H., Nilsen, F., & Gjevik, B. (2010). Barotropic instability in the West Spitsbergen Current. Journal of Geophysical Research: Oceans, 115(C7).
Tverberg, V., & Nøst, O. (2009). Eddy overturning across a shelf edge front: Kongsfjorden, west Spitsbergen. Journal of Geophysical Research: Oceans, 114(C4).
Veloso, M., Greinert, J., Mienert, J., & De Batist, M. (2015). A new methodology for quantifying bubble flow rates in deep water using splitbeam echosounders: Examples from the Arctic offshore NW-Svalbard. Limnology and Oceanography: Methods, 13(6), 267-287.
von Deimling, J. S., Rehder, G., Greinert, J., McGinnnis, D., Boetius, A., & Linke, P. (2011). Quantification of seep-related methane gas emissions at Tommeliten, North Sea. Continental Shelf Research, 31(7-8), 867-878.
Wallmann, K., Riedel, M., Hong, W., Patton, H., Hubbard, A., Pape, T., . . . Torres, M. (2018). Gas hydrate dissociation off Svalbard induced by isostatic rebound rather than global warming. Nature communications, 9(1), 83.
Wanninkhof, R., Asher, W. E., Ho, D. T., Sweeney, C., & McGillis, W. R. (2009). Advances in quantifying air-sea gas exchange and environmental forcing.

Weiss, R., & Price, B. (1980). Nitrous oxide solubility in water and seawater. Marine chemistry, 8(4), 347-359.
Wekerle, C., Wang, Q., von Appen, W. J., Danilov, S., Schourup-Kristensen, V., & Jung, T. (2017). Eddy-Resolving Simulation of the Atlantic Water Circulation in the Fram Strait With Focus on the Seasonal Cycle. Journal of Geophysical Research: Oceans, 122(11), 8385-8405.
Westbrook, G. K., Thatcher, K. E., Rohling, E. J., Piotrowski, A. M., Pälike, H., Osborne, A. H., . . . James, R. H. (2009). Escape of methane gas from the seabed along the West Spitsbergen continental margin. Geophysical Research Letters, 36(15).
Wiesenburg, D. A., & Guinasso Jr, N. L. (1979). Equilibrium solubilities of methane, carbon monoxide, and hydrogen in water and sea water. Journal of Chemical and Engineering Data, 24(4), 356-360.

[Journal of Geophysical Research: Oceans]

Supporting Information for

Physical controls of dynamics of methane venting from a shallow seep area west of Svalbard

A. Silyakova[1], P. Jansson[1], P. Serov[1], B. Ferré[1], A. K. Pavlov[2], T. Hattermann[3,4], C. A. Graves[5,6], S. M. Platt[7], C. Lund Myhre[7], F. Gründger[1] and H. Niemann[8,1,9]

[1]CAGE-Centre for Arctic Gas Hydrate, Environment and Climate, UiT the Arctic University of Norway in Tromsø, Department of Geosciences, Tromsø, Norway
[2]Norwegian Polar Institute, Fram Centre, Tromsø, Norway
[3]Akvaplan-niva AS, Fram Centre, Tromsø, Norway
[4]Alfred Wegener Institute, Helmholtz Centre for Polar and Marine Research, Bremerhaven, Germany
[5]Leibniz Institute for Baltic Sea Research Warnemünde, Rostock, Germany
[6]Centre for Environment, Fisheries and Aquaculture Science, Lowestoft, UK
[7]NILU - Norwegian Institute for Air Research, Kjeller, Norway
[8]University of Basel, Basel, Switzerland
[9]NIOZ Royal Netherlands Institute for Sea Research, Department of Marine Microbiology & Biogeochemistry, the Netherlands

Contents of this file

Text S1 to S2, Figures S1 to S3

Introduction

Supporting Text S1 and Figure S1 provide details of the method of scaling up gas flow rate estimates to the entire study area.

Supporting Text S2 and Figure S2 provide a detailed description of the water column methane content calculations in different layers.

Supporting Figure S3 shows additional information on bottom water temperature to support the main text in Results and Discussion section 3.1.

Text S1. Method for scaling up the flow rates

Because the fraction of the study area covered by the echosounder was small and slightly different between the three surveys, we applied a scaling up procedure including a Kriging interpolation to facilitate comparison between surveys (Figure S1). The entire area was gridded into cells of 100 ×100 m, and, as a result three types of cells were considered: 1) completely covered, 2) partly covered or 3) not covered by the echosounder beam footprint. For each cell, we estimated methane flow rates: (a) If one or several flares were detected within cell type 1, the estimated flow rate was applied for the entire cell area. (b) In the absence of flares in cell type 1, the flow rate was set to zero. (c) If one or several flares were within cell type 2, the sum of the flow rates within the cell was normalized by the fraction of the cell covered by the beam footprint. (d) In the absence of flares in cell type 2, the flow rate was set to zero. (e) For cell type 3, (no data acquired) we interpolated flow rates from neighbouring cells. In order to find a smooth and plausible flowrate distribution, a 3x3 low-pass filter, and the Kriging interpolation method embedded in ArcGIS was applied. Finally, to calculate the mean flux (mol m^{-2} s^{-1}) in the entire area, the sum of the scaled up flow rates were normalized by the survey area (Table 1).

Text S2. Calculation of methane content in the water column

Methane content in the water column was calculated by integrating distinct methane concentration values over depth. For this approach, we approximated the definite integral linearly by applying the trapezoid rule. For each discrete sampling point shown on Fig. S2, we had a corresponding depth (Z, m) and CH_4 concentration (C, nmol L^{-1}). To determine the vertically integrated methane content (C_{int}) for every depth (meter) of water column between sampling points (nmol L^{-1} m) we interpolated linearly as follows:

$C_{int}=(CS_1+CS_2)/2*(ZS_2-ZS_1)$ (Eq. SI1)

We then summed all C_{int} in each layer and multiplied by 10^3 to obtain methane content per m^2 in every layer (nmol m^{-2}) for each of the CTD stations.

To account for spatial sampling irregularity between CTD stations, we determined the area-weighted average of the CH_4 content for each layer. For this, we created a grid between longitudes 9.5° E and 10.8° E and latitudes 78.4° N and 78.7° N with bin sizes of 0.01 × 0.01° in both directions. The resulting grid included 101×201 points. We then projected C_{int} for each layer and station onto this grid using the Matlab function griddata for horizontal interpolation. Finally, we calculated the area-weighted average using the Matlab function mean2 of the gridded data. Then we scaled up (multiplied) the area-weighted averages for each layer to the size of the investigated area (423 km^2), yielding the total methane content (in mol) for each layer.

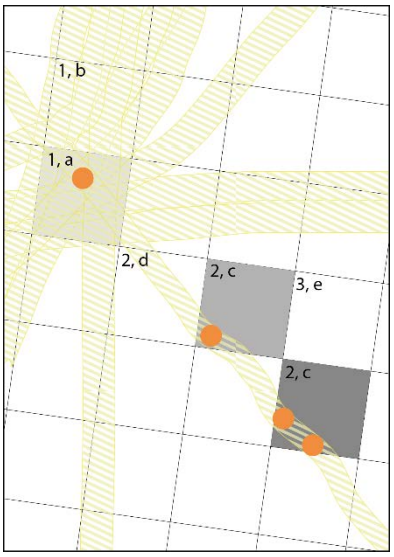

Figure S1. Schematic of flowrate interpolation. Squares indicate 100x100 meter grid cells where the darkness indicates the relative summed flow rates within each cell. Yellow-hashed areas indicate the echosounder beam coverage and dots indicate flares. Cell types 1 – 3 and interpolation schemes a – e are described in the text S1.

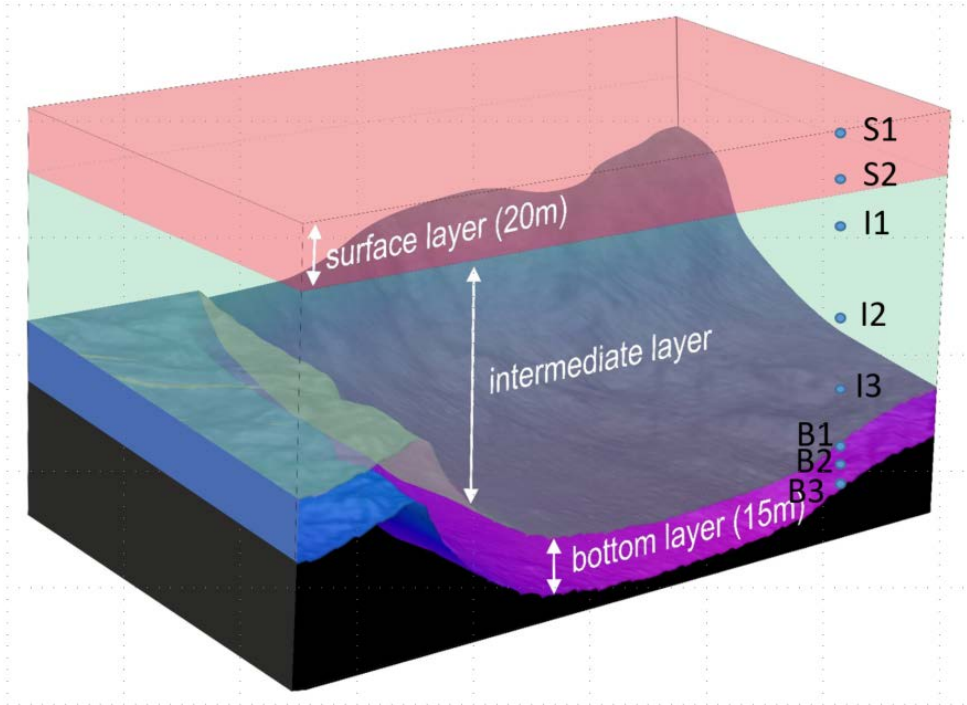

Figure S2. Schematic shows the bottom layer (0-15 meters above seafloor), the intermediate layer (15 meters above seafloor to 20 m water depth) and the surface layer (20 m water depth to sea surface). The blue dots show discrete sampling points in the surface (S1, S2), intermediate (I1, I2, I3) and bottom (B1, B2, B3) layer.

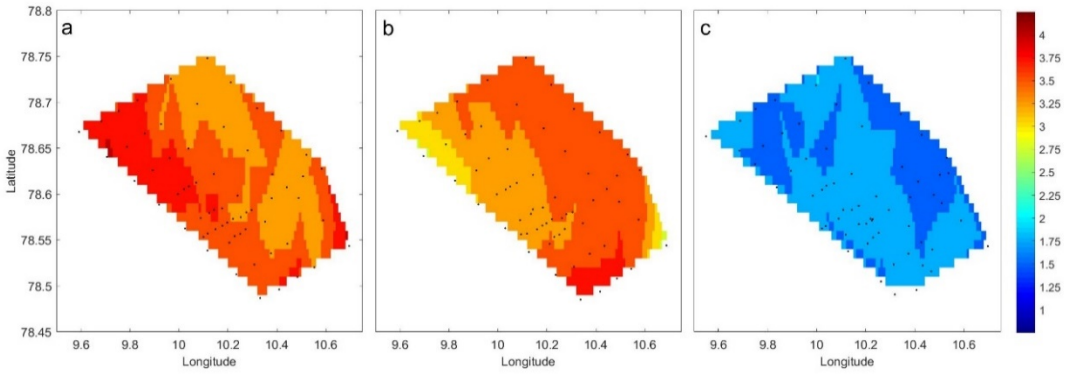

Figure S3. Bottom water temperature during the June-14 (**a**), July-15 (**b**) and May-16 (**c**) surveys.

Paper 3

Title

A new numerical model for understanding free and dissolved gas progression towards the atmosphere in aquatic methane seepage systems

Authors

Pär Jansson[1], Bénédicte Ferré[1], Anna Silyakova[1], Knut Ola Dølven[1], Anders Omstedt[2]

[1] CAGE-Centre for Arctic Gas Hydrate, Environment and Climate, UiT the Arctic University of Norway in Tromsø, Department of Geosciences, Tromsø, Norway.

[2] Department of Marine Sciences, University of Gothenburg, Box 460, SE-405 30 Göteborg, Sweden

Corresponding author

Pär Jansson. Centre for Arctic Gas Hydrate, Environment and Climate

UiT – The Arctic University of Norway. Department of Geoscience

N-9037, Tromsø, Norway; Tel: +47 77646398; per.g.jansson@uit.no; https://cage.uit.no/

Running head

Marine 2 Phase Gas model in 1 dimension

Keywords

Methane, Gas, Model, Bubbles, Dissolution, Arctic Ocean

Abstract

We present a marine two-phase gas model in one dimension (M2PG1) resolving interaction between the free and dissolved gas phases, and the gas propagation towards the atmosphere in aquatic environments. The motivation for the model development was to improve the understanding of benthic methane seepage impact on aquatic environments, and its effect on atmospheric greenhouse gas composition. Rising, dissolution and exsolution of a wide size-range of bubbles comprising several gas species are modelled simultaneously with the evolution of the aqueous gas concentrations. A model sensitivity analysis elucidates the relative importance of process parameterizations and environmental effects on the gas behaviour. The parameterization of transfer velocity across bubble rims has the greatest influence on the resulting gas distribution and bubble sizes are critical for predicting the fate of emitted bubble gas. High salinity increases the rise height of bubbles while temperature does not significantly alter it. Vertical mixing and aerobic oxidation play insignificant roles in environments where advection is important. The model, applied in an Arctic Ocean methane seepage location, showed good agreement with acoustically derived bubble rise heights and in-situ sampled methane concentration profiles. Coupled with numerical ocean circulation and biogeochemical models, M2PG1 could predict the impact of benthic methane emissions on the marine environment and the atmosphere on long time scales and large spatial scales. Because of its flexibility, M2PG1 can be applied in a wide variety of environmental settings and future M2PG1 applications may include gas leakage from seafloor installations and bubble injection by wave action.

Introduction

The importance of natural and anthropogenic methane (CH_4) emissions to the atmosphere has been increasingly recognized in the last few decades as CH_4 contributes to greenhouse warming by about 20% (Edenhofer et al., 2014; Pachauri et al., 2014), and because CH_4 is 32 times more potent than CO_2 in terms of warming potential (Pachauri et al., 2014).

Large CH_4 reservoirs in the form of hydrates, a crystalline structure comprising water molecules encapsulating guest molecules such as CO_2 and hydrocarbons, (Sloan and Koh, 2007) exist in sediments along continental margins worldwide. They are presently estimated to contain 1800 Gt of carbon (Ruppel and Kessler, 2016), equivalent to one-sixth of the global mobile carbon pool. Hydrates are stable under high pressure and low temperature, suggesting that bottom water warming potentially dissociates hydrates at the boundary of their stability (Westbrook et al., 2009). Yearly global flux of CH_4 to the atmosphere associated with dissociation of hydrate deposits is presently estimated at 6 Tg, which amounts to less than 1% of the total CH_4 flux to the atmosphere (Kirschke et al., 2013), but hydrate dissociation rates may increase as ocean bottom water temperatures increase over human time scales (Ferré et al., 2012).

A substantial amount of CH_4 is also found trapped where permafrost (water ice that is frozen all year) caps exist. Gaseous CH_4 trapped under hydrate- and permafrost caps is presently released to through the water column to the atmosphere on the East Siberian Shelf as the caps become more and more permeable due to thawing (Shakhova et al., 2010). In the light of a rapidly warming Arctic Ocean, it is therefore crucial to understand the transport mechanisms of CH_4 from the seabed through the water column and potentially to the atmosphere in order to estimate the impacts of seafloor CH_4 emissions on the climate and the environment.

CH_4 in sediments may be present as hydrates, free (bubbles) and/or dissolved gas in pore water. CH_4 percolating upwards is subject to anaerobic oxidation within the sulphate-methane transition zone (Boetius and Wenzhöfer, 2013) but in high-velocity fluid flow systems, both dissolved CH_4 and bubbles can bypass this filter (Luff et al., 2004; Panieri et al., 2017).

After being released from the seafloor, most of the CH_4 contained in bubbles dissolve in the water column as the bubbles ascend towards the sea surface. Numerical bubble models predict that gas exchange occurs across the bubble rims and a majority of the CH_4 initially present within the bubbles dissolve near the seafloor (Leifer and Patro, 2002; McGinnis et al., 2006). Subsequently, dissolved CH_4 diffuses, is advected by ocean currents away from its source, and is, at least partly oxidized in the presence of methanotrophic bacteria (Damm et al., 2005; Uhlig and Loose, 2017). Biastoch et al., (2011) modelled the effect of microbial CH_4 oxidation on ocean acidification and showed that the ocean pH could decrease by as much as 0.25 units in a 100-year period in some areas of the Arctic Ocean. At shallow water depths, bubbles may transport CH_4 to the upper mixed layer of the ocean, where the now-dissolved CH_4 may be ejected to the atmosphere by diffusive equilibration. Shakhova et al., (2014) reported a significant reduction of dissolved CH_4 concentration in the water column on the shallow East Siberian Arctic Shelf (water depth <50 m) directly after two storm events, suggesting that diffusive emission of CH_4 to the atmosphere was enhanced by the strong vertical mixing induced by the storms. However, large CH_4 emissions from the seafloor at a slightly deeper site (~90m) west of Svalbard in the summer of 2014, did not contribute to increased CH_4 concentration in the atmosphere

(Myhre et al., 2016). Although the acoustic signature of bubble streams was observed to reach close to the sea surface, only traces of the high CH_4 concentration near the seafloor was observed near the surface. This effect was attributed to efficient gas exchange across bubble rims and the presence of a pycnocline was suggested to inhibit vertical turbulent transport of dissolved CH_4 toward the sea surface and atmosphere.

The motivation for this study was to improve the understanding of the role of the hydrosphere in locations where CH_4 is leaking from the seafloor. Specifically, the vertical distribution of free and aqueous CH_4 resulting from seafloor seepage is of great interest in order to assess potential release of CH_4 to the atmosphere and biochemical changes in the aquatic habitat.

In order to predict the fate of CH_4 or any other kind of gas, contained in bubbles in the water column, it is necessary to consider interaction with other kinds of existent gas. Only simultaneous consideration of bubble dissolution and evolution of dissolved gas can allow for understanding these processes and their impact. Numerical bubble models have been developed previously, but each show limitations. Delnoij et al., (1997) developed a bubble model for a gas-liquid column, which resolves bubble-bubble interaction (bouncing and coalescence) but does not take into account gas dissolution or pressure gradients. Johansen, (2000) modelled non-ideal gas behaviour, but ignored ambient dissolved gas and only modelled CH_4. Leifer and Patro, (2002) introduced a bubble model based on empirical observations of bubble rising speeds but assumed spherical bubbles and ignored the non-ideal behaviour of gases due to pressure and temperature. McGinnis et al., (2006) provided a bubble model resolving five bubble gases, Nitrogen (N_2), Oxygen (O_2), Carbon dioxide (CO_2), Methane (CH_4) and Argon (Ar), but did not couple free and dissolved gas and did not consider multiple bubble sizes. Stepanenko et al., (2011) presented a natural process-based model for shallow lakes with the production of CH_4 in the sediment, assuming immediate escape of CH_4 to the atmosphere. Liang et al., (2011) presented a near-surface coupled bubble- and dissolved gas model but used a size spectrum of bubbles ranging from zero to only 0.8 mm, adequately assuming spherical bubbles. Vielstädte et al., (2015) developed a linearized single bubble model with three gas species (N_2, O_2, CH_4) for the North Sea, which is only valid for depths shallower than 100 meters and ignores the evolution of dissolved gases.

All of the above models depend on parameterizations of gas-, water- and bubble properties and so uncertainties associated with those are abundant. The objective of this study is to develop and verify a new numerical model, filling knowledge gaps of previous models. The major improvements of the here presented marine two-phase gas model in one dimension (M2PG1) over previous bubble models are:

1. Dissolution (gas escaping the bubble) and exsolution (gas invading the bubble) to simulate the evolution of the free gas composition of several gas species inside the bubbles.
2. Coupling of the dissolution and exsolution of bubble gas to the temporal evolution of the dissolved gas concentration in the water column.
3. Bubbles of different sizes and size-dependent shapes.

4. Non-ideal gas behaviour for changing temperature and pressure within the bubbles as they rise through the water column.
5. Calculation of pressure-, salinity-, and temperature dependent solubility of five gas species (N_2, O_2, CO_2, CH_4, and Ar).
6. Gas emission of free gas and equilibration of dissolved gas with the atmosphere.
7. Coupling with existing models resolving transport and diffusion of water properties is made possible because of the structure of the model.

To our knowledge, M2PG1 is the first model that is able to simulate free and dissolved gas simultaneously, while using multiple bubble sizes and several gas species in both free and dissolved phases. Non-ideal gas compressibility, environment-dependent solubility, and diffusivity are included in the model as well as interaction with the atmosphere of the free and dissolved phase of all included gas species. This study focuses on CH_4 seepage from the seafloor in a cold (Arctic Ocean) environment and we aim to elucidate on the relative importance of the different included process parameterizations and compare the effects of environmental conditions on the gas dynamics. We first describe the model setup and process parametrizations and subsequently detail a sensitivity analysis, comparing the importance of parameterizations of rising speed, bubble shapes and gas transfer with the importance of bubble sizes, temperature, salinity, CH_4 oxidation rates, dissolved gas concentrations, turbulent vertical mixing and water currents. The model was applied to a known CH_4 seep site West of Svalbard (e.g. Westbrook et al., 2009; Sahling et al., 2014) and a comparison between model results and acquired data is presented.

Method

We developed a numerical marine two-phase gas model in one dimension (M2PG1) to simulate the evolution of free gas (bubbles) rising through the water column while resolving interaction with dissolved gas and the ultimate exchange of gas with the atmosphere via direct bubble transport and/or equilibration with atmospheric gas species. The model incorporates pressure- temperature- and salinity dependent gas compressibility, solubility and diffusivity and simulates multi-gas and multi-size bubbles with user-defined initial gas composition and user-defined bubble size distribution (BSD). Bubbles can be released at any chosen water depth. This study focuses on the evolution of free and dissolved gases occurring after gas (CH_4) bubbles are released from the seafloor, and interaction with atmospheric and dissolved N_2, O_2, CO_2, CH_4, and Ar. The following sections describe how M2PG1 models these processes.

Model implementation

We implemented M2PG1 in PROBE, a well-documented and freely available numerical equation solver (Svensson, 1978; Omstedt, 2011) using a finite volume discretization and FORTRAN. PROBE has been successfully used for prediction of growth and melting of sea ice (Omstedt and Wettlaufer,

1992); Coupling between weather forecasting and a process based ocean model (Gustafsson et al., 1998); Frazil Ice dynamics (Svensson and Omstedt, 1998); Marine climate studies (Hansson and Omstedt, 2008); The effect of wave-dependent momentum flux (Carlsson et al., 2009) and the carbonate system in the Baltic Sea (Edman and Omstedt, 2013). The equation solver supports a process-based approach and is intended for numerical representation of the environment, and to test and build new system understanding. It is well suited for climate impact studies, resolving the vertical structure of the investigated properties of the water column. The present model can be described in two parts: 1) PROBE resolves the evolution of vertical profiles of physical and chemical parameters such as temperature, salinity, and dissolved gas of different species; 2) M2PG1 simulates the evolution of free gas bubbles. The two parts are coupled via the exchange of gas across bubble surfaces. PROBE solves the conservation equations (equation 1) for the state variables, ϕ which in this study are salinity, temperature and dissolved gas species (N_2, O_2, CO_2, CH_4, and Ar).

$$\frac{\partial \phi}{\partial t} + \frac{Q_{IN} - Q_{OUT}}{A} \times \frac{\partial \phi}{\partial z} = \frac{\partial}{\partial z}\left(\Gamma_\phi \frac{\partial \phi}{\partial z}\right) + \theta^\phi \quad (1)$$

The first term ($\frac{\partial \phi}{\partial t}$) represents the local (at depth *z*) change with time of the state variable. The second term ($\frac{Q_{IN}-Q_{OUT}}{A} \times \frac{\partial \phi}{\partial z}$) is the vertical advection given by multiplying the vertical gradient of the state variable by the volume convergence of in- and outflows (Q_{IN} and Q_{OUT}) normalized by the domain area (A). The right-hand side shows diffusion $\left(\frac{\partial}{\partial z}\left(\Gamma_\phi \frac{\partial \phi}{\partial z}\right)\right)$ and local source/sink terms (θ^ϕ). The salinity, temperature, and concentration of dissolved gas species are represented on a vertical finite volume grid. The free gas is represented in an identical vertical grid and in bubble size classes with equivalent radii ($[r - \delta r/2, r + \delta r/2]$).

Free gas (bubbles) rises through the water column at speeds mainly dependent on bubble size and shape, while the exchange of gases across the bubble rims alters the gas composition and concentration inside and outside the bubble. While previous seawater bubble models (e.g. (e.g. Leifer and Patro, 2002; McGinnis et al., 2006; Vielstädte et al., 2015) were Lagrangian, i.e. simulating the evolution of a single bubble, M2PG1 uses a Eulerian, vertically oriented finite volume grid and a bubble size spectrum to simulate any number and sizes of bubbles simultaneously. This requires that bubble rising and shrinking or growing to be discretized. Figure 1 shows a diagram of the processes involved and the numerical grid where light blue indicates dissolved gas and yellow indicates free gas. Temperature and salinity are omitted in the figure for clarity. The model is integrated (moved forward in time) using the Euler method, resolving all the above-described processes simultaneously.

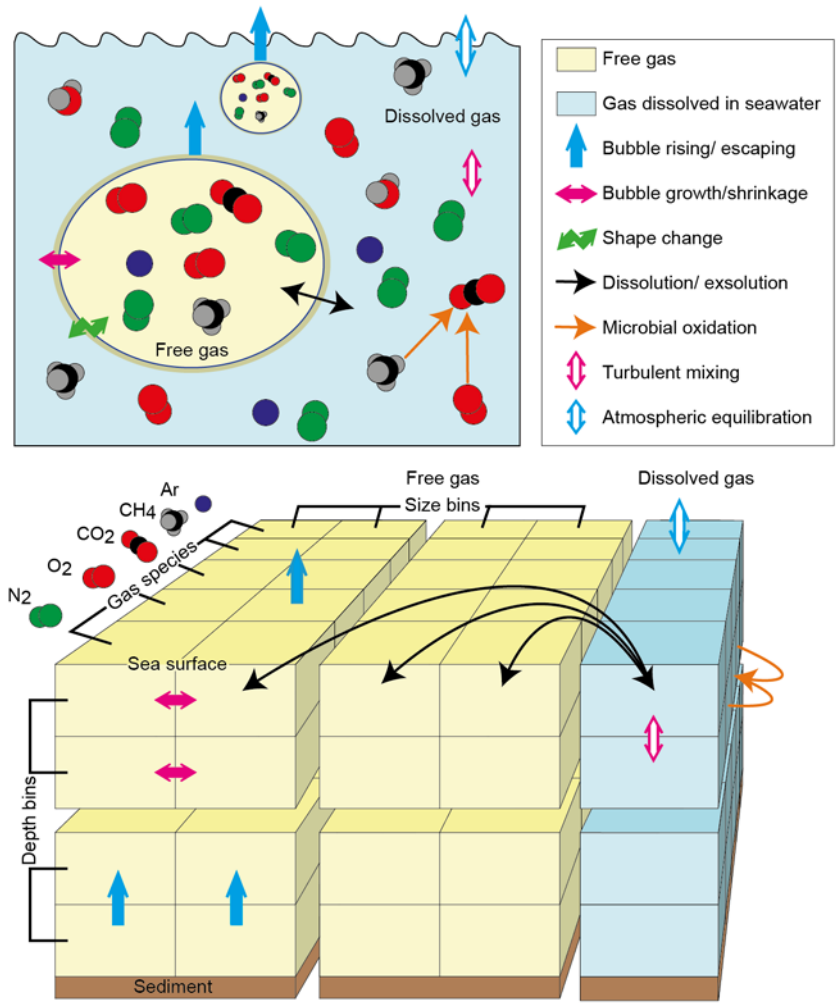

Figure 1. Diagram illustrating the physical processes involved as gas bubbles rises through the water column. Upper panel: Diagram of the natural processes occurring in the water column (blue background) and in the bubbles (yellow background). The black double arrow indicates the dissolution/ exsolution of bubble gas (transfer of different gases across the bubble rim). The solid pink double arrow shows the growth/ shrinkage of bubbles caused by pressure change and gas transfer. The green zigzag arrow indicates the shape-change of bubbles due to growth/ shrinkage. Orange arrows indicate the aerobic oxidation of CH_4, resulting in a production of CO_2 and consumption of O2 and CH_4. The solid blue arrows represent bubble rising and the eventual free gas escape to the atmosphere. The hollow pink double arrow represents the vertical mixing of dissolved gases and the hollow blue arrow indicates equilibration of dissolved gases with the atmosphere. Lower panel: Representation of all of the above-mentioned processes in the numerical model. The left part of the grid (yellow) shows the free gas contained in depth-bins, bubble size bins and gas species, handled in M2PG1. The right (blue) part represents the dissolved gases in the same depth- and species grid mainly handled in PROBE. Arrows of the same appearance in the upper and lower panel represent the same process. For sketch simplicity, only examples of the processes are drawn (e.g., bubble rising potentially occurs between all depth bins and growth/ shrinkage occurs between all size bins).

Coupled conservation equations for free and dissolved gas

The processes constituting the source- and sink terms in equation 1 can be summarized in a set of coupled conservation equations describing the temporal evolution of free gas content and dissolved

gas concentration (equations 2 – 3, where the superscript $j \in [\mathrm{N_2}, \mathrm{O_2}, \mathrm{CO_2}, \mathrm{CH_4}, \mathrm{Ar}]$ denotes gas species and subscripts *i* and *k* indicate indices for depth and bubble size respectively). Additional source/ sink terms at the vertical and lateral domain boundaries are given in equations 4 – 5. Notations are summarized in the supplementary information (SI.1) and each mathematical term in the equations are described in the following sections.

$$\frac{\partial n_{i,k}^{j}}{\partial t} = \frac{\partial n_{R_{i,k}}^{j}}{\partial t} + \frac{\partial n_{D_{i,k}}^{j}}{\partial t} \tag{2}$$

$$\theta_i^{N_2} = -\left(\frac{\sum_k^{NSBIN} \partial n_{D,k}^{N_2}/\partial t}{[\rho_{SW} \times A \times \delta_z]}\right)_i \tag{3a}$$

$$\theta_i^{O_2} = -\left(\frac{\sum_k^{NSBIN} \partial n_{D,k}^{O_2}/\partial t}{[\rho_{SW} \times A \times \delta_z]}\right)_i - k_{MOX} \times \mathrm{C}_i^{\mathrm{CH_4}} \tag{3b}$$

$$\theta_i^{CO_2} = -\left(\frac{\sum_k^{NSBIN} \partial n_{D,k}^{CO_2}/\partial t}{[\rho_{SW} \times A \times \delta_z]}\right)_i + k_{MOX} \times \mathrm{C}_i^{\mathrm{CH_4}} \tag{3c}$$

$$\theta_i^{CH_4} = -\left(\frac{\sum_k^{NSBIN} \partial n_{D,k}^{CH_4}/\partial t}{[\rho_{SW} \times A \times \delta_z]}\right)_i - k_{MOX} \times \mathrm{C}_i^{\mathrm{CH_4}} \tag{3d}$$

$$\theta_i^{Ar} = -\left(\frac{\sum_k^{NSBIN} \partial n_{D,k}^{Ar}/\partial t}{[\rho_{SW} \times A \times \delta_z]}\right)_i \tag{3e}$$

In equation 2, $\frac{\partial n_R}{\partial t}$ is the temporal evolution of free gas due to rising bubbles as visualized in Figure 2 a and quantified in the section "*Rising bubbles*". $\frac{\partial n_D}{\partial t}$ is the free gas evolution due to bubble-dissolution visualized in Figure 2 b and detailed in the section "*Exchange of free and dissolved gas across bubble rims*". In equations 3 a – e, $\left(\frac{\sum_k^{NSBIN} \partial n_{D,k}^{j}/\partial t}{[\rho_{SW} \times A \times \delta_z]}\right)_i$ is the dissolved gas concentration change corresponding to the dissolution occurring in all bubble sizes. Removal of CO_2 and CH_4 and production of CO_2 by aerobic CH_4 oxidation is represented by the second term in 3b, c and d (i.e. $\pm k_{MOX} \times \mathrm{C}_i^{\mathrm{CH_4}}$e.), as illustrated in Figure 1 and quantified in the section "*Aerobic oxidation of CH_4*". Free gas content and dissolved gas concentrations are integrated forward in time simultaneously with temperature and salinity, starting with initial conditions and forced by boundary conditions.

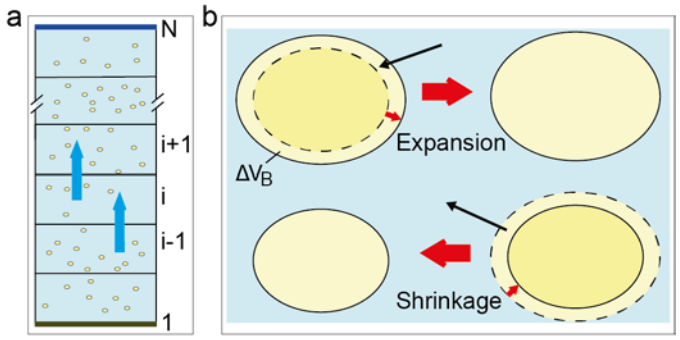

Figure 2. Representation of bubbles rising, expanding, and shrinking. a) Vertical grid with indices starting from 1 at the seafloor and up toward the surface bin, N. Ellipses illustrate bubbles within each depth bin and blue arrows indicate bubbles rising to the current bin from below and rising up to the next higher bin. b) Bubbles shrinking or expanding as described in the text. The volumetric difference between bubbles in adjacent size bins is indicated by ΔV_B and small red arrows. Bubbles are assumed oblate spheroids. Here, a denotes the length of the horizontal (semi-major) axis and b denotes the length of the vertical (semi-minor) axis.

Initial- and boundary conditions

Supplementary to the local sources and sinks, free gas content and dissolved gas concentration are affected by fluxes across the domain boundaries. Equation 4 describes the source- and sink terms of free gas at the vertical boundaries and equation 5, the source- and sink terms of dissolved gas at the lateral and vertical boundary. It is assumed that there is no dissolved gas emitted from the seafloor and no free gas is transported from beyond the lateral boundary.

$$\frac{\partial}{\partial t}\left(n^{j}_{i\in[bot,surf],k}\right) = Q^{j}_{EF_k} - Q^{j}_{AF_k} \tag{4}$$

$$\theta^{j}_{B_i} = Q_{IN_i} \times C^{j}_{B_i} - Q_{OUT_i} \times C^{j}_{SW\,i} - \left(\frac{Q^{j}_{AEQ_i}}{\rho_{SW_i} \times A_i \times \delta_{z_i}}\right)_{i=surf} \tag{5}$$

In equation 4, Q_{EF} represents the emitted free gas (here CH_4 bubbling from the seafloor) and Q_{AF} is the bubble gas escaping to the atmosphere from the sea surface. In equation 5, $\left(Q_{IN_i} \times C^{j}_{B_i} - Q_{OUT_i} \times C_{SW\,i}{}^{j}\right)_i$ is the concentration change due to the lateral transport of dissolved gas j in and out of the model domain. Q_{IN_i} and Q_{OUT_i} are the volumetric in- and outflow respectively from the boundary at depth $z(i)$, C_{B_i} is the concentration at the boundary and C_{SW_i} is the concentration in the modelled water column. $\left(\frac{Q^{j}_{AEQ}}{\rho_{SW} \times A \times \delta_z}\right)_{i=surf}$ represents the concentration change due to equilibration of dissolved gas j with the atmosphere, where Q_{AEQ} is the amount of gas emitted per time unit, ρ_{SW} is the seawater density calculated from temperature and salinity according to Fofonoff, (1985), and A and δ_z are the horizontal area and vertical extent of the model cell respectively. The built-in functionality of PROBE handles fluxes of heat and salinity across the boundary, using the boundary salinity and temperature in conjunction with the in- and outflow.

As bubble-dynamics depend on temperature, salinity and dissolved gas concentration in the water column, initial- and boundary conditions include vertical profiles of the modelled gas concentration and of temperature and salinity. Initial conditions are provided by the user with the same vertical resolution as the model grid (here, the profiles are 400 meters with a 1-meter resolution). M2PG1 can be forced with transient aquatic boundary conditions with vertical resolution matching the vertical grid of the forcing data and transient atmospheric boundary conditions can be specified. As the sensitivity analysis of this study aims at evaluating the influence of implemented parameters individually, we apply vertically homogenous profiles of dissolved gas, temperature, and salinity for the simulations included. The case study, on the other hand, uses measured profiles of temperature, salinity, and oxygen. Gas species, other than oxygen, are expected to be in equilibrium with the atmosphere as we lack measurements of them. The structure of the user-specified initial- and boundary conditions are listed in Table SI.7. Simulations in this analysis use static boundary conditions identical to the initial conditions.

Rising bubbles

In order to evaluate the importance of bubble rising speed on the distribution of gas in the water column, M2PG1 includes different bubble rising speed models (BRSM) that the user can select (Table SI.2). Bubbles accelerate quickly after their emission and reach terminal velocity within milliseconds when the buoyancy and drag forces balance. We therefore assume that the bubble rising speed can be derived from ambient conditions and bubble sizes, and there is no need to simulate acceleration from the moment when bubbles are released from the seafloor. The rising of gas contained in bubbles of specific sizes is discretized as visualized in Figure 2 a. The first term on the right-hand side of equation 2 describes the rate of change with time of the content of a particular gas species at depth z(*i)* for each bubble size resulting from rising bubbles. This is quantified in equation 6, where w_b is the rising speed of the bubble.

$$\frac{\partial n_{R_i}}{\partial t} = \frac{w_{b_{i-1}} \times n_{i-1}}{\delta z_{i-1}} - \frac{w_{b_i} \times n_i}{\delta z_i} \tag{6}$$

Bubble hydrodynamics, and therefore, bubble rising speeds are influenced by surfactants on the bubble rims. Different surfactants such as bacteria (Blanchard, 1989), ions (Collins et al., 1978) and oil (Leifer et al., 2000) may contribute to immobilization of the bubble rim and can change the rising speed of bubbles. The reference case uses the BRSM suggested by Woolf, (1993) because, in spite of its simplicity, it considers both clean and surfactant covered bubbles and because the velocities are intermediate compared to other models over the relevant range of bubble sizes.

Exchange of free and dissolved gas across bubble rims

Transfer of gas molecules across bubble surfaces is a stochastic process, occurring continuously, and the net transfer is zero only when equilibrium arises between the free and the aqueous phase of all gas species simultaneously. Mass conservation requires that the sink of free gas in the bubbles, due to dissolution, $\frac{\partial n^j_{D_{i,k}}}{\partial t}$ in equation 2, is complemented by a source of dissolved gas (equations 3a – e) in the water column. This is quantified by the transfer equation (e.g. Leifer & Patro, 2002; McGinnis et al., 2006), giving the rate of change of bubble gas content resulting from dissolution/ exsolution:

$$\frac{\partial n^j_{D\,i,k}}{\partial t} = A_{BS\,i,k} \times \rho_{SW_i} \times k^j_{T\,i,k} \times \left[C^j_{SW\,i,k} - C^j_{EQ\,i,k}\right] \quad (7)$$

In the following sections, the transfer velocity (k_T in equation 7) models (TVMs) and parameterizations of the surface area of bubbles (A_{BS}) are discussed. C_{EQ} is the dissolved gas concentration, which would result in equilibrium between the dissolved phase and the free gas inside the bubble. It is given by the solubility *S* and the molar fraction ($X = \frac{n^j}{\sum_1^{NGAS} n^j}$) of gas species *j* in the bubble according to:

$$C^j_{EQ\,i,k} = S^j_{i,k} X^j_{i,k} \quad (8)$$

The solubility of bubble-gas in seawater depends on the total pressure inside the bubble, the temperature, and salinity of the surrounding seawater and is specific for each gas species. The pressure inside a gas bubble is affected by the hydrostatic ($P_H(z) = \int_z^0 \rho_{SW} \times g\, dz$) and atmospheric ($P_{ATM}$) pressures as well as the pressure induced by surface tension on the bubble interface (P_{ST_k}). The total pressure inside the bubble $P_{Bb_{i,k}} = P_{H_i} + P_{ATM} + P_{ST_k}$, where $P_{ST_k} = 2\sigma / r_{E\,k}$, r_E is the equivalent bubble radius and σ is the surface tension, taken as tension between air and water. M2PG1 uses the latest parameterizations of solubilities of the included gas species (Table SI.1) that is currently available in the literature.

Gas transfer velocity

According to equation 5, the gas transfer across the bubble interface depends on the transfer velocity, k_T. Jähne et al. (1987) showed that k_T depends on the diffusion coefficient, the Schmidt number, the local small-scale turbulence, the temperature and on surfactants potentially present on the bubble rim. Numerical simulations and empirical observations have been performed, but no observation of gas transfer rates has been conducted in the deep sea and so parameterizations of k_T in natural aquatic environments are not found in the literature. Consequently, M2PG1 allows for a number of TVMs that the user can choose from, similarly to the choice of BRSM. Presently, M2PG1 includes the transfer velocity parameterization of Zheng and Yapa, (2002) for clean bubbles (TVM no. 1), parameterizations for semi-clean (TVM no. 2) and surfactant-covered (TVM no. 3) bubbles (McGinnis et al., 2006). The transfer velocity is strongly dependent on the gas diffusivity for which we rely on parameterizations listed in Table SI.1. The reference case uses the clean bubble parameterization because it produces profiles similar to observations, whereas the two other parameterizations retain gases inside the bubbles for too long. In other environmental settings, for example, where bubbles escape from oily sediments, it may be appropriate to use a TVM based on observations of surfactant-covered bubbles.

Surface areas of non-spherical bubbles

Mass transfer across the bubble rims critically depends on the surface area of bubbles (equation 5) and earlier bubble models (Leifer and Patro, 2002; McGinnis et al., 2006) assumed spherical bubbles. However, it is known that larger bubbles (transition around 1 mm radius) most often have oblate-like shapes (e.g. Rehder et al., 2002; Leblond et al., 2014). M2PG1 includes two parameterizations of bubble flatness, $f \equiv a/b$, where *a* and *b* are the semi major and semi minor axis respectively (Figure 2

b). The first parameterization follows Leblond et al., (2014) who suggest that bubble flatness is a function of the semi-major axis length and found a logarithmic relation by regression: $f = 0.45 + 1.4 \times ln(a)$, with a in mm. This flatness parameterization is valid for $a > 1.48$ mm and smaller bubbles are assumed spherical (blue solid line in Figure 3 a). We introduce a linear flatness parametrization: $f = 1 + 0.3064a$ (blue dashed line in Figure 3 a) incorporating bubbles of small to large sizes. The surface area of an oblate spheroid, $A_{BS} = 2\pi a^2 + \frac{2\pi b^2}{\epsilon} \times \tanh^{-1} \epsilon$, where the eccentricity $\epsilon = \sqrt{1 - \frac{b^2}{a^2}}$ (Al Zaitone, 2018).

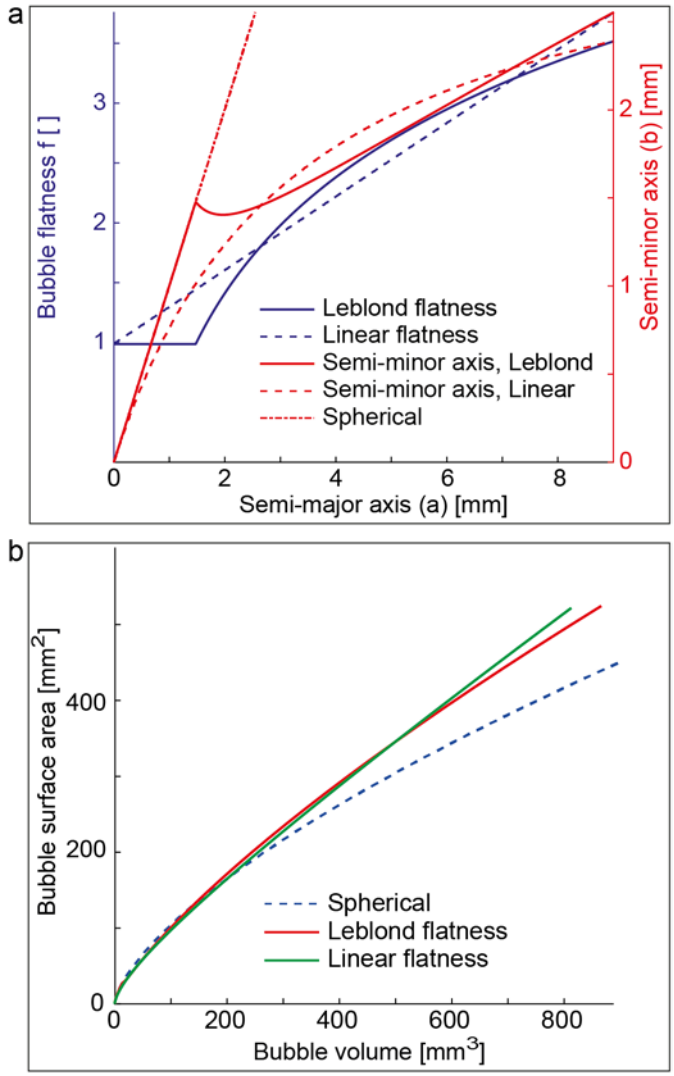

Figure 3 Three parameterizations of bubble shapes. a) The solid blue line indicates flatness as predicted by Leblond et al. (2014), dashed blue line represent the linear flatness. Red lines show the resulting semi-minor axis as functions of semi-major axis for the case of spherical (dot-line), linear flatness (dashed, this study) and Leblond flatness (solid). b) Surface area vs bubble volume as

calculated for the case of spherical bubbles (dashed blue), linear flatness (green, this study) and flatness according to Leblond (red).

The BSD is given as equivalent bubble radius, $r_E = \sqrt[3]{a^2 \times b}$ (Sam et al., 1996), requiring that M2PG1 solves for the semi-major and semi-minor axes during simulation start-up depending on the shape parameterization chosen by the user. The surface area of a flat bubble, relative to bubble volume, is larger than the surface area of a spherical bubble of the same volume (Figure 3 b).

Bubble shrinkage and expansion

Two processes affect bubble volumes simultaneously as bubbles rise through the water column: a) Gas invades or escapes bubbles depending on the dissolved gas concentrations and gas composition in the bubble. Dissolution and exsolution can occur simultaneously if the concentration of one or several gas species is supersaturated with respect to the free gas inside the bubble and another gas species is under-saturated. The bubble volume changes at rates matching the gas transfer of all gas species across the bubble rim, as indicated with black arrows in Figure 1 and Figure 2. This is quantified by $\frac{dV_D}{dt} = \sum_{j=1}^{NGAS} \frac{dn_{D_j}}{dt} \times V_{M_j}$, where $V_{\mathrm{M}}$is the molar volume of the specific gas, calculated from ambient pressure and temperature, compliant with non-ideal gas behaviour and given by the parameterizations referenced in Table SI.1; b) Rising bubbles experience pressure- and temperature change and the volume changes according to $\frac{\mathrm{dV_{PT}}}{\mathrm{dt}} = \sum_{j=1}^{NGAS} \frac{w_b\ \mathrm{n^j}}{\delta z} \times \Delta V_{\mathrm{M}}^{j}$. The total temporal volumetric rate of change of rising bubbles can be written for each bubble size at each depth:

$$\frac{dV}{dt} = \frac{dV_D}{dt} + \frac{dV_{PT}}{dt} \tag{9}$$

Discretizing this process, M2PG1 moves bubble gas between bubble sizes. When bubbles shrink (dV/dt<0), the gas content of species *j* in bubble size *k-1* increases and the content in bubble size *k* will decrease with the same amount as seen in equation 10, where $\Delta \mathrm{V_B}$is the volumetric difference between bubble sizes and *X* is the molar fraction of a particular gas species.

$$\frac{dn_{k-1}^{j}}{dt} = \frac{\frac{\mathrm{dV}}{\mathrm{dt}}}{\Delta \mathrm{V_B}} \times \frac{V_k \times X^j}{\mathrm{V_M^j}}$$
$$\frac{dn_{j,k}}{dt} = -\frac{\frac{\mathrm{dV}}{\mathrm{dt}}}{\Delta \mathrm{V_B}} \times \frac{V_k \times X^j}{V_M^j} \tag{10}$$

When bubbles grow, gas moves from size *k* to size *k+1* in a similar manner. When the largest bubbles (*k*=NSBIN) are predicted to grow and smallest bubbles (*k*=1) are predicted to shrink, the gas is retained in the present bin.

Aerobic oxidation of CH4

Aerobic oxidation of CH_4 in the water column, a biogeochemical process explicated by the chemical reaction $CH_4 + O_2 \implies CO_2 + H_2O$ implies a direct mathematical coupling between dissolved CH_4,

dissolved O_2, and CO_2. The oxidation process occurs at rates $\frac{\partial[CH_4]}{\partial t} = -k_{MOx}[CH_4]$ where k_{MOx} is the oxidation rate constant (time^{-1}) and $[CH_4]$ is the CH_4 concentration (e.g. Graves et al., 2015). Stoichiometry depicts a 1:1:1 relation between the three gas species, yielding removal rates of oxygen and production rates of carbon dioxide equal to oxidation rates of CH_4. k_{MOx} reported in the literature is typically between <0.001 and 0.7 d^{-1} (Angelis and Scranton, 1993; Valentine et al., 2001; Mau et al., 2017). The reference simulation uses a value of 0.01 d^{-1}, which is the average constant calculated by Graves et al., (2015) at the site of our case study.

Turbulent vertical mixing

Dissolved gas in seawater, as well as heat content and salinity, are subject to vertical mixing by turbulent diffusion (e.g. Thorpe, 2007). The rate of change of the state variable (temperature, salinity, gas, or other) due to vertical diffusion is $\frac{\partial}{\partial z}\left(\Gamma\frac{\partial \phi}{\partial z}\right)$, where Γ is the vertical mixing coefficient, which can vary over several orders of magnitude. PROBE has the capability to either use a constant coefficient or calculate the coefficient according to turbulence closure schemes. Here, we apply a constant coefficient in order to isolate the effect of vertical turbulent mixing and we assume that this constant is the same for all gas species.

Atmospheric interaction

Free gas can escape to the atmosphere if bubbles reach the sea surface as seen in Figure 1. For this process, we simply assume that all bubbles reaching the surface z(N) immediately escape to the atmosphere. The flow of free gas of species j to the atmosphere is, therefore, $Q_{AB\,j} = \sum_{k=1}^{NSBIN} n_{N,k}^{j} / \Delta t$, where Δt is the time-step of the model simulation.

Furthermore, dissolved gases in the water column will equilibrate with the atmosphere. The flow rate to the atmosphere is calculated according to Wanninkhof (2014):

$Q_{AEQ}^{j} = A \times k_A^j \times (C_{N-1}^j - Ca^j)$, where $k_A^j(cm\ h^{-1}) = 0.251 \times U^2 \times \left(\frac{Sc^j}{660}\right)^{-\frac{1}{2}}$, and *Sc* is the temperature dependent Schmidt number, calculated for the different gas species according to Wanninkhof, (1992); (2014) and *U* is the wind speed (m s^{-1}) at 10 meters above the sea surface. Positive rates indicate gas flow to the atmosphere.

User-specified simulation details

Environmental conditions controlling the evolution of free and dissolved gas are defined, and bubble shape parameterization, BRSM and TVM are chosen by the user together with horizontal domain area, time-step, interval for model output (detailed in Table SI.4), bubble size distribution (BSD) (Example in Table SI.5), composition of gas contained in emitted bubbles (Table SI.6), free gas flow rate and k_{MOx}. The user can choose between constant or transient mixing coefficients (applied or calculated by the model). Transient oceanic and atmospheric boundary conditions can be used to force the model. All settings are supplied by the user in an initialization file, as detailed in Table SI.7.

Assessment

Budget analysis and numerical precision

The numerical precision of M2PG1 was assessed by simulating a continuous release of 0.1 mol CH_4 s^{-1} emitted at 80 meters water depth as bubbles with 3 mm initial equivalent bubble radii (linearly flat bubbles were assumed). The residual (*res*) was defined as the initial dissolved gas content plus the sources and sinks minus the integrated current free and dissolved gas content (equation 11). A smaller residual means better numerical precision.

$$res(t) = \overbrace{\sum_{i=1}^{N}([CH_4] \times \rho_W \times \delta z \times A)}^{t=0} + \sum_{t_m}^{t_m+\Delta t}\left[\left(Q_{EF} - Q_{AF} - Q_{AEQ} - \sum_{1}^{Nz} Mox\right) \times \delta t\right] - \overbrace{\sum_{i=1}^{N}\sum_{k=1}^{NSBIN} n_{i,k}}^{t} - \overbrace{\sum_{i=1}^{N}([CH_4] \times \rho_W \times \delta_z \times A)}^{t} \quad (11)$$

Here, $\overbrace{\sum_{i=1}^{N}([CH_4] \times \rho_W \times \delta z \times A)}^{t=0}$ represents the initial (t=0) content of dissolved CH_4 and $\overbrace{\sum_{i=1}^{N}([CH_4] \times \rho_W \times \delta_z \times A)}^{t}$ is the content at the time of the model output (every 10 minutes). The term $\sum_{t_m}^{t_m+\Delta t}\left[\left(Q_{EF} - Q_{AF} - Q_{AEQ} - \sum_{i=1}^{N} Mox\,(i)\right) \times \delta t\right]$ represents the sources and sinks at the vertical boundaries and a local sink due to oxidation. These quantities are accumulated over time, written to result-files and reset at time intervals of 10 minutes (Δt=600 s) ($t_m$represents the time of the model output). The model time-step δt=1/16 s. Q_{EF} is the free gas emission to the water columns, emitted at 80 meters water depth for the budget analysis in order to observe both free gas bubbles escaping to the atmosphere and equilibration at the sea surface. Q_{AF} is the free gas emitted into the atmosphere, Q_{AEQ} is the dissolved gas escaping to the atmosphere by means of equilibration, and *MOx* is the CH4 removal by aerobic oxidation. The double summation $\overbrace{\sum_{i=1}^{N}\sum_{k=1}^{NSBIN} n}^{t}$ represents the free

gas CH_4 present at the current time where *n* represents the free gas molar content in bin *i*, *k*. *N* is the number of vertical grid cells, and NSBIN is the number of bubble sizes. The residual was less than 1‰ of the total CH_4 gas content as seen in Figure 4. Thus, the numerical accuracy was better than 99.9% for the test simulation.

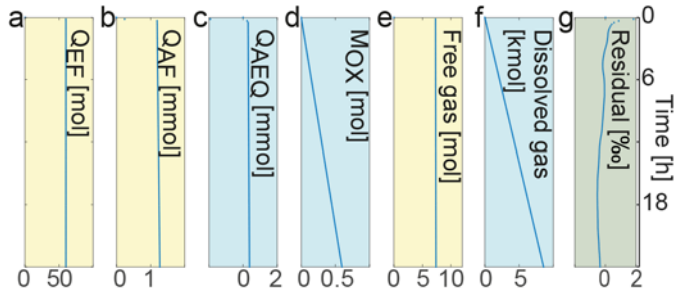

Figure 4. CH_4 budget calculated from the model output and numerical error during simulation. a) Free gas CH_4 emitted from the seafloor, accumulated over the period between model outputs. b) Escape of bubble-mediated CH_4 to the atmosphere accumulated the same way. c) Accumulated dissolved CH_4 equilibration with the atmosphere. d) Accumulated aerobic oxidation of CH_4. e) Total free gas CH_4 content. f) Total dissolved CH_4 content. g) Residual (equation 11) divided by the total CH_4 content in the free and dissolved phase.

Model sensitivity

The model sensitivity was analysed with 53 simulations which were run to steady state, here identified when the relative integrated content difference between time-steps was less than 10^{-6}. The sensitivity analysis was performed by evaluating 1) bubble property parameterizations, 2) environmental influence on the result. Analysis of different parametrizations and environmental conditions were further divided into subgroups consisting of a number of simulations as indicated in Table 1 and detailed in the supplementary information, Table SI.8. The reference case (M2PG1 0.0) uses BRSM no. 7, TVM no. 1, linearly flat bubbles and vertically homogenous dissolved gas profiles at equilibrium with the atmosphere assuming atmospheric mixing ratios of 79% N_2, 20% O_2, 0.97% Ar, 399 ppm CO_2, and 1830 ppb CH_4, where ratios for CO_2 and CH_4 were obtained from the annual global average in 2015 (Ed Dlugokencky, NOAA/ESRL, www.esrl.noaa.gov/gmd/ccgg). It further uses a single bubble size distribution of 3 mm, which is the peak radius of the BSD observed by Veloso et al., (2015); a temperature of 4°C and a salinity of 35 PSU, which was observed near the seafloor during a cruise to the study area as described in the section *Case study*; a flow rate of 0.05 mol s^{-1}, equivalent to the mean flow rate of observed bubble streams during the same cruise; an oxidation rate constant of 0.01 d^{-1}, which is the mean oxidation rate constant determined by Graves et al., (2015) in the same area; a water current of 15 cm s^{-1} as determined from the typical inclination of bubble streams; a vertical mixing coefficient of 0.001 m^2s^{-1}, was applied, which is high compared with sparse literature data from the area (Randelhoff et al., 2015), but in the low range of oceanic values (Wunsch and Ferrari, 2004).

Table 1. Overview of simulations included in the sensitivity analysis.

	Subgroup	Target	Unit	Case settings
Bubble property parameterizations	1	Bubble rising speed	[Model no.]	1, 2, 3, 4, 5, 6, 7*, 8, 9
	2	Bubble shapes	[Model]	Spherical, Leblond, Linear*
	3	Transfer velocity	[Model no.]	1*, 2, 3
Environmental settings	4	Dissolved gas profiles	[µmol kg^{-1}]	Atmospheric equilibrium*, Half O_2, 1/100 O_2, No Argon, Double CO_2, No N_2, Double N_2, Tenfold N_2
	5	Bubble size distribution**	[mm]	1, 2, 3*, 4, 6, 8
	6	Temperature	[°C]	0^1, 1^1, 2^1, 3^1, 4*, 6, 8, 10, 20
	7	Salinity	[PSU]	0, 20, 35*, 40
	8	Flow rate	[mol s^{-1}]	0.025, 0.05*, 0.1, 0.2
	9	Oxidation rate constant	[d^{-1}]	0, 0.01*, 0.1, 1, 10
	10	Water current	[m s^{-1}]	0.025, 0.05, 0.1, 0.15*, 0.2, 0.5
	11	Mixing coefficient	[m^2 s^{-1}]	0.0001, 0.001*, 0.01, 1, 100, 10000

* Used in reference case; ** Single initial bubble radius; [1] Within CH_4-HSZ

Sensitivity to bubble property parameterizations

The sensitivity analysis of the bubble property parameterizations included simulations targeting bubble rising speeds and transfer velocities (Figure 5), and a separate analysis of shape parameterizations. We compared the CH_4 profiles resulting from nine BRSMs (SI.2, Table SI.3, and Figure SI.1). The existence of surfactants on the bubble rim and its effect on the rising speed is beyond the scope of this study, and the resulting profiles do not clearly discriminate between clean and surfactant-covered BRSMs. The transfer velocity parametrizations are coupled to the rising speed of bubbles, which implies that the analysis of BRSMs and TVMs are linked. For that reason, the effect of the choice of BRSMs remains unclear. However, studies suggest that bubbles observed in natural conditions behave as surfactant covered, justifying a reference case based on a surfactant BRSM. On

the other hand, TVMs based on surfactant-covered bubbles yield unrealistic profiles and we therefore chose a clean bubble TVM for the reference case.

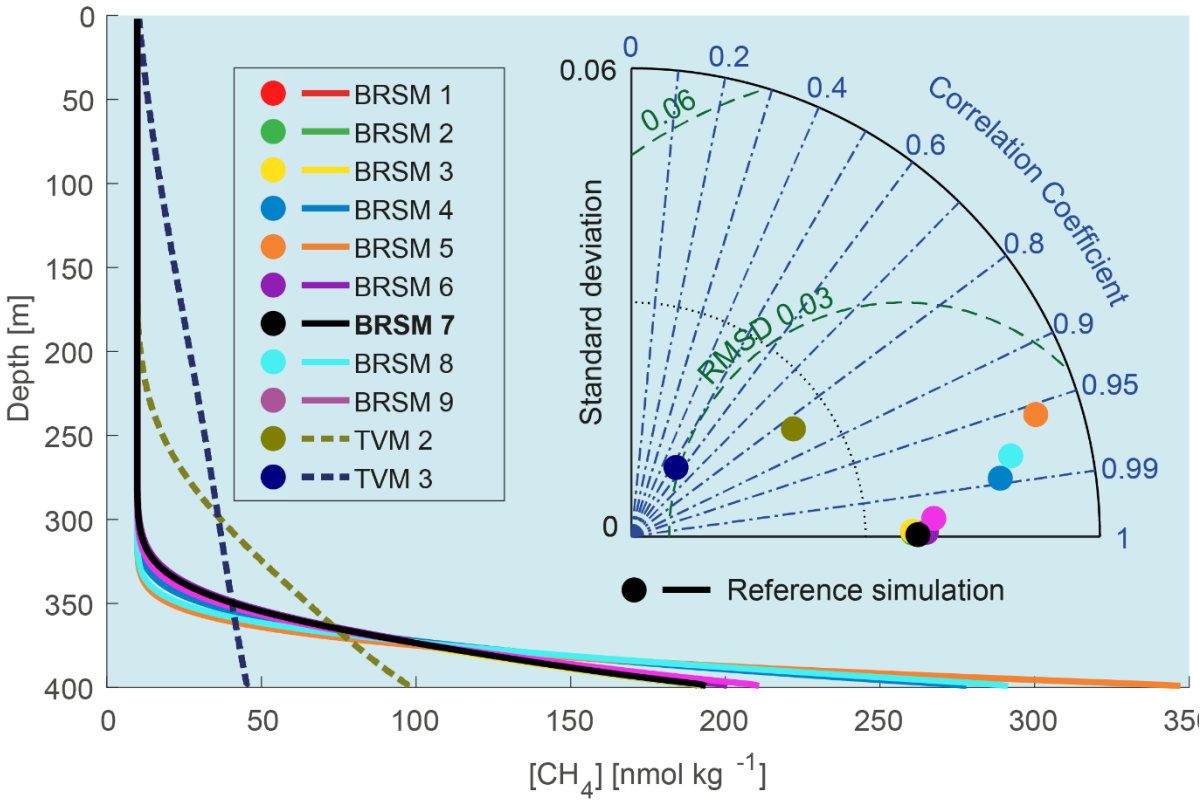

Figure 5. Simulation results targeting BRSMs (solid lines) and TVMs (dashed lines). The main graph shows dissolved CH_4 concentration profiles in the water column after simulations reached steady state. Dots in the Taylor diagram (Taylor, 2001) indicate standard deviation, correlation coefficients, and root mean square differences (RMSD) compared to the reference simulation (black line and dot) and are colour-coordinated with the profiles. The profile resulting from BRSM no. 3 was identical to the reference and is therefore hidden. The nine BRSM simulations use TVM no. 1 and the TVM simulations use BRSM no. 7.

We define the modelled flare height (equivalent to the acoustic signatures of free gas in the water column) as the height where less than a threshold fraction of the emitted gas remains. Here we consider a 10% threshold and hereafter refer to the corresponding 10% flare height. The height of the modelled flares and consequently the vertical distribution of dissolved CH_4 in the water column are affected by the choice of BRSM. Simulations show that the 10% flare height is 41% higher when BRSM no. 9 is chosen compared to when BRSM no. 5 is applied, i.e. 51.6 vs 36.6 m (Table SI.7), despite the fact that both models consider surfactant covered bubbles. The 10% flare heights in the BRSM subgroup were 49.5 ± 6.4 m and the concentration close to the seafloor in the present subgroup was 0.24 ±0.06 µmol kg^{-1}, highlighting the importance of the choice of BRSM in the prediction of the vertical distribution of CH_4 in the water column.

Simulations using TVM for both semi-clean (TVM no. 2) and surfactant (TVM no. 3) yielded strikingly different profiles compared to the reference case (TVM no. 1). Our simulations showed that bubbles rose more than twice as high compared to the reference case with a TVM based on

intermediately surfactant-covered bubble rims. The 10% flare height of TVM no. 2 was 135.8 m compared to 54.6 m for the reference case (TVM no. 1). The surfactant based TVM (no. 3) caused bubbles to reach the surface even from 400 m water depth, which has not been observed in seep sites outside the HSZ.

The importance of the bubble flatness parameterizations was investigated using a bubble size distribution describing single size initial bubbles of 6 mm equivalent bubble radius and otherwise default settings. One case was based on the linear flatness as previously described, which is also used in our reference case; a second case used the flatness parametrization suggested by Leblond et al., (2014), and the third case assumed spherical bubbles. These simulations showed that the 10% flare height was 21% higher when spherical bubbles were applied compared to the two flat bubble parameterizations, which showed similar results (Figure 6). The dissolved CH_4 concentration profiles from these special cases had smaller gradients and the maximum concentration (close to the seafloor) was 23% lower when spherical bubbles were assumed. For 3 mm equivalent radius bubbles, the 10% flare height resulting from the spherical bubble assumption was 5% lower than the flare height of flat bubbles (Table SI.8). The simple linear flatness parameterization produced similar results to the parameterization of Leblond while avoiding the sharp flatness transition at semi-major axis at 1.48 mm and is therefore recommended (Figure 3 a).

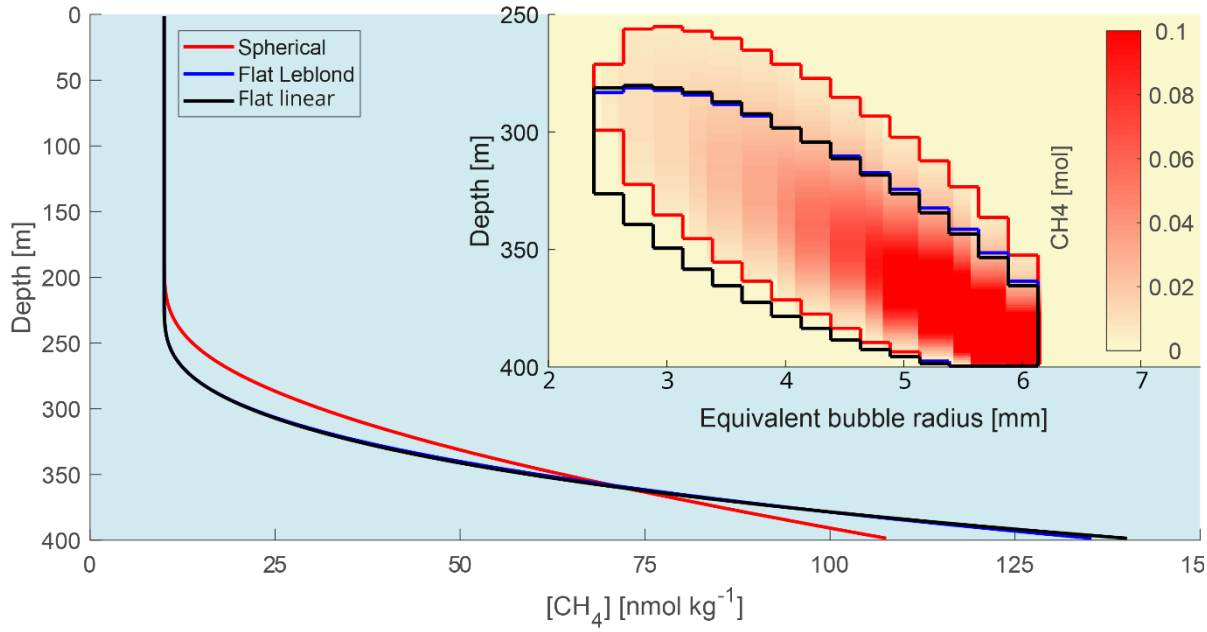

Figure 6. Modelled influence of flat bubble parameterizations. The main graph shows the steady-state profiles of dissolved CH_4 concentrations using 6 mm initial equivalent bubble radius. The red line represents the simulation with spherical bubbles. Black and blue lines show results from linear and Leblond flatness parameterizations respectively. The inset diagram shows free CH_4 gas content at steady state for the three simulations. Red colour scale and bounding polygon indicate the spherical case while black and blue polygons represent Leblond and M2PG1 parameterizations. Polygon boundaries were calculated from a 1-mmol free gas content threshold.

Model sensitivity to environmental conditions

We performed 41 simulations including the reference case with varying settings in order to evaluate the relative importance of environmental conditions (Table 1, subgroups 4 – 11) on the resulting vertical profile of dissolved CH_4. Figure 7 shows an overview of the importance of the environmental parameters. The simulation results obtained from different conditions are summarized in Table SI.8 and the results are evaluated separately in the following sections. Definitions of the correlation coefficient, root mean square difference, and standard deviations are provided in table SI.8.

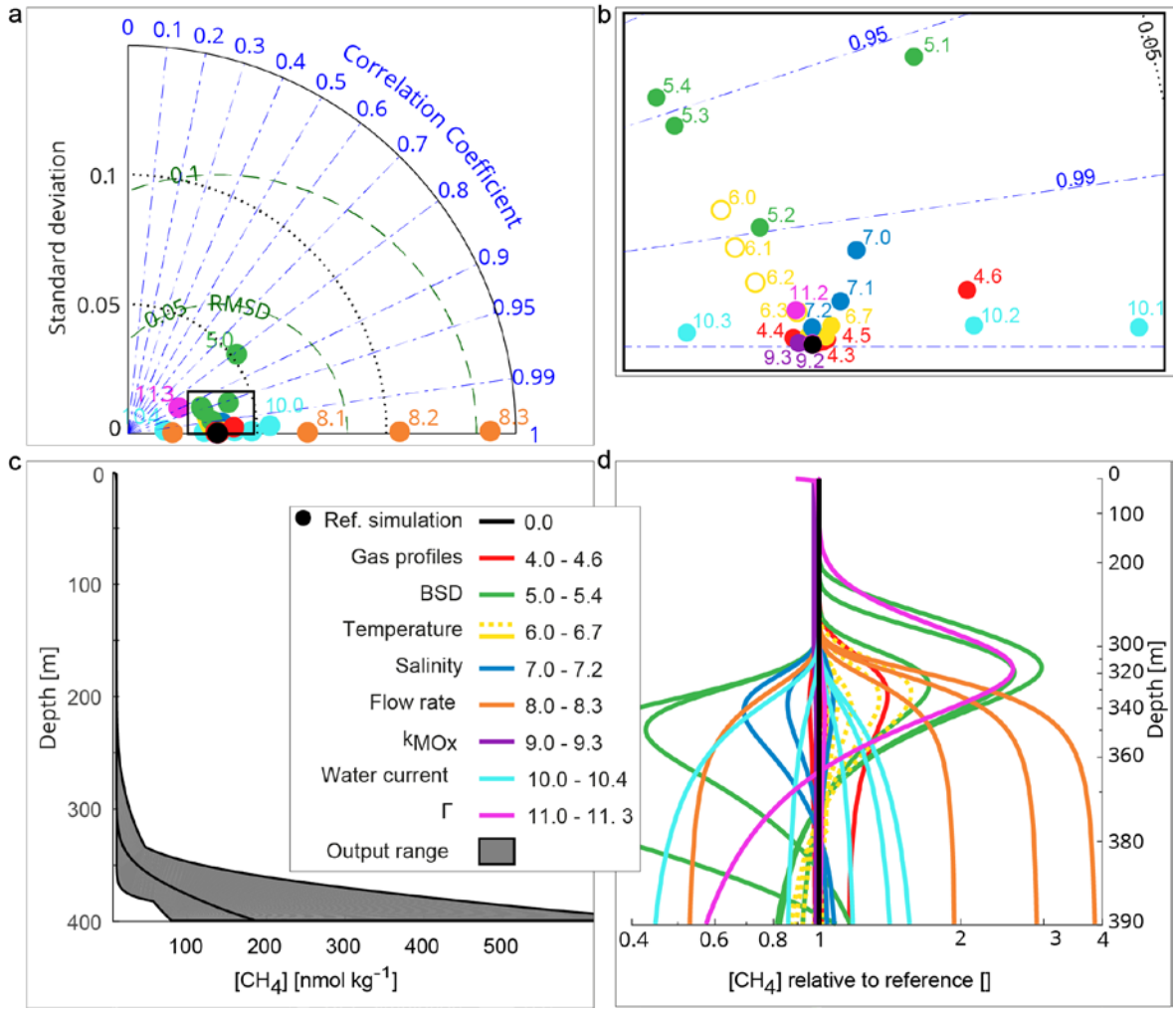

Figure 7. Modelled CH_4 profiles and statistics. a) Taylor diagram showing the standard deviation, root mean square difference (RMSD) and correlation coefficient of simulations compared to the reference case, shown in black. Red dots: varying dissolved gas profiles, green dots: varying BSD, yellow dots: varying temperature, blue dots: varying salinity, orange dots: varying flow rates, purple dots: varying oxidation rate, light blue dots: varying water current and pink dots: varying vertical mixing. b) Zoom of the black rectangle in panel a, with the same colour-coding. c) Dissolved gas vertical profiles after simulations reached steady state. Grey area shows the span of the model output for all simulations with varying environmental aspects. The reference simulation is shown as a black line. d) Steady-state profiles following the same colour coding, normalized by the reference case profile and plotted on a logarithmic depth axis. Dashed (yellow) lines indicate simulations partly within the CH_4-HSZ (see Table SI.8 for details). Simulations 11.0 and 11.1 are not seen here because they coincide with the reference simulation. Note the different depth scales of panel c and d for a more detailed visualization.

Dissolved gas profiles.

We ran seven simulations using different gas profiles (simulations 4.0 – 6; table 1 and SI.8 for details; red dots and lines in Figure 7). Small deviations from the reference case simulation result from changing the ambient dissolved gas profiles. Neither removing the Argon gas, accounting for approximately 1% of the atmospheric gas composition nor reducing the oxygen concentration by 99% changed the rise height of the CH_4 plume. An improbable tenfold increase in N_2 increased the 10% flare height by 13 meters. Simulations suggest that the initial and boundary dissolved gas concentrations within plausible ranges do not significantly influence the rise height of free gas in environments where the water mass is well ventilated like in all our cases.

Bubble size distribution

An important feature of M2PG1 is its capability to simulate bubbles with a range of bubbles sizes, which is typically observed in natural seep systems. However, in order to isolate the effect of different bubble sizes, it was necessary to simplify the size distribution and simulate the release of bubbles, of initially one size. Five single-size bubble simulations were performed (simulations 5.0 - 4; 1, 2, 4, 6, 8 mm equivalent bubble radii; green dots and lines in Figure 7) which showed that the size of bubbles escaping from the seafloor strongly affects the vertical distribution of dissolved CH_4. Compared to 3 mm bubbles (our reference), the 10% CH_4 plume was lower by 57% when 1 mm bubbles were assumed and was higher by 87% when an 8 mm equivalent bubble radius was applied. Small bubbles have the capacity to increase the near-seafloor concentration because they dissolve quickly and rise slowly. – For example, 1 mm bubbles increased the bottom water concentration by 230% compared to 3 mm bubbles.

Temperature

Simulations using eight vertically homogenous temperature profiles (simulations 6.0 – 7; 0 – 3, 6, 8, 10, 20°C) are shown as yellow dots and lines in Figure 7. Bubbles within the HSZ become covered with hydrate skins (e.g. Sauter et al., 2006), but the growth rate of hydrates on bubble rims and their influence on the gas transfer velocity and rising speed are largely unknown and therefore not implemented in this version of M2PG1. Simulations 6.0 – 6.3 with temperatures, $T \in [0, 1, 2, 3]$ °C, are partly within the HSZ and therefore unreliable. To isolate the temperature effect on bubble dynamics, we performed an additional 18 simulations (not shown in Table 1 or SI.8) with the release of CH_4 bubbles from 100 and 200 m water depths, where CH_4 hydrates are unstable at all temperatures. We observe a weak trend towards higher plume heights with higher temperatures (Figure 8), to which we attribute the lower solubility associated with warmer water.

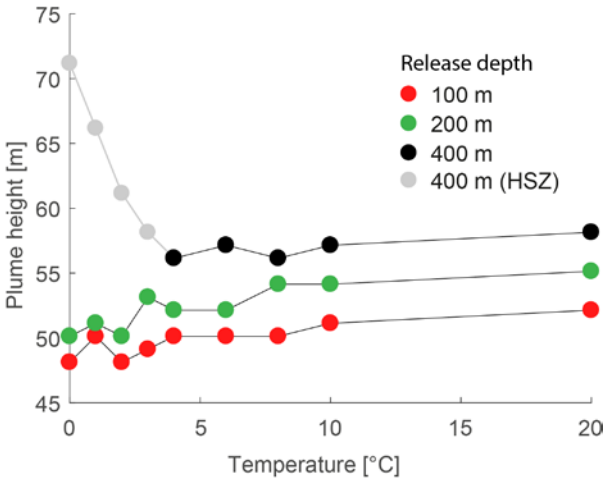

Figure 8. Temperature-dependent dissolved CH_4 plume heights. Plume heights are calculated as the height where the concentration anomaly is less than 10% of the maximum anomaly. Red, green, and black dots represent plume heights from bubbles released at 100, 200, and 400 m respectively. Grey dots indicate that the bubbles are partly within the CH_4-HSZ and therefore represent unrealistic results.

Salinity

Simulations using three different vertically homogenous salinity profiles (simulations 7.0 – 2; 0, 20, 40 PSU) confirm that high salinity causes gas to rise higher. The 40 PSU salinity causes the CH_4 plume to reach 12% higher compared to the 20 PSU case and 21% higher compared to the fresh-water case. This is explained by the lower solubility of CH_4 caused by salts in the water. The plume height difference between the 35 PSU case and the fresh-water case was 12 meters (14%).

Flow rate

Any change in flow rate (simulations 8.0 – 3; 0.025, 0.1, 0.15, 0.2 mol s^{-1}) simply results in an absolute concentration shift. The shape of the dissolved CH_4 profiles (orange dots and lines in Figure 7) did not change due to changed flow rates. This stems from the fact that the modelling approach does not consider bubble-bubble interaction or upwelling flow caused by bubbles.

Aerobic CH4 oxidation rate constant

Five different simulations, using different values of the oxidation rate constant, k_{MOx} (simulations 9.0 - 3; 0, 0.01, 0.1, 1, 10 d^{-1}), yield profiles with a near-perfect match. This implies that aerobic oxidation of CH_4 is negligible on time scales given by relatively strong water currents and small domain sizes: in the simulations, we consider a domain of 1800 m^2, equal to the echosounder beam area of 25 m radius and a default water current of 15 cm s^{-1}, yielding a residence time of 5 minutes, which for $k_{MOx} = 1\ d^{-1}$ would remove less than 5 ‰ of the present.

Water currents

Five simulations addressing the effect of advection through ocean currents (simulations 10.0 – 4; 0.025, 0.05, 0.1, 0.2, 0.5 m s^{-1}; cyan dots in Figure 7) were performed. The profiles of all state variables at the lateral boundary were vertically homogenous throughout our sensitivity simulations and the inflow of dissolved gas nudged the concentration profiles toward the boundary level. Therefore, profiles resulting from strong currents were more similar to the boundary profiles. Specifically, CH_4 profiles displayed smaller gradients and lower concentrations for cases with stronger currents. Plume heights were higher for stronger water currents but not higher by absolute concentrations (Table SI.8). This is consistent with the fact that the ambient concentrations did not affect the bubble rise heights significantly.

Vertical mixing

Wunsch and Ferrari, (2004) reported on oceanic vertical diffusion coefficients ranging from 3×10^{-4} – 500×10^{-4} $m^2\ s^{-1}$. A plausible low eddy diffusion coefficient (simulation 11.0; 10^{-4} $m^2\ s^{-1}$) did not influence the vertical distribution of dissolved CH_4 and neither did a high coefficient (simulation 11.1; 1 $m^2\ s^{-1}$). A mixing coefficient of 100 $m^2\ s^{-1}$, represented by the pink dot (11.2) and hardly visible pink line in Figure 7, only slightly changed the profile. The vertical profile was noticeably altered by the high-end mixing coefficient (simulation 11.3; 10^4 $m^2 s^{-1}$) but such strong vertical mixing is not observed in the ocean. The vertical mixing of dissolved gas is thus negligible in environments where ocean currents carry the dissolved methane away from the source. The fate of seeped methane is only marginally dependent on vertical mixing even away from the source area (Graves et al., 2015) unless turbulence is particularly enhanced.

Case study

We performed a three-day ship-based survey at a known CH_4 seepage site (e.g. Westbrook et al., 2008; Sahling et al., 2014) on the continental slope west of Svalbard in October 2015 (Figure 9 a), where we acquired continuous echosounder data (EK60 operated at 18 and 38 kHz). Flares were inferred from the echosounder data and were observed to rise up to 50 – 150 meters above the seafloor. We performed three Conductivity-Temperature-Depth (CTD) hydrocasts including discrete

water samples in the close vicinity of gas flares (see Figure 9a for locations). Water samples were analysed for dissolved CH_4 concentrations following the headspace gas chromatography method described by Magen et al., (2014). A continuous exponential function was fitted to the discrete CH_4 concentration data and was subsequently used for comparison with model simulations (Figure 9 e).

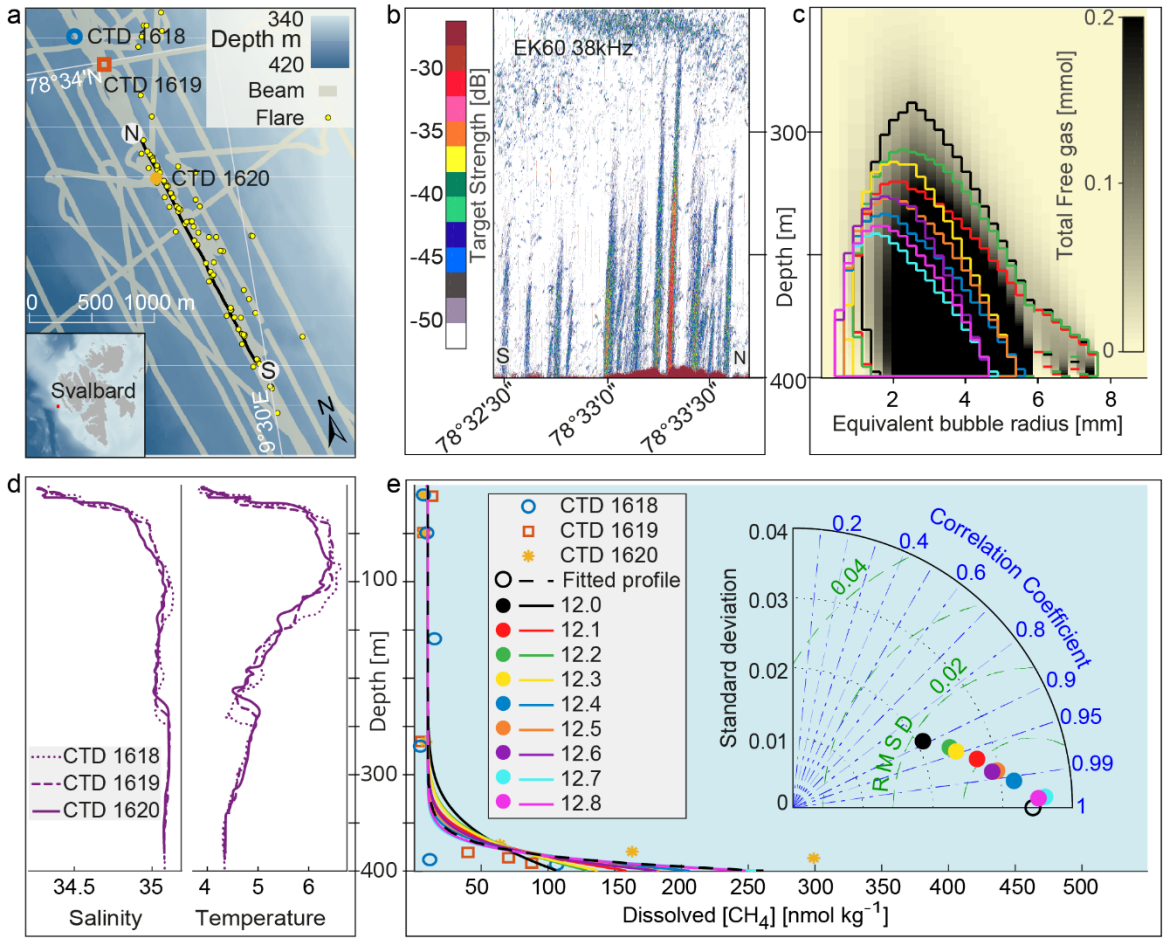

Figure 9. Case study compared to model simulations. a) Map of the case study area showing identified flares (yellow dots), echosounder beam coverage (grey lines), the transect shown in panel b (black line delimited by labels S and N) and CTD cast locations (blue ring (CTD 1618), red square (CTD 1619), and orange star (CTD 1620), referred to in panel d and e). b) Echosounder data acquired from the ship mounted EK60 operated at 38 kHz on October 22, following the track from S to N in panel a. Colours indicate the target strength (dB) – an indicator for the quantity of free gas (bubbles) in the water. c) Grey to black shades indicates the modelled content of free gas (all species) at steady state of simulation 12.0 and its distribution in bubble size- and depth bins. Coloured contour lines indicate the limit where the free gas exceeds 0.05 mmol. Contours for model simulations are colour coded accordingly with the legend in panel e. d) Salinity and temperature profiles of performed CTD casts. e) Discrete CH_4 concentrations acquired from CTD casts and subsequent Gas Chromatograph measurements shown with symbols matching panel a. A continuous dissolved CH_4 profile function, fitted to the discrete data is shown as a dashed black line. Steady state model output profiles are shown as lines with the same colour coding as panel c. Inset Taylor diagram summarizes the correlation coefficient, standard deviation, and root mean square difference between the fitted profile and the model simulations (equations in Table SI.7). Dots in the Taylor diagram are colour coded accordingly with the legend.

We performed nine simulations using the temperature- and salinity data from the three CTD casts (Figure 9 d). For simulations 12.0 – 12.2 we used a Gaussian-like BSD peaking at 3mm equivalent bubble radius which was observed in the area in 2011 and 2012 (Veloso et al., 2015). Simulations 12.3 – 12.5 were set up with smaller bubbles (peak radius of 2 mm) and 12.6 – 12.7 were set up with 1 mm peak radius. The water current was estimated to 18.5 cm s^{-1} based on the inclination of flare spines calculated with the FlareHunter software (Veloso et al., 2015). BRSM no. 7 was used in simulations 12.0, 12.3 and 12.6; BRSM no. 5 was used in 12.1, 12.4, and 12.7; no. 8 was used 12.2, 12.5, and 12.8.

The observed acoustic flare heights (Figure 9 b) were well reproduced by the nine M2PG1 simulations (Figure 9 c and Table SI.7). The simulated rise heights of gas bubbles obtained with the 3 mm peak radius BSD almost matched the highest observed flares while the bubble rise heights obtained from simulations 12.3 – 12.7 (Gaussian BSDs with 2 and 1 mm peak radii) matched the height of the lower flares (Figure 9 b and Figure 9 c). Simulated dissolved CH_4 profiles correlated well ($r>0.9$) with the fitted function and the root mean square difference (RMSD) was less than 0.02 µmol kg^{-1}. The simulations using 3 mm peak radius bubbles show that the modelled dissolved CH_4 concentrations near the seafloor were lower than the concentrations of the fitted curve, but above approximately 15 meters, the simulated concentrations were higher (Figure 9 e). The small bubble simulations (12.7 and 12.8) produced dissolved methane profiles almost identical with the fitted function based on observations. We calculated TS values according to equations 1 – 9 Veloso (2015) by integrating the backscatter area of the simulated bubbles at steady state and we defined TS heights as the height where the simulated TS dropped below -55 dB (Value used for discriminating between gas and water). The resulting heights were 60 – 102 meters above the seafloor for the included cases and were 158 – 183 m for additional simulations using 5 – 8 mm Gaussian BSDs.

Discussion and conclusion

We developed a marine two-phase numerical model in one dimension (M2PG1) that simulates the dynamics of free and dissolved gases in the water column. To our knowledge, it is the first model that simulates the two gas phases simultaneously, with multiple bubble sizes comprising multiple gases. M2PG1 considers non-ideal gas behaviour, pressure- temperature- and salinity dependent solubility and diffusivity. M2PG1 resolves direct bubble-mediated gas escape to the atmosphere as well as diffusive flow of dissolved gas through equilibration with the atmosphere. The model also simulates aerobic oxidation, converting CH_4 into carbon dioxide while consuming oxygen. The numerical accuracy of the model was better than 99.9%, which, in spite of the more complex calculations, is comparable with the model developed by Vielstädte et al., (2015). Predicting the fate of bubble gas in the water column requires knowledge of the sizes and gas composition of the bubbles, water currents, initial-, and boundary conditions of salinity, temperature, and dissolved gas species. Moreover, parameterizations of bubble shapes, rising speeds, and transfer velocities must be applied. We performed 12 simulations to estimate the importance of technical model-settings and another 40 simulations to assess the importance of environmental conditions. We also compared a case of CH_4 gas emission from the seafloor west of Svalbard with simulations.

Technical parameters

Bubble shapes are implicitly considered in the rising speed parameterizations but experiments determining the gas transfer velocities have not addressed bubble shapes and the increased bubble surface of non-spherical bubbles. This analysis showed that applying flat bubble parameterizations

reduced the rise height of gas by 22% for 6mm bubbles and by 5% for 3mm bubbles. TVM no. 3, based on surfactant-covered bubbles, increased the flare height so much that bubbles reached the surface even in our 400-meter deep model. Such high bubble streams are not observed in an environment outside the CH_4 hydrate stability field. Clean bubble TVM simulations produced dissolved CH_4 profiles well correlated (r>= 0.90) with CH_4-profiles observed during the CAGE 15-6 cruise. As the other applied TVMs resulted in deviating CH_4 profiles, we suggest that, for future simulations of Arctic seafloor emissions of CH_4 bubbles, a clean bubble TVM should be used.

Environmental parameters

Varying ambient dissolved gas profiles have little effect on the resulting CH_4 profiles. Only an unlikely tenfold increase of Nitrogen noticeably altered the rise-height of CH_4 and neglecting dissolved Argon gas has no effect on the resulting profiles. Consequently, we suggest that M2PG1 users may assume that dissolved gases are initially in equilibrium with the atmosphere. The resulting vertical distribution of dissolved CH_4 is highly dependent on the initial bubble size and plume heights are roughly 60% lower when using small bubbles and 90% higher when large bubbles are assumed. We therefore stress the importance of acquiring an in-situ bubble size distribution High salinity causes bubbles to rise higher due to the lower solubility in saline water but the response in flare height caused by temperature is limited to a few meters. Simulations show that both MOx and vertical mixing within plausible ranges can be neglected in a seepage region with high water velocity. However, MOx and vertical mixing may still be important for the fate of CH_4 away from the sources on ocean basin scales.

Model comparison with observations

M2PG1 reproduced well (r>0.9 and RMSD<0.02 µmol kg^{-1}) the observed dissolved CH_4 profiles acquired during the CAGE 15-6 cruise, using the BSD observed in the area in 2011 and 2012. Ideally, the simulated profile shapes should have a sharper decrease upwards. Such profiles resulted from simulations using smaller initial bubble sizes. Simulated free gas reached heights consistent with most of the flares seen in the echograms acquired during the same research cruise. However, the most prominent flares, reaching over 150 m above the seafloor, were higher than the model simulations (12.0 – 12.8) predicted. This could be attributed to larger bubble sizes or upwelling caused by intense bubble release. We did not observe enough evidence for small-scale upwelling to explain the extra flare height: The buoyancy frequency was only slightly imaginary ($N^2 \in [-0.5 \times 10^{-6}, 0]$) between the seafloor and up to 20 meters above, in stations 1619 and 1620. When a Gaussian BSD peaking at 6 mm was applied, TS values obtained from simulations suggest that flares should be observable up to 167 m above the seafloor, which matches the highest observed flares. As no upwelling due to bubbles has been observed in the area previously (Sahling et al., 2014), we explain the highest flares with bubble sizes larger than the ones previously observed.

Future use and developments

M2PG1 resolves free and dissolved gas dynamics in shallow to moderately deep aquatic environments, and the depth-limitation is currently given by the depth of the pressure-, temperature-, and salinity dependent hydrate stability zones (HSZs). In order to apply the model at deeper sites, including depths within the HSZs, future versions of M2PG1 should include TVMs and BRSMs for hydrate-coated bubbles, and possibly model growth and dissociation of hydrates on bubble skins and the subsequent effect on gas transfer and bubble rising speeds.

The application of M2PG1 targeting methane seepage from the seafloor provides a basis for future incorporation in three-dimensional ocean models, facilitating prediction of 3-dimensional distribution of methane emissions to the atmosphere.
Future versions of M2PG1 could potentially include the carbonate system similarly to Liang et al., (2011), which would allow for direct simulations of local ocean acidification caused by CH_4 seeps. Alternatively, PROBE's capability of coupling ocean basins may be used to quantify ocean acidification from bubble emissions (CO_2 and/or CH_4 bubbles) on ocean basin scales.
In order to predict the vertical distribution of gas at sites where bubble emission is very intense, bubble-driven upwelling could be incorporated, and may be predicted from the number density and drag of buoyant bubbles on the water.
Newly developed acoustic instruments providing broadband signals could facilitate determination of bubble sizes by inverse acoustic modelling of BSD by remote methods. This would greatly simplify the determination of BSDs, which is important for predicting the vertical distribution of CH_4 emitted from the seafloor.

Although the main interest of this study was related to CH_4, a consequence of the coupled gas system is that, once a process-based model is established, it inevitably provides insight to the evolution of all the present gas species, both in their free and dissolved phases. For example, re-distribution of dissolved CO_2 and O_2 due to CH_4 bubbles can be assessed. The effect of bubbles injected to surface waters by wave action and the fate of gas leakage from industrial seafloor installations can be understood from the same process-based model.

Acknowledgements

This work was supported by the Research Council of Norway through its Centres of Excellence funding scheme, project number 223259. We would like to thank the crew on board R/V Helmer Hanssen for the support during the CAGE 15-6 cruise and the cruise leader Jürgen Mienert. A dataset comprising the executable file, simulation settings and results was deposited in the UiT Open Research Data repository https://doi.org/10.18710/LS2KUX

References

Al Zaitone, B. 2018. Evaporation of oblate spheroidal droplets: A theoretical analysis. Chem. Eng. Commun. 205**:** 110-121, doi: 10.1080/00986445.2017.1374949

Angelis, M. A., and M. I. Scranton. 1993. Fate of methane in the Hudson River and estuary. Global Biogeochem. Cycles 7**:** 509-523, doi: 10.1029/93GB01636

Biastoch, A., T. Treude, L. H. Rüpke and others. 2011. Rising Arctic Ocean temperatures cause gas hydrate destabilization and ocean acidification. Geophys. Res. Lett. 38, doi: 10.1029/2011GL047222

Blanchard, D. C. 1989. The ejection of drops from the sea and their enrichment with bacteria and other materials: A review. Estuaries 12**:** 127-137, doi: 10.2307/1351816

Boetius, A., and F. Wenzhöfer. 2013. Seafloor oxygen consumption fuelled by methane from cold seeps. Nat. Geosci. 6**:** 725-734, doi: 10.1038/ngeo1926

Carlsson, B., A. Rutgersson, and A.-S. Smedman. 2009. Investigating the effect of a wave-dependent momentum flux in a process oriented ocean model. Boreal Environ. Res. 14, doi: 10.1007/s11274-015-1903-5

Collins, G. L., M. Motarjemi, and G. J. Jameson. 1978. A method for measuring the charge on small gas bubbles. J. Colloid Interface Sci. 63**:** 69-75, doi: 10.1016/0021-9797(78)90036-X

Damm, E., A. Mackensen, G. Budéus, E. Faber, and C. Hanfland. 2005. Pathways of methane in seawater: Plume spreading in an Arctic shelf environment (SW-Spitsbergen). Cont. Shelf Res. 25**:** 1453-1472, doi: 10.1016/j.csr.2005.03.003

Delnoij, E., F. Lammers, J. Kuipers, and W. Van Swaaij. 1997. Dynamic simulation of dispersed gas-liquid two-phase flow using a discrete bubble model. Chem. Eng. Sci. 52**:** 1429-1458, doi: 10.1016/S0009-2509(96)00515-5

Edenhofer, O., R. Pichs-Madruga, Y. Sokona and others. 2014. IPCC, 2014: summary for policymakers. Mitigation of Climate Change.

Edman, M., and A. Omstedt. 2013. Modeling the dissolved CO2 system in the redox environment of the Baltic Sea. Limnol. Oceanogr. 58**:** 74-92, doi: 10.4319/lo.2013.58.1.0074

Ferré, B., J. Mienert, and T. Feseker. 2012. Ocean temperature variability for the past 60 years on the Norwegian-Svalbard margin influences gas hydrate stability on human time scales. J. Geophys. Res.: Oceans (1978-2012) 117, doi: 10.1029/2012JC008300

Fofonoff, N. 1985. Physical properties of seawater: A new salinity scale and equation of state for seawater. J. Geophys. Res.: Oceans 90**:** 3332-3342, doi: 10.1029/JC090iC02p03332

Graves, C. A., L. Steinle, G. Rehder and others. 2015. Fluxes and fate of dissolved methane released at the seafloor at the landward limit of the gas hydrate stability zone offshore western Svalbard. J. Geophys. Res.: Oceans 120**:** 6185-6201, doi: 10.1002/2015JC011084

Gustafsson, N., L. Nyberg, and A. Omstedt. 1998. Coupling of a high-resolution atmospheric model and an ocean model for the Baltic Sea. Mon. Weather Rev. 126**:** 2822-2846, doi: 10.1175/1520-0493(1998)126%3C2822:COAHRA%3E2.0.CO;2

Hansson, D., and A. Omstedt. 2008. Modelling the Baltic Sea ocean climate on centennial time scale: temperature and sea ice. Climate Dynamics 30**:** 763-778, doi: 10.1007/s00382-007-0321-2

Johansen, Ø. 2000. DeepBlow – a Lagrangian Plume Model for Deep Water Blowouts. Spill Sci. Technol. Bull. 6**:** 103-111, doi: doi.org/10.1016/S1353-2561(00)00042-6

Kirschke, S., P. Bousquet, P. Ciais and others. 2013. Three decades of global methane sources and sinks. Nat. Geosci. 6**:** 813-823, doi: 10.1038/ngeo1955

Leblond, I., C. Scalabrin, and L. Berger. 2014. Acoustic monitoring of gas emissions from the seafloor. Part I: quantifying the volumetric flow of bubbles. Mar. Geophys. Res. 35**:** 191-210, doi: 10.1007/s11001-014-9223-y

Leifer, I., J. F. Clark, and R. F. Chen. 2000. Modifications of the local environment by natural marine hydrocarbon seeps. Geophys. Res. Lett. 27**:** 3711-3714, doi: 10.1029/2000GL011619

Leifer, I., and R. K. Patro. 2002. The bubble mechanism for methane transport from the shallow sea bed to the surface: A review and sensitivity study. Cont. Shelf Res. 22**:** 2409-2428, doi: 10.1016/S0278-4343(02)00065-1

Liang, J. H., J. C. McWilliams, P. P. Sullivan, and B. Baschek. 2011. Modeling bubbles and dissolved gases in the ocean. J. Geophys. Res.: Oceans (1978-2012) 116, doi: 10.1029/2010JC006579
Luff, R., K. Wallmann, and G. Aloisi. 2004. Numerical modeling of carbonate crust formation at cold vent sites: significance for fluid and methane budgets and chemosynthetic biological communities. Earth Planet. Sci. Lett. 221**:** 337-353, doi: 10.1016/S0012-821X(04)00107-4
Magen, C., L. L. Lapham, J. W. Pohlman, K. Marshall, S. Bosman, M. Casso, and J. P. Chanton. 2014. A simple headspace equilibration method for measuring dissolved methane. Limnol. Oceanogr.: Methods 12**:** 637-650, doi: 10.4319/lom.2014.12.637
Mau, S., M. Römer, M. E. Torres and others. 2017. Widespread methane seepage along the continental margin off Svalbard-from Bjørnøya to Kongsfjorden. Sci. Rep. 7**:** 42997, doi: 10.1038/srep42997
McGinnis, D., J. Greinert, Y. Artemov, S. Beaubien, and A. Wüest. 2006. Fate of rising methane bubbles in stratified waters: How much methane reaches the atmosphere? J. Geophys. Res.: Oceans (1978-2012) 111, doi: 10.1029/2005JC003183
Myhre, C. L., B. Ferré, S. M. Platt and others. 2016. Extensive release of methane from Arctic seabed west of Svalbard during summer 2014 does not influence the atmosphere. Geophys. Res. Lett. 43**:** 4624-4631, doi: 10.1002/2016GL068999
Omstedt, A. 2011. Guide to process based modeling of lakes and coastal seas. Springer.
Omstedt, A., and J. S. Wettlaufer. 1992. Ice growth and oceanic heat flux: Models and measurements. J. Geophys. Res.: Oceans 97**:** 9383-9390, doi: 10.1029/92JC00815
Pachauri, R. K., M. R. Allen, V. R. Barros and others. 2014. Climate change 2014: synthesis report. Contribution of Working Groups I, II and III to the fifth assessment report of the Intergovernmental Panel on Climate Change. IPCC.
Panieri, G., S. Bünz, D. J. Fornari and others. 2017. An integrated view of the methane system in the pockmarks at Vestnesa Ridge, 79° N. Mar. Geol. 390**:** 282-300, doi: 10.1016/j.margeo.2017.06.006
Randelhoff, A., A. Sundfjord, and M. Reigstad. 2015. Seasonal variability and fluxes of nitrate in the surface waters over the Arctic shelf slope. Geophys. Res. Lett. 42**:** 3442-3449, doi: 10.1002/2015GL063655
Rehder, G., P. W. Brewer, E. T. Peltzer, and G. Friederich. 2002. Enhanced lifetime of methane bubble streams within the deep ocean. Geophys. Res. Lett. 29, doi: 10.1029/2001GL013966
Ruppel, C. D., and J. D. Kessler. 2016. The Interaction of Climate Change and Methane Hydrates. Rev. Geophys., doi: 10.1002/2016RG000534
Sahling, H., M. Römer, T. Pape and others. 2014. Gas emissions at the continental margin west of Svalbard: mapping, sampling, and quantification. Biogeosciences 11**:** 6029-6046, doi: 10.5194/bg-11-6029-2014
Sam, A., C. Gomez, and J. Finch. 1996. Axial velocity profiles of single bubbles in water/frother solutions. Int. J. Miner. Process. 47**:** 177-196, doi: 10.1016/0301-7516(95)00088-7
Sauter, E. J., S. I. Muyakshin, J.-L. Charlou and others. 2006. Methane discharge from a deep-sea submarine mud volcano into the upper water column by gas hydrate-coated methane bubbles. Earth Planet. Sci. Lett. 243**:** 354-365, doi: 10.1016/j.epsl.2006.01.041
Shakhova, N., I. Semiletov, I. Leifer and others. 2014. Ebullition and storm-induced methane release from the East Siberian Arctic Shelf. Nat. Geosci. 7**:** 64-70, doi: 10.1038/ngeo2007
Shakhova, N., I. Semiletov, A. Salyuk, V. Yusupov, D. Kosmach, and Ö. Gustafsson. 2010. Extensive Methane Venting to the Atmosphere from Sediments of the East Siberian Arctic Shelf. Science 327**:** 1246-1250, doi: 10.1126/science.1182221
Sloan, E. D., and C. Koh. 2007. Clathrate hydrates of natural gases. CRC press.
Stepanenko, V. M., E. E. Machul'skaya, M. V. Glagolev, and V. N. Lykossov. 2011. Numerical modeling of methane emissions from lakes in the permafrost zone. Izv., Acad. Sci., USSR, Atmos. Oceanic Phys. 47**:** 252-264, doi: 10.1134/s0001433811020113
Svensson, U. 1978. A mathematical model of the seasonal thermocline.
Svensson, U., and A. Omstedt. 1998. Numerical simulations of frazil ice dynamics in the upper layers of the ocean. Cold Reg. Sci. Technol. 28**:** 29-44, doi: 10.1016/S0165-232X(98)00011-1
Taylor, K. E. 2001. Summarizing multiple aspects of model performance in a single diagram. J. Geophys. Res.: Atmos. 106**:** 7183-7192, doi: 10.1029/2000JD900719

Uhlig, C., and B. Loose. 2017. Using stable isotopes and gas concentrations for independent constraints on microbial methane oxidation at Arctic Ocean temperatures. Limnol. Oceanogr.: Methods 15**:** 737-751, doi: 10.1002/lom3.10199

Valentine, D. L., D. C. Blanton, W. S. Reeburgh, and M. Kastner. 2001. Water column methane oxidation adjacent to an area of active hydrate dissociation, Eel River Basin. Geochim. Cosmochim. Acta 65**:** 2633-2640, doi: 10.1016/S0016-7037(01)00625-1

Veloso, M., J. Greinert, J. Mienert, and M. De Batist. 2015. A new methodology for quantifying bubble flow rates in deep water using splitbeam echosounders: Examples from the Arctic offshore NW-Svalbard. Limnol. Oceanogr.: Methods 13**:** 267-287, doi: 10.1002/lom3.10024

Vielstädte, L., J. Karstens, M. Haeckel and others. 2015. Quantification of methane emissions at abandoned gas wells in the Central North Sea. Mar. Pet. Geol., doi: 10.1016/j.marpetgeo.2015.07.030

Wanninkhof, R. 1992. Relationship between wind speed and gas exchange over the ocean. J. Geophys. Res.: Oceans (1978-2012) 97**:** 7373-7382, doi: 10.1029/92JC00188

Wanninkhof, R. 2014. Relationship between wind speed and gas exchange over the ocean revisited. Limnol. Oceanogr.: Methods 12**:** 351-362, doi: 10.4319/lom.2014.12.351

Westbrook, G., S. Chand, G. Rossi and others. 2008. Estimation of gas hydrate concentration from multi-component seismic data at sites on the continental margins of NW Svalbard and the Storegga region of Norway. Mar. Pet. Geol. 25**:** 744-758, doi: 10.1016/j.marpetgeo.2008.02.003

Westbrook, G. K., K. E. Thatcher, E. J. Rohling and others. 2009. Escape of methane gas from the seabed along the West Spitsbergen continental margin. Geophys. Res. Lett. 36, doi: 10.1029/2009GL039191

Woolf, D. K. 1993. Bubbles and the air-sea transfer velocity of gases. Atmos.-Ocean 31**:** 517-540, doi: 10.1080/07055900.1993.9649484

Wunsch, C., and R. Ferrari. 2004. Vertical mixing, energy, and the general circulation of the oceans. Annu. Rev. Fluid Mech. 36**:** 281-314, doi: 10.1146/annurev.fluid.36.050802.122121

Zheng, L., and P. D. Yapa. 2002. Modeling gas dissolution in deepwater oil/gas spills. J Mar Syst 31**:** 299-309, doi: 10.1016/S0924-7963(01)00067-7

SI.1 List of symbols and annotations

Symbols, annotations, and indices used in this study including units and typical values, where applicable.

Symbol/ Notation	Meaning	Units in manuscript	Value(s) used in this study	Units in M2PG1
a	Semi-major axis of bubble	[mm]	0 – 10	[m]
A	Horizontal domain area	[m^2]	1800	[m^2]
A_{BS}	Bubble surface area	[mm^2]	Calculated	[m^2]
b	Semi-minor axis of bubble	[mm]	0 – 10	[m]
Ca	Atmospheric equilibrium concentration	[µmol kg^{-1}]	Calculated	[µmol kg^{-1}]
C_{eq}	Bubble equilibrium concentration	[µmol kg^{-1}]	Calculated	[µmol kg^{-1}]
C_{SW}	Gas concentration	[µmol kg^{-1}]	Calculated	[µmol kg^{-1}]
C_B	Boundary concentration	[µmol kg^{-1}]	Initial	[µmol kg^{-1}]
D	Diffusivity (for transfer velocity)	[$cm^2 s^{-1}$]	Calculated	[$m^2 s^{-1}$]
f	Bubble flatness	[]	Calculated	[]
F_d	Drag force	[N]	Calculated	[N]
F	Gas flux to the atmosphere	[mol m^{-2} s^{-1}]	Calculated	[mol m^{-2} s^{-1}]
k_A	Transfer velocity (ocean to atmosphere)	[m s^{-1}]	Calculated	[m s^{-1}]
k_{MOx}	Oxidation rate constant	[d^{-1}]	0 – 10	[s^{-1}]
k_T	Bubble transfer velocity bubble gas	[cm s^{-1}]	Calculated	[m s^{-1}]
n	Gas content	[mol]	Calculated	[mol]
$\partial n_R/\partial t$	Gas content change from moving bubbles	[mol s^{-1}]	Calculated	[mol s^{-1}]
$\partial n_D/\partial t$	Gas content change from dissolution	[mol s^{-1}]	Calculated	[mol s^{-1}]
$\partial n_B/\partial t$	Gas content change from boundaries	[mol s^{-1}]	Calculated	[mol s^{-1}]

$NGAS$	Number of modeled gases	[]	5	[]
$NSBIN$	Number of bubble size bins	[]	37	[]
N_Z	Number of vertical bins	[]	400	[]
N^2	Buoyancy frequency squared	[s^{-2}]	Calculated	Not used
P_{ATM}	Atmospheric pressure	[Pa]	101325	[Pa]
P_B	Total pressure inside bubble	[Pa]	Calculated	[Pa]
P_H	Hydrostatic pressure	[Pa]	Calculated	[Pa]
P_{ST}	Surface tension pressure	[Pa]	Calculated	[Pa]
Q_{AF}	Bubble gas escape to atmosphere	[mol s^{-1}]	Calculated	[mol s^{-1}]
Q_{AEQ}	Gas emission to atmosphere due to equilibration	[mol s^{-1}]	Calculated	[mol s^{-1}]
Q_{EF}	Free gas emission to the water column (from the seafloor)	[mol s^{-1}]	Calculated	[mol s^{-1}]
r_E	Equivalent bubble radius	[mm]	0 – 9	[m]
res	Model residual error	[mol]	Calculated	[mol]
S	Solubility	[mol kg^{-1}]	Calculated	mol kg^{-1}]
S_G	Source/sink, gas moving between bubble sizes	[mol]	Calculated	[mol]
Sc	Schmidt number	[]	Calculated	[]
t	Time	[s]		[s]
u	Water current	[m s^{-1}]	0 – 30	[m s^{-1}]
U	Wind speed at 10 meters above the seafloor	[cm s^{-1}]	5	[m s^{-1}]
V	Bubble volume	[mm^3]	Calculated	[m^3]
V_M	Molar volume of gas	[m^3 mol^{-1}]	Calculated	[m^3 mol^{-1}]
$\frac{\partial V_D}{\partial t}$	Volume change due to dissolution/ exsolution	[m^3 s^{-1}]	Calculated	[m^3 s^{-1}]

$\frac{\partial V_{PT}}{\partial t}$	Volume change due to pressure/temperature	[$m^3 s^{-1}$]	Calculated	[$m^3 s^{-1}$]
w_B	Bubble rising speed	[cm s^{-1}]	0 – 30	[cm s^{-1}]
X	Molar fraction of free gas in bubbles	[]	Calculated	[]
z	Depth	[m]	0 – 400	[m]
α	Angular eccentricity of bubble	[]	Calculated	[]
δt	Time step of model simulation	[s]	0.0625	[s]
Δt	Result output interval	[s]	600	[s]
ΔV_B	Volume difference of bubble sizes	[mm^3]	Calculated	[m^3]
δ_Z	Vertical bin size	[m]	1	[m]
Γ	Vertical mixing coefficient	[$m^2 s^{-1}$]	$10^{-4} - 10^4$	[$m^2 s^{-1}$]
ρ_{SW}	Seawater density	[kg m^{-3}]	Calculated	[kg m^{-3}]
σ	Surface tension	[N m^{-1}]	0.074	[N m^{-1}]
θ^j	Source term, dissolved gas species	[mol kg^{-1} s^{-1}]	Calculated	[mol kg^{-1} s^{-1}]
μ_{SW}	Seawater dynamic viscosity	[Pa s]	Calculated	[Pa s]
ν_{SW}	Seawater kinematic viscosity	[$m^2 s^{-1}$]	Calculated	[$m^2 s^{-1}$]
i	Index for depth (subscript)	[]		
j	Index for gas species (superscript)	[]		
k	Index for bubble size (subscript)	[]		
surf	Index for surface (subscript)	[]		
bot	Index for bottom (subscript)	[]		

SI.2 Bubble rising speed models in M2PG1

Several bubble rising speed models (BRSMs) exist in the literature, all assuming that the terminal velocity, when buoyancy and frictional forces balance, occurs within milliseconds after the initial release, and so there is no need to resolve acceleration of bubbles. The resulting bubble rising speeds predicted by all the models included in M2PG1 depend mainly on the bubble size, but also on water properties (temperature, density and viscosity) and the surface tension. For speed calculations, the bubble radius, r is taken as the equivalent bubble radius, the water density, ρ_{SW}, and viscosity, μ_{SW} are calculated from salinity and temperature and the surface tension σ is taken as a constant in these calculations.

M2PG1 includes a FORTRAN case structure including the nine BRSMs to facilitate a user-chosen model via the initialization file. The BRSMs incorporated in M2PG1 are seen in table SI.3 and detailed here. Figure SI.1 shows the resulting rising speeds from the nine BRSMs at 20°C.

Fan and Tsuchiya, 1990

Leifer and Patro (2002) modified the formula developed by Fan and Tsuchiya (1990) for the rising speeds and suggested the formula:

$$w_b = \left(\left(\frac{\rho_{sw} g r^2}{3.68 M^{-0.038} \mu_{sw}} \right)^{-d} + \left(\frac{c\sigma}{\rho_{sw} r} + gr \right)^{-\frac{d}{2}} \right)^{-\frac{1}{d}}$$

, where the dimensionless Morton number, $M = \frac{g\mu_{SW}^4}{\rho_{SW}\sigma^3}$, the empirically derived coefficient, c was 1.4 for seawater and 1.2 for freshwater. The coefficient, d varied between 0.8 for surfactant-covered bubbles and 1.6 for clean bubbles. M2PG1 uses c= 1.4 and d=1.6, 1.2 and 0.8 for BRSMs 1, 3 and 9 respectively.

Woolf and Thorpe, 1991

Woolf and Thorpe (1991) predicted velocities of clean and dirty bubbles and suggest a shift in behaviour at 80-150 micrometres. Equations 10 – 11 in their work gives a parameterization of the rising velocity of clean, small, and large bubbles;

$$w_b = \frac{r^2 g}{3\nu_{SW}} \mid r < 80\ \mu m$$

$$w_b = \frac{r^2 g}{\nu_{SW}} \left(18 \left[1 - \frac{2}{\left[1 + (1 + 0.091\chi)^{\frac{1}{2}} \right]} \right] \right)^{-1} \mid r > 150\mu m$$

Here $\chi = gr^3/\nu_{SW}^2$ with $\nu_{SW} = \frac{\mu_{SW}}{\rho_{SW}}$. Rising velocities for bubbles with radius >80 μm and <150 μm are linearly interpolated between the 80 and 150 μm velocities. Authors report on bubble velocities for bubbles sizes up to 500 μm. The authors also give equations (12 and 13 in their paper) for rising speed of surfactant-covered bubbles:

$$w_b = (2r^2 g/9\nu_{SW}) \left[(y^2 + 2y)^{\frac{1}{2}} - y \right]$$

$$w_b = \frac{r^2 g}{\nu_{SW}} \left(18 \left[1 - \frac{2}{\left[1 + (1 + 0.091\chi)^{\frac{1}{2}} \right]} \right] \right)^{-1} \mid r > 150\mu m$$

Where $y = 10.82\chi$

M2PG1 uses equations 10 – 11 for BRSM no. 2 and 12 – 13 for BRSM no. 8.

Leifer & Patro, 2002

Leifer and Patro (2002) reports (equation 16 in their study) on a simple polynomial parameterization for surfactant-covered bubbles, based on a regression of observed data from (Clift et al., 1978):

$$w_b = 276\mathrm{r} - 1648\mathrm{r}^2 + 4882\mathrm{r}^3 - 7429\mathrm{r}^4 + 5618\mathrm{r}^5 - 1670\mathrm{r}^6$$

M2PG1 uses this parameterization in BRSM no. 4.

Leifer, 2000

Leifer et al. (2000b) suggest that the rising speed is temperature-dependent and give the rising speeds for large, clean bubbles:

$$w_b = A\frac{2cgr^d}{9\nu_{SW}^n} + B\left[V_{Bm} + H(r - r_c)^{m2} e^{K(r - r_c)^{m1} T}\right]$$

$$A = \frac{1}{4}\left[1 + \tanh\left(\frac{T_P - T}{\chi_T}\right)\right]\left[1 + \tanh\left(\frac{r_P - r}{\chi_r}\right)\right]$$

$$B = \frac{1}{4}\left[1 + \tanh\left(\frac{T - T_P}{\chi_T}\right)\right]\left[1 + \tanh\left(\frac{r - r_P}{\chi_r}\right)\right]$$

Here, A and B are hyperbolic transition functions to comply with both non-oscillating and oscillating bubbles. Here the coefficients K=4.79×10^{-4}, H=0.733, r_c=0.0584 cm, V_{Bm}=22.16 cm s^{-1} $m1$=-0.815, and $m2$=-0.849 were determined from regression. The transition points are determined by $r_P = 1086 - 16.05T_p$ and the transition widths are: $\chi_r = 0.0015\ cm$, $\chi_T = 2°C$. This parameterization is used in BRSM no 6.

Leifer, surfactant covered bubbles with temperature dependence

BRSM no. 5 uses rising speed data supplied in a Matlab® code by Ira Leifer for inclusion in Veloso et al. (2015) with additional temperature dependence which affects the rising speed by $w_b = \frac{w_{b20}\nu_{SW}^{T_{dep}}}{0.0098^{T_{dep}}}$, where w_{b20} is the observed data at 20°C and $T_{dep} = \begin{pmatrix} -0.5 & r < 60\ \mu m \\ -0.54 & 60 < r < 320\ \mu m \\ -0.64 & r > 320\ \mu m \end{pmatrix}$. The underlying velocity data is found in table SI.

Woolf, 1993

Woolf (1993) worked on ocean surface bubble-enhanced gas exchange and found an approximate bubble rising velocity for both clean and surfactant-covered bubbles:

$$wb = 0.172\mathrm{r}^{1.28}\mathrm{g}^{0.76}\nu_{\mathrm{SW}}^{-0.56} \quad | \; (wb < 0.25\, ms^{-1})$$

$$wb = 0.25\, ms^{-1} \quad | \; (large\ bubbles)$$

This parametrization is used in BRSM no. 7, which is the reference BRSM in this study.

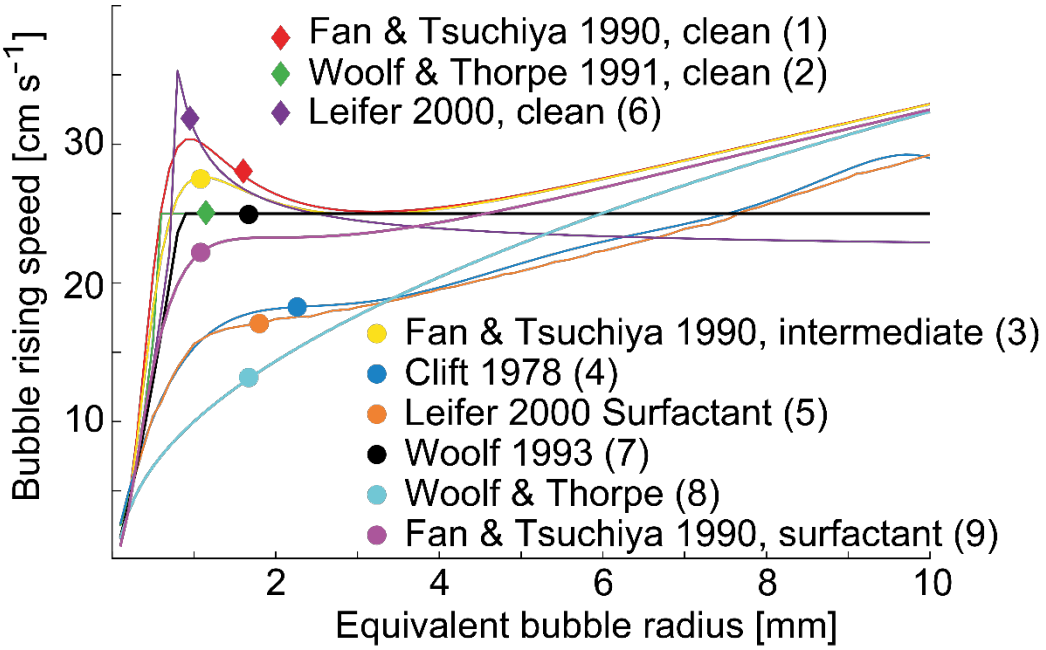

Figure SI.1. Bubble rising speeds as functions of the equivalent bubble radius. Diamonds indicate clean bubble models and dots specify models for surfactant-covered or partially covered bubbles. Colour coding matches Figure 5 in the main manuscript and numbers in parenthesis represents the BRSM no.

Table SI.1. References for M2PG1-implemented Solubility, Molar volume and Diffusivity

Species	Solubility	Molar volume	Diffusivity
N_2	Mao and Duan (2006)	Mao and Duan (2006)	Hayduk and Laudie (1974)
O_2	Geng and Duan (2010)	Schmidt and Wagner (1985)	Boudreau (1997)
CO_2	Duan et al (2006)[1.] Tishchenko et al. (2009)[2.]	Duan and Sun (2003)	Boudreau (1997)
CH_4	Kossel et al. (2013)[3.] Tishchenko et al. (2005)[4.]	Duan and Mao (2006)	Jähne et al. (1987)
Ar	Hamme & Emerson, (2004)[5.]	Weast (1972)	Jähne et al. (1987)

[1] Outside the CO_2-HSZ; [2] Within the CO_2-HSZ.

[3] Outside the CH_4-HSZ; [4] Within the CH_4-HSZ; [5]Extrapolated to high pressure.

Table SI.2. Structure of initial and boundary conditions for M2PG1 simulations. Index 1 is the first water cell above the seafloor.

Index	Temp °C	Salinity PSU	N_2 µmol kg^{-1}	O_2 µmol kg^{-1}	CO_2 µmol kg^{-1}	CH_4 µmol kg^{-1}	Ar µmol kg^{-1}
1	4	35	680	250	25	0.01	0.14
2	4	35	680	250	25	0.01	0.14
3	4	35	680	250	25	0.01	0.14
4	4	35	680	250	25	0.01	0.14
5	4	35	680	250	25	0.01	0.14
6	4	35	680	250	25	0.01	0.14
7	4	35	680	250	25	0.01	0.14
.	.	.	.	.	.	.	.
.	.	.	.	.	.	.	.
.	.	.	.	.	.	.	.
398	4	35	680	250	25	0.01	0.14
399	4	35	680	250	25	0.01	0.14
400	4	35	680	250	25	0.01	0.14

Only numeric values (no headings or units) are supplied in the .txt file

Table SI.3. BRSM's incorporated in M2PG1. The size range within which the BRSM is appropriate and the type of bubble (i.e. bubble rims with a surfactant or clean bubble rims) are indicated.

BRSM	Reference	Range	Bubble type	Comment
1	Fan and Tsuchiya (1990)	0 – 10 mm	Clean	n=1.6 in eq. 2.11
2	Woolf and Thorpe (1991)	0 – 0.5 mm [1.]	Clean	Eq. 10, 11

3	Fan and Tsuchiya (1990)	0 – 10 mm	Intermediate	n=1.2 in eq. 2.11
4	Leifer and Patro (2002)	0.6 – 10 mm	Surfactant	Polynomial fit to data (eq. 16)
5	Leifer et al. (2000)	0-4.5 mm	T dependent, Surfactant	Data plus temperature dependence
6	Leifer et al. (2000)	0-4.5 mm	T dependent, Clean	Eq. 10 -17
7	Woolf (1993)	0.1mm – 4mm [1.]	Both	Eq. 38
8	Woolf and Thorpe (1991)	0 – 0.5 mm [1.]	Surfactant	Eq. 12, 13
9	Fan and Tsuchiya (1990)	0 – 10 mm	Surfactant	n=0.8 in eq. 2.11

Table SI.4. Output description

File name	Description / Units
M2PG1_FREEGASx.dat[1]	Free gas content (mol) of species x (N_2, O_2, CO_2, CH_4, Ar)
	[Time (h), depth (m), size bin 1, bin 2, …, bin NSBIN)]
M2PG1_DISSOLVEDGASES.dat[1]	Dissolved gas concentrations (µmol kg-1)
	[Time (h), depth (m), N_2, O_2, CO_2, CH_4, Ar]
M2PG1_bottomsource.dat [2]	Source of gas at the source depth (mol)
	[Time (h), N_2, O_2, CO_2, CH_4, Ar]
M2PG1_atm_eq.dat [2]	Ocean – Atmosphere equilibration (mol)
	[Time (h), N_2, O_2, CO_2, CH_4, Ar]
M2PG1_atm_fr_gas_esc.dat [2]	Ocean - Atmosphere free gas ebullition (mol)
	[Time (h), N_2, O_2, CO_2, CH_4, Ar]
M2PG1_TS.dat[1]	Temperature and salinity. (°C, PSU)
	[Time (h), depth (m), T, S]

[1] Snapshot of the content/ concentration. Output interval is specified in the .ini file

[2] Flow quantities, accumulated until written to result-file

Table SI.5. Example BSD

radius [m]	**Probability**		
0.00001	0	0.0045	0.33784
0.00025	0	0.00475	0.22973
0.0005	0	0.005	0.25676
0.00075	0	0.00525	0.17568
0.001	0.054054	0.0055	0.13514
0.00125	0.081081	0.00575	0.094595
0.0015	0.21622	0.006	0
0.00175	0.39189	0.00625	0
0.002	0.66216	0.0065	0
0.00225	0.74324	0.00675	0.013514
0.0025	0.66216	0.007	0
0.00275	0.75676	0.00725	0
0.003	1	0.0075	0.013514
0.00325	0.90541	0.00775	0
0.0035	0.60811	0.008	0
0.00375	0.41892	0.00825	0
0.004	0.48649	0.0085	0
0.00425	0.41892	0.00875	0
		0.009	0

Table SI.6. Gas mixing ratio of released bubbles

Mixing ratio	Species
0	N_2
0	O_2
0	CO_2
1	CH_4
0	Ar

Table SI.7. Organization of M2PG1 initialization file

Entry	Explanation
M2PG1_0.0	Simulation name
400	Number of vertical grid cells (N in PROBE)
35	Number of water cells in oceanographic forcing model if transient
1	Type of area (1=vertically same) (INDARE in PROBE)
1800	Area m^2 (AREAHZ in PROBE)
400	Water depth (m)
0.0625	Time-step (s) (TFRAC(2) in PROBE
-1	Last time-step (LSTEP in PROBE) -1 indicates run to steady state
60	Time-steps between output
7	Bubble rising speed model number
2	Bubble flatness (0 for spherical bubbles, 1 for Leblond, 2 for Linear)
1	Gas transfer velocity model number
1	Probe turbulence model (ITURBM in PROBE)
1	Probe type of Prandtl number (IPRSC in PROBE).
1.00E-03	Constant vertical mixing coefficient (m^2 s^{-1}) (EMUCON in PROBE).
1.00E-02	kMOx. Methane oxidation rate constant (d^{-1})
0.05	Free gas flow rate in the area (mol s^{-1})
0.15	Barotropic current across the boundary (ms^{-1}) (-999 = dynamic forcing)
'IN\INITIAL400M_simple.txt'	Path to Initial profiles file
'IN\BSD_for_M2PG1_3mm.txt'	Path to Bubble size distribution file (size, probability)
'IN\Gascomposition.txt'	Composition of released gases
0	0= Don't use atmospheric data
''	Path to atmospheric transient boundary condition file
0	0= Don't use transient oceanographic boundary.
''	Path to oceanographic transient boundary file.

Table SI.8a.
Simulation settings

Code	Case focus	BRSM #	Bubble shape	TVM #	Aqueous gas profiles	BSD -	Temp °C	Sal. PSU	Flow rate mol s^{-1}	kMOx d^{-1}	In/ Out flow ms^{-1}	Mixing coefficient m^2s^{-1}
0.0	Reference case	7	Linear	1	Atm. eq.	3 mm	4	35	0.05	1.00E-02	0.15	1.00E-03
1.0	Bubble rising speed	1	Linear	1	Atm. eq.	3 mm	4	35	0.05	1.00E-02	0.15	1.00E-03
1.1	Bubble rising speed	2	Linear	1	Atm. eq.	3 mm	4	35	0.05	1.00E-02	0.15	1.00E-03
1.2	Bubble rising speed	3	Linear	1	Atm. eq.	3 mm	4	35	0.05	1.00E-02	0.15	1.00E-03
1.3	Bubble rising speed	4	Linear	1	Atm. eq.	3 mm	4	35	0.05	1.00E-02	0.15	1.00E-03
1.4	Bubble rising speed	5	Linear	1	Atm. eq.	3 mm	4	35	0.05	1.00E-02	0.15	1.00E-03
1.5	Bubble rising speed	6	Linear	1	Atm. eq.	3 mm	4	35	0.05	1.00E-02	0.15	1.00E-03
1.6	Bubble rising speed	8	Linear	1	Atm. eq.	3 mm	4	35	0.05	1.00E-02	0.15	1.00E-03
1.7	Bubble rising speed	9	Linear	1	Atm. eq.	3 mm	4	35	0.05	1.00E-02	0.15	1.00E-03
2.0	Bubble shapes	7	Spheric	1	Atm. eq.	3 mm	4	35	0.05	1.00E-02	0.15	1.00E-03

2.1	Bubble shapes	7	Leblond	1	Atm. eq.	3 mm	4	35	0.05	1.00E-02	0.15	1.00E-03
3.0	Transfer velocity	7	Linear	2	Atm. eq.	3 mm	4	35	0.05	1.00E-02	0.15	1.00E-03
3.1	Transfer velocity	7	Linear	3	Atm. eq.	3 mm	4	35	0.05	1.00E-02	0.15	1.00E-03
4.0	Aqueous gas profiles	7	Linear	1	Half Oxygen	3 mm	4	35	0.05	1.00E-02	0.15	1.00E-03
4.1	Aqueous gas profiles	7	Linear	1	1/100 O_2	3 mm	4	35	0.05	1.00E-02	0.15	1.00E-03
4.2	Aqueous gas profiles	7	Linear	1	No Ar	3 mm	4	35	0.05	1.00E-02	0.15	1.00E-03
4.3	Aqueous gas profiles	7	Linear	1	Double CO_2	3 mm	4	35	0.05	1.00E-02	0.15	1.00E-03
4.4	Aqueous gas profiles	7	Linear	1	No N_2	3 mm	4	35	0.05	1.00E-02	0.15	1.00E-03
4.5	Aqueous gas profiles	7	Linear	1	Double N_2	3 mm	4	35	0.05	1.00E-02	0.15	1.00E-03
4.6	Aqueous gas profiles	7	Linear	1	Tenfold N_2	3 mm	4	35	0.05	1.00E-02	0.15	1.00E-03
5.0	Bubble sizes	7	Linear	1	Atm. eq.	1 mm	4	35	0.05	1.00E-02	0.15	1.00E-03
5.1	Bubble sizes	7	Linear	1	Atm. eq.	2 mm	4	35	0.05	1.00E-02	0.15	1.00E-03
5.2	Bubble sizes	7	Linear	1	Atm. eq.	4 mm	4	35	0.05	1.00E-02	0.15	1.00E-03
5.3	Bubble sizes	7	Linear	1	Atm. eq.	6 mm	4	35	0.05	1.00E-02	0.15	1.00E-03
5.4	Bubble sizes	7	Linear	1	Atm. eq.	8 mm	4	35	0.05	1.00E-02	0.15	1.00E-03
6.0	Temperature	7	Linear	1	Atm. eq.	3 mm	0*	35	0.05	1.00E-02	0.15	1.00E-03

6.1	Temperature	7	Linear	1	Atm. eq.	3 mm	1*	35	0.05	1.00E-02	0.15	1.00E-03
6.2	Temperature	7	Linear	1	Atm. eq.	3 mm	2*	35	0.05	1.00E-02	0.15	1.00E-03
6.3	Temperature	7	Linear	1	Atm. eq.	3 mm	3*	35	0.05	1.00E-02	0.15	1.00E-03
6.4	Temperature	7	Linear	1	Atm. eq.	3 mm	6	35	0.05	1.00E-02	0.15	1.00E-03
6.5	Temperature	7	Linear	1	Atm. eq.	3 mm	8	35	0.05	1.00E-02	0.15	1.00E-03
6.6	Temperature	7	Linear	1	Atm. eq.	3 mm	10	35	0.05	1.00E-02	0.15	1.00E-03
6.7	Temperature	7	Linear	1	Atm. eq.	3 mm	20	35	0.05	1.00E-02	0.15	1.00E-03
7.0	Salinity	7	Linear	1	Atm. eq.	3 mm	4	0	0.05	1.00E-02	0.15	1.00E-03
7.1	Salinity	7	Linear	1	Atm. eq.	3 mm	4	20	0.05	1.00E-02	0.15	1.00E-03
7.2	Salinity	7	Linear	1	Atm. eq.	3 mm	4	40	0.05	1.00E-02	0.15	1.00E-03
8.0	Flow rate	7	Linear	1	Atm. eq.	3 mm	4	35	0.025	1.00E-02	0.15	1.00E-03
8.1	Flow rate	7	Linear	1	Atm. eq.	3 mm	4	35	0.1	1.00E-02	0.15	1.00E-03
8.2	Flow rate	7	Linear	1	Atm. eq.	3 mm	4	35	0.15	1.00E-02	0.15	1.00E-03
8.3	Flow rate	7	Linear	1	Atm. eq.	3 mm	4	35	0.2	1.00E-02	0.15	1.00E-03
9.0	Oxidation turnover	7	Linear	1	Atm. eq.	3 mm	4	35	0.05	0	0.15	1.00E-03
9.1	Oxidation turnover	7	Linear	1	Atm. eq.	3 mm	4	35	0.05	0.1	0.15	1.00E-03

9.2	Oxidation turnover	7	Linear	1	Atm. eq.	3 mm	4	35	0.05	1	0.15	1.00E-03
9.3	Oxidation turnover	7	Linear	1	Atm. eq.	3 mm	4	35	0.05	10	0.15	1.00E-03
10.0	Water current	7	Linear	1	Atm. eq.	3 mm	4	35	0.05	1.00E-02	0.025	1.00E-03
10.1	Water current	7	Linear	1	Atm. eq.	3 mm	4	35	0.05	1.00E-02	0.05	1.00E-03
10.2	Water current	7	Linear	1	Atm. eq.	3 mm	4	35	0.05	1.00E-02	0.1	1.00E-03
10.3	Water current	7	Linear	1	Atm. eq.	3 mm	4	35	0.05	1.00E-02	0.2	1.00E-03
10.4	Water current	7	Linear	1	Atm. eq.	3 mm	4	35	0.05	1.00E-02	0.5	1.00E-03
11.0	Mixing coefficient	7	Linear	1	Atm. eq.	3 mm	4	35	0.05	1.00E-02	0.15	1.00E-04
11.1	Mixing coefficient	7	Linear	1	Atm. eq.	3 mm	4	35	0.05	1.00E-02	0.15	1
11.2	Mixing coefficient	7	Linear	1	Atm. eq.	3 mm	4	35	0.05	1.00E-02	0.15	100
11.3	Mixing coefficient	7	Linear	1	Atm. eq.	3 mm	4	35	0.05	1.00E-02	0.15	10000
12.0	Case 15-6 cruise	7	Linear	1	O_2 CTD	Veloso	CTD	CTD	0.005**	1.00E-02	0.185	1.00E-03
12.1	Case 15-6 cruise	5	Linear	1	O_2 CTD	Veloso	CTD	CTD	0.005**	1.00E-02	0.185	1.00E-03
12.2	Case 15-6 cruise	8	Linear	1	O_2 CTD	Veloso	CTD	CTD	0.005**	1.00E-02	0.185	1.00E-03
12.3	Case 15-6 cruise	7	Linear	1	O_2 CTD	2mm ^	CTD	CTD	0.005**	1.00E-02	0.185	1.00E-03
12.4	Case 15-6 cruise	5	Linear	1	O_2 CTD	2mm ^	CTD	CTD	0.005**	1.00E-02	0.185	1.00E-03

12.5	Case 15-6 cruise	8	Linear	1	O_2 CTD	2mm ^	CTD	CTD	0.005**	1.00E-02	0.185	1.00E-03
12.6	Case 15-6 cruise	7	Linear	1	O_2 CTD	1mm ^	CTD	CTD	0.005**	1.00E-02	0.185	1.00E-03
12.7	Case 15-6 cruise	5	Linear	1	O_2 CTD	1mm ^	CTD	CTD	0.005**	1.00E-02	0.185	1.00E-03
12.8	Case 15-6 cruise	8	Linear	1	O_2 CTD	1mm ^	CTD	CTD	0.005**	1.00E-02	0.185	1.00E-03

* Simulations within the CH_4-HSZ; ** Mean single flare flow rate from Flarehunter analysis; ^ Peak radius of Gaussian distribution

Table SI.8b.
Simulation results

Name	plume height 1% m	plume height 10% m	plume height 20% m	Flare height 1% m	Flare height 10% m	Flare height 20% m	COR1 []	RMSD2 µmol kg^{-1}	STD3 µmol kg^{-1}	Max conc µmol kg^{-1}
M2PG1 0.0	83.7	56.6	44.6	88.7	54.6	41.6	1.0000	0.0000	0.0348	0.1851
M2PG1 1.0	88.7	58.6	46.6	89.7	54.6	41.6	0.9997	0.0021	0.0368	0.1929
M2PG1 1.1	86.7	57.6	45.6	88.7	54.6	41.6	0.9999	0.0017	0.0364	0.1913
M2PG1 1.2	85.7	57.6	45.6	88.7	53.6	41.6	1.0000	0.0016	0.0364	0.1924
M2PG1 1.3	71.7	46.6	36.6	72.7	43.6	33.6	0.9912	0.0144	0.0481	0.2782
M2PG1 1.4	59.6	37.6	28.6	61.7	36.6	27.6	0.9639	0.0228	0.0544	0.3473
M2PG1 1.5	88.7	58.6	46.6	88.7	53.6	40.6	0.9998	0.0034	0.0381	0.2008
M2PG1 1.6	63.7	42.6	33.6	66.7	42.6	32.6	0.9829	0.0170	0.0500	0.2916
M2PG1 1.7	80.7	53.6	42.6	83.7	51.6	39.6	0.9994	0.0045	0.0391	0.2111
M2PG1 2.0	88.7	60.7	48.6	92.7	57.6	44.6	0.9982	0.0022	0.0341	0.1700
M2PG1 2.1	83.7	55.6	43.6	88.7	54.6	41.6	0.9999	0.0008	0.0354	0.1906

M2PG1 3.0	189.0	142.9	115.8	218.0	135.8	104.8	0.8241	0.0200	0.0257	0.0987
M2PG1 3.1	195.0	151.9	100.8	NaN	335.3	258.1	0.5710	0.0301	0.0104	0.0454
M2PG1 4.0	84.7	56.6	44.6	88.7	54.6	41.6	1.0000	0.0004	0.0353	0.1868
M2PG1 4.1	83.7	56.6	44.6	88.7	54.6	41.6	1.0000	0.0001	0.0350	0.1856
M2PG1 4.2	83.7	56.6	44.6	88.7	54.6	41.6	1.0000	0.0000	0.0348	0.1851
M2PG1 4.3	84.7	56.6	44.6	88.7	54.6	41.6	1.0000	0.0003	0.0351	0.1863
M2PG1 4.4	82.7	55.6	44.6	85.7	53.6	40.6	1.0000	0.0008	0.0341	0.1819
M2PG1 4.5	84.7	56.6	44.6	91.7	55.6	42.6	1.0000	0.0006	0.0354	0.1876
M2PG1 4.6	96.7	61.7	48.6	123.8	69.7	51.6	0.9986	0.0067	0.0412	0.2119
M2PG1 5.0	31.6	18.5	14.5	35.6	20.6	15.5	0.8113	0.0313	0.0521	0.4293
M2PG1 5.1	56.6	35.6	27.6	61.7	36.6	27.6	0.9579	0.0124	0.0407	0.2635
M2PG1 5.2	106.8	72.7	56.6	112.8	70.7	54.6	0.9896	0.0052	0.0330	0.1644
M2PG1 5.3	140.9	95.7	72.7	149.9	95.7	72.7	0.9569	0.0105	0.0305	0.1403
M2PG1 5.4	163.9	107.8	79.7	176.9	109.8	81.7	0.9434	0.0119	0.0302	0.1368
M2PG1 6.0	100.8	71.7	57.6	103.8	67.7	52.6	0.9850	0.0066	0.0316	0.1491
M2PG1 6.1	93.7	66.7	53.6	97.7	62.7	49.6	0.9924	0.0050	0.0319	0.1554

M2PG1 6.2	87.7	61.7	49.6	91.7	58.6	45.6	0.9970	0.0034	0.0326	0.1633
M2PG1 6.3	85.7	58.6	46.6	89.7	55.6	42.6	0.9993	0.0015	0.0342	0.1752
M2PG1 6.4	85.7	57.6	45.6	89.7	54.6	42.6	1.0000	0.0006	0.0354	0.1868
M2PG1 6.5	84.7	56.6	45.6	89.7	55.6	42.6	1.0000	0.0003	0.0348	0.1843
M2PG1 6.6	84.7	57.6	45.6	90.7	55.6	42.6	1.0000	0.0004	0.0347	0.1833
M2PG1 6.7	87.7	58.6	46.6	92.7	56.6	42.6	0.9998	0.0011	0.0356	0.1867
M2PG1 7.0	71.7	47.6	37.6	74.7	45.6	34.6	0.9946	0.0042	0.0368	0.2058
M2PG1 7.1	77.7	52.6	41.6	82.7	50.6	38.6	0.9988	0.0021	0.0360	0.1970
M2PG1 7.2	86.7	57.6	45.6	90.7	55.6	42.6	0.9998	0.0007	0.0348	0.1828
M2PG1 8.0	83.7	55.6	43.6	88.7	54.6	41.6	1.0000	0.0174	0.0174	0.0976
M2PG1 8.1	83.7	56.6	45.6	88.7	54.6	41.6	1.0000	0.0348	0.0697	0.3602
M2PG1 8.2	84.7	57.6	45.6	88.7	54.6	41.6	1.0000	0.0705	0.1053	0.5386
M2PG1 8.3	84.7	57.6	45.6	88.7	54.6	41.6	1.0000	0.1055	0.1404	0.7145
M2PG1 9.0	83.7	56.6	44.6	88.7	54.6	41.6	1.0000	0.0000	0.0348	0.1851
M2PG1 9.1	83.7	56.6	44.6	88.7	54.6	41.6	1.0000	0.0000	0.0348	0.1851
M2PG1 9.2	83.7	56.6	44.6	88.7	54.6	41.6	1.0000	0.0001	0.0348	0.1848

M2PG1 9.3	83.7	56.6	44.6	88.7	54.6	41.6	1.0000	0.0006	0.0343	0.1818
M2PG1 10.0	80.7	52.6	41.6	88.7	54.6	41.6	0.9987	0.0205	0.0552	0.3007
M2PG1 10.1	81.7	53.6	42.6	88.7	54.6	41.6	0.9992	0.0152	0.0499	0.2703
M2PG1 10.2	82.7	55.6	43.6	88.7	54.6	41.6	0.9998	0.0066	0.0414	0.2216
M2PG1 10.3	84.7	57.6	45.6	88.7	54.6	41.6	0.9999	0.0051	0.0297	0.1573
M2PG1 10.4	88.7	60.7	48.6	88.7	54.6	41.6	0.9975	0.0203	0.0146	0.0790
M2PG1 11.0	83.7	56.6	44.6	88.7	54.6	41.6	1.0000	0.0000	0.0348	0.1851
M2PG1 11.1	83.7	56.6	44.6	88.7	54.6	41.6	1.0000	0.0000	0.0348	0.1847
M2PG1 11.2	85.7	58.6	46.6	88.7	54.6	41.6	0.9992	0.0015	0.0342	0.1700
M2PG1 11.3	170.9	111.8	88.7	88.7	54.6	41.6	0.8981	0.0178	0.0221	0.0871
M2PG1 12.0	133.8	80.7	59.6	125.8	73.7	54.6	0.9810	0.0149	0.0209	0.1054
M2PG1 12.1	86.7	52.6	39.6	84.7	49.6	36.6	0.9969	0.0080	0.0273	0.1582
M2PG1 12.2	105.8	64.7	48.6	104.8	61.7	45.6	0.9976	0.0110	0.0241	0.1289
M2PG1 12.3	105.8	61.7	45.6	99.7	56.6	41.6	0.9985	0.0103	0.0247	0.1367
M2PG1 12.4	68.7	40.6	30.6	66.7	38.6	28.6	0.9738	0.0082	0.0319	0.2055
M2PG1 12.5	77.7	45.6	33.6	76.7	43.6	32.6	0.9866	0.0074	0.0297	0.1827

M2PG1 12.6	85.7	47.6	34.6	83.7	45.6	33.6	0.9873	0.0077	0.0290	0.1809
M2PG1 12.7	58.6	33.6	24.6	57.6	31.6	23.6	0.9392	0.0124	0.0361	0.2562
M2PG1 12.8	62.7	34.6	24.6	62.7	34.6	24.6	0.9459	0.0115	0.0352	0.2471

[1] $R = \frac{\sum([C-\bar{C}]\times[C_r-\overline{C_r}])}{N\times STD(C)\times STD(Cr)}$; [2] $RMSD = \sqrt{\frac{\sum([C-\bar{C}]-[C_r-\overline{C_r}]^2)}{N}}$; [3] $\mathrm{STD} = \sqrt{\frac{\sum([C-\bar{C}]^2)}{N}}$. C is the case value and Cr is the reference value

Table SI.9. Bubble rising speed data for BRSM no. 5. 20°C surfactant covered.

radius [cm]	Velocity [cm s^{-1}]	radius [cm]	Velocity [cm s^{-1}]	radius [cm]	Velocity [cm s^{-1}]
0.0025	0.18	0.18	17.1	0.49	20.75
0.005	0.65	0.19	17.2	0.5	20.85
0.0075	1.2	0.2	17.35	0.51	21
0.01	1.7	0.21	17.45	0.52	21.15
0.0125	2.2	0.22	17.5	0.53	21.3
0.015	2.8	0.23	17.6	0.54	21.45
0.0175	3.5	0.24	17.65	0.55	21.6
0.02	4	0.25	17.7	0.56	21.7
0.025	5.4	0.26	17.85	0.57	21.85
0.03	6.4	0.27	17.95	0.58	22
0.035	7.5	0.28	18.05	0.59	22.2
0.04	8.5	0.29	18.1	0.6	22.35
0.045	9.2	0.3	18.25	0.62	22.6
0.05	10.05	0.31	18.35	0.64	22.9
0.055	10.9	0.32	18.45	0.66	23.2
0.06	11.4	0.33	18.55	0.68	23.5
0.065	12.1	0.34	18.7	0.7	23.85
0.07	12.8	0.35	18.8	0.72	24.15
0.075	13.3	0.36	18.95	0.74	24.4
0.08	13.9	0.37	19.1	0.76	24.8
0.085	14.3	0.38	19.25	0.78	25.3
0.09	14.75	0.39	19.35	0.8	25.65
0.095	15.1	0.4	19.5	0.82	26.05
0.1	15.45	0.41	19.65	0.84	26.45
0.11	15.95	0.42	19.75	0.86	26.8
0.12	16.3	0.43	19.85	0.88	27.2
0.13	16.5	0.44	20.05	0.9	27.6
0.14	16.7	0.45	20.2	0.92	28
0.15	16.8	0.46	20.3	0.94	28.25
0.16	16.9	0.47	20.45	0.96	28.55
0.17	17	0.48	20.6	0.98	28.9
				1	29.25

Paper 4

Insights from underwater high resolution dissolved methane sensing over a known methane seepage site west of Svalbard

Jack triest[1*], Pär Jansson[2*], Roberto Grilli[1], Bénédicte Ferré[2], Anna Silyakova[2], Jürgen Mienert[2], Jérôme Chappelaz[1]

[1] Institute of Geoscience and Environment, Université Grenoble Alpes, CNRS, F-38000 Grenoble, France
[2] CAGE-Center for Arctic Gas Hydrate, Environment, and Climate, Department of Geosciences, UiT-The Arctic University of Norway, 9037 Norway.

* Corresponding authors: Jack Triest (Subocean2015@gmail.com), Pär Jansson (per.g.jansson@uit.no)

Key Points:

- A new fast-response membrane inlet laser spectrometer sensor provided high-resolution measurements of dissolved CH_4 offshore Svalbard near intensive bubble seepage
- Towed instrument profiles uncovered both horizontal and vertical CH_4 structure with unprecedented details, highlighting the need for high-resolution sensing for accurate CH_4 inventories and flux estimates
- New control volume and 2-dimensional models, based on seepage locations and flow rates, reproduced the high-resolution observations

Abstract

Methane (CH_4) in marine sediments have the potential to contribute to changes in the ocean- and climate system. The distribution of dissolved CH_4 in the oceans and lakes is influenced by physical and biochemical processes that are difficult to quantify with current standard methods such as acoustic surveys and discrete sampling. Detailed observations of subsea CH_4 concentrations are required to better understand the CH_4 dynamics in the water column, which effects ocean acidification, chemosynthetic ecosystems and the atmospheric gas composition. Here we present high-resolution in-situ measurements of dissolved CH_4 throughout the water column at a 400 m deep CH_4 seepage area west of Svalbard, obtained with a new fast-response membrane-inlet laser spectrometer sensor. We observe decameter-scale variations of dissolved CH_4 concentrations over the CH_4 seepage zone, well reproduced with a numerical model based on acoustically detected free gas emissions from the seafloor, whereas previous studies could not resolve the variability and assumed smoother distributions. We show good repeatability of the measurements by the instrument, which are also in agreement with discrete sampling. We identify sources of CH_4, not detected by echosounder, and rapid dispersion of dissolved CH_4 away from the sources. Results from this unique continuous data have and modelling efforts have a significant impact on the understanding of CH_4 fluxes and its spatial distribution over a CH_4 degassing area.

Plain Language Summary

Methane bubbles escaping from the seafloor may, if they reach the atmosphere contribute to the global warming effect caused by greenhouse gases (gases that can trap heat in the Earth's atmosphere). Such gas bubbles are observed in, among other places, the Arctic Ocean. Using a newly developed high-resolution methane sensor near a bubble seep location west of Svalbard revealed a patchy pattern with unprecedented details. Newly constructed numerical models reproduced the high-resolution measurements and sparse water sampling with subsequent analysis using traditional methods (gas chromatography) confirmed the sensibility and accuracy of the new sensor. Previous studies have measured with course resolution, most likely wrongly estimating the amount of methane in the seawater. For the first time, methane distribution was mapped in high resolution, which brought new insights to the bubble-mediated methane dynamics in aquatic environments. We hope that the development of the new sensor and models will bring about more similar research to provide details of methane seepage in locations worldwide.

1 Introduction

CH_4 fluxes from gas bearing ocean sediments have been a matter of concern for many years (e.g. Westbrook et al., 2009; Ferré et al., 2012; Ruppel and Kessler, 2016). Warming of bottom waters, geological triggering and local glacier state development could, at different time scales, lead to CH_4 gas release from the seabed. The magnitude and trend of such a phenomenon is still under debate (e.g. Hong et al., 2018; Ruppel and Kessler, 2016; Andreassen et al., 2017). Once released and dissolved in the water column, the CH_4 gas diffuses and is partly oxidized in the water column (Reeburgh, 2007), contributing to the ocean acidification (Biastoch et al., 2011) and minimum oxygen zones formation (Boetius and Wenzhöfer, 2013). At shallow seepage sites, CH_4 could ultimately reach the atmosphere and amplify greenhouse warming (Shakhova et al., 2010; Shakhova et al., 2014)
Most previous studies of CH_4 fluxes and distribution in the water column over hydrate-rich sediments relied on indirect or discrete sample (DS) measurements (Damm et al., 2005; Westbrook et al., 2009;

Gentz et al., 2014). Using hydro-acoustic imaging and additional bubble catcher, the bubble size and rising speed are used to derive CH_4 flow rates (Sahling et al., 2014; Weber et al., 2014; Veloso et al., 2015). This indirect method can only quantify the CH_4 flux from acoustically detectable or visible bubbles. It cannot detect CH_4 from sources other than free gas seepage and does not provide details on the distribution of dissolved CH_4 in the water column. Using this method, Sahling et al. (2014) estimated an average flowrate of 56.7 l min^{-1} using this method in the area of the present study. The authors assumed that each of the 452 detected flares (the acoustic signatures of one ore many bubble streams observed in echograms) were composed of six bubble streams with an average flow rate of 20,9 ml min^{-1}, and compared it to previous studies (Reagan Matthew et al., 2011; Westbrook et al., 2009; Marín-Moreno et al., 2013; Berndt et al., 2014).
Discrete sampling with Niskin bottles allows direct measurement of the dissolved CH_4 but at limited spatial resolution. The same seep area has been documented with this method by Graves et al. (2015) and the low resolution led to an artificially smoothed spatial distribution and to a high estimation of average dissolved CH_4 concentration.

Current commercial underwater CH_4 sensors are mostly designed for long-term monitoring and do not have the required response time for accurate high-resolution mapping. (Gentz et al., 2014) deployed an underwater membrane inlet mass spectrometer with a fast response time for mapping of CH_4 in the same region but only at shallow (10 m) depths. One of their main hypotheses, that the vertical distribution of the CH_4 is limited due to stratification, is still based on discrete samples. Boulart et al. (2013) used an in situ, real time sensor in the Baltic Sea but it was not deployed over a comparable CH_4 hydrate zone and the reported instrument response time of 1 – 2 minutes and a detection limit of 3 nmol l^{-1} are still limiting for fast profiling and background concentration studies linked to the atmosphere.

In this work, we present for the first time in-situ high-resolution mapping of dissolved CH_4 in seawater over active seepage, obtained by deploying a patent-pending membrane inlet laser spectrometer (MILS) (Triest et al. patent France No. 17 50063). The investigated area is located at 78°33´N 9°30´E, where the average water depth is ~390 m and more than 250 flares have been previously detected (e.g. Sahling et al., 2014; Westbrook et al., 2009; Damm et al., 2005; Graves et al., 2015). The new high-resolution measurements, together with echosounder data, sparse discrete water sampling and newly constructed control volume- (CV) and 2-dimensional (2D) models allow for a better understanding of CH_4 flux from the seabed and its subsequent fate in the surrounding water.

The hydrography of the area is mainly controlled by the northward flowing West Spitsbergen Current (WSC), which transports Atlantic Water (AW, S>34,9 PSU, T>3° C) (Schauer et al., 2004). The East Spitsbergen Current (ESC), flows south-westward from the East Spitsbergen coast, and northward along the western Svalbard margin, carrying Arctic Surface Water (ASW, $34.4 \leqslant S \leqslant 34.9$ PSU) and Polar Water (PW, S<34.4 PSU) above the Atlantic Water (Skogseth et al., 2005) via the Coastal Current (CC) (Loeng, 1991; Skogseth et al., 2005). The lower Arctic Intermediate Water (LAIW, S>34.90‰, $T \leqslant 3$ °C) flows below the Atlantic Water.

2 Materials and Methods

The survey was performed with RV Helmer Hanssen in October 2015 (CAGE 15-6 field campaign) over a well-documented area of active CH_4 venting (Damm et al., 2005; Westbrook et al., 2009; Sahling et al., 2014) west of Prins Karls Forland, Svalbard (Figure 1a) in 2015. Over a period of three

days (October 21 – 23), water column data was collected over an area of ~18 km^2 with a water depth of ~ 350 – 420 m.

2.1 Hydrocasts with discrete water sampling

Vertical profiles of seawater salinity, temperature and pressure were recorded at 10 stations (Figure 1.) using a SBE 911 plus CTD (Conductivity, Temperature, Salinity) probe mounted on a rosette, which also carried 12 Niskin bottles of 5 litres. The Niskin bottles were closed during the up-casts collecting seawater at different depths for following analysis. Gas chromatography (GC) analysis for CH4 concentrations was carried out in the laboratory at the Department of Geoscience, The Arctic University of Norway in Tromsø. The operated GC, a ThermoScientific Trace 1310, was equipped with a FID and a ThermoScientific TG-Bond Msieve 5A column. Hydrogen was used as the carrier gas with a flow of 10 ml/min. The temperature of the oven was a constant 150°C. Calibration of the setup was performed using three standards with known mixing ratios of 1.8, 19 and 1800 ppm CH_4. The instrument precision was estimated to 4%, based on the standard deviation of replicate samples. The resulting headspace mixing ratios (ppmv) were converted to in-situ concentrations (nmol l^{-1}), taking into account dilution of the samples from addition of reaction stopper (1 ml of 1M NaOH solution), and removal of sample water while introducing headspace gas (5 ml of pure N_2).

2.2 High-resolution CH_4 sensing

The MILS was towed each of the survey days, collecting in-situ data during a total of 28 hours with a sampling rate of 1 s^{-1}. The instrument was lowered and heaved in the water for vertical casts and towed along lines with varying heights above the seabed. The five lines closest (~15 m) to the seafloor are shown in figure 1.

The battery-powered sensor (Figure 1b) has an inlet system with a polydimethylsiloxane membrane, linked to an optical feedback cavity-enhanced absorption spectrometer (OFCEAS) and an integrated PC for control and data storage. SHDSL-communication over an 11 mm Norddeutsche Seekabelwerke CB7000 coaxial winch cable enabled real-time instrument control and data monitoring from the vessel, allowing instant decision-making and ensuring optimal sensor operation. This proved particularly useful to maintain a consistent distance from the seafloor while towing by monitoring the pressure and controlling the winch cable payout.

Sensors with membrane inlets can be sensitive to fluctuating water flow over the membrane, which can result in artificial variability of measured concentrations. This has been avoided by careful positioning of the Sea-Bird SBE5T water pump to minimize inlet/outlet pressure changes and subsequent flow variations.

The MILS was towed together with an Aanderaa, Seaguard TD262a CTD, providing temperature, salinity and dissolved oxygen data as well as pressure.

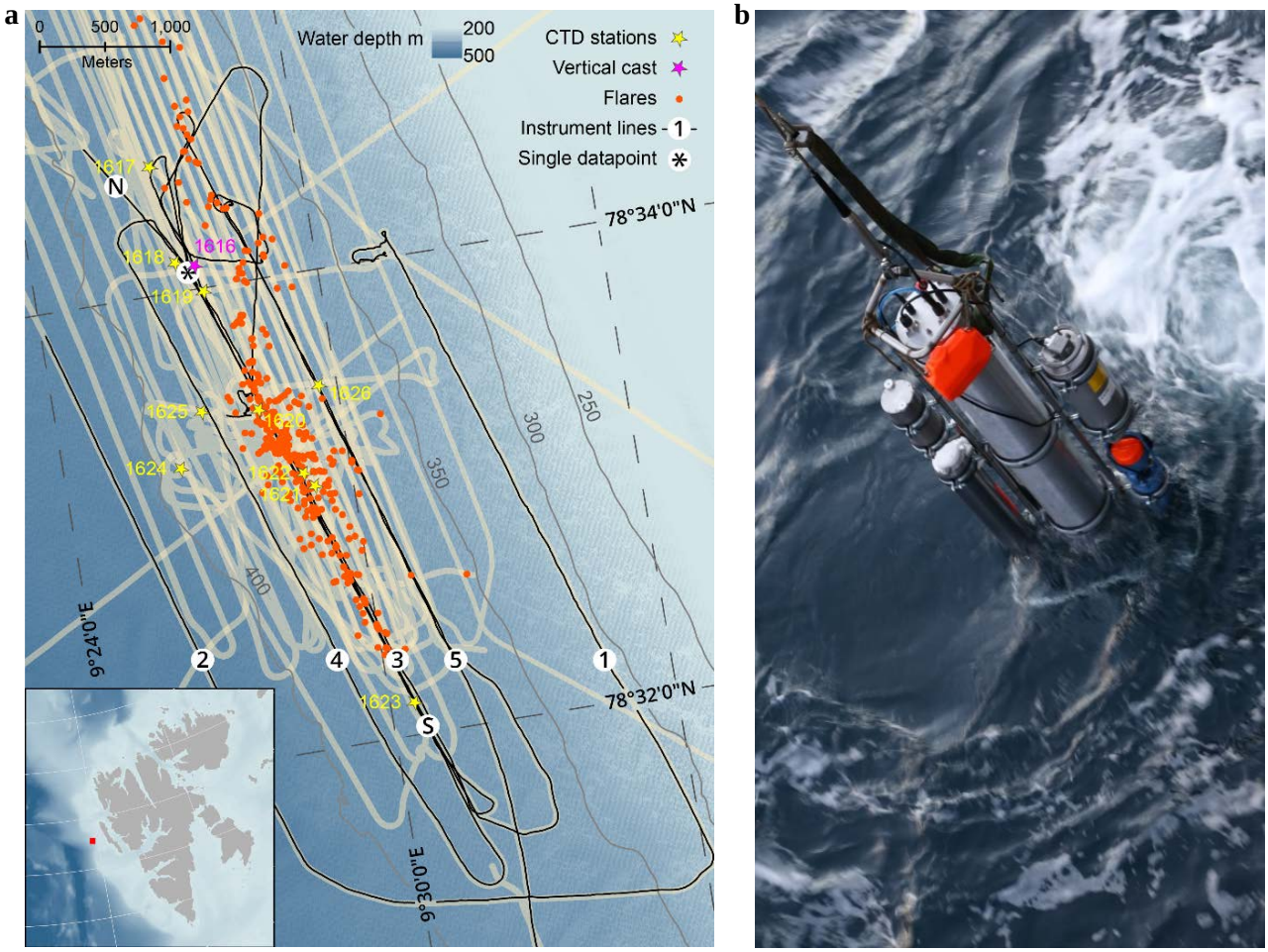

Figure 1. Map of the surveyed area and instrument assembly. **a)** Survey lines and sampling locations over the study area at the Svalbard continental margin. Black lines show the ship trajectory with line numbers assigned in the order they were surveyed. Beige areas (appearing as thick lines) indicate echo sounder beam coverage from this campaign and previous cruises (2010, 2013). The start- and end-locations of line 3 are indicated with N and S respectively and the black asterisk indicates the position of the data point along line 3, used for comparison with discrete samples and vertical cast. Known flare locations from this survey and CAGE-surveys in 2010 and 2013 are marked by orange dots. Discrete sampling/CTD stations are marked with yellow stars and the vertical instrument cast with a purple star. The inset image shows an overview of Svalbard with the survey location indicated with a red square. **b)** Instrument assembly. The main central tube is the prototype MILS sensor. The stainless steel frame acts as a stable platform and allows attachment of instrument battery (top right side), CTD (blue at the bottom right) and a commercial CH_4 sensor and its battery pack.

A stainless steel frame attached to the winch cable served as a platform to which instruments and battery (STR Seacell NiMH, 36Ah, 26VDC, 12 hours autonomy) were attached. Total height of the assembly was ~1.4 m with a total weight in air of ~160 kg and a negative buoyancy of ~52 kg. All the parameters from the MILS sensor, including gas flow, pressure, sample humidity, and internal temperature were logged to process and evaluate the CH_4 data. A dedicated ship mounted GPS was used to log positional data for accurate synchronization of the towed instrument data with ship position.

A position correction, essential for correct interpretation of data, was applied to the towed instrument data, accounting for the lag between the probe and the ship. We simulated a towing scenario (Dewey, 1999), using the instrument assembly, namely a 1.68 m long cylinder with 0.28 m diameter and a negative buoyancy of 52 kg. From the simulation, a speed-factor equation ($y = -0.2211x^5 + 1.355x^4 - 3.0126x^3 + 2.6741x^2 - 0.1609x$) was derived to account for the combined ship- and water current velocities (x). The distance of the probe behind the ship, and the corresponding required time-shift, was calculated by multiplying the speed-factor (y) by the instrument depth at each data point. This approach allows for a dynamic correction of the data positions accounting for towing with or against the current, and a near-stationary ship during vertical profiling. Correction for tidal currents was neglected since tides constituted less than 1 cm s^{-1} during our deployments according to the tide model TPXO (Egbert and Erofeeva, 2002).

The water pump inlet has a fine mesh filter and a shield to avoid entry of free gas bubbles and possible subsequent artefacts resulting from gas bubbles entering the water sampling unit and reaching the membrane surface.

We converted MILS measured mixing ratios (ppmv) into aqueous concentrations (nmol l^{-1}) by accounting for fugacity, in-situ temperature, salinity, water vapor, and using the solubility coefficients determined by Wiesenburg and Guinasso Jr (1979).

2.3 Acoustic mapping and quantification of benthic CH_4 emissions

Gas bubbles in the water column are efficient sound scatterers and scientific echosounders can therefore be used for identifying and quantifying gas emissions. (Weber et al., 2014; Veloso et al., 2015). The target strength (TS), being the 10-base logarithmic measurements of acoustic cross sections, reveal the existence of objects in the water column. High TS values indicate high abundance of sound-scattering objects and collected time series of TS are seen in so-called echograms. Acoustic backscatter was continuously acquired from the 38 kHz channel of the ship-mounted single beam Simrad EK-60 echosounder during the entire survey. So-called flares (bubble plumes detected in the echograms) can be identified manually and distinguished from other acoustic scatterers such as fish schools, dense plankton aggregations and strong density gradients.

We used the methodology suggested by Veloso et al. (2015) and the prescribed Flarehunter software for mapping and quantifying the benthic gas release. Temperature, salinity, pressure and sound velocities are required for correct quantification and so we used water properties from the CTD-casts. The bubble size distribution observed in the study area in 2011 and 2012 (Veloso et al., 2015) was applied for the flow rate calculations, which were finally performed with the bundled Flare Flow Module. The resulting flow rates and positions were used in the mass balance calculation and in the two-dimensional model described in section 2.4 and 2.5 respectively.

2.4 Control volume model

The temporal evolution of a solute's concentration C within a control volume $V=\Delta x \times \Delta y \times \Delta z$, oriented so that water flows through it in the x-direction can be written as:

$$\frac{dC}{dt} = \frac{Q_{IN} \times C_B}{V} - \frac{Q_{OUT} \times C}{V} + \frac{F}{V} + k\nabla^2 C \qquad (1)$$

With the following assumptions we can find an analytical solution for Equation 1: The in- and outflows (Q_{IN}, Q_{OUT}) are balanced and given by the width (Δy) and height (Δz) of the volume and a steady water current; The diffusion coefficient, k is constant; The background concentration does not change; The flow, F of the solute into the volume is constant.

Equation 1 can be understood as a first order differential equation and for the case of CH_4-bubble-emission from the seafloor, F denotes the bubble flow rate into the volume. If we assume that the emitted bubble gas dissolves within the volume, and diffusion occurs across the domain (in the y-direction), the aqueous CH4 reaches the steady state concentration:

$$C_{t=\infty} = \frac{\left(\frac{Q_{IN} \times C_B}{V} + \frac{F}{V} + \frac{2k \times C_B}{(\Delta y)^2}\right)}{\frac{Q_{OUT}}{V} + \frac{2k}{(\Delta y)^2}} \quad (2)$$

2.5 Two-dimensional model

In order to gain insight to the physical processes behind the observed CH_4 variability, we constructed a two-dimensional (2D) numerical model, resolving the evolution of dissolved CH_4 in the water column. The model domain was made 400 m high (in the z-direction) and 4.5 km long (in the x-direction), oriented along the slope, corresponding to MILS line 3 (Figure 1). The navigation data along line 3 was linearly interpolated, to form the basis for a 1-meter gridded model domain starting at 78°34.54'N 9°25.92'E and ending at 78°32.1'N 9°30.58'E as indicated by N and S, in Figure 1. Flarehunter derived flow rates within 50 m from line 3 were projected onto the model domain in appropriate x/z positions.

The bubble-mediated dissolved CH_4 sources were distributed vertically by deriving a non-dimensional dissolution-function $S0(z) = 6.6 \times 10^{-5} \times e^{-0.066 \times z}$, with $\int S0(z)\, dz = 1$, based on the detected vertical CH_4 distribution near bubble streams (CTD casts 1618, 1619 and 1620). Source distribution functions, *S(z)* were calculated by scaling *S0(z)* with the Flarehunter derived flow rates and distributed into current-corrected x/z nodes with volumes $\delta v = \delta x \times \delta y \times \delta z$, where δx=δz=1 m and δy is the model width.

The 2D model was run to steady state while simulating horizontal CH_4 diffusion across the domain and advection with water currents, similarly with the CV model.

3 Results

3.1 Water properties

The pressure- salinity and temperature measurements from both the towed CTD and vertical casts indicate that the water is well mixed in the bottommost 150 meters and continuously stratified from 250 to 50 mbsl with a squared buoyancy frequency of ~$N^2 < 4 \times 10^{-5}$ s^{-2}. A pycnocline was observed at 10 – 30 mbsl (Figure 2a) with N^2 up to 10^{-4} s^{-2}. Temperature and salinity measurements indicate that mainly AW is present below ~20 mbsl and the overlying water is intermediate (IW) and surface water (SW) as seen in Figures 2c and 2d. The temperature close to the seafloor was 4.2 – 4.4 °C, which is more than 1°C above the CH_4 hydrate stability zone calculated according to Tishchenko et al. (2005) with a salinity of 35.1 PSU as indicated in Figure 2a.

The velocity of the WSC was between 0.1 and 0.3 ms^{-1} (Figure 2b), inferred from the inclination of flare spines (Veloso et al., 2015), which is consistent with previous findings (Graves et al., 2015; Gentz et al., 2014).

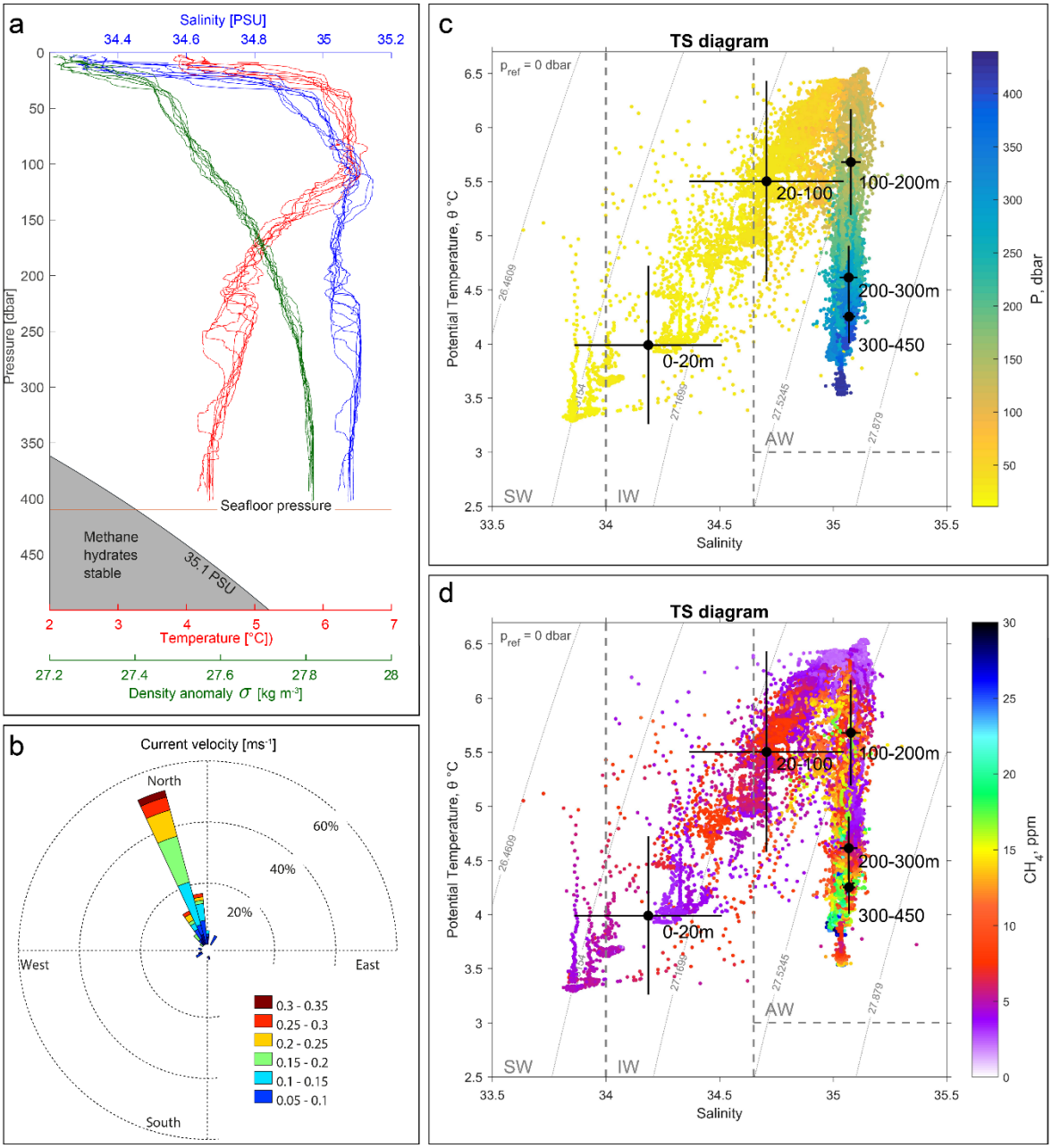

Figure 2. Hydrography during the campaign. **a)** CTD casts 1617- 1626 showing potential temperature (red), practical salinity (blue) and density anomaly calculated with Gibbs sweater package (McDougall and Barker, 2011) (green). **b)** Ocean currents inferred from inclination of flare spines (Veloso et al., 2015) and a mean bubble rising speed of 23 cm s^{-1}. **c)** Temperature and salinity diagram colored by pressure (dbar). AW indicates Atlantic Water, IW is Intermediate Water and SW is surface Water. Back dots indicate the mean water properties for layers [0 – 20, 20 – 100, 100-200, 200-300, 300-450 mbsl]. Crosses indicate the standard deviation within the corresponding layer. **d)** TS diagram colored by CH_4 mixing rations (ppmv) measured with the MILS. Grey curved lines in the background indicate isopycnals (constant density (σ) lines). Black dots are average temperature and salinity at water depths

0-20m, 20-100m, 100-200m, 200-300m, 300-400m. Bars indicate standard deviations of potential temperature (θ) and salinity.

The mean salinity in layers [0 – 20, 20 – 100, 100 – 200, 200 – 300, 300 – 400 m] were [34.19, 34.71, 35.08, 35.07, 35.07 PSU] with standard deviations [0.32, 0.34, 0.04, 0.04, 0.03 PSU] and the corresponding potential temperatures were [3.99, 5.50, 5.68, 4.61, 4.25 °C] with standard deviations [0.73, 0.93, 0.49, 0.29, 0.25 °C] as seen in Figure 2c and 2d. Warm and saline water is present in the layer between 100 and 200 meters water depth, which we consider the core of the WSC which is normally found 50 – 150 mbsl (e.g. Saloranta and Svendsen, 2001). The exact depth of the core varies with oceanographic factors with season and with mesoscale variability on weekly time scales and atmospheric forcing.

Dashed lines in Figures 2c and 2d indicate water masses according to classification by Cottier et al. (2005). This data suggest a clear dominance of Atlantic Water (AW) with T>3°C and S>34.65 during the survey. However, one should keep in mind a possible bias, since most of the data was collected at the depth of the core of the WSC.

3.2 Measured and modeled CH_4 distribution

The high-resolution dissolved CH_4 concentration profiles resulting from towing the MILS along five lines approximately 15 m above the seafloor show high variability (Figure 3), especially over line 3, which geographically matches the main distribution of bubble plumes (Figure 1). On the landward side (line 1 and 5), the concentration is relatively smooth, but considerably elevated (background CH_4 concentration of ~ 30 nmol l^{-1}). On the offshore side (line 2 and 4), the average concentrations are lower (~ 15 and 10 nmol l^{-1}) but we observe elevated CH_4 without hydroacoustic evidence of sources.

The down- and upward sequences obtained from the vertical MILS cast at station 1616 (Figure 1), which was recorded during 25 minutes shows excellent repeatability after accounting for the instrument lag time (corresponding to the gas flushing from the membrane to the cell) of 15 seconds (Figure 4). The sensor shows no memory effects following elevated concentrations, which are typical for other membrane-based sensors. In addition, despite spatial and temporal variations, comparison with discrete measurements from a nearby CTD cast taken a few hours later, confirms the qualitative match of the MILs measured CH_4 concentrations. The apparent discrepancy between the MILS data and the discrete measurements below 350 m depth is due to a slight difference in sampling location. The discrete data from station 1619 and MILS data from line 3 at the same location (asterisk in figure 4) matches extraordinarily well, supporting the qualitative match between the methods and confirms the significant spatial variability of the dissolved CH_4. An exponential function was fitted to the entire dataset (shown as a dotted line in figure 4) and was nondimensionalized for inclusion in the 2D model. Comparison of the MILS technique against discrete sampling has been conducted in the laboratory and will be reported in a separate publication.

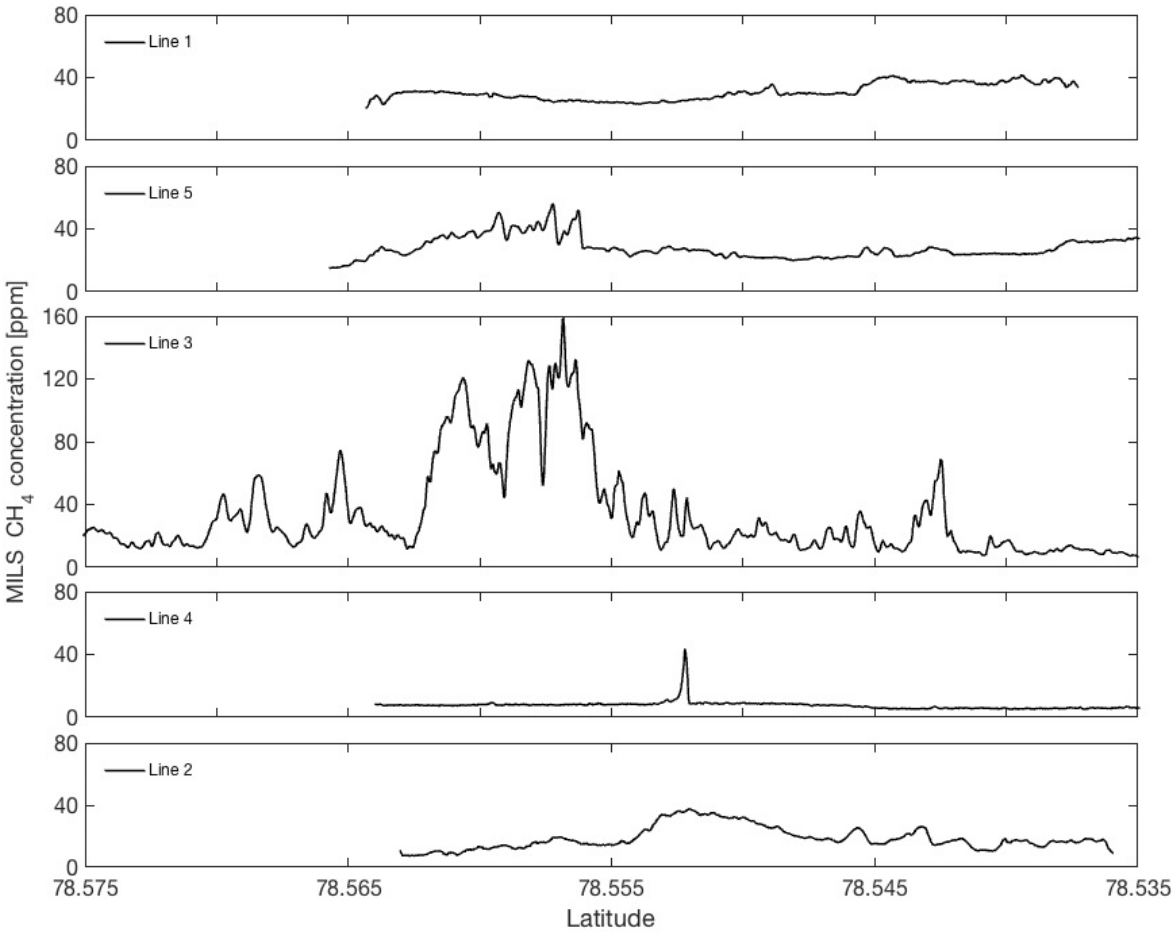

Figure 3. Dissolved CH4 concentrations along trajectories. The panels show data acquired with the towed MILS along lines 1 – 5, shown in order of proximity to the shore with line 1 closest to the shore and line 2 furthest offshore. Figure 1a shows the horizontal trajectories of the lines.

Elevated concentrations peaking at ~160 and ~220 mbsl revealed by the continuous vertical profiling was not identified with the discrete sampling in either of the nearby CTD stations (1618 and 1619) because of the sparse sampling (Figure 4). The MILS data collected 15 meters above seafloor along line 3 and near the vertical MILS-cast (1616), does not reveal the high concentrations (~200 nmol/L) measured during the vertical profiling, emphasizing the temporal variability of the CH_4 distribution.

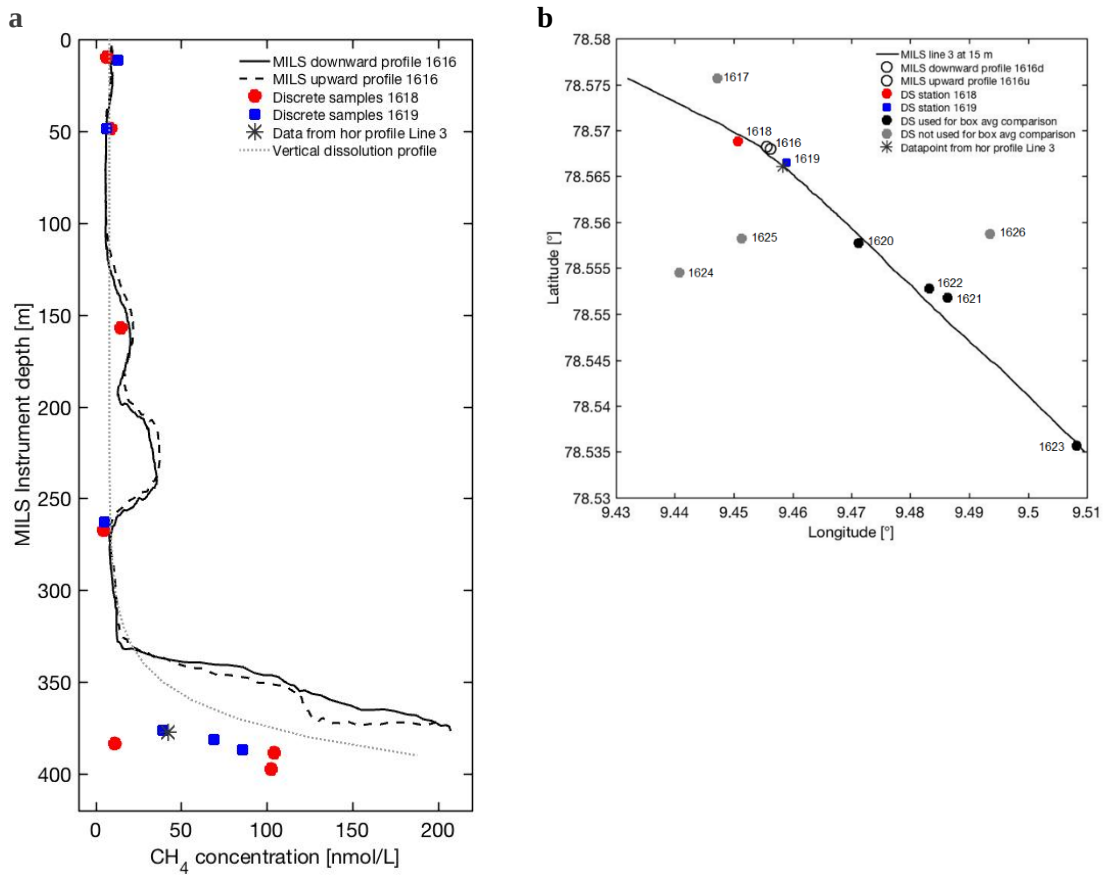

Figure 4. Vertical high-resolution CH_4 profiles and discrete samples. **a)** The solid and dashed black lines represent the continuous downward and upward profiles after correction for instrument response time. Discrete sample data is shown as red dots and blue squares for comparison. The black star indicates the data point from the continuous horizontal profile along line 3, closest to the vertical cast 1616. The dotted line indicates an exponential function fitted to the CH_4 concentrations of the discrete samples. **b)** Location of discrete sampling stations and vertical profile positions in relation to the horizontal profile of line3 (black line).

We observe high CH_4 variability in the horizontal profiles (Figure 3). Hence, we focus on a trajectory (line 3, towed in north-south direction at ~0.8 m s^{-1}) directly over the flares for further analysis. The fast response time of the MILS sensor (T_{90}<30 secs) revealed decameter-scale variations of the dissolved CH_4 concentrations with high values well correlated with the echo-sounder signal (Figure 5) after correcting for the towed instrument position.

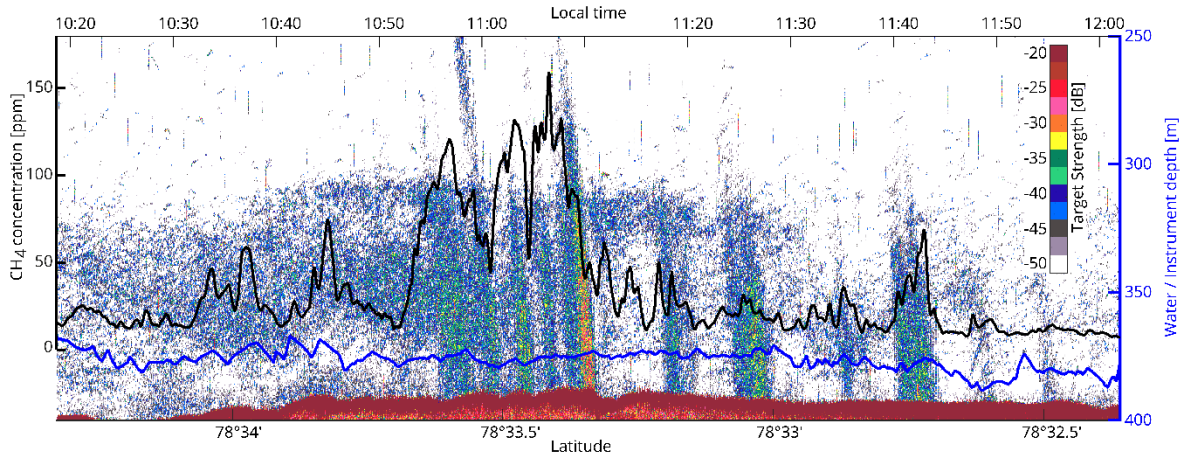

Figure 5. Towed MILS data overlying echo sounder data. The black line shows the CH_4 concentration along line no. 3 (see Fig. 1 for location) at ~15 m from the seafloor. The blue line indicates the depth of the towed instruments. The echogram displaying TS (color bar) values from the 38 kHz channel is shown in the background. Brown and red indicates strong backscattering, seen at the seafloor and in some of the most intense flares.

Correlations of CH_4 concentrations versus depth and speed changes were low (R= 0.0133, -0.0001, -0.0094, 0.0028 for ship speed, ship acceleration, vertical instrument speed and instrument acceleration respectively), showing the stability of the instrument during rapid movements and no effect from fluctuating flow over the membrane was detected.

Methane sources forcing the CV- and 2D model were obtained from the acoustic mapping and quantification described in section 2.3. During the entire survey, we identified 68 unique (107 before clustering) bubble plumes (flares in the echograms) emissions with an average flow rate of 192 ml min^{-1} and a standard deviation of 198 ml min^{-1}. In close vicinity of line 3, 31 bubble streams were identified, with an average flow rate of 240 ml min^{-1} (s.d. 261 ml min^{-1}) amounting to 7.44 l min^{-1}.

These flow rates were taken as sources in both the CV- and the 2D model, but since the flow rates were calculated in a layer 5 – 10 m above the seafloor, they were upscaled by 40% to compensate for bubble dissolution near the seafloor.

The dimensions of the models were chosen to match line 3, which has a length of ~4.5 km. A height of 75 m was chosen for the control volume, since we assume that the bulk of the emitted CH_4 dissolves within this distance from the seafloor. The 2D model resolved the full height of the water column (400 m) and the width of both models were set to 50 meters.

The 2D model was run to steady state with different diffusion coefficients, $k \in [0.3 - 4.9\ m^2\ s^{-1}]$, which were adopted from dye-experiment results in the shelf sea offshore Rhode Island (Sundermeyer and Ledwell, 2001). Results revealed that the best fit (R=0.81) was achieved during a simulation with k=1.5 m^2s^{-1} which reached steady state after ~1 hour. The resulting range of model outputs and the best fit-model simulation are visualized in Figure 5.

Applying the same diffusion coefficient in the CV model resulted in a steady state concentration of 23.5 nmol l^{-1} (23.2 nmol l^{-1} was reached in 53 min).

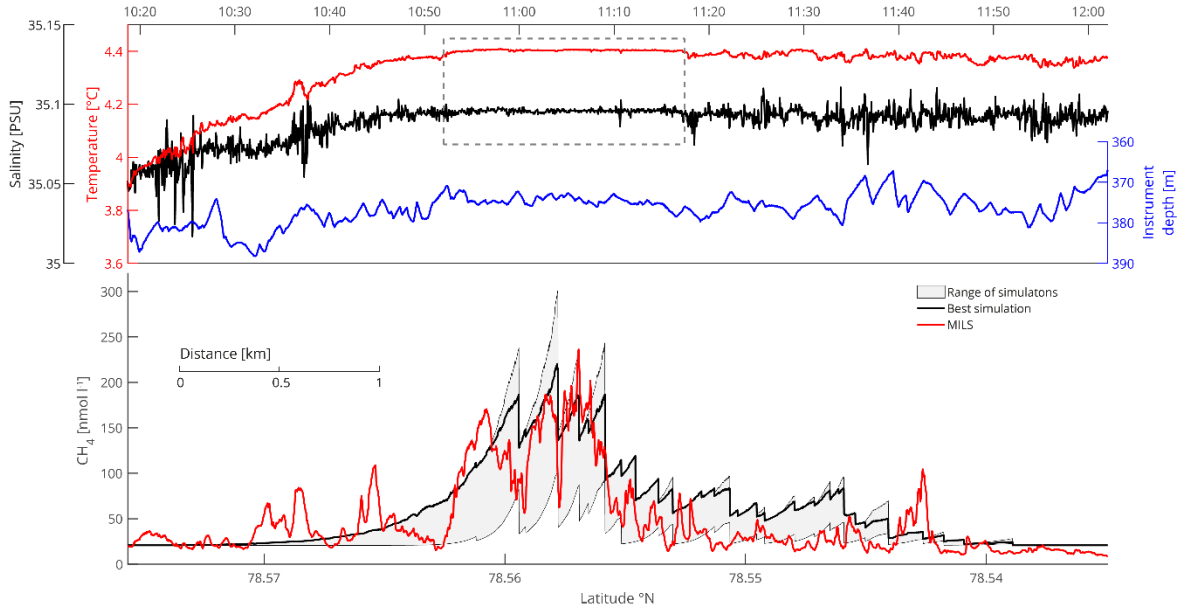

Figure 6. Water properties and qualitative comparison between modelled and measured dissolved CH4 concentrations. Top panel shows temperature and salinity data together with the depth of the towed instruments. The dashed-line box highlights the area of intense mixing. In the lower panel, the red line shows the dissolved CH_4 measured by the MILS. The grey area indicates the range of CH_4 concentrations from the model simulations. The black line depicts the model simulation run with the best fit (R=0.81) to the measured data.

The measured continuous profile along line 3, together with the range of 2D model outputs and the best-fit simulation (k=1.5 m^2s-1) are seen in Figure 6. Despite applying a high diffusivity, the model always shows a residual downstream tailing, not evident in the measured data, which we attribute to the fact that the model accounts for diffusion across, but not along the model domain.

The inferred high diffusion is supported by the salinity and temperature profiles of the towed CTD, which indicate well-mixed water due to intense mixing, particularly over the most prominent gas flares. Here, the standard deviation of the temperature and salinity drops by a factor of four (dashed line box in Figure 6) compared to the rest of the data.

3.6 Methane inventory using different methods

In order to evaluate how different methods may influence CH4 inventory calculations, we applied different methods on the same geometry.

We defined a virtual control volume (here called “box”) along the slope, which was 4500 m long and equivalent to the MILS tow line no. 3. A width of 50 m was chosen to match the echosounder beam width and limit uncertainties of contributions from neighboring bubble plumes. The height was limited to 75 m above the seabed as this is the most dynamic and CH_4 enriched zone and similar to the typical bubble rise height. Thus, the geometry of the “box” was 4500×50×75 m.

Data from different heights above the seafloor were used as foundations for the different calculations. Continuous horizontal profiles based on discrete samples were constructed by linear interpolation between samples from similar depths, i.e. samples from ~5, ~15 and ~20 m from the seafloor (Figure

7). Vertical gradients matching the dissolution function were applied to the horizontally interpolated data in order to arrive at vertical distributions along the horizontal. A horizontal gradient, across the width of the box, of 1.5 nmol l^{-1} m^{-1} was used to account for turbulent dispersion. Integration of the data and subsequent scaling by the box geometry gave the average concentrations (nmol l^{-1}). The method was repeated for 5, 15 and 20 m based data and results are reported as "box" values in Table 1.

The line-average concentration from the 2D model was calculated from depths following the MILS trajectory and the 2D model box-average was extracted from 390 – 315 m water depth (the 2D model is 400 m deep along the entire box). The CV model yielded one value for the entire line/box.

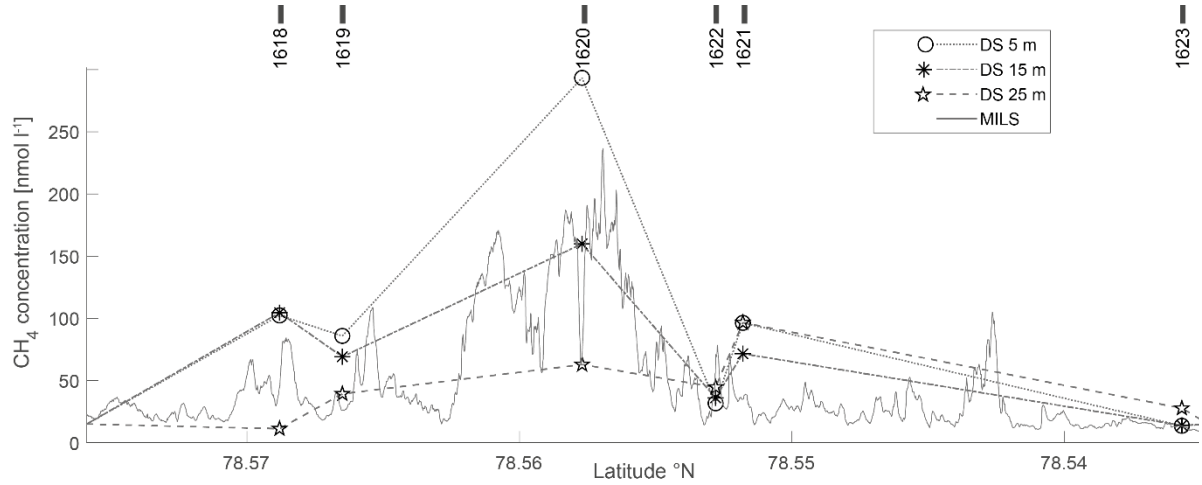

Figure 7. Continuous MILS profile along line 3 compared to discrete samples concentrations at various depths. Simple line averages were calculated along the box, considering either high-resolution measurements, model results or values linearly interpolated between discrete points. These results are denoted "line" in Table 1.

Despite high flow rates and additional CH4 from an unknown source, the average CH_4 concentration in the box volume, based on continuous data, is essentially the same as the average obtained from discrete data acquired 15 m above the seafloor (27 vs 29 nmol l^{-1}), while the numerical models yield slightly lower averages (19 and 20 nmol l^{-1}). The initial CH_4 box-concentration (93 nmol l-1) estimated by Graves et al. (2015) was obtained from a CTD transect across the slope and directly over the most active bubble plumes and should not be directly compared with our estimates.

Table 1. Average concentrations (nmol l^{-1}) calculated with different methods. Points indicate simple average of sparse sampling and High res. /Interpolated indicates high-resolution measurements and Interpolated values respectively.

		Line		Box
Dataset	Meters above seafloor	Points	High resolution / Interpolated	High resolution / Interpolated
CV model	-	20		
MILS	~15	-	63	27
2D model	~15*	-	58	19
DS low	~5	104	102	45
DS intermediate	~15	76	71	29
DS high	~20	47	49	19

* Concentrations from the 2D model were extracted from depths matching the MILS instrument depth for direct comparison

4 Discussion

The flow rates acquired with Flarehunter agrees well with an example flow rate of 232 ml min^{-1} for a single flare, using a bubble catcher (Cluster C5, Table 5 (Sahling et al., 2014)). The average flowrate obtained along line 3 (240 ml min^{-1}) is almost double the average of 125 ml min^{-1} (6×20.9 mL min^{-1}) per bubble stream cluster estimated by Sahling et al. (2014). Our estimated average is higher because line 3 is directly over, and limited to, the most active venting zone in the area. The sum of the observed flow rates from 68 bubbles streams amounted to 13 l min^{-1}, which translates to 180 t y^{-1}, assuming constant flow. This may be compared to ~600 t y^{-1} estimated for a bigger area by Veloso et al. (2015) and 400 t y^{-1} (area 3) by Sahling et al. (2014) encompassing our area and more active seepage further north.

The MILS data collected 15 meters above seafloor along line 3 and near the vertical MILS-cast 1616 did not reveal the high concentrations (~ 200-nmol l^{-1}) measured during the vertical cast, emphasizing the heterogeneous CH_4 distribution, and the need for high-resolution sensing, rather than sparse discrete sampling.

Downstream tailing of CH_4 concentrations seen in the model was not observed anywhere with the MILS. In fact, a careful analysis reveal equal distribution of down-and upstream gradients. We explain the discrepancy by the fact that the model does not resolve diffusion along the model domain. If instrument response-time was a limiting factor, it would reduce both up- and downstream gradients equally and reveal any asymmetry if present. The observed symmetry suggest that CH_4 disperses equally in all horizontal directions around the bubble plumes while being advected away from bubble plumes. With that inference, it would be feasible to determine CH_4 flux from the seafloor by high-

resolution sensing during surveys designed with trajectory-spacing equal to single beam echosounder swath widths.

Enhanced CH_4 concentrations are mainly observed up to 75-100 meters above the seabed, which is supported by bubble models (e.g. McGinnis et al., 2006), showing that bubbles of observed sizes (~3 mm equivalent radius) transport CH_4 up to approximately this height. We suggest that this height limit is a result of rapid horizontal and inefficient vertical mixing. Density stratification plays an important role in the vertical distribution of CH_4 because considerable turbulent energy is required to mix solvents across diapycnals. Vertical mixing of solvents including CH_4 is therefore inhibited even without a strong pycnocline, contrary to the conception of Gentz et al. (2014), and Myhre et al. (2016), suggesting that a pycnocline is necessary as a barrier for the vertical transport.

Enhanced CH_4 concentrations up to 100 nmol l^{-1} without the acoustic signature of flares were observed north of the active flare zone (Figure 4 and 5b). Echograms from the CAGE 15-6 survey and previous surveys (2010 and 2013) did not reveal flares in the vicinity. This may indicate one of the following: a) CH_4 enriched water seepage from the seafloor exist nearby, b) bubble streams with bubbles too small for detection by echosounder emanates from the seafloor, or c) CH_4 was advected from a nearby bubble plume source, but not along the trajectory of the instruments. In our case, a temperature- and salinity anomaly reveals mixing of AW with colder and fresher water. Because mixing lines drawn in TS diagrams point to PW rather than a fresh water source, we favor the hypothesis that the additional CH_4 was transported downslope with AW mixed with some PW.

The numerical model relies on mapped bubble plumes, and the difference between measured and modelled CH_4 is obvious from 10:30 to 10:50 in Fig 7B. The additional CH_4 from high-resolution data underscores that echosounder mapping and modelling is not enough to acquire a correct estimate of a CH_4 inventory.

Methane Concentrations peaking in midwater (~160 and 220 m) picked up by the vertical MILS cast (1616) would only by chance be picked up with discrete water sampling and could not have been inferred from echosounding, highlighting the usefulness of high-resolution CH_4 profiling. We did not identify the source of the elevated CH_4 in this location, but it may be may be attributed to nearby seepage. Known seepage locations exist only a few km away from the location at the shallow shelf (50 – 150 mbsl) and the shelf-break (~250 mbsl) (Veloso et al., 2015), but it is doubtful if seepage from these locations can reach the surveyed area, as the WSC is persistently northbound.

The continuous profile from the MILS results in a lower average concentration due to the high variability. The choice of discrete sample locations and depths can significantly affect the resulting average and highlights the consequence of low-resolution sampling and subsequent interpolation.

Even though results for the average concentrations in a specific volume can (by chance) be similar for high resolution profiling and discrete sampling, the added detail of the structure allows for better understanding of the processes that influence the dissolved gas.

5 Conclusion

The MILS sensor was successfully deployed from the ship while providing real-time telemetry and obtaining unprecedented details of both vertical and horizontal distribution of dissolved CH_4 in an area of intense seepage. Owing to the high-resolution data, we perceived more heterogeneous CH_4 distribution than previously presumed.

Discrete sampling with subsequent GC analysis of CH_4 concentrations agreed well with the MILS data while highlighting the importance of high-resolution sampling in order to resolve the variability of the CH_4. Average concentrations given by discrete sampling coincided, by chance, with the average from high-resolution measurements, but we showed that sparse sampling may seriously over- or underestimate averages, which may have serious consequences if the acquired concentrations are included in circulation- or climate models.

The heterogeneous distribution of the measured CH_4 matched with acoustic backscatter data, with very high concentrations close to the most intense flares and lower concentrations away from them. Nevertheless, we observed high concentrations also without acoustic evidence of CH_4 sources, even after checking additional acoustic datasets from previous surveys covering the same area. Similarly, midwater high concentrations were missed by discrete sampling during a vertical cast.

Properly accounting for the time lag between instrument- and ship observations proved essential for the data analysis, and puts forward the importance of monitoring instrument depth and cable payout during similar tow-surveys. The method could be further improved by attaching an acoustic underwater positioning device on the instrument assembly.

The high-resolution data was compared with a new 2D model, which required a high diffusion coefficient in order to reproduce the variability of measurements. This is confirmed by high turbulence in the area, understood by the strong currents.

Despite high flow rates and additional CH4 with unknown sources, the average CH_4 concentrations are relatively low in the area, which we attribute to fast dispersion away from the bubble plumes. The origin of the additional CH_4, not from local bubble plumes, remain unknown, which calls for further surveys in the area to better understand the total contribution of CH_4 from the area and reveal additional sources if present.

In summary, we have presented new methods for understanding the dynamics of CH_4 after its release from the seafloor, including a reliable and fast CH4 sensor giving high-resolution data. We employed an inverse acoustic model for seepage gas quantification, providing the basis for a new 2D forward model and a new control volume model, both in good agreement with observations. This is promising for future work of similar kind and we see many potential uses for high-resolution CH_4 sensing with the MILS within environmental studies and CH_4 sniffing, desired by the oil- and gas industry for gas leakage detection.

6 Acknowledgements and data

The research leading to these results has received funding from the European Community's Seventh Framework Programs ERC-2011-AdG under grant agreement n° 291062 (ERC ICE&LASERS), as well as ERC-2015-PoC under grant agreement n° 713619 (ERC OCEAN-IDs). Additional funding support was provided by SATT Linksium of Grenoble, France (maturation project SubOcean CM2015/07/18). The collaboration between CAGE and IGE was initiated thanks to the European COST Action ES902 PERGAMON. The research is part of the Centre for Arctic Gas Hydrate, Environment and Climate (CAGE) and is supported by the Research Council of Norway through its Centers of Excellence funding scheme grant No. 223259. We thank the crew on-board RV Helmer Hanssen for the assistance during the cruise, and the University of Svalbard for the logistics support. A dataset comprising the MILS sensor data and echosounder files is available from the UiT Open Research Data repository https://doi.org/10.18710/UWP6LL

References

Andreassen, K., Hubbard, A., Winsborrow, M., Patton, H., Vadakkepuliyambatta, S., Plaza-Faverola, A., Gudlaugsson, E., Serov, P., Deryabin, A., Mattingsdal, R., Mienert, J. & Bünz, S. 2017. Massive blow-out craters formed by hydrate-controlled methane expulsion from the Arctic seafloor. *Science*, 356(6341), pp. 948-953. doi: 10.1126/science.aal4500.

Berndt, C., Feseker, T., Treude, T., Krastel, S., Liebetrau, V., Niemann, H., Bertics, V. J., Dumke, I., Dünnbier, K., Ferré, B., Graves, C., Gross, F., Hissmann, K., Hühnerbach, V., Krause, S., Lieser, K., Schauer, J. & Steinle, L. 2014. Temporal Constraints on Hydrate-Controlled Methane Seepage off Svalbard. *Science*, 343(6168), p. 284. doi: 10.1126/science.1246298.

Biastoch, A., Treude, T., Rüpke, L. H., Riebesell, U., Roth, C., Burwicz, E. B., Park, W., Latif, M., Böning, C. W. & Madec, G. 2011. Rising Arctic Ocean temperatures cause gas hydrate destabilization and ocean acidification. *Geophysical Research Letters*, 38(8). doi: 10.1029/2011GL047222.

Boetius, A. & Wenzhöfer, F. 2013. Seafloor oxygen consumption fuelled by methane from cold seeps. *Nature Geoscience*, 6(9), pp. 725-734. doi: 10.1038/ngeo1926.

Boulart, C., Prien, R., Chavagnac, V. & Dutasta, J.-P. 2013. Sensing Dissolved Methane in Aquatic Environments: An Experiment in the Central Baltic Sea Using Surface Plasmon Resonance. *Environmental Science & Technology*, 47(15), pp. 8582-8590. doi: 10.1021/es4011916.

Cottier, F., Tverberg, V., Inall, M., Svendsen, H., Nilsen, F. & Griffiths, C. 2005. Water mass modification in an Arctic fjord through cross-shelf exchange: The seasonal hydrography of Kongsfjorden, Svalbard. *Journal of Geophysical Research: Oceans*, 110(C12). doi: 10.1029/2004JC002757.

Damm, E., Mackensen, A., Budéus, G., Faber, E. & Hanfland, C. 2005. Pathways of methane in seawater: Plume spreading in an Arctic shelf environment (SW-Spitsbergen). *Continental Shelf Research*, 25(12), pp. 1453-1472. doi: 10.1016/j.csr.2005.03.003.

Dewey, R. K. 1999. Mooring Design & Dynamics—a Matlab® package for designing and analyzing oceanographic moorings. *Marine Models*, 1(1), pp. 103-157. doi: 10.1016/S1369-9350(00)00002-X.

Egbert, G. D. & Erofeeva, S. Y. 2002. Efficient Inverse Modeling of Barotropic Ocean Tides. *Journal of Atmospheric and Oceanic Technology*, 19(2), pp. 183-204. doi: 10.1175/1520-0426(2002)019<0183:EIMOBO>2.0.CO;2.

Ferré, B., Mienert, J. & Feseker, T. 2012. Ocean temperature variability for the past 60 years on the Norwegian - Svalbard margin influences gas hydrate stability on human time scales. *Journal of Geophysical Research: Oceans (1978–2012)*, 117(C10). doi: 10.1029/2012JC008300.

Gentz, T., Damm, E., Schneider von Deimling, J., Mau, S., McGinnis, D. F. & Schlüter, M. 2014. A water column study of methane around gas flares located at the West Spitsbergen continental margin. *Continental Shelf Research*, 72, pp. 107-118. doi: 10.1016/j.csr.2013.07.013.

Graves, C. A., Steinle, L., Rehder, G., Niemann, H., Connelly, D. P., Lowry, D., Fisher, R. E., Stott, A. W., Sahling, H. & James, R. H. 2015. Fluxes and fate of dissolved methane released at the seafloor at the landward limit of the gas hydrate stability zone offshore western Svalbard. *Journal of Geophysical Research: Oceans*, 120(9), pp. 6185-6201. doi: 10.1002/2015JC011084.

Hong, W. L., Torres, M. E., Portnov, A., Waage, M., Haley, B. & Lepland, A. 2018. Variations in Gas and Water Pulses at an Arctic Seep: Fluid Sources and Methane Transport. *Geophysical Research Letters*, 45(9), pp. 4153-4162. doi: 10.1029/2018GL077309.

Loeng, H. 1991. Features of the physical oceanographic conditions of the Barents Sea. *Polar Research*, 10(1), pp. 5-18. doi: 10.3402/polar.v10i1.6723.

Marín-Moreno, H., Minshull Timothy, A., Westbrook Graham, K., Sinha, B. & Sarkar, S. 2013. The response of methane hydrate beneath the seabed offshore Svalbard to ocean warming during the next three centuries. *Geophysical Research Letters*, 40(19), pp. 5159-5163. doi: 10.1002/grl.50985.

McDougall, T. J. & Barker, P. M. 2011. Getting started with TEOS-10 and the Gibbs Seawater (GSW) oceanographic toolbox. *SCOR/IAPSO WG*, 127, pp. 1-28.

McGinnis, D., Greinert, J., Artemov, Y., Beaubien, S. & Wüest, A. 2006. Fate of rising methane bubbles in stratified waters: How much methane reaches the atmosphere? *Journal of Geophysical Research: Oceans (1978–2012)*, 111(C9). doi: 10.1029/2005JC003183.

Myhre, C. L., Ferré, B., Platt, S. M., Silyakova, A., Hermansen, O., Allen, G., Pisso, I., Schmidbauer, N., Stohl, A. & Pitt, J. 2016. Extensive release of methane from Arctic seabed west of Svalbard during summer 2014 does not influence the atmosphere. *Geophysical Research Letters*, 43(9), pp. 4624-4631. doi: 10.1002/2016GL068999.

Reagan Matthew, T., Moridis George, J., Elliott Scott, M. & Maltrud, M. 2011. Contribution of oceanic gas hydrate dissociation to the formation of Arctic Ocean methane plumes. *Journal of Geophysical Research: Oceans*, 116(C9). doi: 10.1029/2011JC007189.

Reeburgh, W. S. 2007. Oceanic Methane Biogeochemistry. *Chemical Reviews*, 107(2), pp. 486-513. doi: 10.1021/cr050362v.

Ruppel, C. D. & Kessler, J. D. 2016. The Interaction of Climate Change and Methane Hydrates. *Reviews of Geophysics*. doi: 10.1002/2016RG000534.

Sahling, H., Römer, M., Pape, T., Bergès, B., dos Santos Fereirra, C., Boelmann, J., Geprägs, P., Tomczyk, M., Nowald, N. & Dimmler, W. 2014. Gas emissions at the continental margin west of Svalbard: mapping, sampling, and quantification. *Biogeosciences*, 11(21), pp. 6029-6046. doi: 10.5194/bg-11-6029-2014.

Saloranta, T. M. & Svendsen, H. 2001. Across the Arctic front west of Spitsbergen: high-resolution CTD sections from 1998–2000. *Polar Research*, 20(2), pp. 177-184. doi: 10.3402/polar.v20i2.6515.

Schauer, U., Fahrbach, E., Osterhus, S. & Rohardt, G. 2004. Arctic warming through the Fram Strait: Oceanic heat transport from 3 years of measurements. *Journal of Geophysical Research: Oceans*, 109(C6). doi: 10.1029/2003JC001823.

Shakhova, N., Semiletov, I., Leifer, I., Sergienko, V., Salyuk, A., Kosmach, D., Chernykh, D., Stubbs, C., Nicolsky, D., Tumskoy, V. & Gustafsson, O. 2014. Ebullition and storm-induced methane release from the East Siberian Arctic Shelf. *Nature Geosci*, 7(1), pp. 64-70. doi: 10.1038/ngeo2007.

Shakhova, N., Semiletov, I., Salyuk, A., Yusupov, V., Kosmach, D. & Gustafsson, Ö. 2010. Extensive Methane Venting to the Atmosphere from Sediments of the East Siberian Arctic Shelf. *Science*, 327(5970), pp. 1246-1250. doi: 10.1126/science.1182221.

Skogseth, R., Haugan, P. M. & Jakobsson, M. 2005. Watermass transformations in Storfjorden. *Continental Shelf Research*, 25(5), pp. 667-695. doi: 10.1016/j.csr.2004.10.005.

Sundermeyer, M. A. & Ledwell, J. R. 2001. Lateral dispersion over the continental shelf: Analysis of dye release experiments. *Journal of Geophysical Research: Oceans*, 106(C5), pp. 9603-9621. doi: 10.1029/2000JC900138.

Tishchenko, P., Hensen, C., Wallmann, K. & Wong, C. S. 2005. Calculation of the stability and solubility of methane hydrate in seawater. *Chemical geology*, 219(1), pp. 37-52. doi: 10.1016/j.chemgeo.2005.02.008.

Veloso, M., Greinert, J., Mienert, J. & De Batist, M. 2015. A new methodology for quantifying bubble flow rates in deep water using splitbeam echosounders: Examples from the Arctic offshore NW‐Svalbard. *Limnology and Oceanography: Methods*, 13(6), pp. 267-287. doi: 10.1002/lom3.10024.

Weber, T. C., Mayer, L., Jerram, K., Beaudoin, J., Rzhanov, Y. & Lovalvo, D. 2014. Acoustic estimates of methane gas flux from the seabed in a 6000 km2 region in the Northern Gulf of Mexico. *Geochemistry, Geophysics, Geosystems*, 15(5), pp. 1911-1925. doi: 10.1002/2014GC005271.

Westbrook, G. K., Thatcher, K. E., Rohling, E. J., Piotrowski, A. M., Pälike, H., Osborne, A. H., Nisbet, E. G., Minshull, T. A., Lanoisellé, M. & James, R. H. 2009. Escape of methane gas from the seabed along the West Spitsbergen continental margin. *Geophysical Research Letters*, 36(15). doi: 10.1029/2009GL039191.

Wiesenburg, D. A. & Guinasso Jr, N. L. 1979. Equilibrium solubilities of methane, carbon monoxide, and hydrogen in water and sea water. *Journal of Chemical and Engineering Data*, 24(4), pp. 356-360. doi: 10.1021/je60083a006.